Composites of Porous Materials with Ionic Liquids: Synthesis, Characterization, and Selective Gas Sorption Applications

by

Özce Durak

A Thesis Submitted to the
Graduate School of Engineering
in Partial Fulfillment of the Requirements
for the Degree of

Master of Science
In
Chemical and Biological Engineering

August 2022

Composites of Porous Materials with Ionic Liquids: Synthesis, Characterization, and Selective Gas Sorption Applications

Koç University
Graduate School of Science and Engineering

This is to certify that I have examined this copy of a master's thesis by

Özce Durak

and have found that it is complete and satisfactory in all respects,
and that any and all revisions required by the final
examining committee have been made.

Committee Members:

Prof. Alper Uzun (Advisor, Koç University)

Prof. Seda Keskin Avcı (Co-Advisor, Koç University)

Prof. Şahika Sena Bayazit (Beykent University)

Assoc. Prof. Damla Eroğlu Pala (Boğaziçi University)

Assoc. Prof. Uğur Ünal (Koç University)

Date: 12.08.2022

To my beloved mom, dad, Demirtoş, and Olive.

ABSTRACT

Hybrid composites prepared by combining ionic liquids (ILs) with porous materials have become an increasingly important research field over the last few years owing to their tunable physicochemical properties. The enormous and continuous growth in the number of publications on the synthesis of such IL/porous materials and their exceptional performances in many different applications, mainly in gas sorption and separation applications, is a proof of importance of this field. Combined advantages of ILs and porous materials provide great potentials in gas sorption and separation owing to the superior performance measures of the hybrid composites. In this thesis, it was aimed to provide a contribute to the evolution of IL/porous material composites as a research field by considering two different types of porous materials, including metal-organic frameworks (MOFs) and carbonaceous-materials. Accordingly, in depth analyses on the synthesis methods, characterization techniques, and selective gas separation performance of IL-modified porous materials were conducted to provide important insights into the design of novel IL/porous material composites and to identify the most promising hybrid materials for gas sorption and separation applications. Examination of the structural factors controlling the chemical and thermal stabilities of novel IL/MOF composites was made to elucidate the resulting changes in the physicochemical structure of pristine MOF upon the incorporation of IL. Results illustrated that the composite with the ligand-functionalized MOF exhibited a lower degree of decrease in the thermal stability limits compared to the those containing non-functionalized counterpart. Then, systematic changes in the structure of MOF were further investigated by incorporating the same IL, into the cages of three different Zr-MOFs and extraordinary performance improvements in the selective gas separation were achieved emphasizing the significance of MOF selection on the resulting molecular affinity. Motivated from the superior performance obtained through the presence of a surface IL layer, a core-shell type IL/MOF composite was designed by an integrated computational-experimental hierarchical approach for improved air separation application. Later on, an activated carbon (AC) was modified with IL to extent the scope of the field by utilizing a cost-effective and chemically robust porous material for enhanced CO_2 separation performance. The main challenges and opportunities in synthesis methods, characterization techniques, and gas sorption applications of IL/porous materials were discussed in detail to create a road map for the era. Recent advances of the field addressed in this thesis will provide a more in-depth insight into the design and development of these novel hybrid materials and their replacement with conventional materials.

ÖZET

İyonik sıvıların (İS'ler) gözenekli malzemelerle birleştirilmesiyle hazırlanan hibrit kompozitler, ayarlanabilir fizikokimyasal özellikleri nedeniyle son birkaç yılda giderek daha önemli bir araştırma alanı haline geldi. Bu tür İS/gözenekli malzemelerin sentezine ilişkin yayınların sayısındaki sürekli büyüme ve bunların birçok farklı uygulamada, özellikle gaz sorpsiyon ve ayırma uygulamalarında, gösterdikleri olağanüstü performans bu alanın öneminin bir kanıtıdır. İS'lerin ve gözenekli malzemelerin birleşik avantajları, hibrit kompozitlerin gaz sorpsiyonunda ve seçici ayırmada üstün performans göstermeleri yönünde büyük bir potansiyel sağlar. Bu tezde, metal-organik çerçeveler (MOF'lar) ve karbonlu malzemeler olmak üzere iki farklı gözenekli malzeme türü ele alınarak, İS/gözenekli malzeme kompozitlerinin bir araştırma alanı olarak evrimine katkıda bulunmak amaçlandı. Yeni İS/gözenekli malzeme kompozitlerinin tasarımı hakkında önemli bilgiler sağlamak ve yüksek gaz ayırma performanslı hibrit malzemeleri belirlemek için İS ile modifiye edilmiş gözenekli malzemelerin sentez yöntemleri, karakterizasyon teknikleri ve seçici gaz ayırma performansları hakkında derinlemesine analizler yapıldı. Bu doğrultuda, İS'in dahil edilmesi üzerine MOF'un fizikokimyasal yapısında ortaya çıkan değişiklikleri aydınlatmak için İS/MOF kompozitlerinin kimyasal ve termal stabilitelerini kontrol eden yapısal faktörler incelendi. Sonuçlar, ligandla işlevselleştirilmiş MOF'a sahip kompozitin, işlevselleştirilmemiş muadili içerenlere kıyasla termal stabilite limitlerinde daha düşük bir azalma derecesi sergilediğini gösterdi. Daha sonra, aynı İS'in üç farklı Zr-MOF'un yapısına dahil edilerek MOF yapısındaki sistematik değişikliklerin etkisi daha fazla araştırıldı ve MOF seçiminin ortaya çıkan moleküler afinite ve seçici gaz ayrımı performansı üzerindeki önemi vurgulandı. Yüzeyde bulunan İS tabakasının varlığında elde edilen üstün performanstan ilham alarak, yüksek O_2 ayırma performanslı çekirdek-kabuk tipi bir İS/MOF kompoziti geliştirildi ve bu kompozit tasarımında entegre bir hesaplamalı-deneysel hiyerarşik yaklaşım kullanıldı. Daha sonra, İS/gözenekli malzeme araştırma alanının kapsamını genişletmek adına uygun maliyetli ve kimyasal olarak sağlam bir aktif karbon gözenekli malzemesi yüksek CO_2 ayırma performansı için İS ile modifiye edildi. Sentez yöntemleri, karakterizasyon teknikleri ve gaz sorpsiyon uygulamalarındaki temel zorluklar ve fırsatlar, dönem için bir yol haritası oluşturmak amacıyla ayrıntılı olarak tartışıldı. Bu tezde ele alınan alandaki son gelişmeler, İS/gözenekli yapı hibrit malzemelerinin tasarımı, geliştirilmesi ve geleneksel malzemeler yerine kullanılması hakkında daha derinlemesine bir anlayış sağlayacaktır.

ACKNOWLEDGEMENTS

First and foremost, I would like to express my sincere gratitude to my academic advisors, Prof. Alper Uzun and Prof. Seda Keskin Avcı, for their endless support, guidance, many life lessons, and incomparable contributions towards my education from the first day of my undergraduate degree to the last day of my graduate degree. They always trusted and encouraged me to think out of the box to discover new things by providing space for new research ideas. I am immensely grateful and feeling extremely lucky to be a part of their research teams, Uzun Lab and NEMO, which provided excellent opportunities for me throughout my research adventure.

I am thankful to my MSc committee members, Prof. Şahika Sena Bayazit, Assoc. Prof. Damla Eroğlu Pala, and Assoc. Prof Uğur Ünal who have spent their valuable time in guiding and evaluating my thesis. Moreover, I sincerely acknowledge the support of Koc University TUPRAS Energy Center (KUTEM) and Koc University Surface Science and Technology Center (KUYTAM), particularly, Dr. Barış Yağcı, Dr. Gülsu Şimşek, Dr. Amir Motallebzadeh, and Dr. Hadi Jahangiri for their guidance and support in characterization tests.

I also would like to express my deepest gratitude to my undergraduate professors Prof. Yaman Arkun, Prof. Can Erkey, and Asst. Prof. Cem Albayrak for their support, guidance, patience, and wisdom. They have answered my endless questions about everything in deep detail and devoted their valuable time to discuss different perspectives.

I thankfully acknowledge the financial support provided by the European Research Council (ERC) under the European Union's Horizon 2020 Research and Innovation Programme (ERC-2017-Starting Grant, Grant Agreement No 756489-COSMOS).

My sincere and special thanks go to my dear friends and collaborators Hasan Can Gülbalkan and Nitasha Habib for all our conversation sessions, zoom meetings, dinners, and motivational speeches. I appreciate their endless research contributions, support, and friendship. They have been great friends and colleagues in every way possible. I would like to thank both for motivating me at every step of the way and providing a workplace which I very much enjoyed being in. I also would like to thank my “real life” best friend, Yasemin Barutçuoğlu, and my “lab” best friend, Amin Mohammadpour, for their extreme kindness and help throughout my research studies. I feel lucky to have their wonderful friendship in my life which gives me comfort and happiness.

I would like to thank all past and present NEMO and Uzun Lab members individually for all the night discussions, help, friendship, and fun memories. Many thanks to NEMO group

members; Dr. Muhammad Zeeshan, Dr. Çiğdem Altıntaş, Dr. Zeynep Pınar Haslak, Hilal Dağlar, Gökhan Önder Aksu, Göktuğ Erçakır, and Sena Aydın. I am also thankful to my labmates from Uzun Lab; Dr. Melike Babucci, Dr. Samira Fatma Kurtoğlu-Öztulum, Dr. Özge Deniz Bozkurt, Fulya Erdem, Kaan Yalçın, Ezgi Demiröz, Gizem Sultan İş, Yuxin Zhao, Hatice Pelin Çağlayan, Kübra Tıraş, Harun Kulak, Safiyye Kavak, and H. Mert Polat. Moreover, I would like to thank Dr. Navid Solati, Emre Usman, and Seda Sarp for their friendship and help during my studies.

Finally, I would like to express my immense gratitude, appreciation, and love to my dear family who were there on my side at every failure and success. Thank you, *mom and dad,* for supporting me and always putting my dreams before your own comfort. I have reached where I am today only because of your hard work aimed to provide the best of everything for me. Thank you, *my baby brother Demir aka "Demirtoş",* for being my joy and emotional support child for nine big years. I appreciate your patience and tolerance every time when I couldn't spare time for you. You are teaching me how to love unconditionally every single day with your little heart. I am looking forward to the day that you will thank me in your thesis. Also, thank you, *my puppy Olive,* for being the smartest puppy alive and helping me (sleeping on my lap) during the writing of my thesis. I cannot express how much I love and owe each one of you!

Last but not least, I would like to thank myself for every sleepless night, every missed social event, and every missed family time. I have willingly sacrificed so much of my time, joy, and tears to construct this thesis for three years. And now, finalizing this word document gives me an extreme happiness by knowing that I have accomplished all my aimed milestones up to this point. Nonetheless, I am thankful for every step that I have taken in this roller-coaster ride of academia. Though I made a lot of mistakes, I am glad to have that passion to try one more time every single day.

TABLE OF CONTENTS

LIST OF TABLES

LIST OF FIGURES

LIST OF PUBLICATIONS

1. **Durak O.,** Kulak H., Kavak S., Polat H.M., Keskin S. and Uzun A. "Towards complete elucidation of structural factors controlling thermal stability of IL/MOF composites: Effects of ligand functionalization on MOFs" Journal of Physics: Condensed Matter Special Issue: Metal-Organic Frameworks in Physics 32, 48 (**2020**).

2. Zeeshan M., Kulak H., Kavak S., Polat H.M., **Durak O.,** Keskin S., and Uzun A. "Influence of anion size and electronic structure on the gas separation performance of ionic liquid/ZIF-8 composites" Microporous and Mesoporous Materials 306, 110446 (**2020**).

3. Kavak S.,* **Durak O.,*** Kulak H., Polat H.M., Keskin S. and Uzun A. "Enhanced Wastewater Treatment Performance of Ionic Liquid Impregnated MOF: Dye Removal by [BMIM][PF_6]/MIL-53(Al) Composite" Frontiers in Chemistry 8, 622567 (**2021**).***Equal contribution**

4. **Durak O.,** Zeeshan M., Habib N., Gulbalkan H. C., Alsuhile A., Caglayan H. P., Kurtoglu-Oztulum S. F., Zhao Y., Haslak Z. P., Uzun A., and Keskin S. "Composites of Porous Materials with Ionic liquids: Synthesis, Characterization, Applications, and Beyond" Microporous and Mesoporous Materials 332, 111703 (**2022**).

5. **Durak O.,** Zeeshan M., Keskin S., and Uzun A. "[BMIM][OAc] Coating Layer Makes Activated Carbon Almost Completely Selective for CO_2" Chemical Engineering Journal 437, 135436 (**2022**).

6. Habib N., **Durak O.**, Zeeshan M., Uzun A., and Keskin S., "A Novel IL/MOF/Polymer Mixed Matrix Membrane having Superior CO_2/N_2 Selectivity" Journal of Membrane Science, 120712 (**2022**).

7. Zeeshan M.,* Gulbalkan H. C.,* **Durak O.,*** Haslak Z. P., Unal U., Keskin S., and Uzun A. "An integrated computational-experimental hierarchical approach for the rational design of an IL/UiO-66 composite offering infinite CO_2 selectivity" Advanced Functional Materials, 2204149 (**2022**). ***Equal contribution**

NOMENCLATURE

IL = Ionic Liquid

MOF = Metal-Organic Framework

AC = Activated Carbon

COF = Covalent Organic Framework

XRF = X-ray Fluorescence

SEM = Scanning Electron Microscopy

EDX = Energy Dispersive X-ray

BET = Brunauer-Emmett-Teller

BJH = Barrett, Joyner and Halenda

XRD = X-ray Diffraction

TGA = Thermal Gravimetric Analysis

DTG = Derivative Thermal Gravimetric

FTIR = Fourier-Transform Infrared

ATR = Attenuated Total Reflectance

KBr = Potassium Bromide

XPS = X-ray Photoelectron Spectroscopy

TEM = Transmission Electron Microscopy

ICP-MS = Inductively Coupled Plasma Mass Spectrometry

NMR = Nuclear Magnetic Resonance

DLS = Dynamic Light Scattering

RBF = Round Bottom Flask

DFT = Density Functional Theory

IAST = Ideal Adsorbed Solution Theory

GCMC = Grand Canonical Monte Carlo

COSMO-RS = Conductor-like Screening MOdel for Realistic Solvents

CSD = The Cambridge Structural Database

MIL = Materials Institute Lavoisier

PSD = Pore Size Distribution

S_{BET} = BET surface area (m^2/g)

T_{onset} = Onset temperature (°C)

T'_{onset} = Derivative onset temperature (°C)

V_{pore} = BJH pore volume (cm^3/g)

ZIF = Zeolitic imidazolate framework

rGA = Reduced Graphene Aerogel

Zr-MOFs = Zirconium-based MOFs

PCN = Porous Coordination Network

Chapter 1: Introduction*

*This chapter is a section of Review article published in *Microporous and Mesoporous Materials 332, 111703 (2022)* by authors Özce Durak, Muhammad Zeeshan, Nitasha Habib, Hasan Can Gülbalkan, Ala Abdulalem Abdo Moqbel Alsuhile, Hatice Pelin Çağlayan, Samira F. Kurtoğlu-Öztulum, Yuxin Zhao, Zeynep Pınar Haşlak, Alper Uzun, and Seda Keskin. The related part presented here was written mainly by the author of this thesis.

Post-synthesis modification of a porous material offers the opportunity to design a composite material with task-specific properties desirable for any targeted application. In this regard, hybrid composites that can be synthesized by combining two or more materials with different physicochemical properties provide various advantages. Such hybrid composites exhibit almost limitless possibilities for superior performance in any target application with enhanced structural characteristics that offer improved chemical and thermal properties and novel functionalities. Among different guest molecules, ILs provide a high degree of flexibility owing to the availability of a theoretically unlimited number of cation-anion combinations, high thermal/chemical stabilities, and low vapor pressures. ILs are molten salts in the liquid phase at room temperature and are commonly used as solvents. Most of ILs have more environmentally-friendly production pathways compared to conventional solvents, and thus can be considered as alternative "green solvents" to volatile organic compounds (VOCs).[1]

Over the last two decades, a myriad of porous materials has been utilized and modified with ILs for hybrid composite generation.[2-8] Among them, MOFs, COFs, zeolites, and carbonaceous materials have become the focus for engineering processes owing to their unique and versatile physicochemical properties, such as high surface area and porosity, structural tunability, and flexibility.[9] In these hybrid materials, ILs can be used as different types of modifying agents, such as a functional ligand for structural modifications or a solvent for the synthesis of a composite material. In addition, ILs are directly used to prepare membranes with IL/porous material composites and are introduced as a third component to improve the interface adhesion between polymer and inorganic fillers for the preparation of mixed matrix membranes (MMM).

The fast-growing field of hybridization with ILs generated several different types of hybrid composite materials, such as IL/MOFs,[2, 5, 10-13] IL/COFs,[14, 15] IL/zeolites,[16, 17] and IL/carbonaceous-materials,[4, 18, 19] for potential applications in adsorption-based separation processes.[5, 10] On the other hand, various types of membranes with IL/porous material composites including supported IL membranes (SILMs),[20] IL polymer membranes (ILPMs),[21] IL/MOF mixed matrix membranes (IL/MOF MMMs),[22] and poly(ionic liquid) membranes (PILMs)[23, 24] have shown promising improvements in membrane-based gas separation applications as well.[25] These hybrid materials provide

cost-efficiency, superior performances, and new possibilities for many applications, such as catalysis [26, 27], liquid-phase adsorption and separation,[8, 28] and ionic conductivity [29-31] as shown in Figure 1.1.

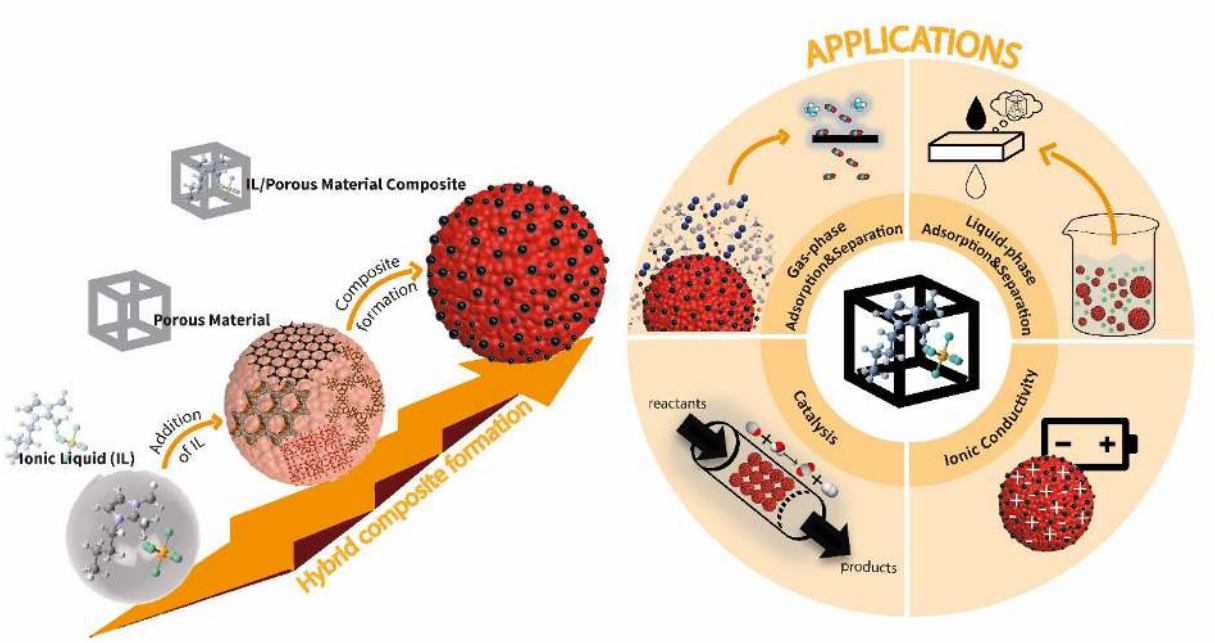

Figure 1.1. Representative illustration for composite formation and the scope of application for IL/porous material composites.

The historical evolution of IL/porous material composites starting from the investigation of the first protic IL in 1914 is illustrated in Figure 1.2. To the best of our knowledge, the field of IL/porous material composites started in 1997 with the IL-incorporated composite membranes to enhance the stability of membrane structure for ionic conductivity studies.[32] Then, in 2002, the solvothermal synthesis of a MOF was conducted by utilizing an IL as the solvent and structure-directing agent, which was eventually named as ionothermal synthesis.[33, 34] Later in 2004 and 2010, IL usage was extended to other types of porous materials covering the synthesis of zeolites and functionalized graphene, respectively.[35, 36] Thereafter, in 2008, an IL/carbonaceous-material composite was used for catalysis application.[26]

With increasing experimental research studies in the field, the need for more extensive screening methods has become a critical issue. Thus, computational screening methods were developed to screen thousands of different IL/porous material composites to address future directions in experimental research.[6, 37] In 2014, the first experimental

study on IL-impregnated MOF composite was performed for the case of liquid-phase adsorptive desulfurization.[38] After that point, the scope of application for IL/porous material composites was extended to various research fields from gas adsorption to catalysis with various types of IL/porous material composites.[2, 4, 10, 14, 23] There exists a large number of promising studies in the literature for each application field, and the scale of screening is enhanced to a level where the best-performing combinations of materials can be determined among more than thousands of candidates for experimental testing.[8, 13, 39-41]

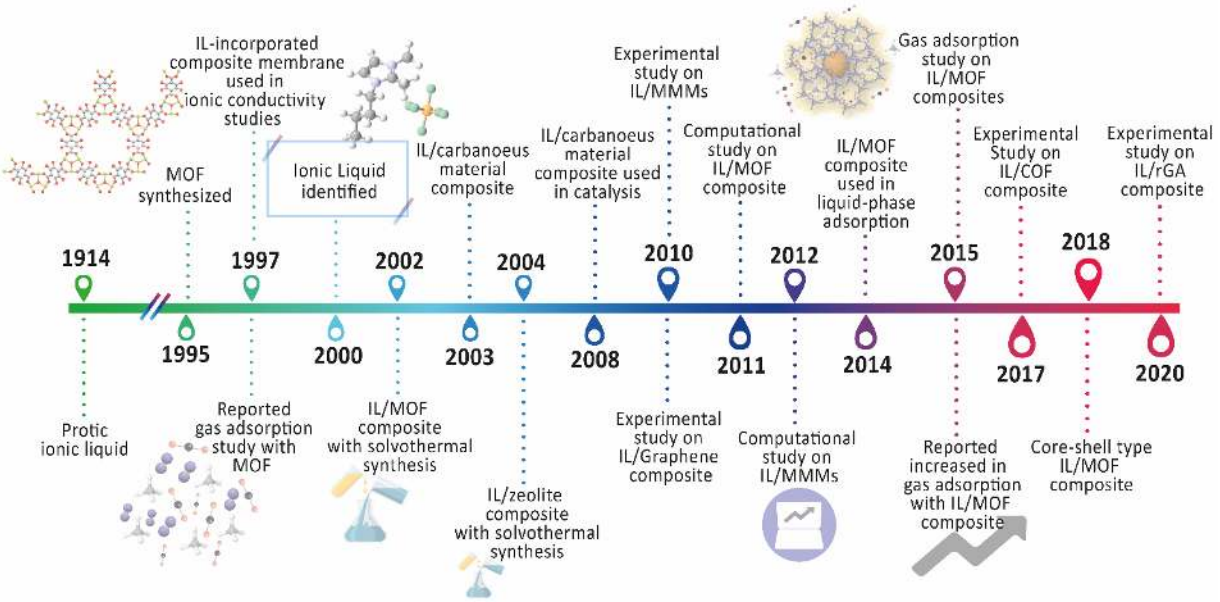

Figure 1.2. The progress in the historical evolution of IL/porous material composites.

In this thesis, each chapter represents a different research study to elucidate the impact of IL-incorporation on the structural properties and gas separation performance of porous materials, namely MOFs and ACs. In Chapter 2, it is aimed to present a comprehensive overview of the recent advances in the synthesis methods, characterization techniques, and gas separation performance of IL/porous material composites, namely IL/MOFs and IL/ACs, covering state-of-the-art experimental advances. In Chapter 3, synthesis of IL-incorporated composites and experimental methodologies including various characterization techniques are explained in detail. In addition to these, computational methodologies and calculation methods that are critical to identify the promising composites and quantify the interactions between ILs and porous materials, are highlighted in this chapter.

In Chapter 4, elucidation of structural factors controlling the thermal stability limits of IL/MOF composites and the effect of MOF's ligand functionalization were discussed. A hydrophilic IL, [BMIM][$MeSO_4$], was incorporated into UiO-66 and its ligand functionalized counterpart, NH_2-UiO-66, and the resulting changes in thermal stability limits were investigated with the help of several characterization techniques.

In Chapter 5, the effect of MOF's organic linker was investigated by post-synthetically incorporating a hydrophilic IL, [BMIM][$C(CN)_3$], into three different zirconium-based MOFs synthesized by using different organic linkers, namely UiO-66, UiO-67, and Zr-Fumarate. Results utilized to obtain a fundamental level understanding of the structure-performance relationship for synthesized IL/MOF composites by analyzing their corresponding structural changes and gas separation performance.

Placement of IL molecules in IL/MOF composites holds a significant importance owing to its vital effect on the gas sorption performance. Accordingly, there can be two possible placements: (i) IL molecules can be positioned inside the cages of MOFs by interacting with the pore walls, (ii) IL molecules can be positioned on the surface of MOF as they cannot enter into the pores because of their sizes. Positioning inside the cages of MOFs offers improved gas selectivity performance, however, comes with a trade-off between gas sorption capacity and selectivity due to the pore occupation with IL molecules. On the other hand, positioning on the surface of MOF cages offers a core-shell type structure with improved gas selectivity performance and sorption capacity, however, the smart-selection of a bulky IL must be made prior to the synthesis of IL/MOF composite. In Chapter 6, PCN-250(Fe) was modified by using a phosphonium-based IL, [$P_{6,6,6,14}$][DCA], with a significantly large molecular size to form a "core-shell" type of IL/MOF composite. Composites were characterized in detail by several characterization techniques and utilized in air separation application with the aim of selectively separating O_2 from N_2.

Post-synthetic modification of porous materials with ILs were identified as a prominent technique to enhance the gas separation performance of various porous materials. However, this technique still mainly utilized for MOFs compared to the other porous material types. Therefore, other cost-efficient, thermally stable porous materials, such as carbonaceous materials, should be investigated for improved gas separation performance upon IL-incorporation. In Chapter 7, an AC was modified with

[BMIM][OAc] to investigate the resulting changes in CO_2 separation performance. Synthesized IL/AC composites were characterized and analyzed in detail to demonstrate an understanding of structure-performance relationship.

In Chapter 8, main conclusions drawn from each study are discussed briefly. Current challenges and opportunities in various applications of IL/porous material composites including the rational design of composites, stability of materials, elucidation of the structural factors that control various performance measures, applicability into real-life processes, cost, and combination of experiments with computational studies are provided to suggest directions for the prospective studies.

Chapter 2: Literature Review*

*This chapter is a section of Review article published in *Microporous and Mesoporous Materials 332, 111703 (2022)* by authors Özce Durak, Muhammad Zeeshan, Nitasha Habib, Hasan Can Gülbalkan, Ala Abdulalem Abdo Moqbel Alsuhile, Hatice Pelin Çağlayan, Samira F. Kurtoğlu-Öztulum, Yuxin Zhao, Zeynep Pınar Haşlak, Alper Uzun, and Seda Keskin. The related part presented here was written mainly by the author of this thesis.

In this chapter, a comprehensive literature review on synthesis, characterization, and gas adsorption/separation performance of IL-incorporated composites, mainly IL/MOFs and IL/carbonaceous materials, is presented.

2.1 Preparation of IL-based Hybrid Materials

In-situ techniques, such as ionothermal synthesis, and post-synthesis modification techniques, such as capillary action, wet impregnation, ship-in-a-bottle, and grafting, are widely used to prepare new hybrid materials consisting of porous materials and ILs. These techniques provide a wide range of possibilities for higher performance and create opportunities to tune the porous structure accordingly. In this section, IL/porous material composites, which emerged because of the post-synthesis modification with IL, will be highlighted after a brief discussion on the *in-situ* synthesis of IL-based hybrid materials via ionothermal synthesis and reports on different chemical procedures.

2.1.1 *In situ* Synthesis of IL-based Hybrid Materials

Hybrid materials can be defined as the mixture of two different constituents combined at a molecular level. Throughout this section, solid porous materials with ILs as a constituent in their structure will be discussed as IL-based hybrid materials. During the *in-situ* synthesis of solid porous material, ILs can be used as a multi-functional green solvent by acting as both solvent and structure-directing agents. This method, called ionothermal synthesis, directly parallels the well-known hydrothermal synthesis with the only difference being the usage of IL as the solvent.[34] Moreover, ionothermal synthesis eliminates the possibility of any competition between the ions of solvent and ions of structure-directing agent during the growth of the porous solid by using one species simultaneously for both purposes.

Several *in-situ* synthesis techniques have been reported in the literature with ionothermal synthesis to obtain different porous materials, starting from zeolite analogues,[36] such as zeolites,[42] MOFs,[33] COFs,[43] and carbonaceous-materials.[44] Detailed review articles are also available on ionothermal synthesis of organic/inorganic porous solid materials.[42, 45, 46] However, there are certain limitations for this method in terms of matching of IL structure with the desired final porous material structure. The similarity between the common organic templates of zeolites and the cation part of IL significantly benefits the synthesis of zeolite-like

structures. However, there is also anion part present in the structure of IL and should be carefully selected according to the desired final structure. Anion part of the IL plays an important role in controlling the chemical and electronic nature of IL structure; therefore, it directly affects the synthesized porous solid during the synthesis.[47] Similarly, for IL/carbonaceous-material, the IL should have a high affinity towards carbonaceous-material to maintain the structural integrity, whereas, in the case of IL/MOF or IL/COF composites, organic linkers and metal salts should have sufficient solubility in ILs for *in-situ* synthesis. Moreover, for IL/MOF or IL/COF combinations, the organic linker's reactivity with the IL and the resulting charge neutrality of the surface can be listed as the other limitations. For instance, cation-templating and anion-templating synthesis routes of ionothermal synthesis result in charged structure where the size and the electronic structure of both constituents create an important impact on the final product. While the main goal of templating-based synthesis is to have a precise control over the final architecture, changing the size and electronic structure of the constituents does not produce very specific outcomes for precise structural architecture of the final porous material.

In the first attempt for ionothermal synthesis of the coordination polymer, [Cu(I)(bpp)][BF_4], [BMIM][BF_4] was used as a solvent, and the IL-based hybrid material contained only the anion of the IL, whereas cations remained in the solution to maintain the surface neutrality.[33, 48] Similarly, there are studies where the structure contains only the cationic part of the IL which acts as a structure directing agent,[42] and the IL is multi-functionalized through various templating routes with both constituents.[49] Consequently, the resulting structure, in which only one component is present, cannot reproduce the desired properties of the IL in the composite, and the precise control over the architectural design of final porous material cannot be maintained due to the possible multifunctionality of ILs.

Besides ionothermal synthesis, ILs are also used in different reaction routes to synthesize IL-based hybrid materials. In the synthesis of a graphene-like carbonaceous material, IL/graphene layered films were synthesized in the presence of IL, which played a crucial role in controlling the spacing between graphene layers during the direct reduction of graphene oxide.[35] Resulting IL-based hybrid materials, generally called graphene IL layered films, contain IL molecules in-between graphene layers. Similarly, in another study, an IL was used as a stabilizing agent during the exfoliation of graphite to obtain IL/graphene hybrid material.[50] Surfactant-like property of ILs makes them

suitable for usage as a stabilizing agent during exfoliation of graphite. Moreover, synthesis techniques such as the sol-gel method is also used to confine IL molecules inside pores of porous materials to obtain IL-based hybrid materials.[51, 52]

2.1.2 Post-synthesis Modification Techniques to Prepare IL/Porous Material Composites

To overcome the challenges mentioned in the previous section and to provide a more straightforward methodology compared to *in-situ* synthesis routes, post-synthesis modification strategies have been developed, as presented in Figure 3. ILs are incorporated into the pores or deposited on the external surfaces of porous material supports by taking advantage of the IL's liquid nature, extremely low vapor pressure, and the capability of creating interactions with the pores or surfaces of porous material. Post-synthesis modifications can be achieved by applying various methods, such as wet impregnation,[53] incipient wetness,[54] capillary action,[14] ship-in-a-bottle,[9] and grafting.[55] Among these methods, wet impregnation is the most used post-synthesis modification method applied to the porous materials to prepare their composites with ILs. In this method, the IL is first dissolved in an excess amount of solvent, such as acetone, dichloromethane, ethanol etc. Then, the pristine porous material is added to the mixture solution impregnation to reach a homogenous dispersion of the IL. The resulting mixture is stirred at mild temperatures followed by solvent evaporation, and then the homogeneous composite is further dried to remove the solvent completely and to form the final sample in powder form. Various studies on different applications use this post-synthesis modification method to successfully prepare IL-impregnated composites.[2, 4, 5, 8, 10-13, 24, 28, 38, 41, 53, 56-66] Similar to wet impregnation, incipient wetness technique includes same experimental steps; however, the only difference is the amount of solvent that is used to dissolve the IL. In the incipient wetness method, the amount of the IL/solvent mixture is adjusted to have enough volume to fill the pores of the desired porous material.[54, 67] The capillary action method is another technique for post-synthesis modifications, where IL and pristine porous material are directly mixed using pestle and mortar. The amount of IL and porous material are determined by using a certain volumetric occupancy ratio. The resulting mixture is then placed inside an oven for overnight heat treatment to facilitate the diffusion of IL into the pores.[14, 29, 66, 68, 69]

Unlike the impregnation techniques described above, the "ship-in-a-bottle" method consists of cation and anion precursors of IL (ship) and pores of a porous material (bottle). In this technique, the precursors of the IL are dissolved in a solvent, and then they are impregnated onto the porous materials to allow diffusion inside the pores (bottle), where they react to form the IL molecules (ships). Then, the remaining non-reacted IL molecules are removed by washing the material with a solvent, and the obtained wet composite is then dried. The advantage of this method is that the IL molecules larger than the pore openings of the porous material can be trapped inside the cavities successfully.[9, 70-72]

Composite preparation with the grafting method can be mainly defined as the insertion of IL molecules on the surface of the porous material. There are two different grafting methods called grafting-from and grafting-to. For the grafting-from method, modification agents, ILs, grow *in-situ* on the surface of the porous support with the help of a previously anchored initiator.[73] For the grafting-to method, a reaction is induced between the IL molecules and the surface of porous support to attach IL molecules onto the surface.[74-77] In the case of IL/porous material composites, the grafting-to method is widely preferred due to its highly controllable nature for locating IL molecules and high stability of deposited molecules on the surface of the porous support. Especially in the field of catalysis, the grafting-to method enables the immobilization of catalytically active metal sites and stabilizes these catalytically active complexes or metal nanoparticles formed on the interface, which improve the stability and recyclability of these composites.[78]

To select a post-synthesis modification, desired IL loading can be considered as a subject of interest. In the case of impregnation method, a variety of ILs with different chemical and physical properties can be incorporated to porous adsorbents up to their wetness point. For instance, 30 wt.% was reported as the wetness limit of IL for IL/MOF composite, [BMIM][BF_4]/CuBTC,[5] whereas 50 wt.% was reported for IL/rGA composite, [BMIM][PF_6]/rGA.[4] However, beyond a certain loading point, leaching issues due to weak molecular interactions or formation of a muddy composite can be observed. Alternatively, more stable composites can be formed with the grafting method considering stronger molecular bonding interactions. However, a limited number of ILs can be loaded due to the chemistry restrictions which makes it difficult to control ILs

on the surface.[74] Overall, for higher IL loadings up to wetness point, use of impregnation method will be more beneficial, while for lower IL loadings, use of grafting will be more appropriate in terms of structural stability.

2.2 Characterization of IL/Porous Material Composites

To characterize the resulting IL/porous material composites, investigations on their morphology, crystal structure, surface area and pore size distribution, surface interactions, elemental composition, and molecular-level investigations are conducted by different techniques. In this section, characterization techniques of IL/porous material composites will be highlighted.

Rational design of new IL/porous material composites is only possible with an understanding of (i) the individual amounts of IL and porous material in the composite; (ii) interactions between the IL molecules and the porous materials; (iii) dependency of these interactions to the structures of the individual components; and (iv) their consequences on different performance measures.[53, 79] Presence of ILs can modify many properties of the host material, such as morphology, crystal structure, surface area, pore volume, thermal and chemical stability, and surface interactions. Various characterization techniques are used to provide an understanding of what is physically/chemically happening in the host material upon IL incorporation. Among these techniques, XRF spectroscopy and ICP-MS are powerful in determining the IL loading as in the cases of [BMIM][PF_6]/ZIF-8[11] and [BMIM][BF_4]/ZIF-8.[12] In these studies, actual IL loading of the composites were mostly determined by XRF and ICP-MS using the obtained quantification of distinctive elemental species, like phosphorus, and boron (together with zinc).

To determine the IL loading, it is necessary for both host and guest materials to have at least one distinct elemental species due to limitations of these characterization techniques, such as the inability to measure lighter elements and matrix definition for quantitative analysis.[80] For instance, it will not be possible to back-calculate IL loading of a non-functionalized carbonaceous material, such as activated carbon, graphene, carbon black etc., due to lack of distinctive elemental species of the porous material. For those cases, other characterization methods, such as TGA analysis[81] or quantitative washing experiments[2] can be referred. Besides, thermal analysis, TGA, can also be utilized to prove the formation of a newly synthesized hybrid material.[53] Generally, newly synthesized IL/porous material composites

provide a two-step decomposition curve, representing IL and porous material, during thermal analysis different than their one-step pristine and bulk counterparts. In a study of investigating the thermal stability of different IL/porous material composites of CuBTC and ZIF-8, lower and higher thermal stability limits were obtained compared to those of pristine ILs used to prepare the composites, demonstrating newly formed hybrid materials with different thermal stabilities.[79] Data illustrated that thermal stability limits of ILs in IL/MOF composites were generally decreased with increasing alkyl chain length and functionalization of imidazolium ring, whereas increased with fluorination of the anion. In the study of Kinik et al.[11] such a decrease in the decomposition temperature was discussed based on the newly formed strong interactions between IL and MOF with the help of FTIR spectroscopy complemented by DFT calculations. Deconvolution of FTIR spectra provides detailed information on newly formed intermolecular weak interactions such as van der Walls interactions, π-π interactions, dipole-dipole interactions, or hydrogen bonding interactions, through red- or blue-shifts of designated characteristic peaks.

To gain further insights on the composites, SEM, EDX, TEM, and XRD spectroscopy can be used to analyze the changes in the morphology and crystal structure upon the addition of IL. In some cases, such as core-shell type composites, IL layer formation on the surface of supports can be directly observed by TEM imaging. Furthermore, for IL/rGA composites, the uniformly distributed presence of IL molecules were proven with SEM/EDX images, where it was reported that the wrinkled-sheet-like structure of rGA stays intact.[4] Moreover, the images were combined with XRD results to analyze the crystal structures of prepared composites.[3, 13, 17, 41] Due to the nature of post-synthesis modification strategies, crystal structure is generally expected to be unchanged without any disturbance on the skeleton after the deposition of IL molecules. However, having a significant change in XRD spectra demonstrates the change in structure for a porous material, which can yield an unwanted decrease in porosity or surface area. Moreover, Raman spectra hold great importance, especially for carbonaceous materials in terms of detecting changes in the surface defects upon IL incorporation, which control the performance measures.[4, 18] Nevertheless, investigation of surface defects can be quite challenging, especially for the composites with IL layer formation and evaluation should be conducted with regards to obtained XRD data.

To complement the interface analysis conducted on the surface of composites, newly formed surface interactions are defined by XP spectroscopy to understand the nature of the

interactions. Also, the addition of advanced techniques, such as layer-by-layer etching with XP spectroscopy, is possible for the identification of IL accumulation sites, if present any, or for the identification of IL layer formation on the surface. Similarly, the presence of IL in the porous structure is confirmed by applying BET analysis. However, in most cases, BET does not provide reliable results due to the poor nitrogen solubility of ILs, especially at the measurement conditions. Thus, (i) the solubility of probing gas molecule inside the bulk IL and (ii) the location of IL molecules in the composite holds significant importance for BET analysis. Determination of gas solubility for ILs can be obtained through experimental studies or computational tools, such as COSMO-RS calculations.[82, 83] Quantitative precision of COSMO-RS calculations can be debatable due to the different phenomena observed during the dissolution of gas molecules inside the bulk IL, such as chemisorption through reacting IL's anion or cation.[84] However, COSMO-RS calculations provide a rough estimate on the gas solubilities in ILs. Location of IL molecules becomes the other main consideration because when the IL molecules are located at the pore openings, they might block the passage of the probing molecule, which leads to considerably lower BET area results compared to the real case.[5, 53, 79] Washing experiments complemented by spectroscopy can be used to identify the exact position of IL molecules whether they are located inside the cages or on the external surface of the porous material. For example, in the case of core-shell type [HEMIM][DCA]/ZIF-8 composite, the location of the IL was confirmed by washing experiments and complemented with TEM images, providing the direct evidence.[2] [HEMIM][DCA]/ZIF-8 composite was washed with a solvent, dimethylformamide (DMF), which cannot fit into the pores of ZIF-8, and results illustrated that the IL molecules were deposited on the external surface of MOF creating a layer consistent with TEM images.

In the light of mentioned characterization techniques, it is appropriate to state that the characteristic spectra of IL-incorporated porous composites, such as crystal structure and morphology, are closer to the characteristics of porous materials rather than bulk ILs due to the employment of the post-synthesis modification techniques. For composite materials, the IL remains as the component with a lower quantity compared to that of host porous material. Thus, the focus of this study was mostly on the consequences of IL incorporation on the properties of the porous host material. For these hybrid materials, IL only acts as a modifying agent to tune the properties of porous material such as porosity, affinity, catalytic activity, ion mobility by locating on the walls/surface. Therefore, the effect of IL after incorporation can be detected

by the deviations from the characteristics of porous material. Moreover, ideally, evaluation of each characterization technique mentioned is equally required for each application area to reach a fundamental-level of understanding on the structure-performance relationships.

2.3 Gas Storage and Separation Performance of IL/Porous Material Composites

2.3.1 IL/MOFs

To date, IL-incorporated MOF composites have been the focus of attention for gas adsorption and separation applications considering their facile synthesis route and enhanced performance measures. As it is repeatedly demonstrated in the literature, gas adsorption and separation performances of pristine MOF enhance significantly upon the incorporation of IL. Ban et al.[23] were the first to observe an increase in the CO_2 adsorption capacity by incorporating [BMIM][NTf_2] into the nanocages of ZIF-8 for tailoring its molecular sieving property. High solubility of CO_2 in IL and its high affinity towards the IL molecules allow CO_2 to have more adsorption sites and thus to be adsorbed more than the other gases. A new type of IL-incorporated MOF composite for high selective separation of CH_4 and CO_2, N_2, H_2 gases was suggested by Sezginel et al.[5] in which [BMIM][BF_4]/CuBTC composite showed improved selectivity performance for CH_4 compared to the pristine MOF. These enhancements are attributed to the modifications in the pore environments, formation of new adsorption sites, and enhanced interactions of guest molecules with IL-MOF interfaces.

Realizing the potential of IL/MOF composites in gas separation applications, [BMIM][PF_6] was incorporated into a different MOF, ZIF-8, to achieve superior CO_2 separation performance.[85] For the first time, experimental results were complemented by molecular simulations to gain deeper insights into the IL-MOF interactions in the composite. Results showed that CO_2/CH_4 and CO_2/N_2 selectivities of IL/ZIF-8 composite were doubled compared to the corresponding selectivities of pristine ZIF-8 at low pressures. Later on, [BMIM][BF_4]/ZIF-8 composite was prepared to achieve high CO_2 separation performance considering the significantly improved gas separation performance of [BMIM][PF_6]/ZIF-8. As in the former composite's case, CO_2/CH_4 and CO_2/N_2 selectivities doubled at 0.1 bar. In another study from Amr Henni et al., CO_2 adsorption capacity of ZIF-8 increased seven times by the incorporation of [BMIM][Ac] and 18 times higher CO_2/N_2 selectivity was obtained by

incorporating [EMIM][Ac] into ZIF-8.[86] With these studies, introducing ILs into ZIF-8 cages as favorable sites for CO_2 is shown to be a promising method for high selective CO_2 separation.

Ferreira et al. conducted a more detailed study to investigate the influence of IL cation/anion type on the gas adsorption and CO_2/CH_4 separation performance of IL/ZIF-8 composites.[87] A total ten different imidazolium-based ILs were impregnated into ZIF-8, and CO_2 and CH_4 adsorption isotherms were measured for each IL/ZIF-8 composite. To understand the IL influence on gas separation performance of composite samples, the normalized data were presented through mapping of IL/ZIF-8 data at high pressure as a function of the low-pressure. According to the results obtained, each IL-impregnated ZIF-8 composite has lower CO_2 and CH_4 uptakes compared to the that of pristine ZIF-8. However, most of the IL/ZIF-8 composites showed higher CO_2/CH_4 selectivities at low pressure than the CO_2/CH_4 selectivity of pristine material. With these studies, introducing ILs into ZIF-8 cages as favorable sites for CO_2 is shown to be a promising method for high selective CO_2 separation.

Besides wet-impregnation method for the synthesis for IL-incorporated MOF composites, a new strategy was proposed to confine imidazolium-based ILs in the pores of MIL-101. Accordingly, polymerized-ILs@MIL-101 composite was prepared via in situ polymerization method.[88] The confinement of polyILs in MOF pores introduced newly formed Lewis base active sites which resulted in better CO_2 uptake compared to the that of pristine MIL-101. Furthermore, encapsulation of polyIL within the MIL-101 pores led to improved recyclability and stability. In another study, amine functionalized $[C_3NH_2bim][Tf_2N]$ IL was impregnated into NH_2-MIL-101(Cr) and gas adsorption tests indicated that uptakes of CO_2 and N_2 are lower in IL/MOF composite compared to that of pristine MOF due to the reduced pore volume upon the confinement of IL into MOF pores.[24] However, the decrease in the adsorption capacity of N_2 was higher compared to the CO_2 adsorption capacity, which resulted in doubled CO_2/N_2 separation performance because of the excellent affinity of CO_2 towards amine-functionalized IL. With the aim to prevent the reduction of gas uptake arising from the occupation of pores of the MOF by the IL molecules introduced, a new class of core-shell type IL/MOF composite was demonstrated by depositing [HEMIM][DCA] on the external surface of ZIF-8 to retain the original pore volume of the parent MOF.[2] The prepared core (MOF)-shell (IL) type composite showed 5.7-times higher CO_2 uptake compared to the pristine ZIF-8 at low pressure with a record high CO_2/CH_4 selectivity of 110 which is almost 45-times higher compared to the corresponding selectivity of pristine MOF at similar operating conditions.

In an attempt to study the effect of structural differences of ILs on the gas separation performances of IL/MOF composites, five different imidazolium-based ILs were selected and incorporated into MIL-53(Al) by wet-impregnation method.[89] Among five IL/MOF composites, [BMIM][PF_6]/MIL-53(Al) showed the highest increase in CO_2/CH_4 selectivity (2.8 times) than that of pristine MIL-53(Al), while [BMIM][$MeSO_4$]/MIL-53(Al) exhibited 3.3 times higher CO_2/N_2 selectivity compared to that of pristine MIL-53(Al). Furthermore, the separation performances of the prepared IL/MIL-53(Al) composites were compared with the previously reported CuBTC and ZIF-8 composites of the same ILs. The results showed that [BMIM][BF_4] and [BMIM][PF_6] incorporated MIL-53(Al) structures showed superior CO_2/CH_4 and CO_2/N_2 selectivities in the whole pressure range of 1–5 bar.

To understand the effect of the anion size and its electronic structure on the gas separation performance of IL/ZIF-8 composites, four different ILs were considered which have a common cation $[BMIM]^+$ and different anions.[41] Results illustrated that when the IL contained a fluorinated anion, the resulting IL/ZIF-8 composite showed 3-times higher CO_2/CH_4 selectivity compared to the non-fluorinated IL/ZIF-8 composites. Besides, when the IL with a small anion was incorporated into ZIF-8, the composite material showed higher CO_2/N_2 and CH_4/N_2 selectivities compared to IL/ZIF-8 composite which has a bulky anion.

Recently, our group demonstrated an integrated computational-experimental hierarchical approach for the rational design of an IL/MOF composite with a superior CO_2 separation performance.[90] Considering the possibility of forming theoretically unlimited numbers of IL-MOF combinations, identifying the best performing composite for a targeted gas separation application holds a significant importance. In this study, three computational tool, namely COSMO-RS calculations, DFT calculations, and GCMC simulations, were used to predict the best performing IL/UiO-66 composite for CO_2 separation applications. Later, identified composite, [BMPyrr][DCA]/UiO-66, was experimentally synthesized and characterized in detail. Results demonstrated that the discovered composite provides infinite CO_2/N_2 and CH_4/N_2 selectivities at low pressures and 15 °C. This study presented a novel methodology to design task-spesific IL/MOF composites compared to the frequently used experimental trial-and-error technique and paves the way for the rational design of new IL/MOF composites with superior adsorption/separation performance.

2.3.2 IL/Carbonaceous Materials

Carbon-based porous materials create many opportunities for extended modifications with their tunable porosity and structural diversity as a promising branch among adsorbent materials. However, harsh and high-temperature conditions of carbonization reactions make IL utilization quite difficult during in-situ synthesis of randomly oriented carbon-based structures, such as activated carbon, porous carbon etc., due to the relatively low thermal stabilities of most ILs. On the other hand, sophisticated new techniques can be introduced for carbon-based structures with higher complexity, as in the case of the layer-by-layer reassembly technique for IL/graphene films where the nanospace formed between sp^2-hybridized carbon nanosheets enhanced the affinity towards toxic aromatic hydrocarbons.[35] Yet, IL usage through post-synthesis methods constitutes the majority of the research conducted on the field.

In the case of selection, there are a variety of options for IL-incorporation starting from complex 3D-structured carbonaceous materials to commercially abundant and cost-effective ones. For instance, in the study of Erto et al., different commercial activated carbons (ACs), Filtrasolb 400, and Nuchar RGC30 were modified with amino acid-based ILs, [HMIM][BF_4] and [EMIM][Gly], through impregnation and their CO_2 capture performances were investigated accordingly.[91] The study highlighted that sterically hindered IL molecules, [HMIM][BF_4] in this case, can create a blockage in the pores of AC, leading to a decrease in CO_2 adsorption. Even though [HMIM][BF_4] is classified as a physical solvent for CO_2, less sterically hindered [EMIM][Gly] increases the adsorption capacity while a decrease is observed for the composite with [HMIM][BF_4]. Similarly, the same pore blockage phenomenon was observed in the cases of both amine-functionalized ILs,[92] and phosphonium based ILs.[93] Enhanced CO_2 adsorption capacity can be attributed to the newly formed interactions between the IL and AC where new adsorption sites became available, similar to the study where Lewis-acidic IL (choline chloride-zinc chloride) was used to change the CO_2 adsorption mechanism of pristine AC.[3] IL/AC composite materials were also used for selective removal of other gaseous species such as mercury capture from natural gas[94] and SO_2 capture.[95]

Among all the possible strategies for enhanced performance measures, functionalization of IL for higher molecular affinity towards the desired molecules has created another possibility for gas storage enhancement through post-synthesis techniques. Tamilarasan et al. modified graphene,[18, 75] and carbon nanotubes[96] by using non-functionalized IL, functionalized IL,

polymerized IL (PIL), and amine-rich IL (ARIL) to obtain higher CO_2 adsorption by increasing the CO_2 affinity of used IL. They obtained an enhancement in CO_2 gas adsorption capacity for all composites. However, composites with functionalized-IL, PIL, and ARIL, showed a higher increase compared to non-functionalized counterparts.[18, 75, 96] Yet, it is better to mention the main drawback of impregnation methods, especially for carbon nanotube bundles, where the impregnation solvent causes aggregation of the bundles, which can lead to insufficient impregnation due to lack of homogeneity of the support material.

Likewise, functionalization of porous materials before IL-impregnation has become a new research field to explore the molecular affinities as in IL-modified graphitic carbon nitride nanosheets and rGAs.[4, 97] In recent years, an IL/rGA composite was introduced for the first time by modifying graphene aerogel first through a thermal reduction treatment followed by the deposition of [BMIM][PF_6] on its surface. The data showed a remarkable increase with more than 20-times enhancement in the CO_2/CH_4 selectivity upon the deposition of the IL, attributing to the newly formed interactions between impregnated [BMIM][PF_6] and rGA. Consequently, IL/carbonaceous-material composites provide an extended possibility of functionalization and constitute a promising class of IL-incorporated composites for further research.

Chapter 3: Methodology*

*Experimental methodology part of this chapter has been published as methodology section in *Chemical Engineering Journal 437 135436 (2022)* by authors Özce Durak, Muhammad Zeeshan, Seda Keskin, and Alper Uzun. The original manuscript has been rearranged to conform to the format requirements of the thesis.

This chapter contains computational and experimental methodology for examining IL/porous materials. Details of materials, sample synthesis, and characterization techniques are discussed in detail.

3.1 Materials

All reagents were purchased from commercial vendors. UiO-66 and NH_2-UiO-66 (used in Chapter 4) were purchased from ACSYNAM (Advanced Chemical Synthesis and Manufacturing, Canada). UiO-66, UiO-67, and MOF-801 (used in Chapter 5) were kindly provided by Beykent University. Activated carbon (AC), DESOREX© K33, was kindly provided from Mikropor Company. PCN-250(Fe) sample was kindly provided by Framergy. ILs were purchased from Iolitec (>95%). Corresponding structures of all chemical compounds mentioned above can be seen in **Table 3.1.1**. Used solvent, acetone, dichloromethane (DCM), chloroform, and dimethylformamide (DMF) (reagent grade, >99.5%), were purchased from Sigma-Aldrich. MOFs and ILs were stored in an Ar-filled MBraun glovebox. Gasses, He (>99.9 vol.%), CH_4 (99.95 vol.%), CO_2 (99.9 vol.%), N_2 (>99.9 vol.%) and O_2 (>99.5 vol.%), used in synthesis and gas sorption studies were purchased from Linde gas company.

Table 3.1.1 Corresponding material name, formula, and representative structure of used materials.

Material Name	**Formula**	**Structure**[98]
UiO-66	$C_{48}H_{28}O_{32}Zr_6$	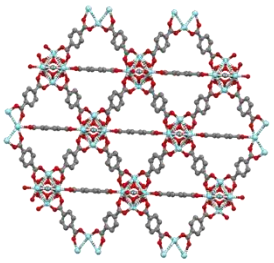
NH_2-UiO-66	$C_{48}H_{34}N_6O_{32}Zr_6$	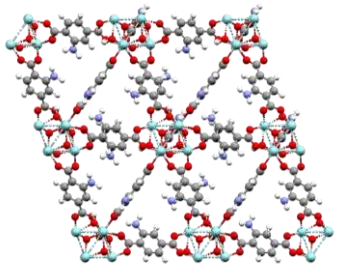

UiO-67	$C_{84}H_8O_{32}Zr_6$	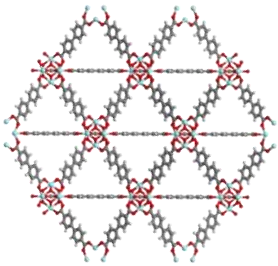
MOF-801 (Zr-Fumarate MOF)	$C_{24}H_{16}O_{32}Zr_6$	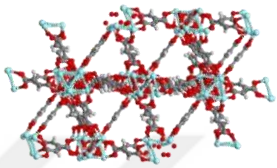
Activated Carbon	C_xH_yO	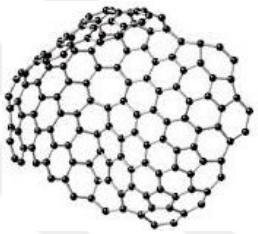
PCN-250(Fe)	$Fe_3(\mu_3\text{-}O)(CH_3COO)_6$	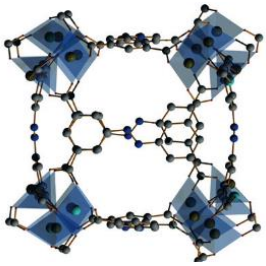
[BMIM][$MeSO_4$]	$C_9H_{18}N_2O_4S$	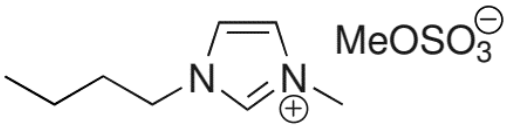
[BMIM][$C(CN)_3$]	$C_{12}H_{15}N_5$	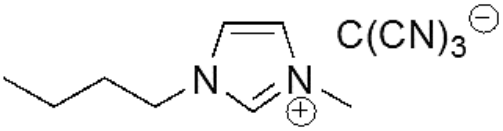

[BMIM][OAc]	$C_{10}H_{18}N_2O_2$	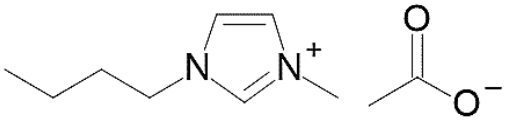
$[P_{6,6,6,14}][DCA]$	$C_{34}H_{68}PN_3$	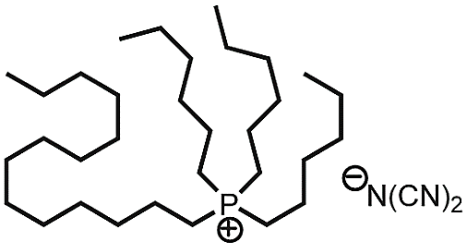

3.2 Sample Preparation

3.2.1 Sample Preparation via Wet Impregnation Technique

IL/UiO-66, IL/UiO-67, IL/Zr-Fumarate, and IL/AC composites were prepared by using wet impregnation method.[85] The porous material was pre-treated overnight at 105/125 °C under vacuum prior to the composite preparation. Simply, IL/porous material composites were prepared by solving IL in the selected solvent (acetone, DCM or DMF) as the first step, adding porous material into the solution as the second step, and then evaporating the solvent as the third step. For 5 wt.% IL loading, 0.05 g of IL was dissolved in 30 ml solvent for 1-h duration under constant mixing at 250 rpm. Then, 0.95 g of porous material was added into the solution. Resulting mixture was left under mild temperature and continuous mixing at 150 rpm for 6 h for evaporation of the solvent. After that, obtained powder was put into oven overnight at 105 °C to evaporate the remaining solvent. Resulting powder composite was placed in the glovebox to prevent moisture formation. Samples with 5, 10, 20, 30, and 35 wt.% IL loadings were prepared by following the same procedure explained above.

3.2.2 Sample Preparation via air exclusion technique

All IL/PCN-250(Fe) composites studied in this thesis were synthesized by using wet impregnation method complemented with air exclusion techniques. All samples were stored in an Ar-filled glovebox after synthesis. Prior to the synthesis, pristine PCN-250(Fe) sample was

isothermally treated at 150 °C for 12 h in a Quantachrome XeriPrep Degasser under vacuum conditions. After heat treatment for 12 h, PCN-250(Fe) sample was placed inside the glovebox to prevent any air or moisture exposure. Similarly, used IL, $[P_{6,6,6,14}][DCA]$, was removed from glovebox and isothermally treated overnight in an oven at 80 °C to remove any remaining moisture. Afterwards, 0.45 g of IL was dissolved in 30 mL acetone/chloroform/DMF with constant stirring at 300 rpm for 1 h under ambient conditions and was sealed sufficiently to apply gas bubbling step. Sealed mixture was placed inside an ice bath and bubbled with He for 45-min to remove dissolved air. After 45 min, mixture was cooled down to room temperature and stirred for another 30 min at 300 rpm. To reach an approximate stoichiometric IL loading of 45 wt.%, 0.55 g of MOF was put into a RBF inside an Ar-filled glovebox and was sealed sufficiently to prevent any air exposure. Samples prepared for dispersion or particle size effect has an additional step before the transfer of IL-solvent mixture. In that additional step, approximately 15 ml of solvent was added into the RBF containing pristine PCN-250(Fe) and the resulting mixture was sonicated, or ultrasound sonicated (US) for 10 minutes. US was conducted by using a Bandelin Sonopuls HD 2070.2 Ultrasonic Homogeniser at 10% intensity setting under constant argon flow. Then, He-bubbled IL-acetone mixture was carefully added to the cap-sealed RBF containing MOF by using double tipped needles under constant He flow to prevent air exposure. The double-sided stainless-steel cannula having the exiting He flow from IL-acetone mixture was placed inside the RBF and immediately after, another double-sided needle was placed to relieve the pressure build-up. To transfer the obtained IL-acetone liquid, one side of the needle, which was connecting both flasks, was touched to the liquid and with the help of the pressure difference, the liquid was transferred from one flask to the other. Upon the addition of IL-acetone mixture, double tipped needles were removed from the RBF in the order of exiting He flow to entering He flow. Instantly, the septum was sealed with vacuum grease and parafilm to prevent any exposure of air or moisture. Obtained mixture containing dissolved IL in acetone and PCN-250 was left for stirring at 300 rpm overnight under room temperature to allow the incorporation of IL molecules on the porous host material, MOF. Then, the mixture was connected to the Schlenk line for drying. Resulting dried composite in RBF was placed inside an Ar-filled glovebox and stored for further characterization and performance analysis. Same procedure was repeated for the samples synthesized with PCN-250(Fe) treated at 240 °C. Wetness point of PCN-250(Fe) was

determined as 45 wt.% for the used IL, $[P_{6,6,6,14}][DCA]$. Formation of a muddy composite was observed after the stated wetness point.

3.3 Characterization Techniques

3.3.1 X-Ray Fluorescence Spectroscopy

Approximate IL loadings of the prepared samples were determined by XRF spectroscopy technique with the help of a Bruker S8 Tiger spectrometer using an X-ray tube with a 4 kW Rh anode. Analyses were performed under helium atmosphere. The SpectraPlus Eval2 V2.2.454 software was used for the data interpretation.

3.3.2 Brunauer−Emmett−Teller Surface Area and Barrett−Joyner−Halenda Pore Volume Analyses

Surface area determination of pristine AC and IL-impregnated composites were performed by using a Micromeritics ASAP 2020 physisorption analyzer. Obtained N_2 physical adsorption and desorption data were analyzed both for surface area and pore volume, accordingly. Prior to measurement, each sample was activated by degassing overnight at 105 °C for 12 h under vacuum. After activation step, samples were cooled down to -196 °C by liquid nitrogen and free space measurements were performed using He gas. Later on, N_2 adsorption and desorption isotherms were obtained between a pressure range of 10^{-6} and 1 bar. Pressure steps between 0.05 and 0.3 bar was fitted to BET equation and t-plot analysis was conducted. Afterwards, obtained data was used to determine the surface area and pore volumes of each sample, respectively. Pore size distribution were calculated by the Barrett–Joyner–Halenda (BJH) method.

3.3.3 Scanning Electron Microscopy

SEM images of pristine materials and composites were obtained by using a Zeiss Evo LS 15 scanning electron microscope. Analyses were conducted under vacuum with an accelerating voltage of 3 kV and a working distance of 3-3.3 mm. Images were taken with a magnification of 1/10/20 k×. Prior to the analysis, PCN-250(Fe) samples were coated with gold to prevent any charging issues.

3.3.4 Energy Dispersive X-ray Spectroscopy

EDX mapping data was obtained by using a Zeiss Evo LS 15 scanning electron microscope equipped with Bruker Xflash 5010 EDX detector. Images were collected with 123 eV resolution, EHT of 5 kV and working distance of 6 mm for both pristine material and composite.

3.3.5 X-Ray Diffraction Spectroscopy

XRD spectroscopy of pristine materials and composites were performed by using a Bruker D2 Phaser instrument with a Lynxeye detector. For X-ray generator, Cu-Kα_1 radiation source with a wavelength of 1.54060 Å was used at 30 kV voltage and 10 mA current to obtain XRD patterns. Slit size of 0.2 mm was used for Lynxeye detector, whereas the diffraction data was collected between the 2θ range of 5-50° with a step size of 0.0204°. Deconvolution of XRD pattern was made with XPSPeak version 4.1 software by using Newton method for optimization of the designated peaks. Crystallite lateral size (L_a), lateral height (L_c), and d spacing calculations were made by using Scherrer Equation and Bragg's Law, respectively, as given below.[99]

$$L_a = \frac{k_a \lambda}{\beta_{hkl} \cos(\theta)} \quad (1)$$

$$L_c = \frac{k_c \lambda}{\beta_{hkl} \cos(\theta)} \quad (2)$$

$$\lambda = 2d \sin(\theta) \quad (3)$$

Where, k_a and k_c represent Scherrer constant, λ represent wavelength of the radiation source used during XRD analysis, β_{hkl} represent full width half maximum (FWHM) of designated XRD peak in radians, θ represents the half of 2θ peak position in radians. XRD patterns of pristine PCN-250(Fe) simulated by using VESTA software.[100]

3.3.6 Thermal Gravimetric Analysis

Thermal stability measurements were conducted by using a TA Instruments Q500 Thermogravimetric Analyzer with a platinum pan. Prior to the measurement, approximately 10

mg of sample was placed on the pan for pristine porous material, bulk IL, and IL/porous material composites. Same procedure was applied to each measurement. A constant temperature ramp rate of 5 °C/min was employed up to 105/125/150/240 °C and the samples were treated isothermally for 9 h. Afterwards, the temperature was increased to 700 °C at a ramp rate of 2 °C/min. All measurements were conducted under N_2 flow with the balance and purge gas rates of 40 and 60 mL/min, respectively. To analyze the thermal stability, the onset (T_{onset}) and derivative onset (T'_{onset}) temperatures were determined from the thermogravimetric and derivative TG curves, respectively. In the study, the T'_{onset} values were considered as the temperature point where the thermal decomposition initiated regarding that T'_{onset} values generally overestimate the thermal decomposition temperatures.[33]

3.3.7 Raman Spectroscopy

Raman spectra of all carbon-based samples were obtained using RENISHAW/INVIA Raman microscope between the region of 2000-800 cm^{-1}. Laser excitation wavelength of Raman microscope was set to 532 nm with an objective of 50x. Obtained data was fitted with the help of XPSPeak version 4.1 software by using Newton method for optimization of the designated peaks.

3.3.8 Fourier-Transform Infrared Spectroscopy

IR spectra were obtained by using a Bruker Vertex 80v IR spectrometer equipped with a platinum attenuated total reflection (ATR) accessory. Data were collected as an average of 256 scans for both the samples and their respective backgrounds. Measurements were performed at a spectral resolution of 2 cm^{-1} under atmospheric pressure between the wavelength range of 4000-400 cm^{-1}. Obtained data was compensated for atmospheric gasses, such as H_2O and CO_2, and corrected by using extended ATR modification with the help of OPUS software. Deconvolution of the obtained IR bands were conducted by using Fityk software using the Voigt function.[101] For air-sensitive PCN-250(Fe) samples, IR spectra was obtained with the help of two KBr (potassium bromide) windows in the spectral range of 4000-400 cm^{-1}. Data analysis and corresponding baseline corrections were made by using OPUS software. Pristine PCN-250(Fe) and IL/PCN-250(Fe) composites were directly placed between two KBr

windows, whereas the bulk ILs were mixed with KBr powder (>99%, purchased from Merck) prior to the analysis.

3.3.9 X-ray Photoelectron Spectroscopy Analysis

A Thermo Scientific K-Alpha spectrometer equipped with an aluminum anode (Al Kα = 1468.3 eV) was used to obtain the XPS spectra of both pristine porous materials and their composites with the IL. The electron take-off angle was set to 90º. Obtained spectra were recorded and analyzed by Avantage 5.9 software. During analysis, binding energies were calibrated by assigning the C 1s signal to 284.8 eV.

3.3.10 Nuclear Magnetic Resonance Spectroscopy

^{13}C and ^{1}H NMR spectrum of bulk [BMIM][OAc], CO_2-saturated [BMIM][OAc] and CH_4-saturated [BMIM][OAc] were obtained by using a Bruker Advance Neo 500 MHz NMR spectrometer. Deuterium oxide (D_2O, purity >99.9%) was purchased from Sigma-Aldrich and used as a locking agent in NMR sample with a volumetric ratio of 80%. Data was collected for 1024 scans and TopSpin 4.1.1 software was utilized to analyze the data. ^{1}H NMR results were calibrated for used locking solvent (D_2O) with H_2O signal at 4.88 ppm.

3.3.11 Dynamic Light Scattering

Dynamic light scattering analyses of pristine PCN-250(Fe) samples were conducted with Malvern Zetasizer Nano ZS by using a quartz-cuvette. Scan number of 10 and run number of 3 were used for each sample with an analysis temperature of 25 °C. Z-Average sizes obtained from intensity-based results were reported.

3.3.12 Washing Experiments

Washing experiments were performed either to determine the position of IL or to estimate the approximate IL loading of IL/MOF composites. Composites (100 mg of powder samples) were washed with 4 mL of selected solvent at mild temperatures (approx. 45 °C) repeatedly for three times. Later on, washing filtrate was collected in a container for further analysis. Washed wet composite samples were dried in an oven for 4-h at 105 °C. Obtained powder products were used for further characterization.

3.3.13 Boehm Titration Method

Boehm titration method was used to analyze the surface functional groups of pristine AC for oxygen containing acidic functional groups as carboxylic, phenolic, and lactonic groups.[102] Procedure was applied to 0.5 g of pristine AC by using back-titration method with three different reaction bases as NaOH, $NaHCO_3$, and Na_2CO_3. Among these three different reaction bases, NaOH neutralizes all surface acidic functional groups, whereas Na_2CO_3 neutralizes both surface carboxylic and lactonic groups, and $NaHCO_3$ neutralizes only surface carboxylic groups. 50 ml of 0.05 M NaOH, $NaHCO_3$ and Na_2CO_3 solutions were added to 0.5 g of pristine AC and obtained AC containing solutions were agitated by shaking for 24-h then let stand for 6-h for precipitation of added AC. Afterwards, solutions were filtrated by using 3 layers of filtration paper and 10 ml aliquots were taken from each filtrate. Excess amount of 0.05 M HCl solution was added to acidify each aliquot as 15 ml for aliquots taken from NaOH and $NaHCO_3$ solutions, and 30 ml for the aliquot taken from Na_2CO_3 solution. Obtained samples were bubbled with N_2 for 2 h to expel CO_2 molecules located on the surface. Then, back-titration was conducted by using 0.05 M NaOH titrant. Titration curve was obtained by a WTW Inolab pH 7110 pH-meter with ±0.01 accuracy and calibrated by 3-point calibration with a standard pH 4.01, 7.00 and 10.00 buffers. The endpoint of titration was determined from titration curve by taking the data point where pH equals to 7, and the volume of NaOH titrant recorded respectively for solutions of all three reaction bases. Carbon surface functionality was calculated with the formula given below.

$$\dot{n}_{csf} = \frac{n_{HCl}}{n_b}[B]V_b - ([HCl]V_{HCl} - [NaOH]V_{NaOH})\frac{V_B}{V_a} \quad (4)$$

$$n_{csf} = \frac{\dot{n}_{csf}}{m_{AC}} \quad (5)$$

where, n_{csf} represents mole of carbon surface functionality per gram, while n_{HCl}, n_B, [B], [HCl], V_{HCl}, V_B represents moles, concentration, and volume of reaction base and HCl, respectively. [NaOH] and V_{NaOH} represents the concentration and the amount of NaOH titrant used in the titration and V_a represents the volume of aliquot taken. During calculations, acid to base ratio was taken into consideration due to the difference in the reacting basic sites of NaOH, $NaHCO_3$ and Na_2CO_3. For NaOH and $NaHCO_3$, neutralization reaction takes place with 1:1

ratio, whereas for Na_2CO_3, it is 2:1. Mole of surface functional groups per gram pristine AC, n_{csf}, was calculated for each reaction base and denoted as $n_{csf}(NaOH)$ $n_{csf}(NaHCO_3)$ and $n_{csf}(Na_2CO_3)$. Corresponding moles of surface functional groups were found by taking the differences between the found $n_{csf}(NaOH)$ $n_{csf}(NaHCO_3)$ and $n_{csf}(Na_2CO_3)$ values as below.[103]

$$n_{carbocxylic} = n_{Csf}(NaHCO_3) \quad (6)$$

$$n_{lactonic} = n_{csf}(Na_2CO_3) - n_{csf}(NaHCO_3) \quad (7)$$

$$n_{phenolic} = n_{csf}(NaOH) - n_{lactonic} \quad (8)$$

3.3.14 Conductor-like Screening MOdel for Real Solvents

COSMOthermX(C30_160) software was used to perform COSMO-RS calculations.[104] COSMO-RS is a widely utilized computational modeling tool for qualitatively estimating the solubilities of different gases in bulk ILs.[105-107] The TZVPD-FINE parameterizations were used to obtain the solvent capacity ($C_{i,j}^{\infty}$) of bulk ILs for the selected gasses at infinite dilution condition. The Henry's law constant (K_i) of component "i" in the IL was calculated by dividing the vapor pressure of the pure component i (P_i^{vap}) by solvent ($C_{i,j}^{\infty}$). The Henry's constants of selected gasses in 36,456 ILs (combination of 372 cations and 98 anions) were computed at 25 °C. Calculations for gas solubility in bulk IL were performed between the pressure range of 0.1 and 1 bar with respective triple-z valence polarized basis set (TZVP) parameterizations.

3.4 Gas Sorption and Separation Performance Measurements

3.4.1 High-pressure Volumetric Gas Sorption Measurements

Volumetric gas sorption measurements of the samples were performed for each gas, CH_4, CO_2, N_2, and O_2 with the utilization of Quantachrome Instruments High-Pressure Volumetric Gas Adsorption Analyzer iSorb HP2. Approximately 0.4 g of sample was used for the measurements. Prior to measurements, samples degassed overnight for approximately 10 h while isothermally keeping them under vacuum at 105/125/150/240 °C with a vacuum pressure of 10^{-6} bar. After the activation step, the gas sorption isotherms for CH_4, CO_2, and N_2 were

obtained at 15, 25, and 35 °C (or 10, 25, and 40 °C) between the pressure range of 0.01-1 bar. Then, data was collected by using the iSorbHPwin High Pressure Isotherms software. Isotherm fittings were determined by using IAST++ software.[108] Langmuir-Freundlich (LF), Dual-Site Langmuir (DSL), and Dual-Site Langmuir Freundlich (DSLF) models were used to fit the isotherms as given below.

$$\mathrm{LF} \rightarrow \mathrm{n(P)} = \mathrm{q} \times \frac{(\mathrm{k}\times\mathrm{P})^{\mathrm{n}}}{(1+\mathrm{k}\times\mathrm{P})^{\mathrm{n}}} \tag{9}$$

$$\mathrm{DSL} \rightarrow \mathrm{n(P)} = \mathrm{q_1} \times \frac{\mathrm{k_1}\times\mathrm{P}}{1+\mathrm{k_1}\times\mathrm{P}} + \mathrm{q_2} \times \frac{\mathrm{k_2}\times\mathrm{P}}{1+\mathrm{k_2}\times\mathrm{P}} \tag{10}$$

$$DSLF \rightarrow n(P) = q_1 \times \frac{(k_1\times P)^{n_1}}{(1+k_1\times P)^{n_1}} + q_2 \times \frac{(k_2\times P)^{n_2}}{(1+k_2\times P)^{n_2}} \tag{11}$$

where *n(P)* adsorption quantity (mmol or cc) under equilibrium temperature and *P* pressure. q_1 and q_2 represent the maximum adsorption capacity on sites #1 and #2, while k_1 and k_2 are the temperature-dependent equilibrium constants. n_1 and n_2 are the fitting parameters.

Ideal Adsorbed Solution Theory (IAST) was utilized to predict the behavior of each sample under mixture gas conditions.[109, 110] IAST was employed to calculate mixture selectivities of pristine porous materials and IL-incorporated composites with the help of IAST++ software. During the calculations, measured single-component gas sorption data was used for each sample. Mixture selectivity was calculated according to the equation given below.

$$S = \frac{n_{O_2}/n_{N_2}}{x_{O_2}/x_{N_2}} \tag{12}$$

where n_i is the quantity adsorbed of each component in the mixture calculated with IAST and x_i is the mole fraction of each component in the mixture.

Enthalpy of sorption (ΔH_{sorp}) was calculated by using Clausius-Clapeyron equation given below as Eq. 13 and the isosteric heats of sorption (Q_{st}) was obtained from the relationship given in Eq. 14. Ideal gas constant (R) was taken as 8.314 J/(mol.K), while temperature (T) was taken in units of kelvin (K).

$$\Delta H_{ads} = -R\left[\frac{d(lnP)}{d(1/T)}\right] \tag{13}$$

$$\Delta H_{ads} = -Q_{st} \tag{14}$$

To investigate the regeneration ability and reproducibility of the prepared composites, another batch of best performing composite was prepared using the same preparation technique. Afterwards, cyclic gas sorption measurements were conducted consecutively by degassing for 2-h at the same conditions in between gas sorption analysis using the same equipment mention above for both the 1st and the 2nd batch of the best performing composite.

3.4.2 Gas Saturation Studies

Bulk [BMIM][OAc] was saturated with CH_4 and CO_2 gasses prior to liquid-state ^{13}C – ^{1}H NMR and FTIR analyses by bubbling with the corresponding gases under atmospheric pressure. Approximately 5 mg of bulk [BMIM][OAc] was added in a capped glass bottle and sealed with parafilm. Then, CH_4 gas was bubbled through the liquid [BMIM][OAc] for 6 h under atmospheric pressure at 25 °C. Atmospheric pressure inside the sealed glass bottle was maintained by using double-tipped needle purchased from Sigma-Aldrich. Same procedure was repeated for CO_2 saturation experiments of bulk [BMIM][OAc].

Pristine AC and IL/AC composites were saturated with CH_4, CO_2 and N_2 gasses prior to FTIR analysis by using a Micromeritics (Particulate Systems) High-Pressure Volumetric Analyzer (HPVA II-200). Approximately 120 mg of sample was added in the sample holder and degassed under the pressure of 10^{-6} bar at 105 °C for 6 h. Later on, the sample was saturated with CH_4 under 35 bar at 25 °C for 6 h. Subsequently, IR analysis was performed for the CH_4-saturated sample. Similar procedure was repeated for CO_2 and N_2 saturation experiments of each sample.

3.4.3 Column Breakthrough Measurements

Experimental set-up used in dynamic breakthrough measurements was presented in **Figure 3.4.3.1**. Two gas cylinders, He and dry air, were used in gas manifold part of the set-up with corresponding mass flow controllers. Adsorption column was packed with adsorbent with the help of glass bead sandwich bed inside an Argon filled glovebox and both ends were sealed with two-way valve to prevent any air exposure prior to the breakthrough measurement. Then, fixed-bed column was vacuumed overnight at room temperature by using Schlenk line to activate the packed sorbent material. Gas flow coming from the exit of fixed-bed column

was swept with continues He flow having 45 ml/min flow rate to accommodate the minimum gas suction requirement (>30 ml/min) of used Hiden Analytical QGA mass spectrometer. Continuous flow of 5 ml/min He was fed to the fixed-bed column for 20 minutes before sending the analysis gas, dry air. After 20 minutes, continuous flow of 5 ml/min dry air was fed to the column with the help of a three-way valve. Gas exiting from the fixed-bad column was analyzed by mass spectrometer. Results were obtained and visualized through Hiden Analytical QGA software by using a suitable calibration run.

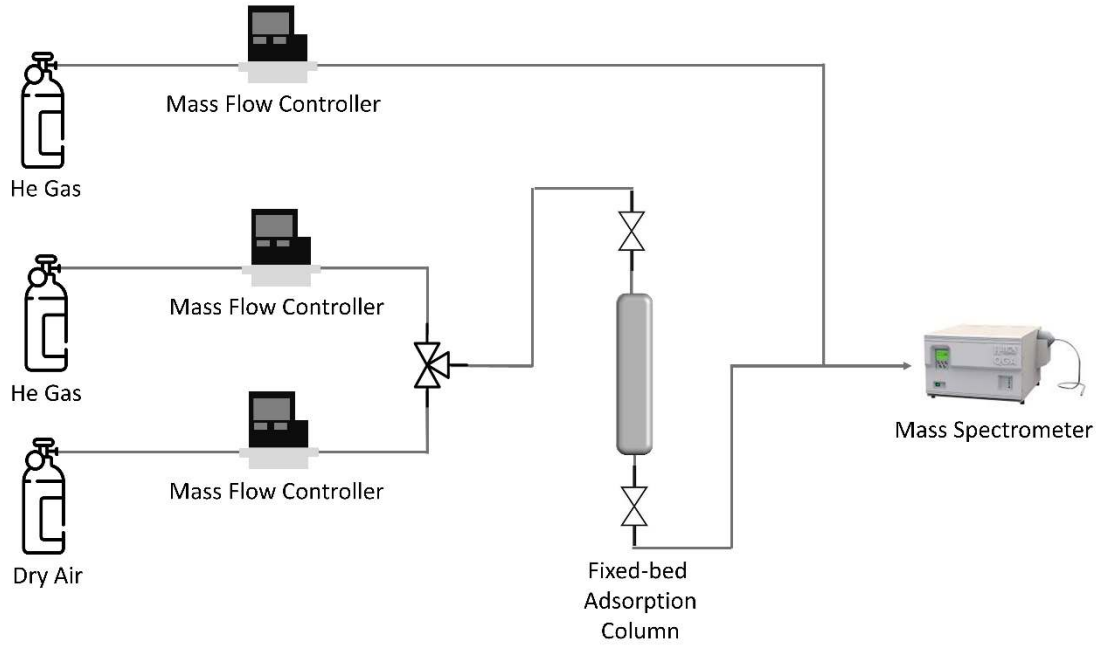

Figure 3.4.3.1. Schematic representations of used column breakthrough set-up.

Chapter 4: Towards Complete Elucidation of Structural Factors Controlling Thermal Stability of IL/MOF Composites: Effects of Ligand Functionalization on MOFs*

*This chapter has been published as a part of the research article in *Journal of Physics: Condensed Matter 32(48) 484001 (2019)* by authors Özce Durak, Harun Kulak, Safiyye Kavak, H. Mert Polat, Seda Keskin, and Alper Uzun. The original manuscript has been rearranged and shortened to conform to the format requirements of the thesis.

In this chapter, we incorporated an ionic liquid (IL), 1-*n*-butyl-3-methylimidazolium methyl sulfate ([BMIM][$MeSO_4$]) into two different metal organic frameworks (MOFs), UiO-66, and its amino-functionalized counterpart, NH_2-UiO-66, to investigate the effects of ligand-functionalization on the thermal stability limits of IL/MOF composites. The as-synthesized IL/MOF composites were characterized in detail by combining Brunauer-Emmett-Teller analysis (BET), infrared spectroscopies (FTIR), and their thermal stability limits were determined by thermogravimetric analysis (TGA). Characterization data confirmed the successful incorporation of the IL into each MOF and indicated the presence of direct interactions between them. A comparison of the interactions in [BMIM][$MeSO_4$]-incorporated UiO-66 and NH_2-UiO-66 with those in their 1-butyl-3-methylimidazolium hexafluorophosphate ([BMIM][PF_6])-incorporated counterparts showed that the hydrophilic IL, [BMIM][$MeSO_4$], interacts with the 1,4-benzenedicarboxylate (BDC) ligand of the UiO-66, while the hydrophobic IL, [BMIM][PF_6], is interacting with the joints where zirconium metal cluster coordinates with BDC ligand. The TGA data demonstrated that the composite with the ligand-functionalized MOF, NH_2-UiO-66, exhibited a lower percentage decrease in the maximum tolerable temperature compared to those of IL/UiO-66 composites. Moreover, it is discovered that when the IL is hydrophilic, its hydrogen bonding ability can be utilized to designate an interaction site on MOF's ligand structure which will lead to a lower reduction in thermal stability limits. These results provide insights for the rational design of IL/MOF composites and contribute towards the complete elucidation of structural factors controlling the thermal stability.

This research study was published in the *Journal of Physics: Condensed Matter*. I would like to thank my co-authors Harun Kulak, Safiyye Kavak, and H. Mert Polat for their contributions in sample characterization, validation, and writing of the original draft.

4.1 Background

MOFs have emerged as promising materials for a wide range of applications, such as gas storage and separation,[111-114] drug delivery,[115-117] purification,[118-120] catalysis,[121-123] sensors,[124-126] and batteries[127-129] owing to their large surface areas, high pore volumes, and tunable pore sizes and shapes.[130] These porous materials are hybrid networks assembled by the coordination of metal nodes with organic ligands and it is possible to tune their textural and structural properties by changing the combination of metals and linkers for any desired application.[131-133] Apart from such tunability of the metal nodes and linkers, novel approaches including ligand functionalization,[134] mixed-metal or mixed-linker combinations,[135] functionalization of open metal sites,[136] and defect engineering[137] have been introduced to modify the MOF structures to make them more efficient in different applications. Among these approaches, modifying them with ionic liquids (ILs) either by externally coating[2] or incorporating[85] into has been gaining a broad interest.[31]

ILs consist of ionically linked cations and anions, and they are mostly liquids at room temperature. They have unique features, such as low volatility, tunable design, miscibility, high thermal stability, and conductivity. As in the case of MOFs, the tunable structure of ILs enable the synthesis of an almost infinite number of different ILs with a wide range of physical and chemical characteristics. Broad structural diversity of these compounds makes them promising agents for modifying different materials, such as MOFs[2, 31, 85, 138] and supported metal catalysts, for improved performance.[139-141] For instance, in recent years, ILs have been introduced into the pores of MOFs and these IL/MOF composites have been reported to significantly improve the pristine MOFs' performance for gas adsorption and separation applications.[5, 12, 31, 86, 88, 142-144] These studies demonstrated that once incorporated into the pores of a MOF, the IL molecules do not leach out easily, even if the composite is washed with some solvents, which are molecularly larger in size than the pore openings of the MOFs at relatively high temperatures.[2, 79, 119, 145, 146]

High thermal stability is a distinctive criterion and a must-have quality for every material, where the definition of "high" depends on the application. Hence, determination of the structural factors controlling the thermal stability limits is crucial for rational design of materials. There are various reports on the thermal stability limits of both ILs and MOFs. For

instance, in the study of Kandiah *et* al.,[147] thermal stability limits of a zirconium-based MOF, UiO-66, was investigated by using three different ligand functionalization as, H_2N-H_2BDC, O_2N-H_2BDC, and Br-H_2BDC. They reported that thermal stability limit of UiO-66 was decreased after ligand-functionalization, however, the resulting composites considered as thermally stable at high temperatures regardless of the ligand functionalization. Similarly, DeCoste *et* al.[148] investigated the thermal and chemical stability of the zirconium-based MOFs, UiO-66 with BDC linker and UiO-67 with BPDC linker, and reported that with an increase in the number of aromatic rings in the ligand structure, MOF became more susceptible to chemical degradation by water and hydrochloric acid. Moreover, they observed that NH_2-UiO-66 has a respectively lower thermal stability due to weakening of the C–C bond between the carboxylate group and aromatic ring in the ligand's structure. Adamová *et* al.[149] reported 12 different phosphonium-based ILs and compared their thermal stabilities, melting points and viscosities according to the alkyl chain length. Besides these studies on the thermal stabilities of the individual components of the IL/MOF composites, the pristine MOFs and the bulk ILs, we previously reported the effects of different structural factors on imidazolium ILs on the thermal stability limits of the corresponding IL/MOF composites.[79] The next step in this direction is investigating the consequences of systematic structural changes on MOFs on the thermal stability of IL/MOF composites having the same IL. In this regard, a possible systematic structural variation on a MOF is the ligand-functionalization. Here, we considered two different MOFs, UiO-66 and its NH_2-functionalized form, NH_2-UiO-66, and incorporated an IL with a hydrophilic character, 1-*n*-butyl-3-methylimidazolium methyl sulfate ([BMIM][$MeSO_4$]), into each of them. Detailed characterization of these composites revealed the differences in the structures and the interactions between the individual components of the composites. Results of the TGA were evaluated based on these structural insights and structural factors determining the thermal stability limits of these composites and their dependency on the ligand functionalization of the MOF has been revealed. These results extend the knowledge on the structural factors controlling the thermal stability limits of these novel composites and offer opportunities for tailoring the structures of the individual components towards the rational design for any specific application.

4.2 Results and Discussion

The surface areas and pore volumes of the pristine MOFs and the IL/MOF composites determined by BET and *t*-plot analyses are given in **Table 4.2.1** and related N_2 isotherms are presented as **Figure 4.2.1**. Accordingly, the IL incorporation resulted in a decrease in the surface areas of both MOFs. This change in surface areas indicates the successful incorporation of the IL into the pores of MOFs.[2, 12, 85, 150, 151] However, the BET results are not very reliable for the IL/MOF composites, as N_2 has a very low solubility in the IL at the BET measurement conditions; and because of this reason, N_2 passage through the pores might be blocked by the IL, especially if the IL molecules are located at the pore openings.[145] As a result, pore volumes of none of the composites could not be determined (**Table 4.2.1**).

Table 4.2.1 BET surface areas (S_{BET}) and pore volumes (V_{pore}) of pristine MOFs and [BMIM][$MeSO_4$]/MOF composites.

Sample	S_{BET} [$m^2\ g^{-1}$]	V_{pore} [$cm^3\ g^{-1}$]
UiO-66	878	0.39
[BMIM][$MeSO_4$]/UiO-66	14.2	n/a*
NH_2-UiO-66	712	0.31
[BMIM][$MeSO_4$]/NH_2-UiO-66	3.6	n/a*

*Could not be measured.

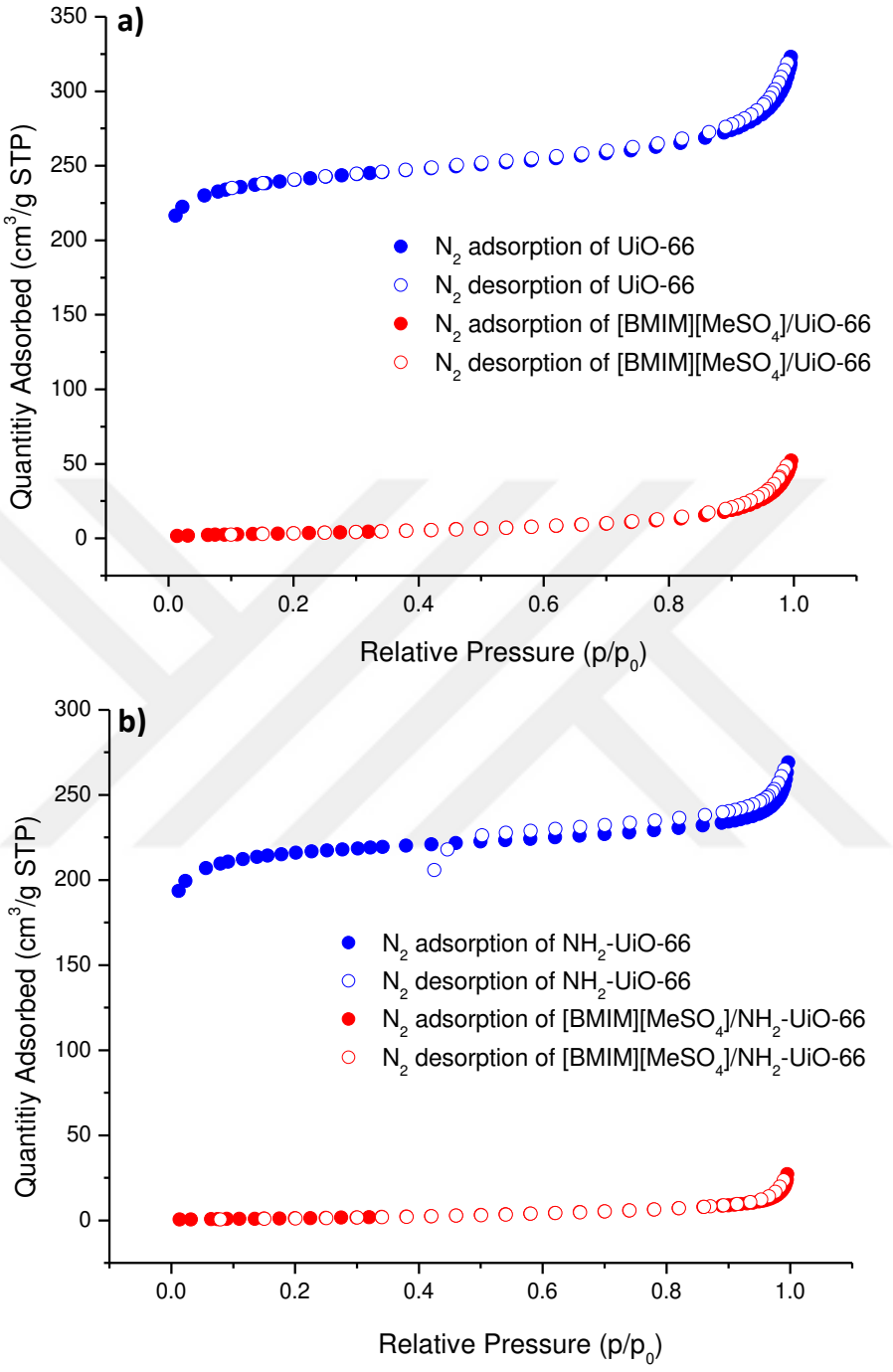

Figure 4.2.1 (a) N_2 adsorption-desorption isotherms of pristine UiO-66 and [BMIM][$MeSO_4$]/UiO-66 composite at -196.15 °C. (b) N_2 adsorption-desorption isotherms of pristine NH_2-UiO-66 and [BMIM][$MeSO_4$]/NH_2-UiO-66 composite at -196.15 °C.

Figure 4.2.2 illustrates the IR spectra of [BMIM][$MeSO_4$], UiO-66, and [BMIM][$MeSO_4$]/UiO-66 composite in the spectral ranges of 1800-650 cm^{-1} and 3200-2700 cm^{-1}. IR spectra obtained for the composite demonstrates the presence of IL-related features, confirming the successful IL incorporation into the MOF.[138] The peaks located at approximately 1217, 1007, and 743 cm^{-1} in the spectra of [BMIM][$MeSO_4$]/UiO-66 composite were assigned to the stretching vibrations of —SO_3 in the anion of IL (ν_{as}(—SO_3), ν_s(—SO_3), and ν_s(S—O), respectively.[152, 153] Likewise, the newly formed peaks in the high wavenumber region observed at 3152 and 3109 cm^{-1} in the spectra of the composite material were assigned to ν(C2H) and ν(HC4C5H) on the ring structure of IL's cation, respectively.[154]

To better understand the possible interactions between [BMIM][$MeSO_4$] and MOFs, we focused on the main characteristic IR peaks, and identified the band positions and the corresponding shifts, if any, in the spectra of the corresponding composite. We draw our main conclusions based on the shifts higher than the spectral resolution of the measurements which are broadly consistent with our previous reports.[79, 138, 150] First, we considered the case with IL/UiO-66 composite. Compared to the IR spectrum of the bulk IL, the peak located at 730 cm^{-1} blue shifted to 743 cm^{-1}, which can be interpreted as the strengthening of the bond between S-O in the anion at the expense of a weakening of the interionic interactions between the anion and the cation of the IL. The peaks located at 1217 and 1007 cm^{-1} did not show any shifts, however, the absorbance intensity of these peaks decreased dramatically, which can be interpreted as an indication of interactions between the anion of the IL and the structure of the UiO-66. Moreover, a blue shift from 3080/3150 to 3109/3152 cm^{-1} was observed on the band position of ν(C2H)/ν(HC4C5H) of the cation. Presence of such blue-shifts on these band positions correspond to a reduction in the strength of interionic interactions in the IL, further confirming the interactions between the MOF and the anion of the IL.[155-157]

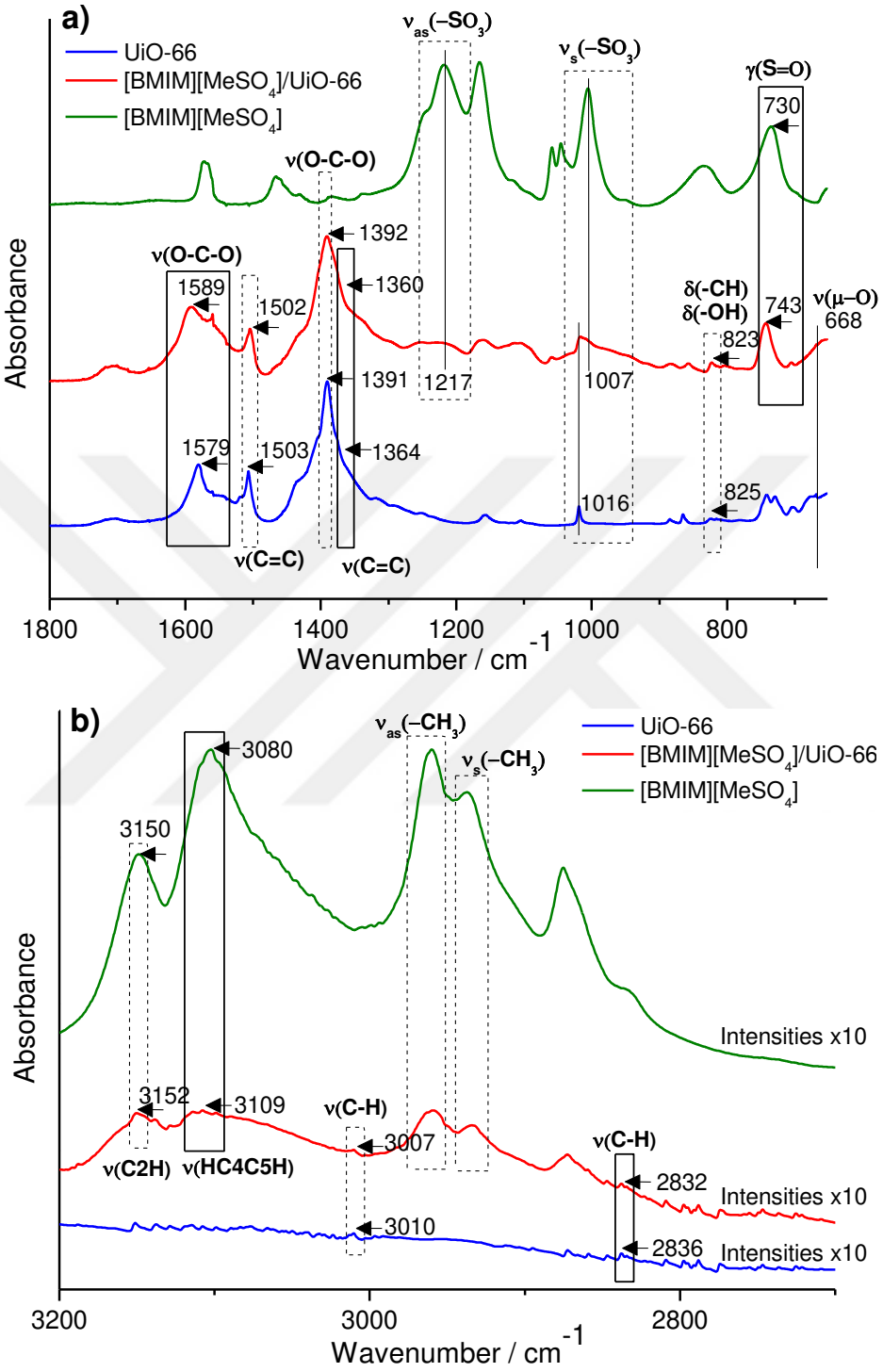

Figure 4.2.2 FTIR spectra of pristine MOF, UiO-66 (blue), IL/MOF composite (red), and bulk [BMIM][$MeSO_4$] (green) obtained in the spectral ranges between (a) 1800 and 650 cm^{-1} and (b) 3200 and 2700 cm^{-1}. Dashed line (--)/straight line (-) indicates shifts which are below/above the spectral resolution.

Furthermore, numerous shifts in the positions of the characteristic bands of UiO-66 were observed as well. The peak located at 668 cm^{-1}, identified as the stretching band of μ_3-O bridging bond did not shift and this result demonstrates the lack of any interactions of the metal nodes with the IL molecules.[158, 159] Slight blue shifts observed in the positions of the bands in a range of 750-700 cm^{-1} (from 741, 729, and 704 cm^{-1} to 743, 731, and 706, respectively) were identified as the Zr–O node vibrations mixed with –OH and –CH bending.[159] For the specific peaks of BDC ligand, the peak at 825 cm^{-1} red shifted to 823 cm^{-1} and this result indicates the weakening of the bending vibrations of –OH and –CH.[160] Moreover, C=C vibration band of benzene ring red-shifted from 1503 and 1364 cm^{-1} to 1502 and 1360 cm^{-1}, indicating the presence of a possible interaction between the benzene ring of the ligand and the IL molecule.

In addition to these changes in the peak positions, the O–C–O asymmetric and symmetric stretching bands of the carboxylate group at 1579 and 1391 cm^{-1} blue-shifted to 1589 and 1392 cm^{-1}, respectively. This shift was interpreted as the weakening of the bond between the Zr node and the ligand.[159] However, structural integrity was still maintained as evidenced from the appearance of the specific peak at 1016 cm^{-1} indicating the presence of BDC ligand coordination with Zr nodes.[161] These changes can be considered as the evidence of the direct interactions between UiO-66 and the anion of the IL. Consistently, the stretching bands of ν(C–H) in the MOF's ligand red-shifted from 3010 and 2836 cm^{-1} to 3007 and 2832 cm^{-1}, respectively, and indicated a decrease in the bond energy of C–H groups present on the benzene ring.[158] This result shows the presence of a direct interaction between the –CH groups of the benzene ring and the anion of IL, and it is consisted with the literature findings for the possible H-bonding capability of the $[MeSO_4]^-$ anion.[153] Consequently, the presence of the interactions between the –CH group of UiO-66 and anion of [BMIM][$MeSO_4$] was confirmed.

For the amino-functionalized MOF, it was reported that the —NH_2 groups do not coordinate with the metal modes of UiO-66 structure and maintain their interaction with the benzene ring of the ligand after the synthesis.[162] Accordingly, it can be deduced that the amino groups are located inside the micropores of UiO-66, which is also proven by the given pore volume results of the pristine MOFs. Therefore, the changes in the IR bands of the IL-incorporated NH_2-UiO-66 composite indicate the direct interactions between IL and MOF. The position of the primary amino group has a major importance to investigate these interactions because of its strategic location.

In **Figure 4.2.3**, the IR spectra of [BMIM][$MeSO_4$], NH_2-UiO-66, and [BMIM][$MeSO_4$]/NH_2-UiO-66 composite are given in the ranges of 1800-650 cm^{-1} and 3200-2700 cm^{-1}. The IR spectrum of the composite demonstrates peaks at 3152, 3109, 1214, 1005, and 750 cm^{-1}, which were not present on the spectrum of the pristine NH_2-UiO-66. These new bands characterizing confined [BMIM][$MeSO_4$] indicate the successful incorporation of IL into the MOF. Furthermore, characteristic peaks of $-NH_2$ can still be detected in the IR spectrum of the IL-MOF composite. Thus, we inferred that no structural deformation on the functionalized ligand occurred upon the incorporation of IL.

In the IR spectrum of the IL-incorporated NH_2-UiO-66, the characteristic peaks of μ_3-O stretching and Zr–O node stretching located at 668 cm^{-1} did not show any shifts indicating the absence of any direct interactions between the IL molecules and the metal nodes.[158] On the other hand, ν(C=C) of ligand's benzene ring red-shifted from 1497 and 1334 cm^{-1} to 1495 and 1333 cm^{-1}, and the symmetric and asymmetric stretching of the O–C–O in the carboxylate group of the ligand red-shifted from 1382 and 1569 cm^{-1} to 1380 and 1567 cm^{-1}, respectively.[158, 159, 163] These red-shifts demonstrate the reduction of the bond energy in the ligand because of the presence of a possible interaction between the IL and the amino-functionalized ligand of the MOF. Moreover, decreases in the intensities were observed on the characteristic peaks of ν(C–N) stretching of aromatic amines located at 1425 and 1256 cm^{-1}. This change in intensities confirm the presence of direct interactions between the amino group of the ligand and the IL.[147, 164]

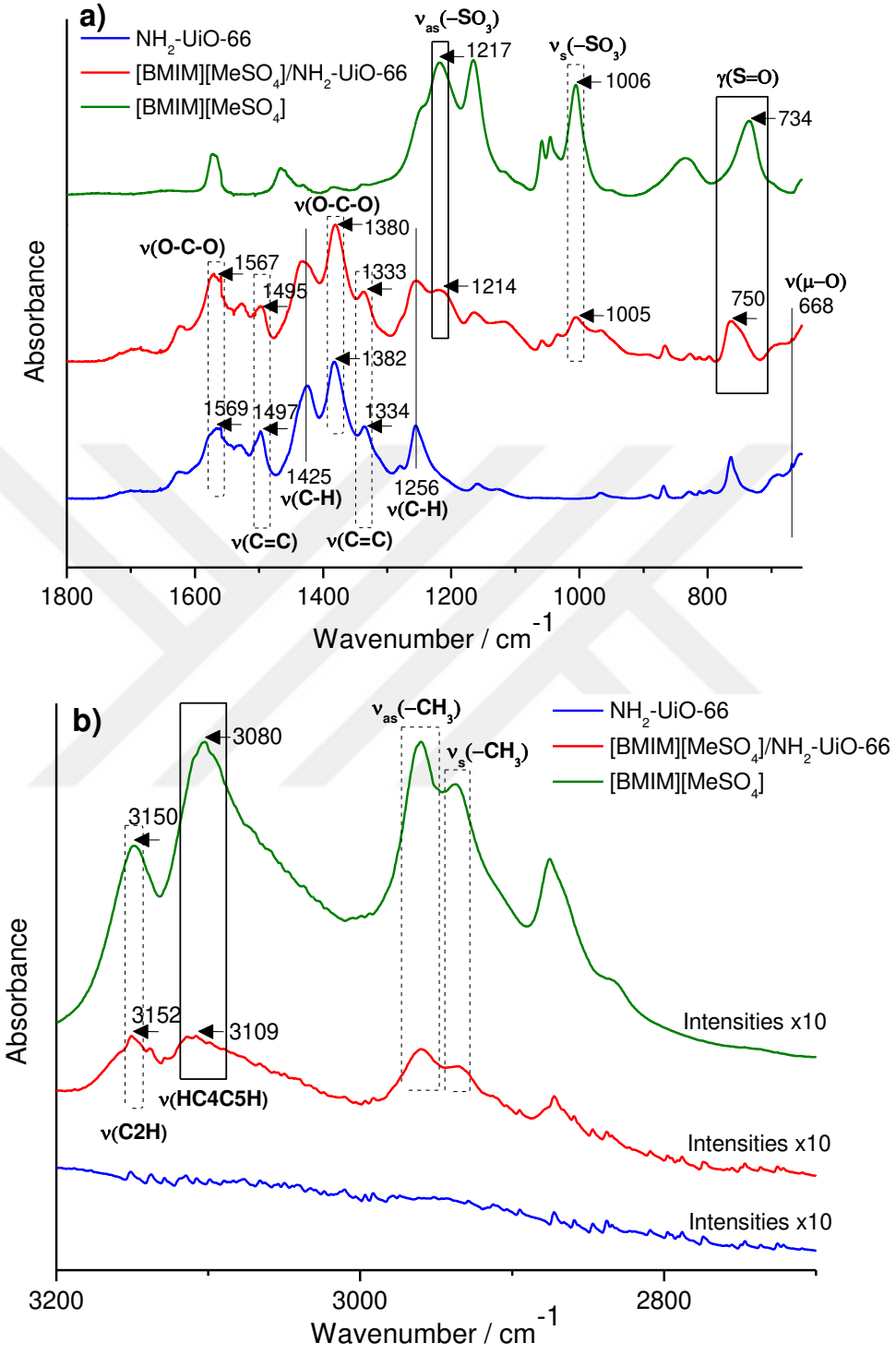

Figure 4.2.3 FTIR spectra of pristine MOF, NH_2-UiO-66 (blue), IL/MOF composite (red), and bulk [BMIM][$MeSO_4$] (green) obtained in the spectral range between (a) 1800 and 650 cm^{-1} and (b) 3200 and 2700 cm^{-1}. Dashed line (--)/straight line (-) indicates shifts which are below/above the spectral resolution.

In **Figure 4.2.4**, the bands present at 3482 and 3373 cm^{-1} in the spectra of NH_2-UiO-66 were assigned to the stretching vibration of —NH_2 groups as ν_{as}(—NH_2) and ν_s(—NH_2), respectively.[165-167] These peaks showed red-shifts in the composite material to 3457 and 3345 cm^{-1}, respectively. The bands associated with the asymmetric and symmetric —SO_3 vibrations of IL also showed red-shift from 1217 and 1006 cm^{-1} to 1214 and 1005 cm^{-1}, respectively, upon IL incorporation.

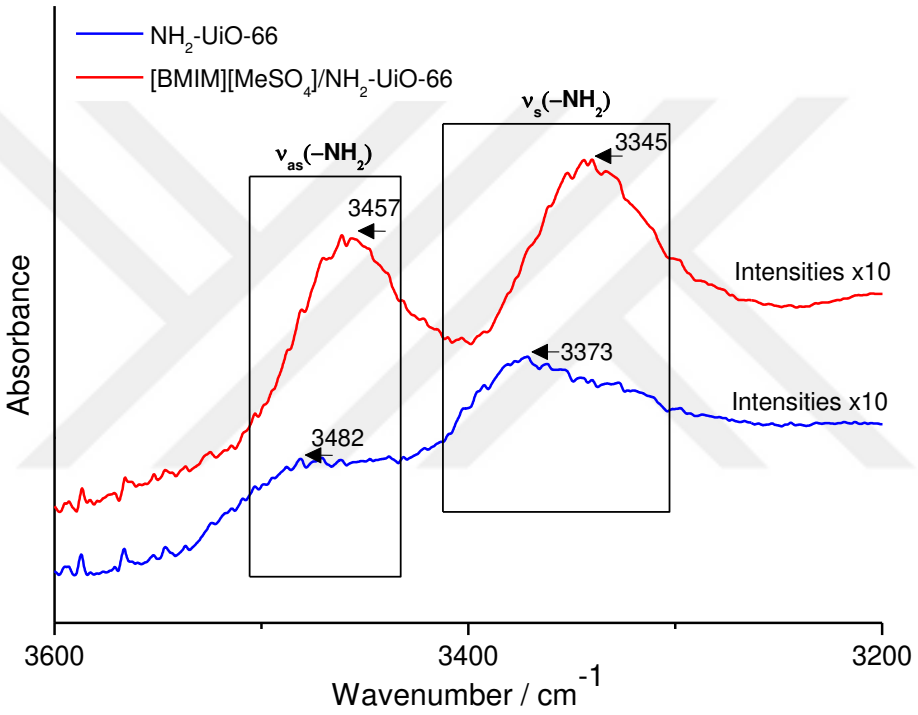

Figure 4.2.4 FTIR spectra of NH_2-UiO-66 (blue) and IL/MOF composite (red) in the range of 3600 and 3200 cm^{-1}. Straight line (-) indicates shifts which are above the spectral resolution.

Moreover, the rocking vibration band of S=O in the anion, γ(S=O), blue-shifted to from 734 to 750 cm^{-1} demonstrating an increase in the bond strength of the anion structure because of the weakening in the interionic interactions of the IL.[168] Also, *ν*(C2H)/*ν*(HC4C5H) band in the cation blue-shifted from 3080/3150 to 3109/3152 cm^{-1}, which further proves this weakening. Based on these results, it can be inferred that the major interactions between the IL molecules and the amino-functionalized MOF were taking place through the amino groups of NH_2-UiO-66 and the anion of IL. As in the case of UiO-66, $[MeSO_4]^-$ still prefers to interact with the hydrogen atom at the same position of the benzene ring. However, due to the amino

occupancy on this position, it interacts with the hydrogen of —NH_2 group of the functionalized ligand instead. The nature of the interaction can be compared according to the reduction of the interionic interaction energy of the IL for both composites. In the case of IL/UiO-66 composite, the peak intensities of ν_{as}(—SO_3) and ν_s(—SO_3) dramatically decreased, whereas for IL/NH_2-UiO-66 composite, the peaks were still visible in the IR spectra. This observation demonstrates the difference in the interaction strengths between the anion and the MOFs. The anion forms a much stronger interaction with the UiO-66 compared to the case with its functionalized counterpart.

We compared these interactions with those observed on [BMIM][PF_6]/UiO-66 and [BMIM][PF_6]/NH_2-UiO-66 composites, retrieved from our previous work.[119] For both IL/MOF composites with [BMIM][PF_6], the cation of the IL interacts with the joint where metal cluster and the BDC linker coordinate. Related shifts of the characteristic vibration bands, ν(O−H), ν(C=O), and ν(O−C−O) for the MOFs, ν(C2H) and ν(C5H) for the IL, were given as evidence for the designation of the stated interaction site. Moreover, results can imply that when the IL has a hydrophilic character as in the case of [BMIM][$MeSO_4$], it interacts with the hydrogen atoms in the linker, whereas when it has a hydrophobic character as [BMIM][PF_6] does, the metal nodes become the interaction sites. Thus, this comparison indicates that the structure of IL is important in mandating the interactions with the MOFs as well. Changes in the interactions between the IL molecules and the MOFs were reported to be responsible for changes in the thermal decomposition mechanisms of ILs in MOF cages.[2, 5, 79, 85, 86, 145, 150] Thus, we focused on investigating how thermal stability limits alter as the molecular level interactions identified above change.

TGA results of the bulk IL, pristine MOFs, and the IL/MOF composites are tabulated in **Table 4.2.2**. For comparison, corresponding data previously reported[119] for the analogous composites having [BMIM][PF_6] as the IL are retrieved and listed. Based on the derivative thermogravimetric (DTG) curves, thermal decomposition temperatures were determined as the derivative onset temperatures (T'_{onset}), which are listed in **Table 4.2.2** with the corresponding weight losses of the materials when the temperature reached to 700 °C.

Table 4.2.2 Derivative onset temperatures (T'_{onset}) and the weight losses of the bulk [BMIM][$MeSO_4$], pristine MOFs, and IL/MOF composites observed during TGA to 700 °C.

Sample	T'_{onset} [°C]	Weight loss at 700 °C [wt.%]
[BMIM][$MeSO_4$]	257	97
[BMIM][PF_6][a]	358	99.7
UiO-66	480	51
[BMIM][$MeSO_4$]/UiO-66	295	70
NH_2-UiO-66	330	44
[BMIM][$MeSO_4$]/NH_2-UiO-66	276	61
[BMIM][PF_6]/UiO-66[a]	245	62
[BMIM][PF_6]/NH_2-UiO-66[a]	220	47

[a]Data retrieved from previous study [119]

Data presented in **Table 4.2.2** indicated that [BMIM][$MeSO_4$] and [BMIM][PF_6] incorporation reduce the thermal decomposition temperatures of the corresponding MOFs, however, the observed T'_{onset} remained higher than those measured for the bulk [BMIM][$MeSO_4$]. Compared to bulk IL, the corresponding increase in T'_{onset} values were 38 and 19 °C for [BMIM][$MeSO_4$]/UiO-66 and [BMIM][$MeSO_4$]/NH_2-UiO-66 composites, respectively. This can be inferred to the strong H-bonding interaction between hydrophilic $[MeSO_4]^-$ anion of [BMIM][$MeSO_4$] and the ligand of MOFs. TGA curves of the samples show an initial weight loss up to 150-200 °C associated with the removal of adsorbed water and solvent molecules from porous surface. Then, the thermal decomposition occurs in one step for bulk ILs and pristine MOFs. On the other hand, the IL-incorporated MOFs showed weight losses at two different temperature ranges corresponding to the decomposition of IL molecules and complete decomposition of the framework and BDC linker degradation.[169]

The ultimate aim of this study was to investigate the consequences of the ligand-functionalization on MOFs on the thermal stability limits of their composites with the same IL. Thus, changes in the T'_{onset} values for each composite were analyzed based on the differences in the interactions between ILs and MOFs. In **Table 4.2.3**, the percentage decrease in the derivative T'_{onset} values were given for each IL/MOF composite according to the T'_{onset} values of pristine MOFs.

Table 4.2.3 Percent decrease in derivative onset temperature (T'_{onset}) for IL/MOF composites according to the T'_{onset} of pristine MOFs

Sample	Decrease in T'_{onset} [%]
[BMIM][$MeSO_4$]/UiO-66	39
[BMIM][$MeSO_4$]/NH_2-UiO-66	16
[BMIM][PF_6]/UiO-66[a]	49
[BMIM][PF_6]/NH_2-UiO-66[a]	33

[a]Data retrieved from previous study[119].

Amino-functionalized UiO-66 provides an opportunity to compare the effects of ligand functionalization on the T'_{onset} values of the IL/MOF composites. According to **Table 4.2.3**, the composites of NH_2-UiO-66 showed a lower degree of decrease in their T'_{onset} values for both ILs, 16 and 33%, compared to their counterparts with UiO-66, 39 and 49%. Even though the pristine NH_2-UiO-66 has a lower thermal stability limit than its non-functionalized counterpart, UiO-66, it showed a relatively lower degree of decrease in the stability limits upon the incorporation of both ILs. Accordingly, it is observed that the IL incorporation causes a higher degree of distortion in the crystal structure of non-functionalized UiO-66, which resulted in a thermally less stable composite. This outcome can be inferred to the larger steric hindrance or electron-rich nature of the NH_2-functionalized UiO-66 compared to its non-functionalized counterpart.[147]

Moreover, in **Table 4.2.3**, [BMIM][PF_6]/IL composites showed a higher degree of decrease in their T'_{onset} values compared to those of [BMIM][$MeSO_4$]/IL composites. This difference can be explained by the nature of the molecular interactions between the ILs and MOFs. In the case of hydrophobic [BMIM][PF_6], cation of the IL interacts with the joint where the metal cluster and BDC linker coordinates. The interaction site is the same for both UiO-66 and NH_2-UiO-66; however, the decrease in the T'_{onset} value is higher for UiO-66, 49%, compared to its counterpart, 33%. On the contrary, the hydrophilic IL, [BMIM][$MeSO_4$], interacts with the aromatic ring of BDC ligand for both MOFs and the decrease in the T'_{onset} value is higher for UiO-66, 39%, compared to its counterpart, [BMIM][$MeSO_4$]/NH_2-UiO-66,

16%. Therefore, it can be interpreted that when the interactions between the IL and the MOF is through the skeletal metal nodes, structural integrity of the MOF crystals can be affected which could lead to thermal decomposition starting at a lower temperature during the ramp.

Since both ILs have different interaction sites independent of whether the MOF is ligand functionalized or not, the differences in thermal stabilities are attributed to the changes in hydrophobicity/hydrophilicity of the selected ILs. In this study, selection of a hydrophilic MOF was found to be more beneficial because of the stabilization by the hydrogen bonding between the IL and the hydrogen atoms in the aromatic ring of ligand. Therefore, impregnation of a hydrophilic ILs into MOF cages can be favored for having a thermally more stable composite, their ability to create H-bonding can be utilized to designate the interaction sites, which can be responsible for different performance measures for different applications.

Results indicate that interactions between the IL and the MOFs play a key role in the thermal stability of the composite materials. A more stable composite can be designed by successful IL/MOF pairing based on their related molecular interactions. For the rational design of IL/MOF composites, most of the previously reported studies considered different families of ILs on a certain MOF and demonstrated that IL structure plays an important role in determining the thermal stability of the composites. However, data that we present here also illustrate that the influence of the IL strongly depends on the interactions between the IL and MOF, which are not only controlled by the IL structure but also depends on ligand structure of the MOFs. Thus, both components of the IL/MOF composites are crucial for determining the thermal stability limits and therefore, the rational design requires insights on the individual effects of different structural factors on both components of these composite materials.

In conclusion, [BMIM][$MeSO_4$] was incorporated into two different MOFs, UiO-66 and NH_2-UiO-66, and characterized in detail for assessing the impact of IL incorporation and the corresponding IL-MOF interactions on the thermal stability limits. Successful IL incorporation into the MOFs was evidenced by the XRF and BET results, and the structural intactness of the MOFs were confirmed by SEM and XRD analyses. The interactions between [BMIM][$MeSO_4$] and each MOF were revealed by FTIR in detail, and these findings were used to identify the structural factors controlling the thermal stability of the composites. Results showed that the thermal stabilities are higher for the composites that have IL-ligand interactions rather than IL-metal node interactions. Moreover, it can be said that hydrophilicity of IL is a desirable feature

to designate specific IL–ligand interaction sites for IL/MOF composites of UiO-66 and its derivatives. These results contribute towards the complete elucidation of structural factors controlling the thermal stability by providing an insight on the consequences of ligand functionalization on MOFs on the thermal stabilities of the corresponding IL/MOF composites.

Chapter 5: The Effect of Ionic Liquid Incorporation on the Gas Adsorption and Separation Performance of Zr-MOFs: Thermal, Structural, and Performance Analysis of [BMIM][$C(CN)_3$]-incorporated UiO-66, UiO-67, and MOF-801

In this chapter, the effect of MOF's organic linker on the gas adsorption and separation performance of three different IL-incorporated Zr-MOFs was investigated by incorporating 1-methyl-3-methylimidazolium tricyanomethanide, [BMIM][C(CN)$_3$], into the cages of three Zr-MOFs, namely, UiO-66, UiO-67, and MOF-801, having 1,4-benzenedicarboxylic acid (BDC), 4,4-biphenyldicarboxylic acid (H_2BPDC), and fumarate as linker, respectively. Synthesized IL/Zr-MOF composites were characterized in depth detail by using several characterization techniques, BET, SEM, XRD, TGA, and FTIR to investigate the resulting changes upon the confinement of IL molecules. Volumetric CO_2, CH_4, C_2H_2, C_2H_4, and N_2 gas adsorption measurements were performed on each sample and the corresponding ideal selectivities were determined to evaluate the separation performance of each composite. [BMIM][C(CN)$_3$]/UiO-66 composite showed remarkable improvements in the ideal selectivities of CO_2, C_2H_4, and C_2H_2 over N_2 reaching practically infinite selectivity values in the order of 10^{11}, associated mostly with the N_2-phobic behavior of the composite. Similarly, significant improvements in the selective separations of CO_2, C_2H_2, and C_2H_4 molecules were obtained in the case of MOF-801, while almost no noticeable selectivity improvement was detected in the case of [BMIM][C(CN)$_3$] incorporated onto UiO-67. Results attributed to the change in intermolecular interactions between the [BMIM][C(CN)$_3$] molecules and Zr-MOFs leading to different molecular affinities. Considering that the geometry of the linker dictates the final structure of the resulting MOF, investigating the linker effect upon the incorporation of the same IL holds a substantial importance to seek a better insight into the nature of these intermolecular interactions. Hence, this study underlines the significance of the organic linker selection for the rational design of novel IL/MOF composites having superior gas separation performance.

I would like to thank Beykent University Chemical Engineering faculty member Prof. Şahika Sena Bayazit for providing the pristine samples of UiO-66, UiO-67, and Zr-Fumarate. I am also thankful to my co-author Nitasha Habib for her contribution in characterization and volumetric gas adsorption tests.

5.1 Background

Post-synthetic modification of MOFs has attracted tremendous attention owing to its tunable nature for target applications. In particular, MOF families having facile synthesis routes, adjustable pore size, and excellent thermal/chemical stability establish wide range of opportunities for post-synthetic modification techniques.[170] Among these families, Zr-MOFs emerge as a prominent option owing to their versatile synthesis, cost-effective nature, rich topology, and excellent structural stability. Presence of Zr(IV)-carboxylate coordination nodes within their coordinatively unsaturated (open) metal framework enable extraordinary thermal/chemical stability for various functionalization techniques. Subsequently, small guest moieties are incorporated into the cages of Zr-MOFs via various post-synthesis modification strategies to achieve desired degree of modification on the physicochemical properties of the parent material in the way of improving the performance for various applications, such as gas storage and separation,[90] liquid-phase adsorption and separation,[8] ionic conductivity,[171] and catalysis.[61, 172]. Accordingly, hybrid composites of Zr-MOFs have provided limitless possibilities with their enhanced structural properties together with improved performance.

Among different guest molecules, ILs provide a high degree of flexibility due to the availability of theoretically unlimited number of cation-anion combinations, high thermal/chemical stabilities, and low vapor pressures. ILs are classified as molten salts, which can be found in liquid-phase at room temperature. Majority of ILs have environmentally-friendly production pathways compared to the conventional industrial solvents, hence they can be considered as “green solvents” alternative to their organic counterparts, which are mostly volatile.[1] These novel materials are composed of a large asymmetric organic cation and an organic/inorganic anion offering almost limitless structural possibilities. Their tunable structures can be utilized in different applications, such as lubricants,[173] catalysis,[174] fuel-cell electrolytes,[175] solid-phase extraction,[176] liquid-liquid extraction,[176] and gas separation.[177] However, owing to their liquid nature, bulk ILs may face barriers upon their integration into real-life processes ,such as recycling, bulk transport, packaging, and product purification.[178, 179] Therefore, by confining them inside a porous material, such as MOFs, it is possible to benefit from their excellent physicochemical properties. In this regard, various types of IL-incorporated MOFs have been reported up to date aiming to tune/enhance parent’s performance together with IL’s usability. The enormous and continuous growth in the number of reports on

the synthesis of such IL/MOF composites and their exceptional performances in different applications, mainly in gas separation, is a proof of importance of this concept.

Hence, modification of versatile Zr-MOFs with ILs can be considered as a versatile modification technique targeting superior gas separation performance without sacrificing from high thermal/chemical stability and crystalline microporous structure. To date, a few IL/Zr-MOF composites have been reported in the literature with excellent gas adsorption performances.[180-182] In this regard, our group reported an integrated computational-experimental hierarchical approach to design an IL/UiO-66 composite with extraordinary CO_2 gas separation performance.[90] The IL/UiO-66 composite, [BMPyrr][DCA]/UiO-66, discovered through this hierarchical design approach showed practically an almost infinite CO_2 selectivity over N_2 at low pressures and 15 °C. Results illustrated that CO_2/N_2 selectivity of pristine UiO-66 increased from 33.8 to $>10^5$ in the low-pressure region presenting more than 3000-times improvement in the CO_2 gas separation performance.

Although, there exist several other studies reporting excellent performance of IL/Zr-MOF composites, literature still lacks systematic analysis of the interface between Zr-MOFs and ILs to elucidate the structural factors controlling gas adsorption and separation performance. Accordingly, selection of a group of Zr-MOFs having different organic linkers can offer much needed basis for the rational investigation of the organic linker effect on gas adsorption and separation performance of IL/Zr-MOF composites. In this chapter, the interface between Zr-MOFs and imidazolium ILs was investigated by incorporating 1-methyl-3-methylimidazolium tricyanomethanide, [BMIM][C(CN)$_3$], IL into the cages of three different Zr-MOFs, UiO-66, UiO-67, and MOF-801 having 1,4-benzenedicarboxylic acid (BDC), 4,4-biphenyldicarboxylic acid (H_2BPDC), and fumarate as linkers, respectively. Used IL, [BMIM][C(CN)$_3$], was chosen due to the high CO_2 affinity of $[C(CN)_3]^-$ anion and resulting high CO_2 solubility of IL.[183, 184] Synthesized MOFs and IL/MOF composites were characterized in detail by using various characterization techniques to highlight the structural changes occurring upon IL incorporation. Then, volumetric gas adsorption tests were performed on each composite to examine their CO_2, CH_4, N_2, C_2H_2, and C_2H_4 gas adsorption performance in a pressure range up to 1 bar at 25 °C. Results demonstrated the structural and thermal changes of UiO-66, UiO-67, and MOF-801 upon [BMIM][C(CN)$_3$] incorporation and corresponding correlations between the obtained alterations and selective gas separation performance.

5.2 Results and Discussion

IL/Zr-MOF composites, [BMIM][$C(CN)_3$]/UiO-66, [BMIM][$C(CN)_3$]/UiO-67, and [BMIM][$C(CN)_3$]/MOF-801, were synthesized via wet impregnation technique with a targeted stoichiometric IL loading of 30 wt.%, as described in Chapter 3. IL loading of 30 wt.% was chosen considering the minimum wetness limit among the determined wetness limits of the used Zr-MOFs, in this case it corresponds to the wetness limit of MOF-801. IL molecules were expected to be incorporated inside the cages of Zr-MOFs considering the relatively larger pore opening sizes of UiO-66 (~ 8 Å), UiO-67 (~ 10 Å), and MOF-801 (~ 7 Å) compared to the molecular size of [BMIM][$C(CN)_3$] (estimated as ~5.9 Å from DFT optimized geometry).[185] To further confirm the successful incorporation of IL and approximate IL loading on each composite, the synthesized composites were washed with acetone as this solvent (~ 6 Å) is small enough to enter the pores and remove the incorporated IL. By repeatedly washing with acetone, IL molecules were successfully removed from each composite. Characteristics IR peaks of IL molecules were almost completely disappeared in the obtained IR spectra of washed and dried composites, indicating the successful removal of IL molecules inside the MOFs' cages as shown in **Figure 5.2.1**. Accordingly, the corresponding IL loading of the composite was back-calculated by using the initial mass of IL/MOF composite and the remaining mass of the washed and dried IL/MOF composite. Results showed approximately 30, 31, and 29 wt.% IL loading for [BMIM][$C(CN)_3$]/UiO-66, [BMIM][$C(CN)_3$]/UiO-67, and [BMIM][$C(CN)_3$]/MOF-801, respectively. Therefore, it can be inferred that the IL/Zr-MOF composites have at least 30 wt.% incorporated IL in the cages of MOFs.

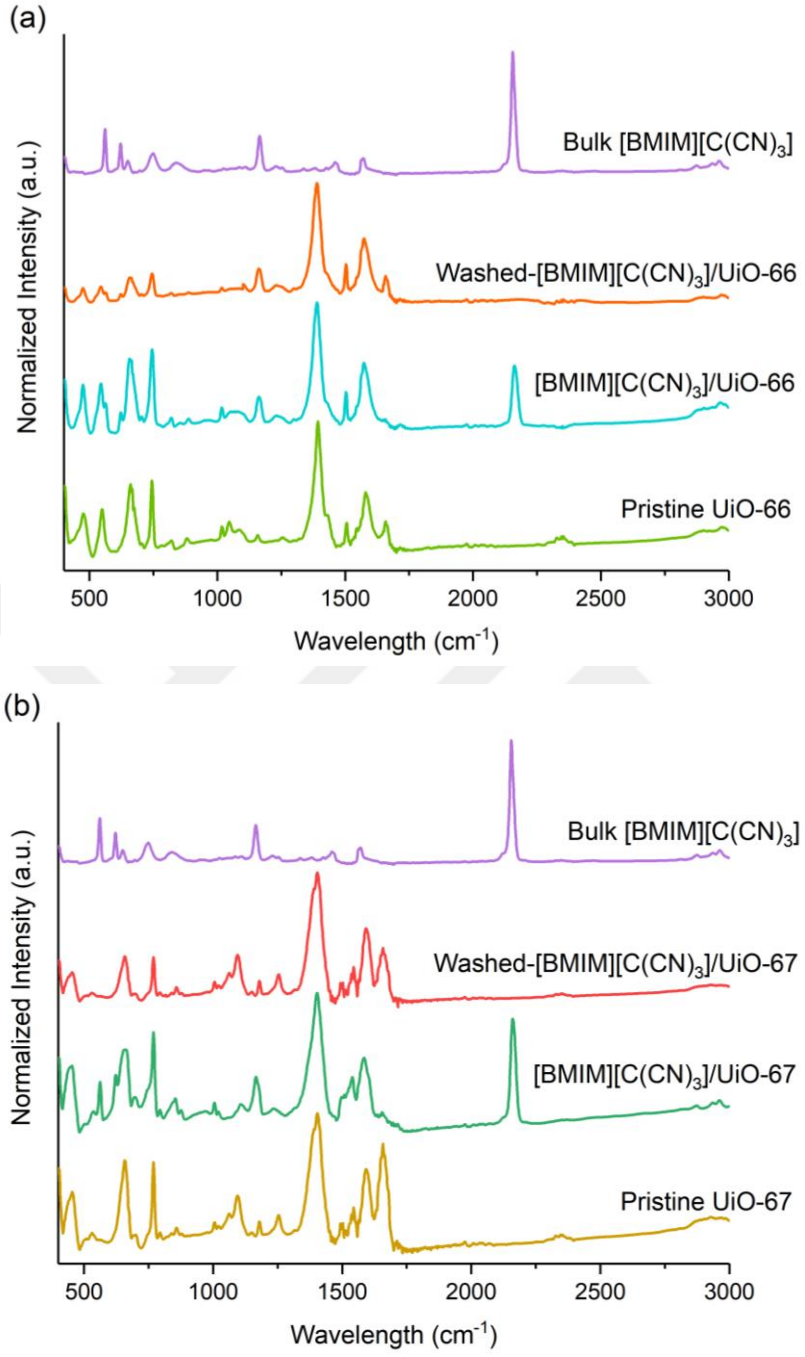
(a)
Normalized Intensity (a.u.)
Bulk [BMIM][C(CN)3]
Washed-[BMIM][C(CN)3]/UiO-66
[BMIM][C(CN)3]/UiO-66
Pristine UiO-66
500
1000
1500
2000
2500
3000
Wavelength (cm-1)
(b)
Normalized Intensity (a.u.)
Bulk [BMIM][C(CN)3]
Washed-[BMIM][C(CN)3]/UiO-67
[BMIM][C(CN)3]/UiO-67
Pristine UiO-67
500
1000
1500
2000
2500
3000
Wavelength (cm-1)

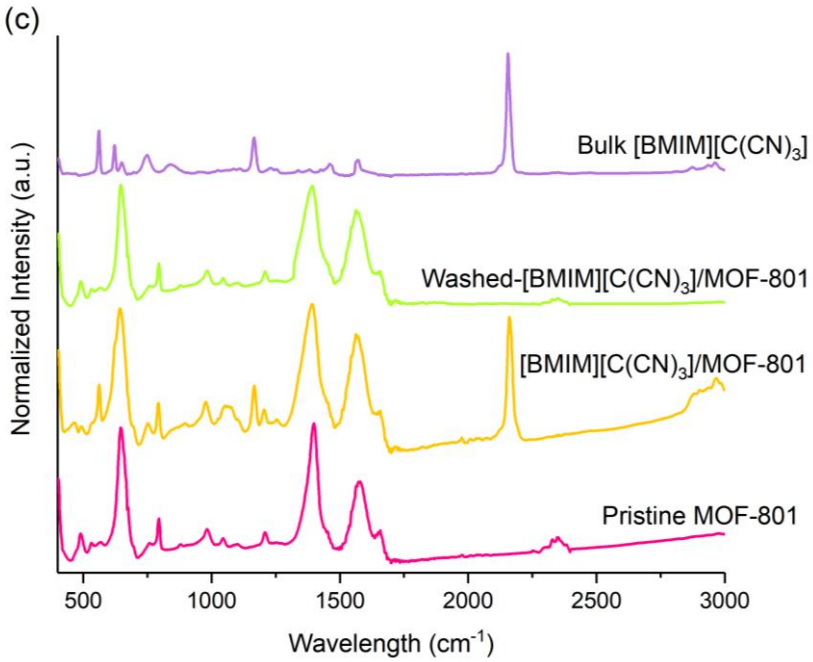

Figure 5.2.1. IR spectra of (a) pristine UiO-66, bulk [BMIM][DCA], and [BMIM][C(CN)$_3$]/UiO-66, (b) pristine UiO-67, bulk [BMIM][C(CN)$_3$], and [BMIM][C(CN)$_3$]/UiO-67, (c) pristine MOF-801, bulk [BMIM][C(CN)$_3$], and [BMIM][C(CN)$_3$]/MOF-801 prior to and after washing with acetone between the range of 3000-400 cm^{-1}.

Morphologies of the as-received pristine MOFs obtained from Beykent University were analyzed by SEM images as given in **Figure 5.2.2**. The images were consistent with the literature indicating the desired crystal morphology and particle size were achieved for the synthesis of IL/Zr-MOF composites.[186, 187] It is noteworthy to mention that the surface morphology of pristine MOF has a significant impact on the resulting IL-incorporated composite since IL molecules only acts as a modifying agent for the host pristine MOFs.

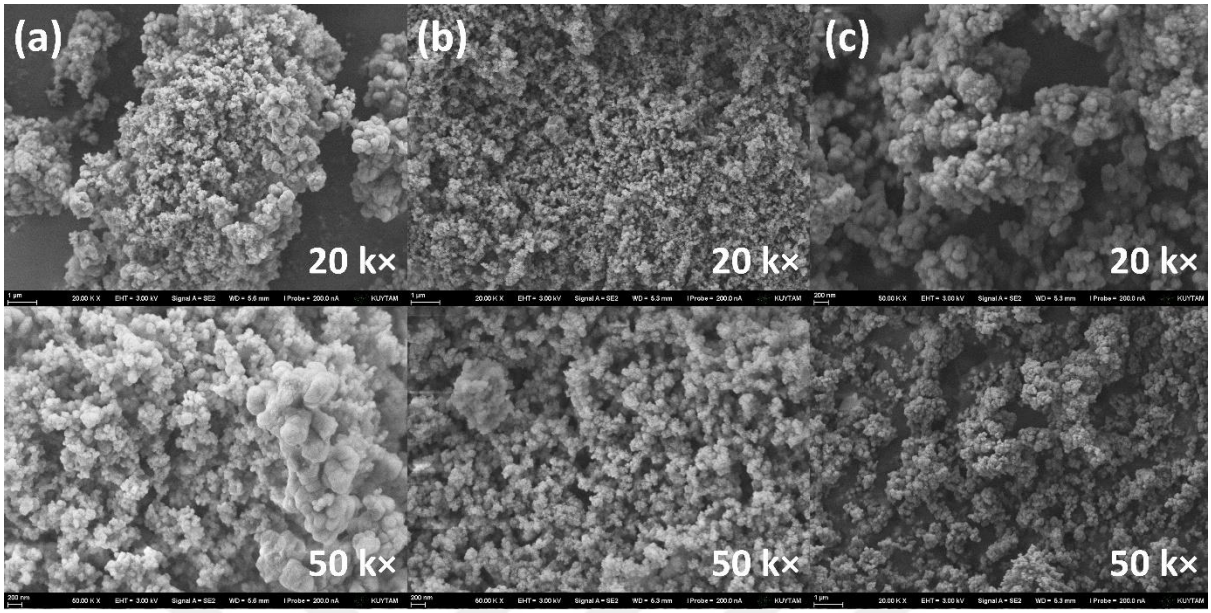

Figure 5.2.2. SEM images of (a) pristine UiO-66, (b) pristine UiO-67, (c) pristine MOF-801, acquired at magnifications of 20 k× and 50 k×.

Surface area and pore volume analysis of samples was conducted by using the obtained N_2 sorption-desorption isotherms, as given in **Figure 5.2.3,** to investigate the effect of IL-incorporation on the surface areas and pore volumes of the pristine MOFs. In **Figure 5.2.3,** the N_2 sorption isotherms of pristine UiO-66, UiO-67, and MOF-801 exhibit Type-I isotherm shape validating the existence of microporous structure consistent with the literature.[90] To further confirm the porous structure of pristine MOFs, BET and Langmuir surface areas were calculated with their corresponding pore volumes as given in **Table 5.2.1**. Accordingly, BET (Langmuir) surface areas and pore volumes of pristine UiO-66, UiO-67, and MOF-801 were calculated as 857, 720, 415 (1264, 1073, 614) m^2/g, and 0.37, 0.40, 0.20 cm^3/g, respectively, which were found to be comparable with the reported literature.[188] Notably, slight deviations in the surface areas were found for each pristine MOFs and these deviations can be associated with the change in synthesis routes. For instance, higher surface area results were reported for the fumarate-based MOF-801 synthesized in the presence of formic acid, which plays a vital role during the formation of crystalline phase.[185] High surface area MOF-801 structures exhibit definite crystalline cages, different from what it was observed in the SEM images of as-received pristine MOF-801 (**Figure 5.2.2(c)**). However, in this study, another synthesis route using HCl as a modulator was utilized during the synthesis of pristine MOF-801.[189] Moreover,

pore size distribution analysis was made for the as-received UiO-66, UiO-67, and MOF-801 as given in **Figure 5.2.4**. Data illustrated that pristine UiO-67 has a wider pore size distribution range compared to the that of pristine UiO-66 and MOF-801 which can be associated with the size of its organic linker.[190] Therefore, pristine UiO-67 is expected to have a higher pore size compared to the other Zr-MOFs considering H_2BPDC organic linker having comparably longer size.

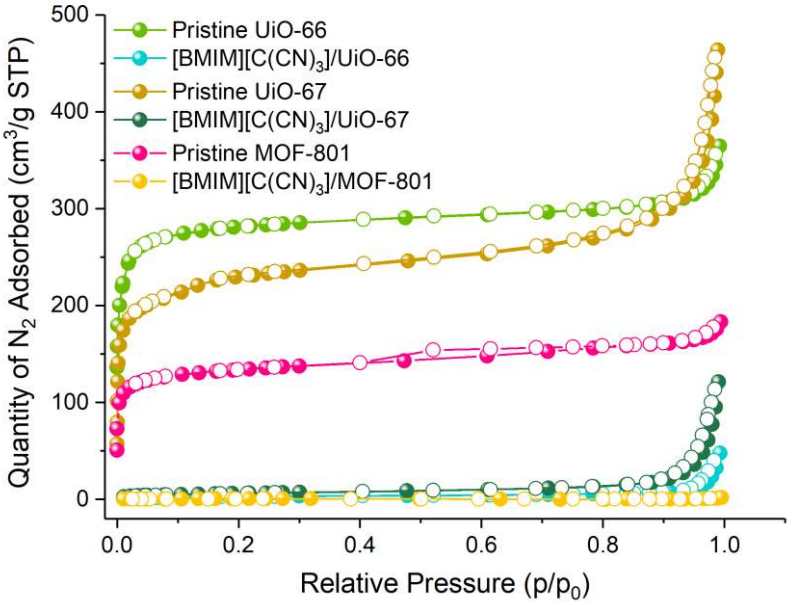

Figure 5.2.3. N_2 adsorption-desorption isotherms of pristine UiO-66, UiO-67, MOF-801 and [BMIM][C(CN)$_3$]/UiO-66, [BMIM][C(CN)$_3$]/UiO-67, [BMIM][C(CN)$_3$]/MOF-801 composites obtained at −196 °C. Filled circles represent adsorption whereas empty circles represent desorption.

Table 5.2.1. BET and Langmuir surface areas of pristine UiO-66, UiO-67, MOF-801 and [BMIM][C(CN)$_3$]/UiO-66, [BMIM][C(CN)$_3$]/UiO-67, [BMIM][C(CN)$_3$]/MOF-801 composites.

Sample	S_{BET} (m^2/g)	$S_{Langmuir}$ (m^2/g)	V_{pore} (cm^3/g)
UiO-66	857	1264	0.37
[BMIM][C(CN)$_3$]/UiO-66	10	17	n/a
UiO-67	720	1073	0.40
[BMIM][C(CN)$_3$]/UiO-67	23	36	n/a
MOF-801	415	614	0.20
[BMIM][C(CN)$_3$]/MOF-801	1.5	2	n/a

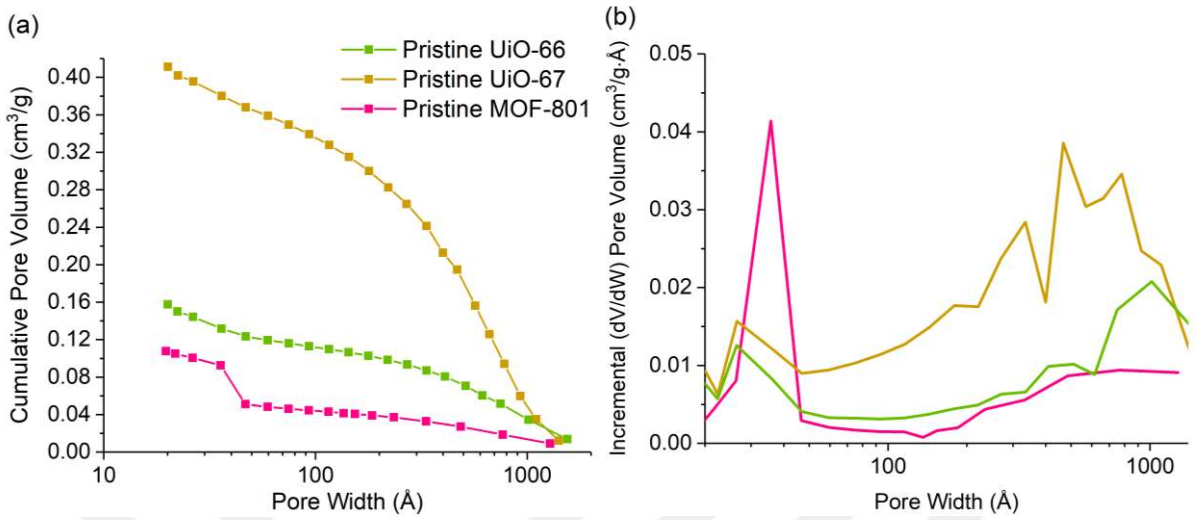

Figure 5.2.4. (a) Cumulative and (b) incremental pore volumes of pristine UiO-66, UiO-67, and MOF-801 with respect to the pore width of the materials. Pore widths are given in logarithmic scale.

In the case of IL-incorporated composites, data illustrated a significant reduction in the surface area results, whereas pore volumes could not be determined. This phenomenon was previously reported by our group for IL/MOFs and other types of IL/porous material composites.[2, 41, 146, 191] The underlying cause is explained as the pore occupation of porous materials by IL molecules with low N_2 solubility. Therefore, BET analysis can be quantitatively misleading for some IL/porous material composites containing an IL with poor N_2 solubility as in the case of [BMIM][C(CN)$_3$]. In this regard, N_2 solubility in bulk [BMIM][C(CN)$_3$] was calculated at 196 °C to mimic the BET measurement conditions by utilizing the COSMO-RS calculations as given in **Figure 5.2.5**. As expected, it was observed that the bulk [BMIM][C(CN)$_3$] has an extremely poor N_2 solubility and subsequently, it can create a blockage for the passage of probe N_2 gas by occupying the pores of Zr-MOFs. Nonetheless, this characterization technique can be used to validate the successful IL-incorporation into the pores of Zr-MOFs. Data illustrated that the pores of pristine UiO-66, UiO-67, and MOF-801 were occupied by IL molecules leading to a significant reduction in the accessible surface area of pristine Zr-MOFs upon IL incorporation.

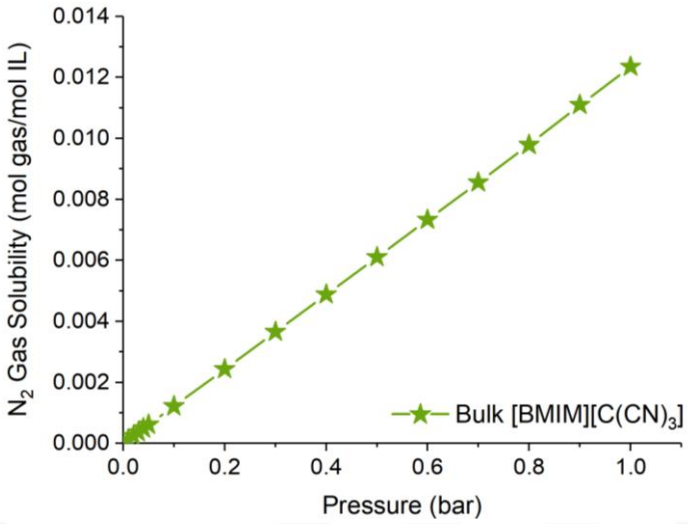

Figure 5.2.5 Solubility N_2 in bulk [BMIM][C(CN)$_3$] computed by COSMO-RS calculations in the range of 0.01-1 bar at BET me-196 °C.

Crystalline structures of pristine UiO-66, UiO-67, MOF-801, and their IL-incorporated composites were examined by XRD measurements. First, the integrity of the crystalline structure was investigated for as-synthesized pristine UiO-66, UiO-67, and MOF-801 to further validate their structural properties. Cubic crystal structure of UiO-66, UiO-67, and MOF-801 have F*m*3*m*, F*m*3*m*, and P*n*-3 symmetries with calculated unit cell parameters of 20.85, 26.81, and 17.85 Å, respectively, consistent with the literature.[190, 192] Characteristic XRD peaks with their corresponding locations can be listed as, (111), (002), and (022) were located at approximately 7.3, 8.5, 12, and 25.6 Å for UiO-66, (111), (002), and (022) were located at approximately 5.7, 6.6, and 9.3 for UiO-67, and (111), (200), (420), and (442) were located at approximately 8.5, 9.9, 19.9, and 30 Å for MOF-801.[193-195] **Figure 5.2.6** illustrated that the XRD spectra of pristine Zr-MOFs were almost completely in accordance with their simulated counterparts by exhibiting each characteristic XRD peak.

Upon the incorporation of IL, the characteristic XRD peaks of Zr-MOFs slightly shifted to lower 2θ values for [BMIM][C(CN)$_3$]/UiO-66 and [BMIM][C(CN)$_3$]/UiO-67 composites indicating an increase in their crystalline unit cell parameter from 20.85 and 26.81 Å to 20.89 and 26.88 Å, respectively. This change can suggest an expansion happening in the unit cell of MOF upon the incorporation of IL inside the cages. Moreover, change in the peak intensities was observed in both the spectra of composite materials. This result can be associated with the change in the surface electron density due to existence of IL molecules. However, in the case

of [BMIM][C(CN)$_3$]/UiO-67, it was observed that the intensities of the characteristic XRD peaks were substantially decreased causing the formation of broader bands in the spectra. This change can be associated with the decreased crystallinity or the disruption of crystalline structure upon the incorporation of IL. Considering the existence of distinguishable characteristic peaks, (111) and (200), it can be said that the IL incorporation damaged the crystal structure of pristine MOF-801 without causing it to collapse entirely. Furthermore, data illustrated that [BMIM][C(CN)$_3$] impregnation into the pores of MOF-801 induced the formation of new defect sites making [BMIM][C(CN)$_3$]/MOF-801 highly defective and amorphous-like compared to the crystalline structure of pristine MOF-801.

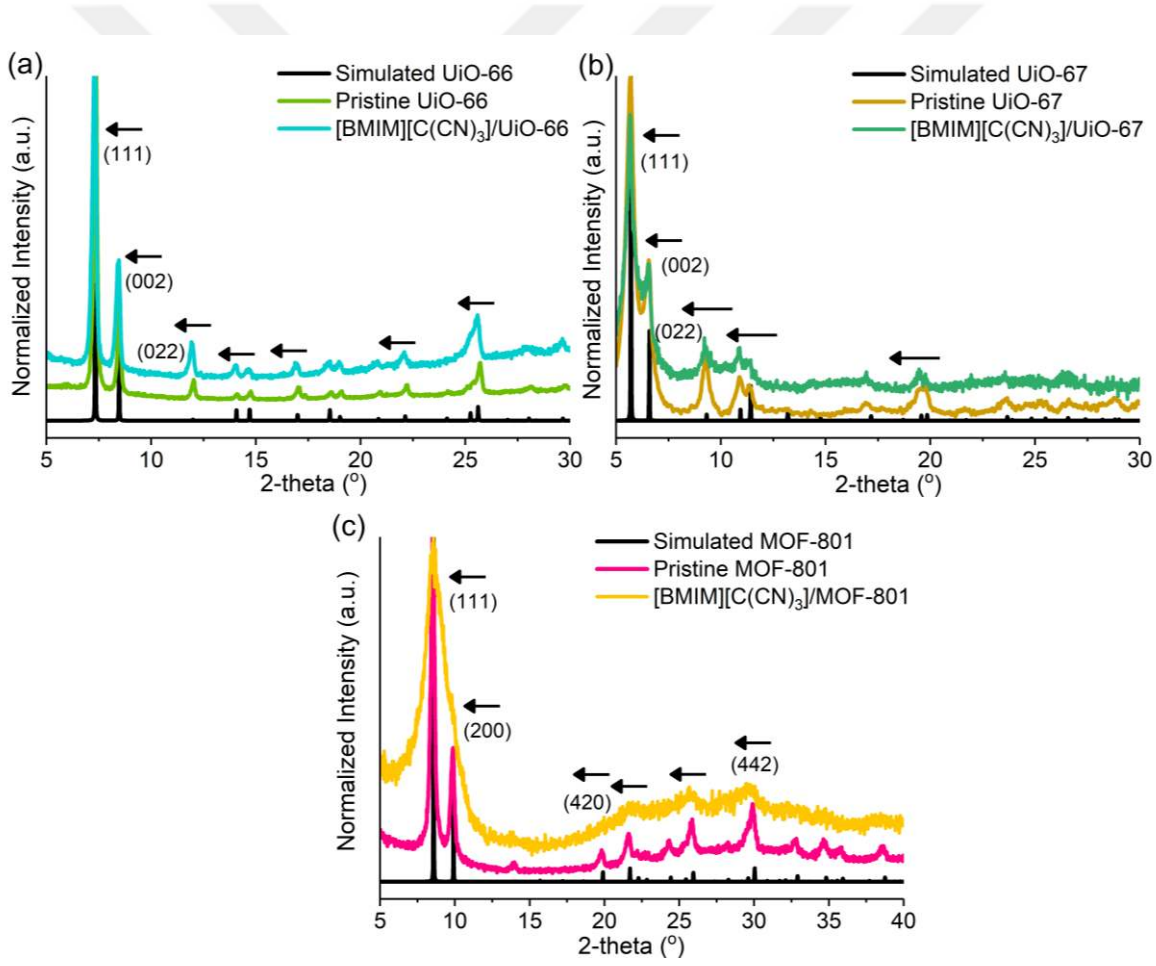

Figure 5.3.6 X-ray diffraction patterns of (a) simulated, pristine, and [BMIM][C(CN)$_3$]-incorporated UiO-66 in 2θ range of 5-30º, (a) simulated, pristine, and [BMIM][C(CN)$_3$]-incorporated UiO-67 in 2θ range of 5-30º, and (c) simulated, pristine, and [BMIM][C(CN)$_3$]-incorporated MOF-801 in 2θ range of 5-40º.

Thermal stability limits of Zr-MOFs and their IL-incorporated composites were investigated by TGA measurements to understand the effect of IL-incorporation on the thermal stability limits of Zr-MOFs. TGA and DTG curves of samples were presented in **Figure 5.2.7.** In **Figure 5.2.7(a)**, pristine UiO-66 and UiO-67 showed a two-step decomposition mechanism representing: (i) evaporation of the moisture content and remaining solvent, (iii) decomposition and collapse of the framework, whereas, for pristine MOF-801, a three-step decomposition mechanism was observed: (i) evaporation of the moisture content and remaining solvent, (ii) decomposition of the organic linker, (iii) decomposition and collapse of the framework, as expected.[90, 196]

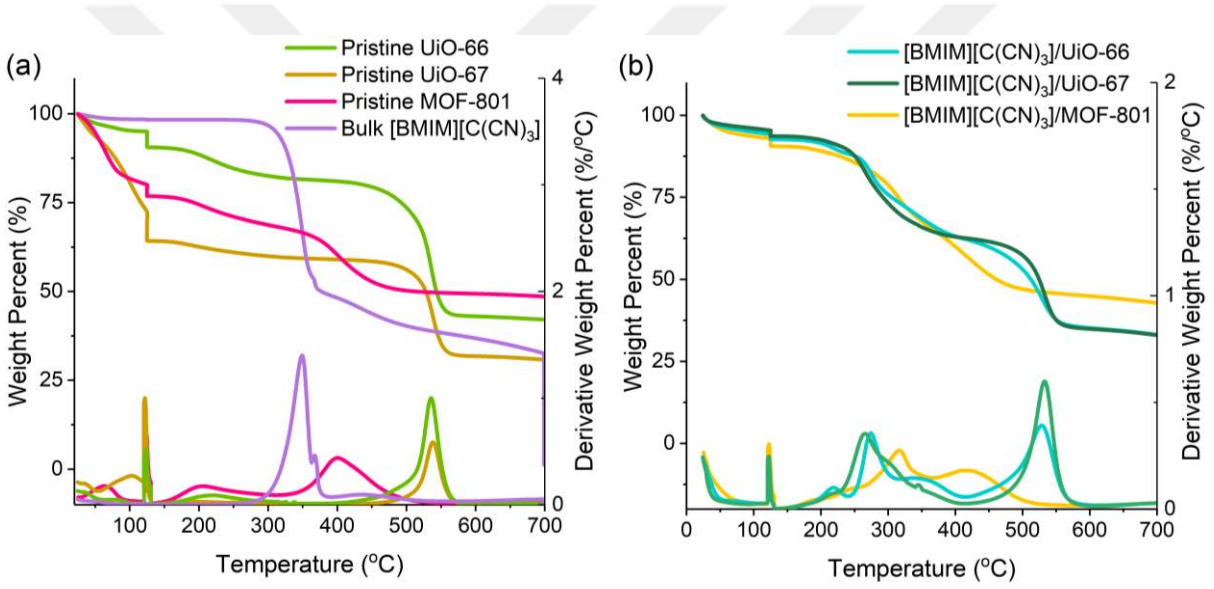

Figure 5.2.7. TGA and DTG curves of (a) pristine UiO-66, UiO-67, MOF-801, and bulk [BMIM][C(CN)$_3$] isothermal at 125 °C and (b) [BMIM][C(CN)$_3$]/UiO-66, [BMIM][C(CN)$_3$]/UiO-67, and [BMIM][C(CN)$_3$]/MOF-801 composites isothermal at 125 °C.

On the other hand, in **Figure 5.2.7(b),** [BMIM][C(CN)$_3$]-incorporated composites showed a three-step decomposition mechanism which might be associated with; (i) the evaporation of the moisture content and remaining solvent, (ii) decomposition of IL molecules together with the organic linker, (iii) decomposition and collapse of the framework. In order to further evaluate the thermal stability limits, T'_{onset} temperatures were estimated from DTG curves of pristine Zr-MOFs, bulk [BMIM][C(CN)$_3$], and [BMIM][C(CN)$_3$]-incorporated composites as tabulated in **Table 5.2.2**. Data demonstrated that the thermal stability limits of

pristine Zr-MOFs and bulk IL were decreased upon IL incorporation showing the impact of newly formed intermolecular interactions between the IL and MOF's cage on the thermal stability limits. These newly formed interactions can cause the observed reduction in the decomposition temperatures considering the molecular-level modification of the MOFs' cage.

Table 5.2.2. Estimated T'_{onset} values of bulk [BMIM][C(CN)$_3$], pristine UiO-66, UiO-67, MOF-801 and their [BMIM][C(CN)$_3$]-incorporated composites. Error bar determined according to the deviation of three consecutive estimations.

Sample	T'_{onset} (°C)
UiO-66	505±8
[BMIM][C(CN)$_3$]/UiO-66	240±9
UiO-67	518±6
[BMIM][C(CN)$_3$]/UiO-67	223±7
MOF-801	354±9
[BMIM][C(CN)$_3$]/MOF-801	232±7
Bulk [BMIM][C(CN)$_3$]	310±4

To get a comprehensive insight into the nature of these newly formed intermolecular interactions, IR spectra of the bulk [BMIM][C(CN)$_3$], pristine UiO-66, UiO-67, MOF-801, and their composites with [BMIM][C(CN)$_3$] were obtained for further characterization. Accordingly, characteristic IR peaks of bulk and pristine materials were identified, and corresponding peak shifts were analyzed to elucidate the newly formed interactions between the structure of Zr-MOFs and [BMIM][C(CN)$_3$] molecules. **Figure 5.2.8** shows the IR spectra of bulk [BMIM][C(CN)$_3$], pristine UiO-66, and [BMIM][C(CN)$_3$]/UiO-66 composite. Characteristic IR peaks of pristine UiO-66 located at approximately 477, 551, 668, 744, 1394, 1506, 1582 cm^{-1} were assigned to in-plane and out of plane δ(COO$^-$), asymmetric ν(Zr−(OC)), ν(μ_3–O) of bridging bond, asymmetric ν(Zr−O), symmetric ν(O−C−O) band of carboxylate, ν(C=C) band of benzene ring, and asymmetric ν(O−C−O) band of carboxylate, respectively; whereas, the characteristic IR peaks of [BMIM][C(CN)$_3$] located at 1400-1600, 2155, 2850-3200 cm^{-1} were identified as the stretching vibrations of imidazolium ring of cation, ν(C≡N) of anion, and C−H stretching bands of imidazolium ring, respectively.[53, 90, 197-199] Data illustrated that asymmetric ν(Zr−O) band of UiO-66 blue-shifted from 744 to 747 cm^{-1} upon IL confinement, while ν(μ_3–O) band of bridging bond did not show any shift indicating the

lack of interactions between the Zr modes of UiO-66 and IL molecules. Consistently, significant red shifts in the vibrational bands of δ(COO$^-$), symmetric ν(O−C−O), ν(C=C), and asymmetric ν(O−C−O) were observed from 477, 1394, 1506, and 1582 cm^{-1} to 474, 1389, 1502, and 1574 cm^{-1}, respectively, suggesting the presence of possible interactions through the organic linker. Moreover, slight red-shift of ν(Zr−(OC)) was interpreted as the weakening of the bond between the Zr modes and organic ligand; however, structural integrity was confirmed through the presence of the Zr-BDC ligand coordination node located at approximately 1018 cm^{-1}. In the case of IL, characteristic ν(C≡N) band of anion exhibited a significant blue-shift from 2155 to 2163 cm^{-1} hinting a weakening of the interionic interactions between the anion and cation of IL. Accordingly, characteristic peaks of imidazolium ring located at 1460 and 1570 cm^{-1} -shifted to lower energies to 1435 and 1543 cm^{-1}, respectively, further validating the presence of an interaction between the cation of IL and the BDC ligand of UiO-66.

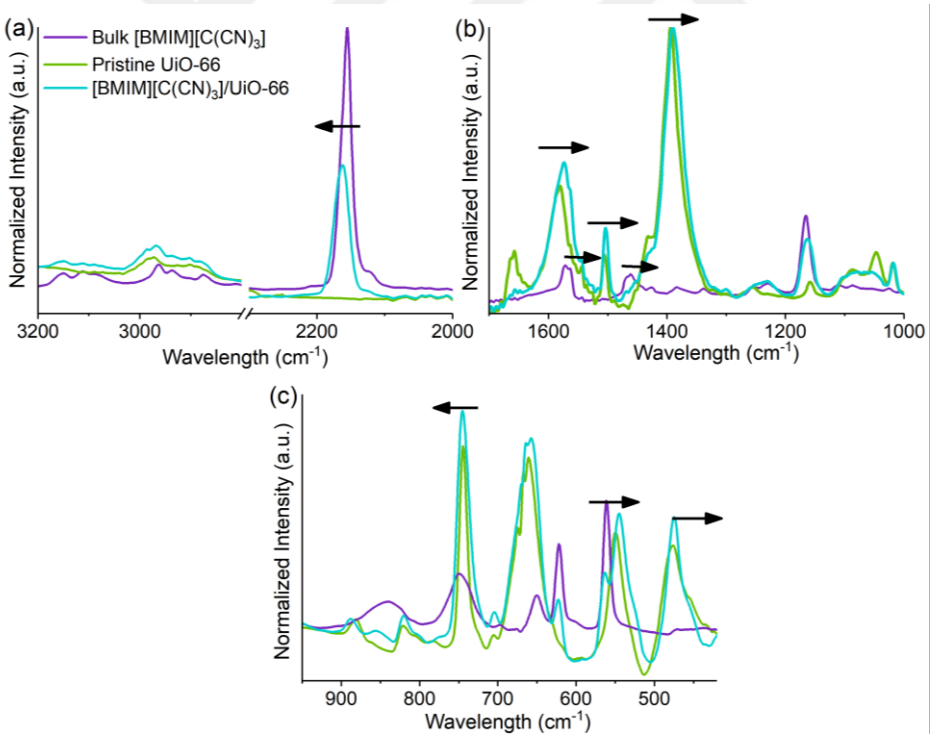

Figure 5.2.8. IR spectra of bulk [BMIM][C(CN)$_3$], pristine UiO-66, and [BMIM][C(CN)$_3$]/UiO-66 in the spectral range of (a) 3200-2000 cm^{-1}, (b) 1700-1000 cm^{-1}, and (c) 950-400 cm^{-1}.

A similar case was observed for the IR spectra of [BMIM][C(CN)$_3$]/UiO-67 as given in **Figure 5.2.9**. Characteristic IR peaks of UiO-67, located at approximately 454, 532, 658, and

769 cm^{-1} corresponding to the stretching vibrational bands of Zr-O nodes, blue-shifted to higher wavenumbers, to 474, 545, 664, and 770 cm^{-1}, respectively, upon the incorporation of IL.[200-203] This change can be interpreted as the strengthening of the bond between Zr metal and bridging oxygen leading to the weakened interactions between the Zr metal nodes and the organic ligand of UiO-67. Comparably, it can be inferred that the electron density on the Zr metal nodes increased more for UiO-67 different from what it was observed in UiO-66 case. Furthermore, characteristic IR peaks related to the carbonyl group of H_2BPDC ligand red shifted from 1403, 1563, and 1658 cm^{-1} to 1390, 1584, and 1640 cm^{-1}, respectively, validating the decreased electron density of the organic linker due to the presence of possible interactions with the IL molecules. These possible interactions were further elucidated with the shifts in IL's characteristic peaks, where a blue-shift to 2165 cm^{-1} and red shifts to 1436 and 1541 cm^{-1} were observed for ν(C≡N) band and imidazolium ring vibrations, respectively, confirming a direct interaction between the H_2BPDC ligand and the cation of [BMIM][C(CN)$_3$].

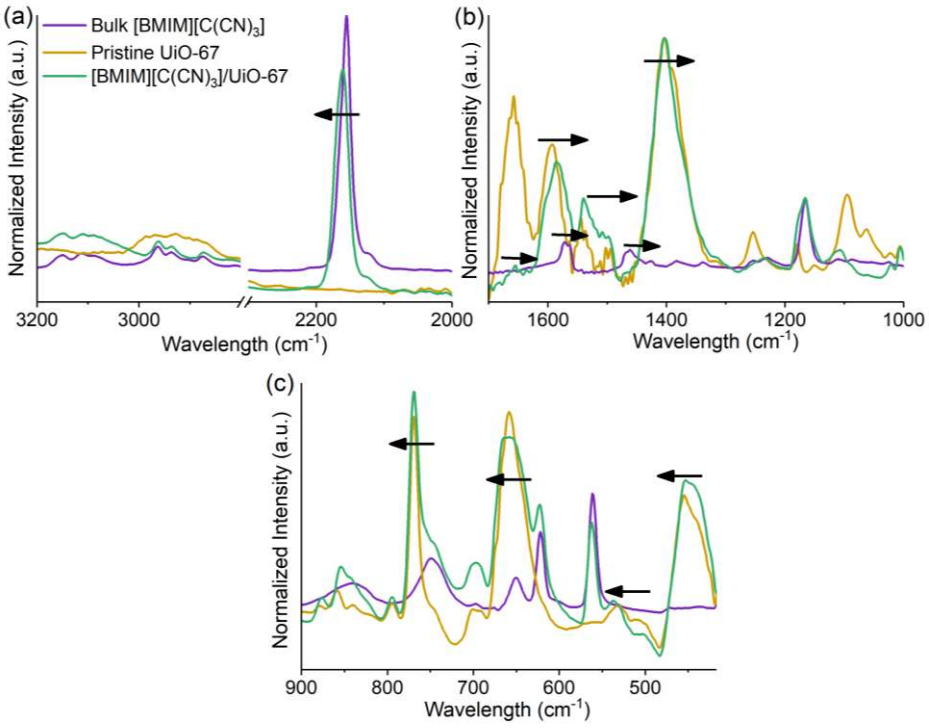

Figure 5.2.9. IR spectra of bulk [BMIM][C(CN)$_3$], pristine UiO-67, and [BMIM][C(CN)$_3$]/UiO-67 in the spectral range of (a) 3200-2000 cm^{-1}, (b) 1700-1000 cm^{-1}, and (c) 900-400 cm^{-1}.

In the case of MOF-801, IR spectra shown in **Figure 5.2.10** illustrated that the asymmetric ν(Zr–(OC)) mode did not show any shift in its IR band located at approximately 490 cm^{-1} indicating the preservation of intermolecular bond strength between the Zr modes and H_2PBDC ligand. However, IR bands representing the stretching vibrations of $Zr_6(OH)_4O_4$ cluster, located at approximately 646 cm^{-1}, and asymmetric and symmetric ν(O–C–O) stretching of carboxylic group, located at approximately 1399 and 1584 cm^{-1}, respectively, both red-shifted to lower wavenumbers (to 639, 1392, and 1573 cm^{-1}, respectively) demonstrating a reduction in bond strength for both the Zr metal nodes and organic ligand of MOF-801 upon IL incorporation.[204] This change can be interpreted as three possible scenarios: (i) presence of two separate interaction sites, (ii) electron reduction on Zr-ligand coordination sites due to newly formed IL-ligand interactions, (iii) electron reduction on ligand associated with the newly formed interactions between IL and Zr-ligand coordination sites. In the case of IL's interaction site, same trend was observed for ν(C≡N) band and imidazolium ring vibrations, where ν(C≡N) blue-shifted from 2155 to 2161 cm^{-1} and imidazolium ring vibrations red-shifted from 1571 to 1562 cm^{-1}. Therefore, IL's interaction site remains the same, as the cation part, while the interaction site of MOF-801 varies from other Zr-MOF structures. This change in interaction site can be attributed to the aliphatic type of organic linker of MOF-801 compared to the that of UiO-66 and UiO-67 whose organic linker contains a ring structure. These inferences can be complemented with the obtained XRD analysis which indicated a significant alteration in the crystal structure of [BMIM][$C(CN)_3$]/MOF-801 composite.

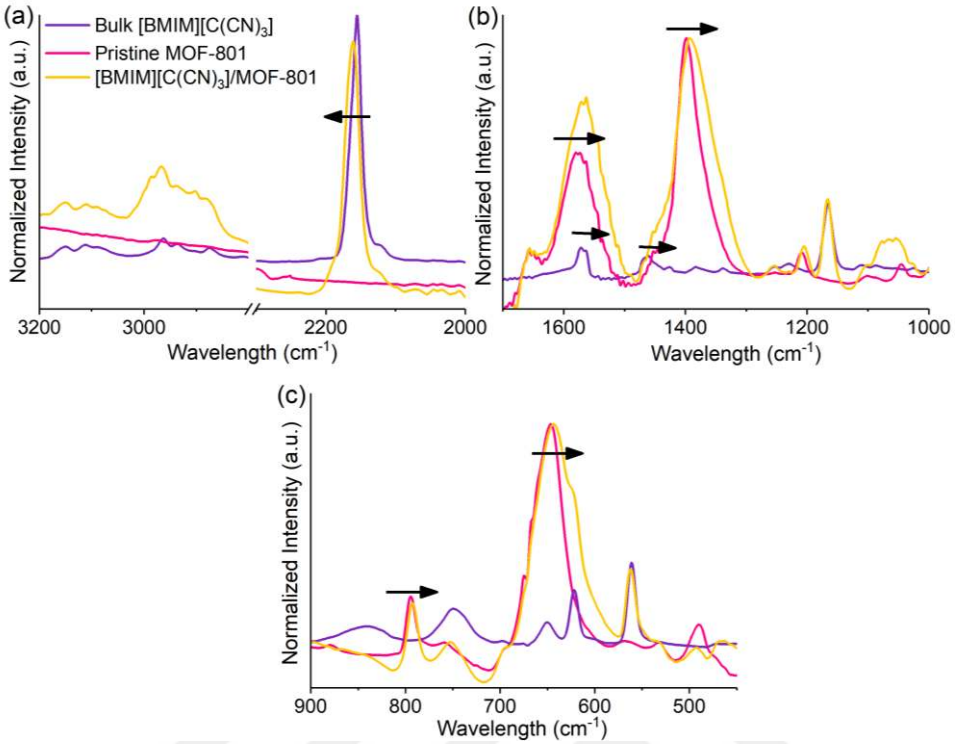

Figure 5.3.10. IR spectra of bulk [BMIM][C(CN)$_3$], pristine MOF-801, and [BMIM][C(CN)$_3$]/MOF-801 in the spectral range of (a) 3200-2000 cm^{-1}, (b) 1700-1000 cm^{-1}, and (c) 900-400 cm^{-1}.

Volumetric CO_2, CH_2, C_2H_2, C_2H_4, and N_2 gas adsorption isotherms were measured in the pressure range of 0.001-5 bar at 25 °C to investigate the effect of [BMIM][C(CN)$_3$] confinement on the gas adsorption performance of the as-received Zr-MOFs; UiO-66, UiO-67, and MOF-801. Results presented in **Figure 5.3.11** demonstrated a significant decrease in the uptakes of all gasses owing to the pore blockage and occupation of pristine MOFs by incorporated IL molecules. Reduction in the uptakes was expected as the successful confinement of [BMIM][C(CN)$_3$] molecules inside the cages of Zr-MOFs was confirmed through various characterization techniques in previous sections. Moreover, it is important to note that all composites exhibited significantly poor N_2 adsorption uptakes, in particular, [BMIM][C(CN)$_3$]/UiO-66 composite showed almost no N_2 adsorption below 1 bar with negative N_2 uptake values suggesting a remarkable N_2-phobicity of the synthesized composite.

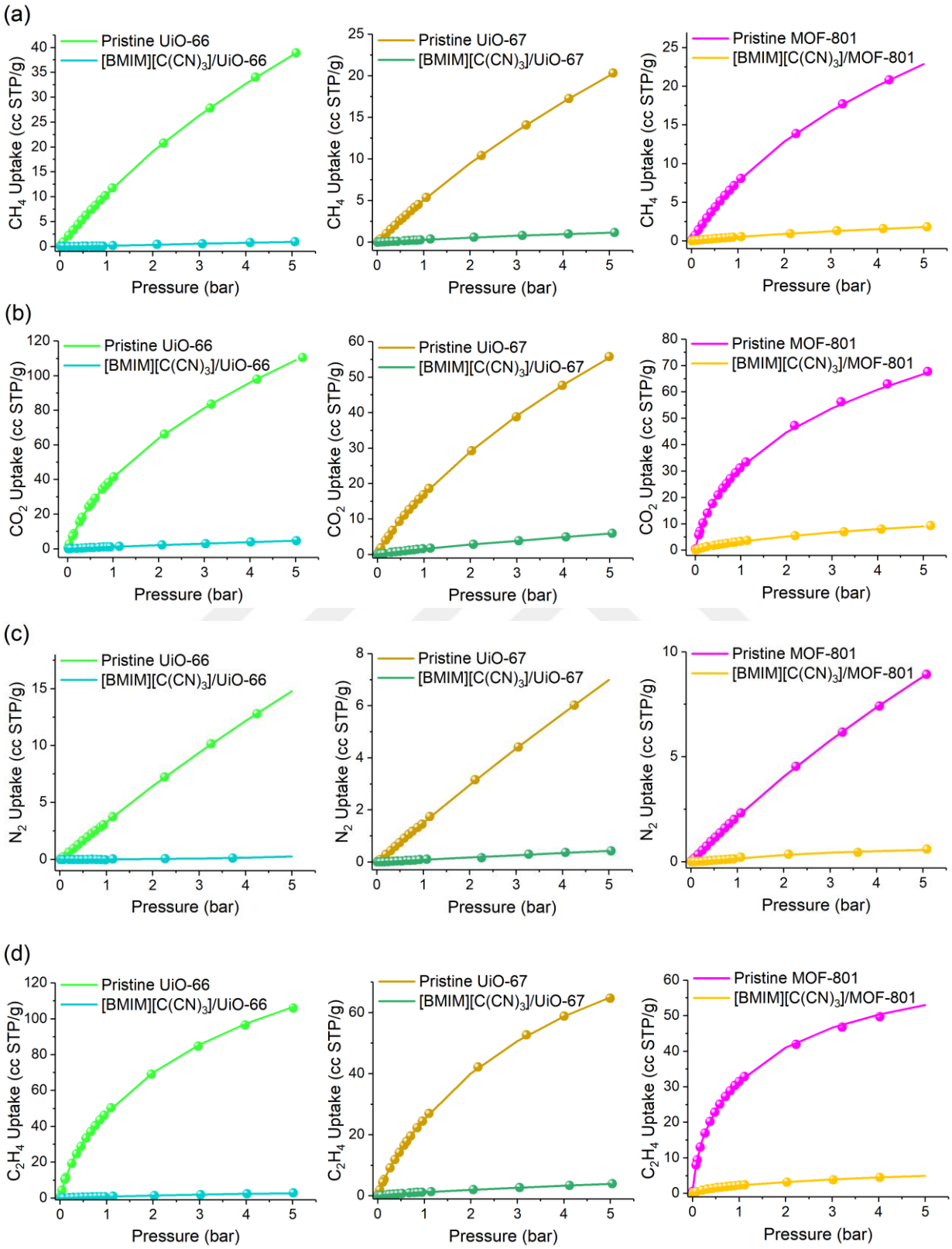
(a)
Pristine UiO-66
[BMIM][C(CN)3]/UiO-66
CH4 Uptake (cc STP/g)
Pressure (bar)
Pristine UiO-67
[BMIM][C(CN)3]/UiO-67
CH4 Uptake (cc STP/g)
Pressure (bar)
Pristine MOF-801
[BMIM][C(CN)3]/MOF-801
CH4 Uptake (cc STP/g)
Pressure (bar)
(b)
Pristine UiO-66
[BMIM][C(CN)3]/UiO-66
CO2 Uptake (cc STP/g)
Pressure (bar)
Pristine UiO-67
[BMIM][C(CN)3]/UiO-67
CO2 Uptake (cc STP/g)
Pressure (bar)
Pristine MOF-801
[BMIM][C(CN)3]/MOF-801
CO2 Uptake (cc STP/g)
Pressure (bar)
(c)
Pristine UiO-66
[BMIM][C(CN)3]/UiO-66
N2 Uptake (cc STP/g)
Pressure (bar)
Pristine UiO-67
[BMIM][C(CN)3]/UiO-67
N2 Uptake (cc STP/g)
Pressure (bar)
Pristine MOF-801
[BMIM][C(CN)3]/MOF-801
N2 Uptake (cc STP/g)
Pressure (bar)
(d)
Pristine UiO-66
[BMIM][C(CN)3]/UiO-66
C2H4 Uptake (cc STP/g)
Pressure (bar)
Pristine UiO-67
[BMIM][C(CN)3]/UiO-67
C2H4 Uptake (cc STP/g)
Pressure (bar)
Pristine MOF-801
[BMIM][C(CN)3]/MOF-801
C2H4 Uptake (cc STP/g)
Pressure (bar)

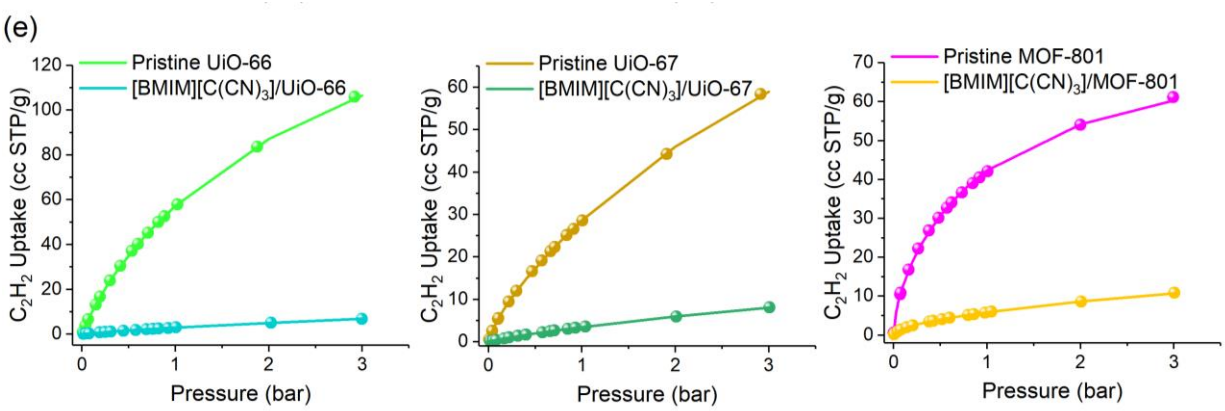

Figure 5.2.11. Volumetric (a) CH_4, (b) CO_2, (c) N_2, (d) C_2H_4, and (e) C_2H_2 gas adsorption isotherms of pristine UiO-66, UiO-67, MOF-801, and their [BMIM][C(CN)$_3$]-incorporated composites in the pressure range of 0.001 to 5 bar at 25 °C. Circle represents the experimentally obtained data and straight line represents isotherm fittings.

Selective gas separation performances of synthesized [BMIM][C(CN)$_3$]/Zr-MOF composites were investigated by calculating ideal selectivities from obtained volumetric gas adsorption data. Mainly, selective separation of CO_2, C_2H_2, and C_2H_4 hydrocarbon gasses were examined to evaluate the effect of IL-incorporation on the selective hydrocarbon separation performance of pristine Zr-MOFs. **In Figure 5.2.12**, ideal CO_2/CH_4 and CO_2/N_2, selectivities of each composite are presented. Selective CO_2 separation performance of each Zr-MOF was enhanced upon [BMIM][C(CN)$_3$] incorporation showing the promising potential of IL confinement inside the cages of Zr-MOFs. These results suggest that the modification of the pore environment by [BMIM][C(CN)$_3$] molecules can be extended to other Zr-MOFs for superior CO_2 separation performance. Furthermore, a remarkable improvement in the selective separation performance of CO_2 from N_2 was observed for [BMIM][C(CN)$_3$]/UiO-66 composite with ideal CO_2/N_2 selectivity results reaching practically infinite level (10^{11}) at low-pressure region. Also, an ideal CO_2/N_2 selectivity of 1091, from 12.5, was achieved at 1 bar for [BMIM][C(CN)$_3$]/UiO-66 composite highlighting the potential usage of synthesized composite for the superior performance in direct CO_2 capture from air.

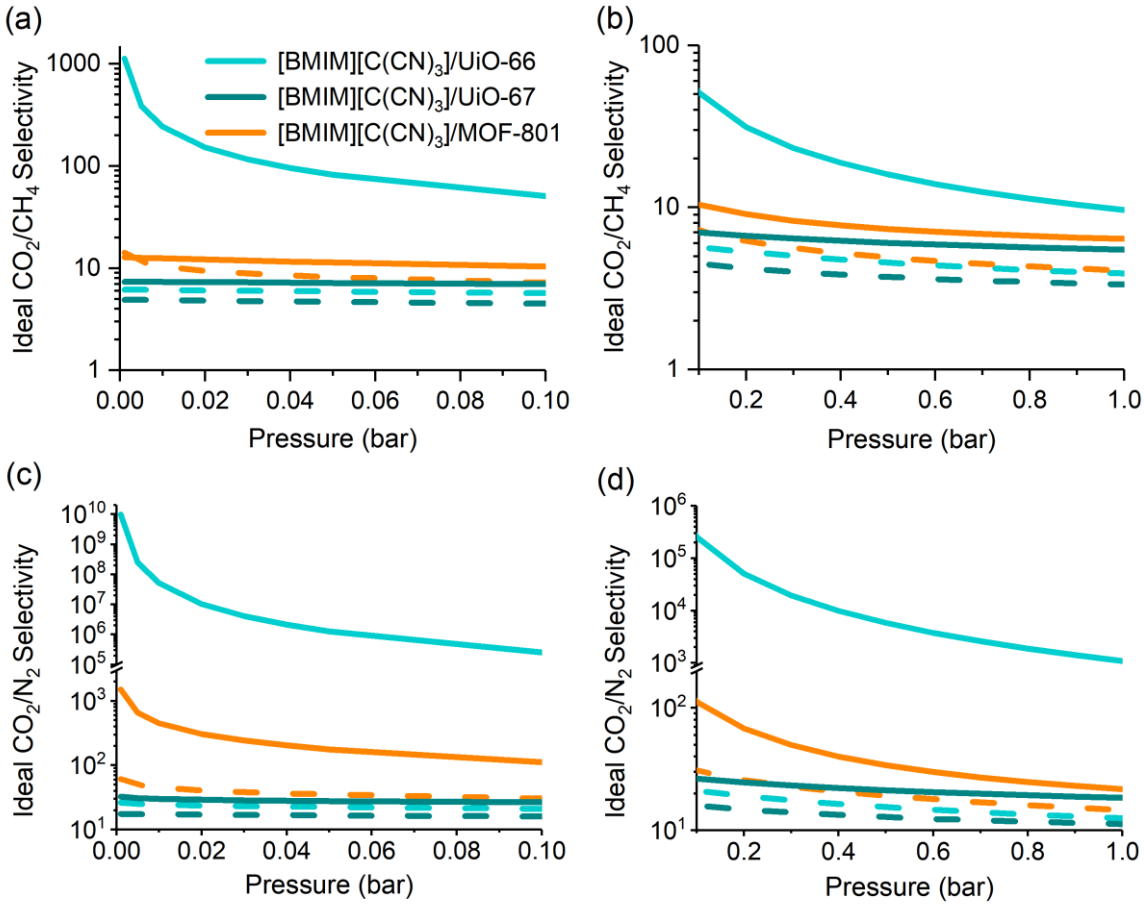

Figure 5.3.12. Ideal (a-b) CO_2/CH_4, (c-d) CO_2/N_2 selectivities of pristine UiO-66, UiO-67, MOF-801, and their [BMIM][C(CN)$_3$]-incorporated composites in the pressure range of (a-c) 0.001 to 0.1 bar and (b-d) 0.1 to 1 bar at 25 °C. Continuous curve represents IL-incorporated composite, and the dashed curve represents pristine material.

Similarly, an improved C_2H_4 separation performance was obtained in the case of [BMIM][C(CN)$_3$]/UiO-66 composite with the observed ideal C_2H_4/N_2 selectivity values of 10^{11} in the low-pressure range as given in **Figure 5.3.13(c)**. Moreover, a noteworthy improvement in the C_2H_4 separation performance of MOF-801 was also observed in low-pressure range. The ideal C_2H_4/N_2 selectivity of 5690 was achieved with a 42-times increase from 135 upon the incorporation of [BMIM][C(CN)$_3$] into the cages of MOF-801. However, there were no noticeable selectivity increase in the ideal C_2H_2/N_2 and C_2H_4/CH_4 selectivities of [BMIM][C(CN)$_3$]/UiO-67 composite indicating a poor affinity towards C_2H_4 molecules with a mediocre C_2H_4 separation performance.

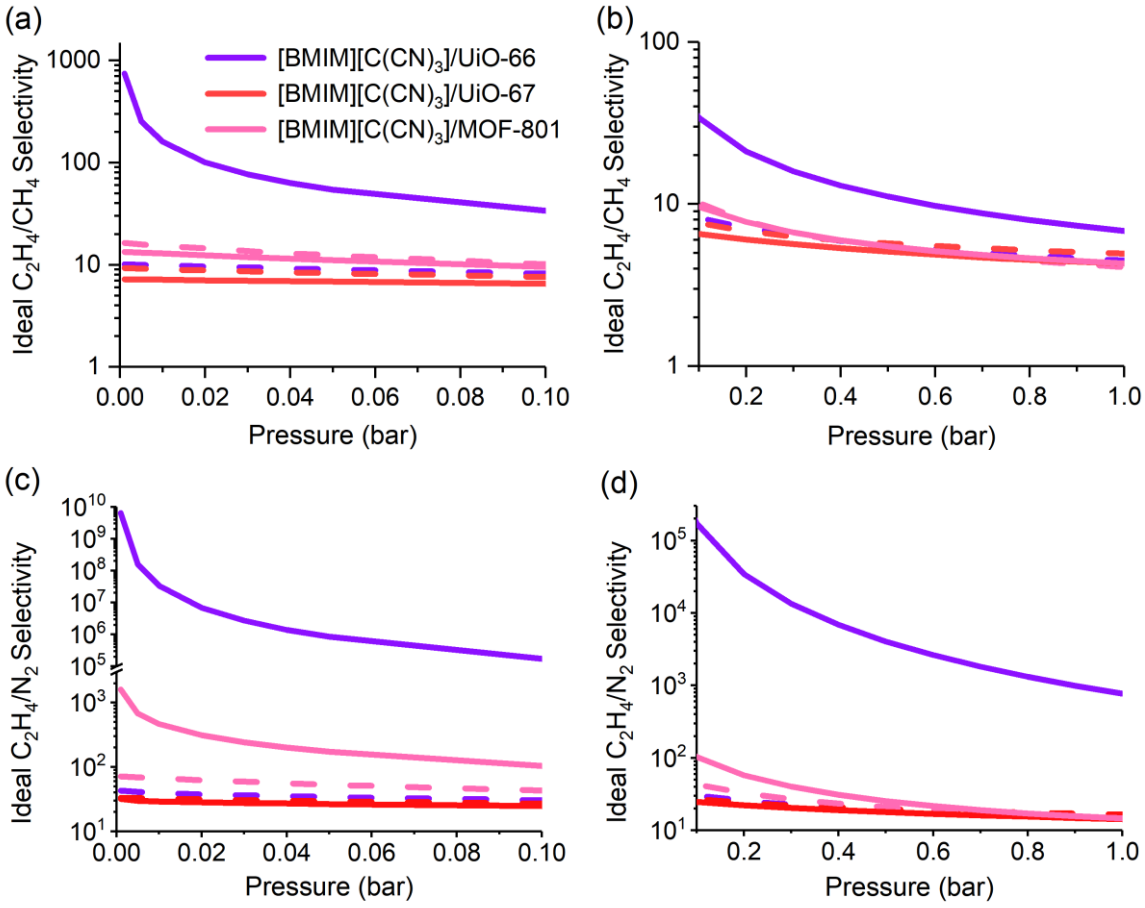

Figure 5.3.13. Ideal (a-b) C_2H_4/CH_4, (c-d) C_2H_4/N_2 selectivities of pristine UiO-66, UiO-67, MOF-801, and their [BMIM][C(CN)$_3$]-incorporated composites in the pressure range of (a-c) 0.001 to 0.1 bar and (b-d) 0.1 to 1 bar at 25 °C. Straight line represents IL-incorporated composite, and the dashed line represents pristine material.

Owing to the obtained almost no uptakes of N_2 adsorption, [BMIM][C(CN)$_3$]/UiO-66 composite was also shown to be highly C_2H_2 selective consistent with our previous findings on other gasses, $_{CO2}$ an C_2H_4. Accordingly, it can be said that the pristine UiO-66 becomes completely selective for hydrocarbon gas molecules over N_2 upon the incorporation of [BMIM][C(CN)$_3$] at low-pressure region. Interestingly, it was also observed that [BMIM][C(CN)$_3$]/UiO-66 showed an increased affinity towards C_2H_2 molecules compared to the that of C_2H_4 with reported 5-times improvement in the ideal C_2H_2/C_2H_4 selectivity, from 0.9 to 4.9. Increased hydrocarbon affinity over N_2 was also demonstrated in the case of MOF-801, illustrating a significant improvement in the ideal C_2H_2/N_2 selectivity. On the other hand,

poor affinity towards hydrocarbon gasses and almost no improvement in the selective C_2H_2 separation performance were observed in the case of [BMIM][C(CN)$_3$]/UiO-67. Results illustrated the different resulting effect of the same modification agent, [BMIM][C(CN)$_3$], incorporated on different Zr-based framework structures revealing the significance of IL-MOF pairing selection. In the cases of UiO-66 and MOF-801, [BMIM][C(CN)$_3$] incorporation induced a positive effect on the molecular affinity towards CO_2, C_2H_2, and C_2H_4 molecules, while the same IL had an almost negligible effect on the selective separation of CO_2, C_2H_2, and C_2H_4 molecules in the case of UiO-67.

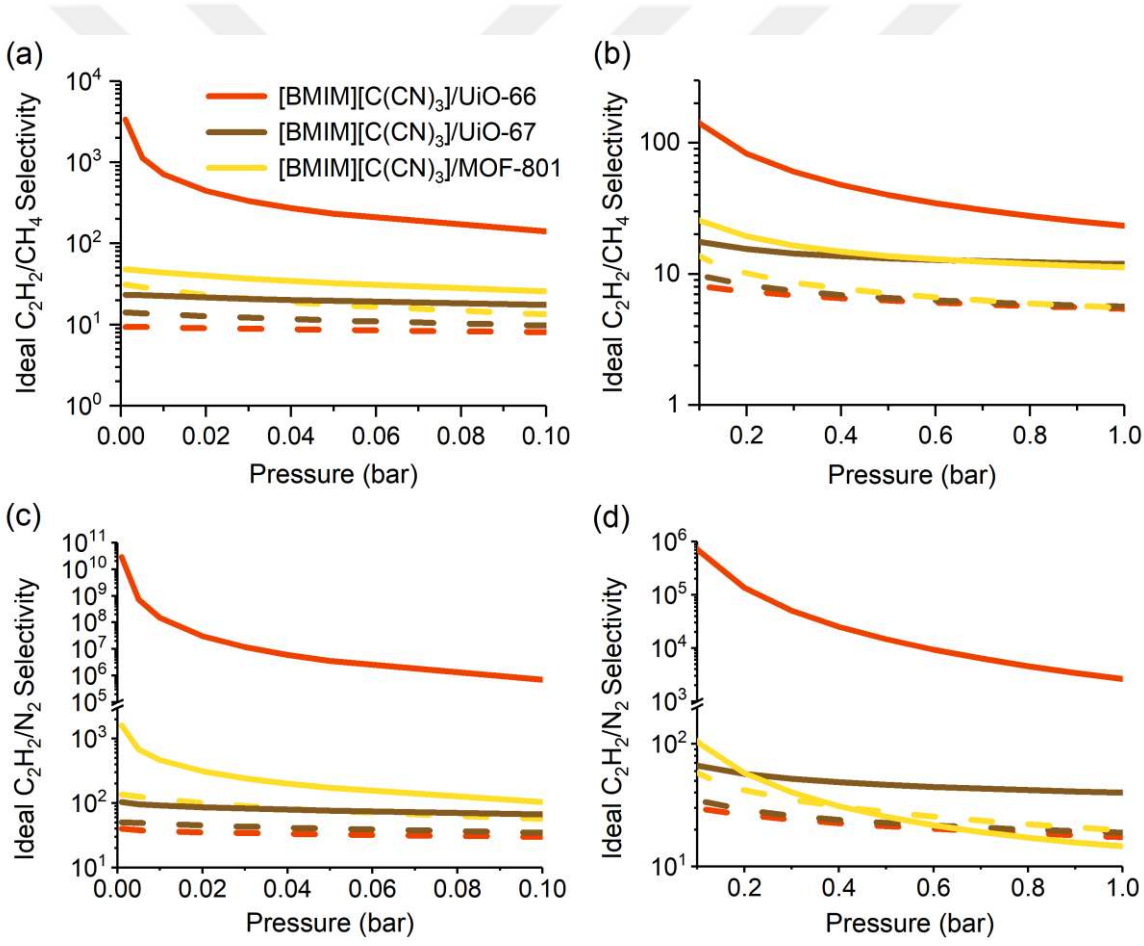

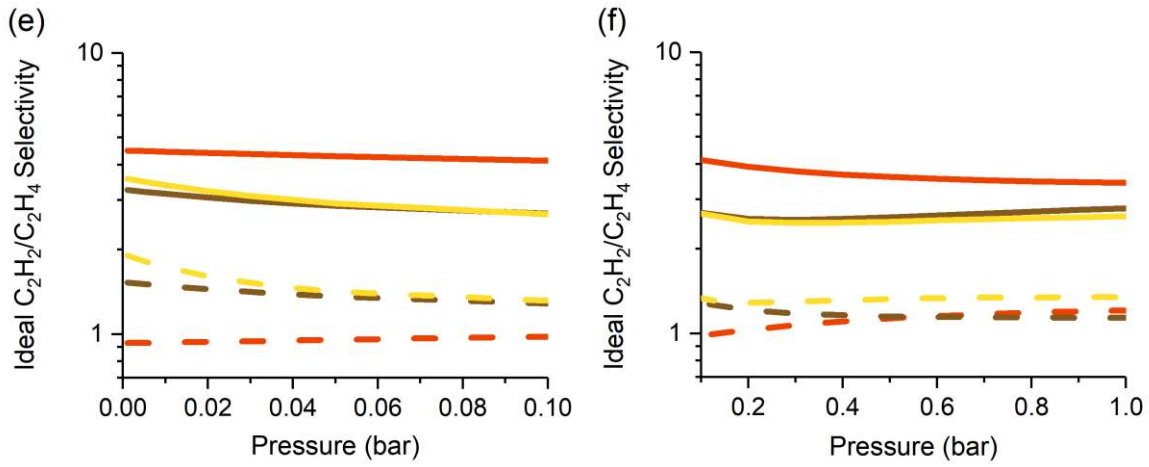

Figure 5.3.14. Ideal (a-b) C_2H_2/CH_4, (c-d) C_2H_2/N_2, (e-f) C_2H_2/C_2H_4 seletivities of pristine UiO-66, UiO-67, MOF-801, and their [BMIM][C(CN)$_3$]-incorporated composites in the pressure range of (a-c-e) 0.001 to 0.1 bar and (b-d-f) 0.1 to 1 bar at 25 °C. Straight line represents IL-incorporated composite, and the dashed line represents pristine material.

In conclusion, the effect of IL incorporation on the gas adsorption and separation performance of three Zr-MOFs, UiO-66, UiO-67, and MOF-801, was investigated by impregnating an imidazolium-based IL, [BMIM][C(CN)$_3$], into the cages of stated Zr-MOFs. [BMIM][C(CN)$_3$]/UiO-66, [BMIM][C(CN)$_3$]/UiO-67, and [BMIM][C(CN)$_3$]/MOF-801 were synthesized via simple wet impregnation technique and samples were characterized in detail with the help of SEM, XRD, BET, TGA, and FTIR techniques. Volumetric CO_2, CH_4, C_2H_4, C_2H_2, and N_2 gas adsorption measurements were performed on each sample. Results illustrated remarkable improvements reaching almost infinity (10^{11}) in the ideal selectivities of CO_2/N_2, C_2H_4/N_2, and C_2H_2/N_2 for [BMIM][C(CN)$_3$]/UiO-66 composite. Similarly, significant enhancement in the selective CO_2, C_2H_4, and C_2H_2 separation performances of MOF-801 were observed indicating an increase in the affinity towards CO_2, C_2H_4, and C_2H_2 molecules upon [BMIM][C(CN)$_3$] incorporation. On the other hand, no noticeable change in the selective separations of CO_2, C_2H_4, and C_2H_2 molecules was observed for [BMIM][C(CN)$_3$]/UiO-67 composite. These results were associated with the influence of newly formed unique intermolecular interactions between the IL, [BMIM][C(CN)$_3$], and the three different Zr-based framework structure, UiO-66, UiO-67, and MOF-801.

Chapter 6: Rational Design of a Core-Shell Type IL/MOF Composite for Superior Air Separation Performance: [$P_{6,6,6,14}$][DCA]/PCN-250(Fe) Composite Offering Exceptional O_2/N_2 Selectivity

In this chapter, rational design of a core-shell type IL/MOF composite was conducted via an integrated computational-experimental approach for air separation. IL and pristine MOF were selected by combining several computational tools, namely, COSMO-RS calculations, DFT calculations, and GCMC simulations, and best predicted core-shell type IL-MOF pairing was utilized to experimentally synthesize a novel IL/MOF composite that achieved a superior air separation performance compared to previously reported materials. As presented by several computational tools, a phosphonium-based IL, trihexytetradecylphosphonium dicyanamide ($[P_{6,6,6,14}][DCA]$), was incorporated on the surface of an iron-based MOF, PCN-250(Fe), for improved O_2 separation performance. Synthesized novel $[P_{6,6,6,14}][DCA]$/PCN-250(Fe) composite was characterized in depth detail by using several characterization tools, as SEM/EDX, BET, XRD, TGA, and FTIR, to elucidate the structural changes occurred upon IL incorporation. Volumetric O_2 and N_2 gas adsorption measurements were conducted to investigate the corresponding O_2/N_2 separation performance of a novel $[P_{6,6,6,14}][DCA]$/PCN-250(Fe) composite. To maximize the performance enhancement by optimizing the core-shell structure, the effect of heat treatment and solvent dispersion of pristine PCN-250(Fe) were systematically investigated. Results illustrated a remarkable improvement in the ideal O_2/N_2 selectivity which is 29-times higher than that of the pristine material together with 3.4-times increase in O_2 adsorption capacity for $[P_{6,6,6,14}][DCA]/PCN\text{-}250(Fe)_{240\text{-}S,Acetone}$ composite, synthesized with pristine PCN-250(Fe) treated at 240 °C and dispersed in acetone by sonication. This study emphasizes the potential of computationally designed novel IL/MOF composites and their systematic experimental optimization for superior gas adsorption and separation performance.

I would like to send my sincere gratitude to Dr. Zeynep Pınar Haşlak for her guidance in DFT calculations. I also would like to thank my collaborator Hasan Can Gülbalkan for his contribution in computational methodologies (DFT calculations and GCMC simulations) and the writing of the discussions related to computational tools. Moreover, I am thankful for my collaborator Nitasha Habib for her contribution in volumetric gas adsorption measurements.

6.1 Background

Separation of high-purity oxygen (>99%) from air is of extreme importance for both medical (i.e., oxygen therapy,[205] mechanical ventilation[206]) and industrial (i.e., oxygen-enriched combustion,[207] fuel gasification,[208] gas conversion[209]) purposes making the discovery of O_2-selective adsorbents is of vital requirement. Especially, providing high-purity O_2 has become the most important medical interference for the ongoing COVID-19 outbreak due to the arising symptoms, such as shortness of breath, as which requires the patient to be put on oxygen support. According to the statistics of World Health Organization (WHO), about 15% of COVID-19 patients with severe illness require oxygen support via mechanical ventilation or oxygen therapy.[210, 211] In this regard, on-site purification of oxygen from air (i.e., oxygen concentrators) has gained noticeable attention considering the elimination of the need for transportation. Oxygen concentrators generally utilize pressure-swing adsorption (PSA) technology to obtain purified oxygen from air with more than 90% concentration.[212] PSA technology regarded as a strong alternative to conventional cryogenic distillation, which requires complex and expensive technology with enormous energy input. However, current pressure-swing adsorption (PSA) technologies lacks on cost-effective and highly selective adsorbent materials.[213] Used conventional adsorbents, such as cation-exchange zeolites 5A (CaA), 13X (NaX), and LiLSX, are generally N_2-selective and requires frequent regeneration cycles/large number of adsorbent quantities considering much higher N_2 (78 vol.%) concentration of air as compared to O_2 (21 vol.%).[214] Moreover, in the case of oxygen purity, it is typically limited to ≤95% for these adsorbents.[213] Hence, the discovery of novel adsorbents that are highly O_2 selective, especially at ambient conditions, holds substantial urgency and could potentially a significant advancement in medical/industrial technologies. Yet, the rational design of O_2-selective adsorbents for air separation, mainly O_2/N_2 separation, possesses challenge due to similar physical and chemical properties of these molecules, such as kinetic diameter (O_2: 3.46 Å, N_2: 3.64 Å), quadrupole moment, and polarizability.[215] In PSA applications, commercial N_2-selective adsorbents exploit the slight differences in both kinetic diameter and quadrupole moment through selective physisorption, but, achieved selectivities are still limited.

In the last decade, MOFs have emerged as a new class of porous materials and several studies reported their promising potential in the case of O_2/N_2 gas separation.[216] Particularly,

MOFs bearing coordinatively unsaturated (open) metal sites are the subject of continuously growing interest owing to existence of redox-active metal centers, providing open binding sites for O_2 by exploiting its redox activity. Subsequently, tunability of MOFs' organic and inorganic constituents can be utilized to design O_2-selective adsorbents with desired redox active binding sites. In this direction, there are various efforts to design promising O_2-selective framework structures (see **Table B.1.1**) such as $K_{1.09}Fe_2(bdp)_3$,[217] $Co_2(OH)_2(BBTA)$,[218] $Cr_3(BTC)_2$,[219] Cr-BTT,[220] $Fe_2(dobdc)$,[221] Co-BTTri,[222] Co-BDTriP,[222] Fe-BTTri,[223] $Cu(Qc)_2$,[224] $1\bullet 2O_2$,[225] MOF-177.[226] While framework structures, such as $K_{1.09}Fe_2(bdp)_3$ and $Co_2(OH)_2(BBTA)$, exhibit strong potential in regards to O_2 adsorption capacity; $K_{1.09}Fe_2(bdp)_3$ suffers from the loss in capacity with multiple cycles, whereas $Co_2(OH)_2(BBTA)$ does not demonstrate subsequent O_2 selectivity at near-ambient temperatures. Referred issues were also observed in the case of MOFs with Cr^{II} open metal sites, as in $Cr_3(BTC)_2$ and Cr-BTT, where they degrade or loose O_2 capacity at humid conditions or elevated temperatures leading to significantly reduced selectivity results. Oftentimes, MOFs display dramatic reduction in O_2 selectivities at room temperature, as in the cases of Co-BTTri and Co-BDTriP observed above 195 K, due to weak physisorption of O_2 and N_2. Moreover, irreversible binding of O_2 molecules has been one of the most challenging subjects for MOFs with redox-active open metal sites. Many reported irreversible O_2 binding at elevated temperatures, where the formation of superoxo species were observed leading to an irreversibly oxidized framework structure.[221, 223] Given that there is a strong need for the smart design of a structurally stable, efficient, and high-performance O_2-selective adsorbent materials, it is crucial to seek alternative modification strategies which will improve structurally stable MOFs' O_2/N_2 separation performance.

Within this scope, post-synthesis modification with ILs have become one of the most prominent methods among various techniques considering its facile application allowing a better control over molecular affinity with the task-specific selection of the IL.[227, 228] ILs are molten salts, consisting of a cation and an anion part with many advantageous characteristics including high thermal stability, negligible vapor pressure, and task-specific tunability. ILs' molecular affinity can be tuned by selecting suitable anion/cation part which enables their utilization as modification agent. Numerous studies reported significantly improved selectivity performances, even benchmark results,[229] for different gas separation applications upon post-synthesis modification with ILs.[2, 4, 12, 41, 85, 191] Therefore, this technique can potentially be

employed to design highly O_2-selective adsorbents with the precise determination of the IL and the host material pair.

Motivated by the discovery of an ideal O_2-selective adsorbent with structural stability, we explored the strategy of IL incorporation with the aim of designing a high performing IL/MOF composite adsorbent. In this regard, a core-shell type IL/MOF structure was chosen strategically for the structural configuration to achieve a superior O_2 selectivity without scarifying from uptake capacity.[2] Given the enormous library of possible anions and cations to construct ILs, employment of computational tools provides time and cost efficiency considering the vast amount of time required for the synthesis, characterization, and testing of the each possible IL/MOF composite. Thus, computational strategies, namely COSMO-RS and DFT calculations, were utilized to predict the choice of IL for superior O_2 molecular affinity. Upon systematical evaluation of 36456 ILs consisted of 7 different cation families, trihexyltetradecylphosphonium dicyanamide, $[P_{6,6,6,14}][DCA]$, was determined as the most suitable candidate for experimental studies. Likewise, the choice of MOF was conducted by means of large-scale computational screening, namely GCMC simulations, to determine structurally stable MOF with redox-active open metal sites from 5629 computation-ready experimental (CoRE) MOFs. PCN-250(Fe) was chosen among top 30 promising candidates considering its identified reversible decarboxylation route.[230] Performance prediction was further validated with experimental studies. $[P_{6,6,6,14}][DCA]$/PCN-250(Fe) synthesized via air exclusion technique and detailed characterization of the materials were performed with the help of various techniques. O_2 and N_2 adsorption measurements were performed for $[P_{6,6,6,14}][DCA]$/PCN-250(Fe) composites and results demonstrated that the composite was capable of selectively separate O_2 from N_2 even at atmospheric pressure without any loss of capacity for at least ten sorption-regeneration cycles. These results illustrate the gate way of designing smart adsorbent materials through facile post synthesis techniques for efficient air separation and O_2 purification.

6.2 Results and Discussion

6.2.1 Design of the Best Performing O_2-selective IL/MOF Composite

The proposed hierarchical approach to select the top performing IL and MOF components of the composite is presented in **Figure 6.2.1.1**. First, the activity coefficients for O_2 and N_2 were estimated by performing COSMO-RS calculations for a large set of 35672 ILs (consisting of 364 cations and 98 anions). Different structural and performance criteria were systematically employed to determine the top performing bulk ILs. A high solvent capacity for O_2 ($C_{O_2}^{\infty}$) and selectivity for O_2 over N_2 (S_{O_2/N_2}) is required to reduce the investment and energy costs,[231, 232] and a high molecular volume is also critical to ensure that the IL does not penetrate into the pores, instead positions itself on the external surface of MOF to form a core-shell type structure. In this respect, the following filters were applied: (i) S_{O_2/N_2}>1.2 filter decreasing the number of ILs from 35672 to 743 (ii) $C_{O_2}^{\infty}$ >5 mol/mol reducing the number of ILs from 743 to 175; (ii) molecular volume>0.8 nm^3/molecule, leading to a further reduction in the number of ILs to 13. Among the remaining 13 ILs, $[P_{6,6,6,14}][DCA]$ was identified as the most promising IL with the lowest $C_{N_2}^{\infty}$.

To identify a promising top MOF for O_2/N_2 separation, we considered the O_2 and N_2 adsorption data of 5629 computation-ready experimental (CoRE) MOFs obtained from our previous work.[233] The structure and performance filters from two machine learning studies[234, 235] focusing on O_2/N_2 separation were combined, and the following criteria were applied: (i) MOFs containing transition metals Cd, Ni, and Fe were considered, reducing the number from 5629 to 788; (ii) MOFs with a density (ρ) between 800-1600 kg/m^3 were selected, which resulted in 652 MOFs; (iii) MOFs with Henry's constant of O_2 (K_{O_2}) in between 1×10^{-6}-4×10^{-6} mol/kg/Pa and K_{N_2} <7.9×10^{-6} mol/kg/Pa further reduced the number to 296. PCN-250(Fe) was selected since it was among the 30 MOFs with the highest O_2 uptake and had a reversible decarboxylation route.[230] As a result, the $[P_{6,6,6,14}][DCA]$/PCN-250(Fe) composite was identified as the most promising candidate for experimental investigation.

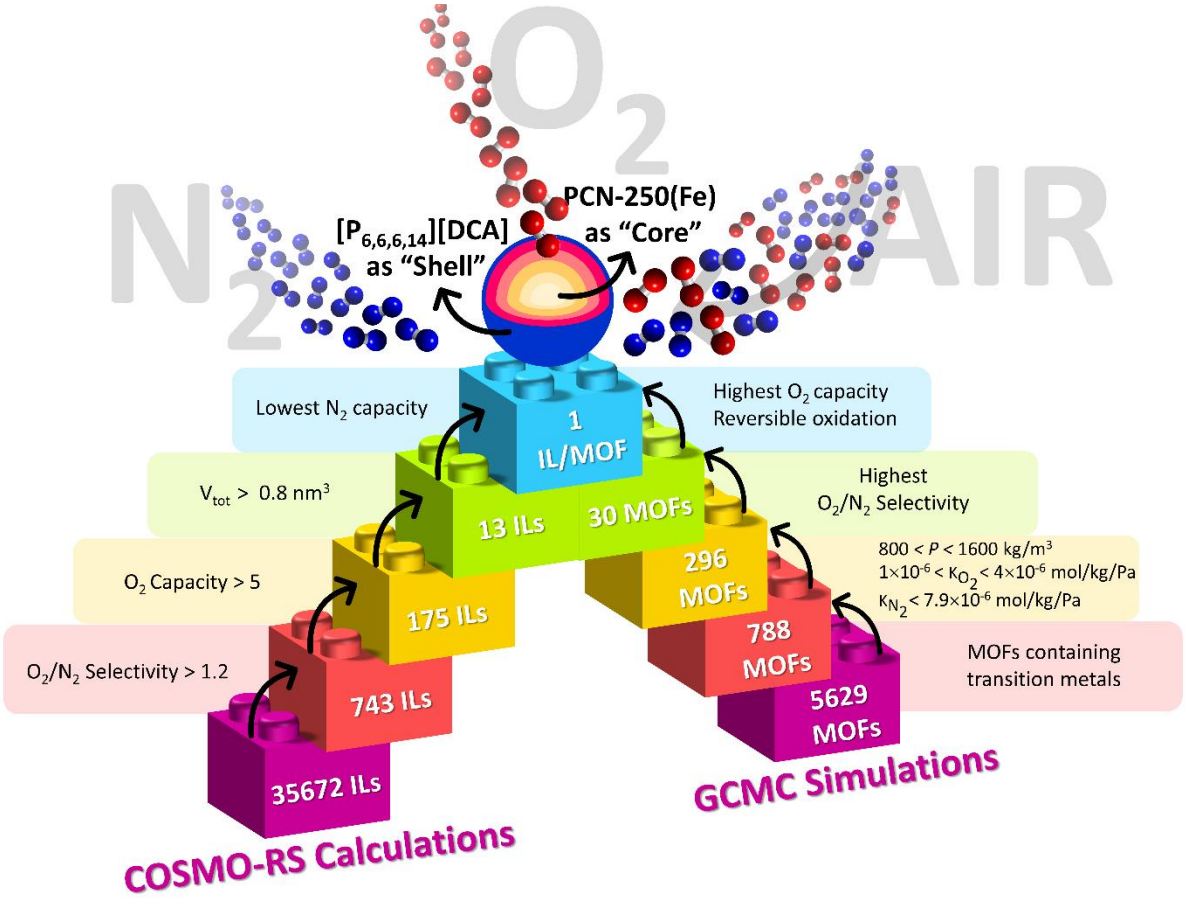

Figure 6.2.1.1. Proposed hierarchical approach for selecting the top-performing IL and MOF for superior O_2/N_2 separation performance.

6.2.2 Interactions Between the Bulk IL and the Gas Molecules

DFT calculations were first performed to investigate the interactions between O_2, N_2 and bulk $[P_{6,6,6,14}][DCA]$ at 25 °C. The optimization of $[P_{6,6,6,14}][DCA]$ in the presence of O_2 and N_2 molecules showed that both gases interact differently with the IL, as presented in **Figure 6.2.2.1**. O_2 makes close contact with both the anion and cation of the IL. As a Lewis base, O_2 donates its lone pair electrons to Lewis acidic positively charged C ($q_c = 0.464e$) of $[DCA]^-$ and forms a strong Lewis acid-base type interaction with C···O1 and C···O2 distances of 2.66 and 2.71 Å, respectively. Cation's hydrogens additionally stabilize O_2 by forming H-bonds. In contrast, the N atoms of the N_2 molecule form weak hydrogen bonds with the cations' hydrogen atoms on the hexyl chain. As a result, O_2 shows a significantly higher affinity towards $[P_{6,6,6,14}][DCA]$ with the calculated binding energy of 30.1 kJ/mol than N_2 which has a calculated binding energy of 8.1 kJ/mol.

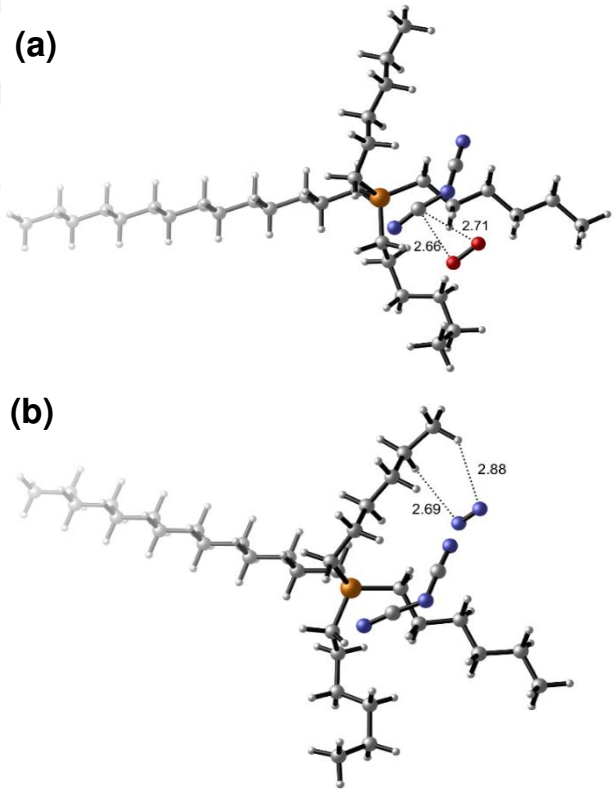

Figure 6.2.2.1. Representation of the equilibrium geometries representing the interactions of $[P_{6,6,6,14}][DCA]$ with (a) O_2 and (b) N_2 molecules calculated at the B3LYP/6-31G(d) level of theory. Bond distances are given in Å. Orange, red, grey, white, and blue spheres represent P, O, C, H, and N atoms, respectively.

Besides DFT calculations, the effect of temperature on O_2 and N_2 solubilities in bulk $[P_{6,6,6,14}][DCA]$ are examined by performing COSMO-RS calculations between 0.001-1 bar at 10, 25, and 40 °C. **Figure 6.2.2.2** demonstrates that O_2 has moderately higher solubility in $[P_{6,6,6,14}][DCA]$ compared to N_2 solubility at all examined temperatures and pressures. In addition, O_2 and N_2 solubilities slightly decrease with increasing temperature due to the decreasing solute density and nonpolar solvation behavior.[236, 237] Nonetheless, data illustrated that the solubility of O_2 and N_2 in $[P_{6,6,6,14}][DCA]$ did not significantly affected from the temperature except for a slight decrease when the temperature changes from 10 to 40 °C.

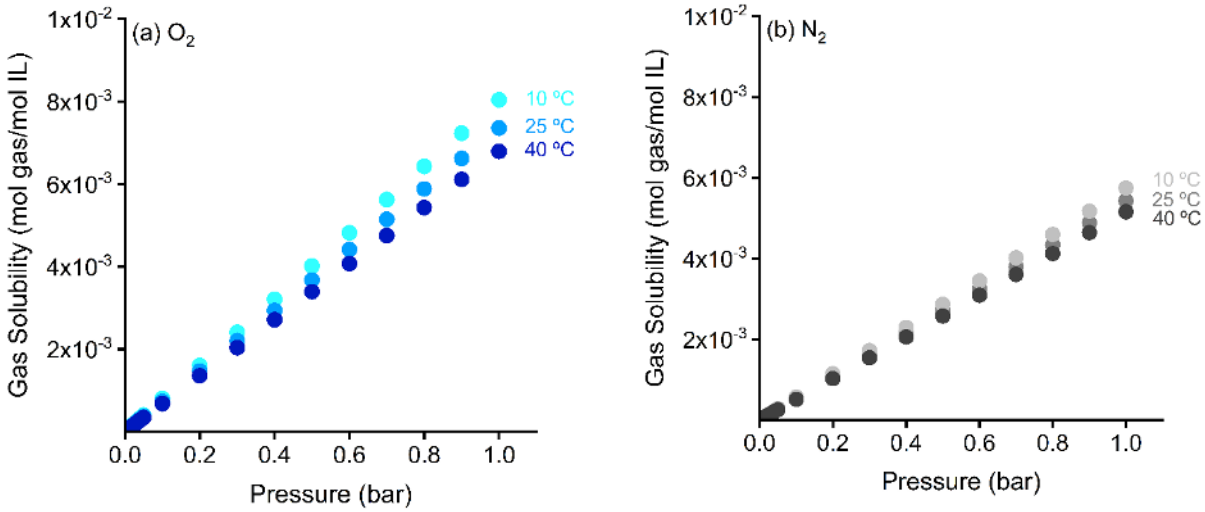

Figure 6.2.2.2 Solubility of O_2 and N_2 in bulk $[P_{6,6,6,14}][DCA]$ computed by COSMO-RS calculations in the range of 0.001-1 bar at 10, 25, and 40 °C.

6.2.3 Characterization of the Synthesized IL/MOF Composite

IL loadings of the as-prepared IL/MOF composites were determined by using XRF analysis. The elemental compositions of $[P_{6,6,6,14}][DCA]/PCN\text{-}250(Fe)_{150}$ and $[P_{6,6,6,14}][DCA]/PCN\text{-}250(Fe)_{240}$ were presented in **Table 6.2.3.1**. The corresponding IL loadings were calculated as approximately 23±0.3 wt.%, respectively for both $[P_{6,6,6,14}][DCA]/PCN\text{-}250(Fe)_{150}$ and $[P_{6,6,6,14}][DCA]/PCN\text{-}250(Fe)_{240}$. Calculated IL loadings can be stated as the maximum possible IL loadings for the prepared IL/MOF composites considering the targeted IL loading, 45 wt.%, which was the determined wetness point.

Table 6.2.3.1. Elemental composition of IL/MOF composites determined by XRF analysis.

Sample	Fe concentration (wt.%)	P concentration (wt.%)	Corresponding IL loading (wt.%)
$[P_{6,6,6,14}][DCA]/PCN\text{-}250(Fe)_{150}$	9.27	1.24	22.9
$[P_{6,6,6,14}][DCA]/PCN\text{-}250(Fe)_{240}$	9.05	1.34	23.3

Prepared composites were expected to form a "core-shell" type structure (core: MOF cage, shell: IL deposited on the surface) considering the PLD of PCN-250(Fe), approximately 5.5 and 4.3 Å respectively for $PCN\text{-}250(Fe)_{150}$ and $PCN\text{-}250(Fe)_{240}$ (obtained from Zeo++), which were insufficient to accommodate the incorporated $[P_{6,6,6,14}][DCA]$ molecules having comparably larger molecular size, approximately 27.1 Å (estimated from DFT optimized geometry). Therefore, IL molecules were expected to be located on the surface of MOF cages forming a shell-like layer structure. Next, SEM images were obtained to investigate the surface morphologies of pristine PCN-250(Fe) and corresponding composites upon $[P_{6,6,6,14}][DCA]$ incorporation. In **Figure 6.2.3.1(a-d)**, no alteration in the crystal morphology and particle size was observed for pristine PCN-250(Fe) after the heat treatment at 240 °C indicating that heat treatment had no adverse effect on the preservation of surface morphology. However, a distinct surface morphology was observed for the composite materials compared to the that of the pristine PCN-250(Fe) upon the incorporation of IL. It was inferred that the surface morphology of PCN-250(Fe) did not preserved upon the incorporation of $[P_{6,6,6,14}][DCA]$ molecules. A visible IL layer was observed on the SEM images of the composites consistent with the expected layer formation on the surface of PCN-250(Fe) particles as given in **Figure 6.2.3.1(e-**

h). Moreover, incorporation of $[P_{6,6,6,14}][DCA]$ molecules was further investigated with the obtained elemental composition of the $[P_{6,6,6,14}][DCA]$/PCN-250(Fe)$_{150}$ and $[P_{6,6,6,14}][DCA]$/PCN-250(Fe)$_{240}$ through EDX mapping. EDX mapping given in **Figure B.2.1** indicated the presence of P atoms, corresponding to the P atoms in the elemental composition of IL molecules, confirming the successful deposition of $[P_{6,6,6,14}][DCA]$ molecules.

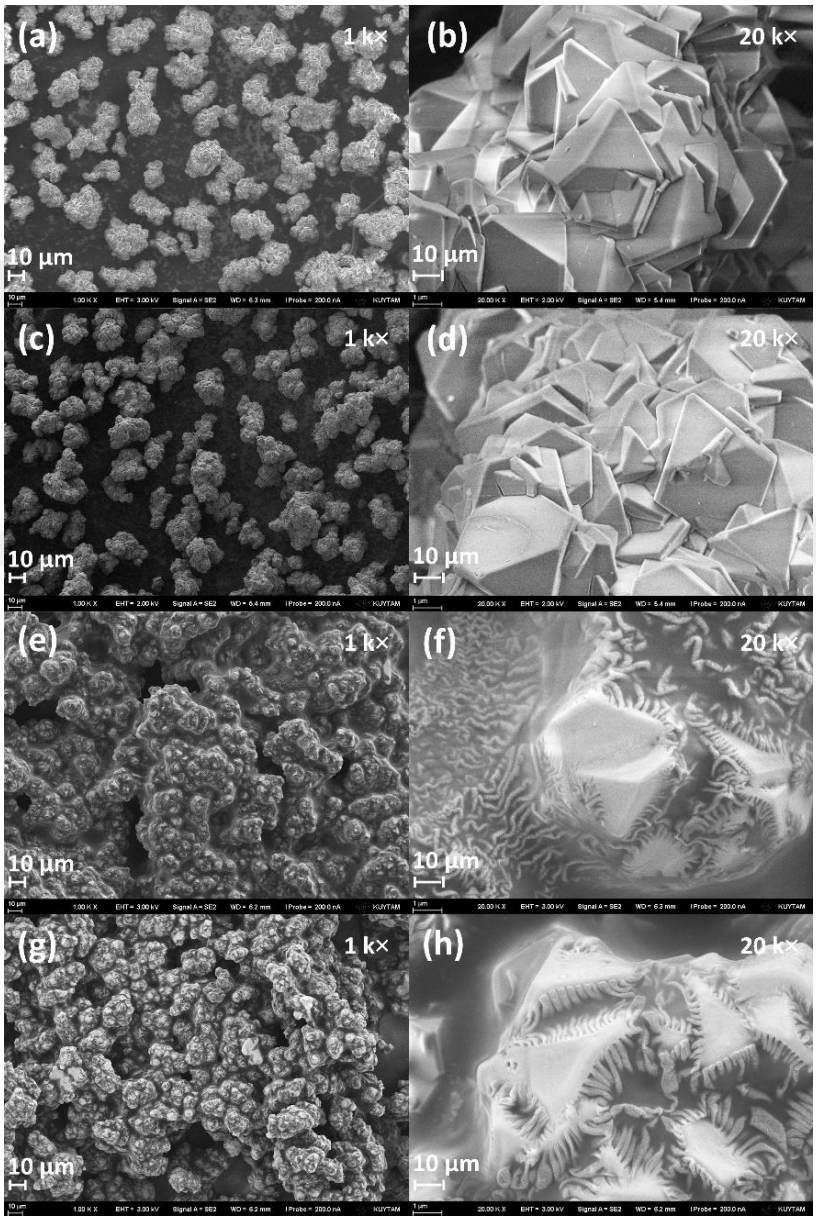

Figure 6.2.3.1. SEM images of (a-b) pristine PCN-250(Fe)$_{150}$, (c-d) pristine PCN-250(Fe)240, (e-f) $[P_{6,6,6,14}][DCA]$/PCN-250(Fe)$_{150}$, and (g-h) $[P_{6,6,6,14}][DCA]$/PCN-250(Fe)$_{240}$ acquired at magnifications of 1 k× and 20 k×.

Surface area and pore volume analyses of the samples were conducted by using their corresponding N_2 sorption-desorption isotherms obtained at -196 °C, as given in **Figure 6.2.3.2**, to further validate the deposition of $[P_{6,6,6,14}][DCA]$ molecules. In the case of pristine PCN-250, an increase in both surface area and pore volume was observed with the increasing heat treatment temperature as given in **Table 6.2.3.2**. BET (Langmuir) surface area of PCN-250(Fe)$_{150}$ increased from 1023 (1509) to 1126 (1657) m^2/g with the increased heat treatment of 240 °C. Similar trend was observed for the pore volumes of pristine PCN-250(Fe)$_{150}$ where cumulative pore volume and incremental pore volumes of higher width pores were increased for the pristine sample treated at 240 °C as given in **Figure 6.2.3.3**.

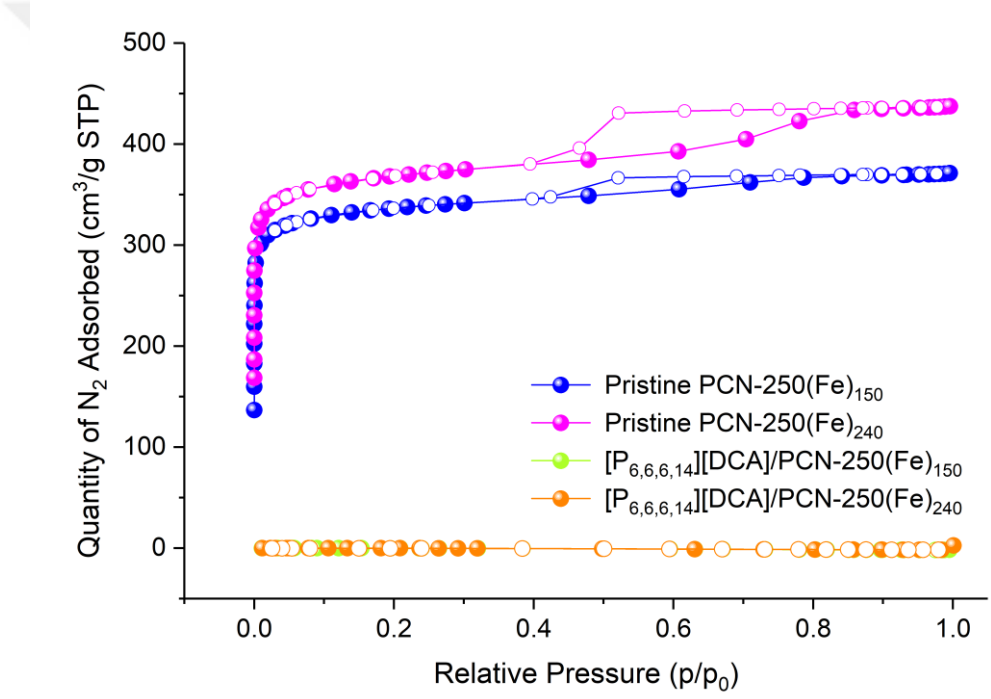

Figure 6.2.3.2. N_2 adsorption-desorption isotherms of pristine PCN-250(Fe) and $[P_{6,6,6,14}][DCA]$/PCN-250(Fe) composites obtained at −196 °C. Filled circles represent adsorption whereas empty circles represent desorption.

Table 6.2.3.2. BET and Langmuir surface areas of PCN-250(Fe) and $[P_{6,6,6,14}][DCA]$/PCN-250(Fe) composites.

Sample	S_{BET} (m^2/g)	$S_{Langmuir}$ (m^2/g)	V_{pore} (m^3/g)
$PCN\text{-}250(Fe)_{150}$	1023	1509	0.448
$PCN\text{-}250(Fe)_{240}$	1126	1657	0.488
$[P_{6,6,6,14}][DCA]/PCN\text{-}250(Fe)_{150}$	0.44	0.48	n/a
$[P_{6,6,6,14}][DCA]/PCN\text{-}250(Fe)_{240}$	0.035	0.039	n/a

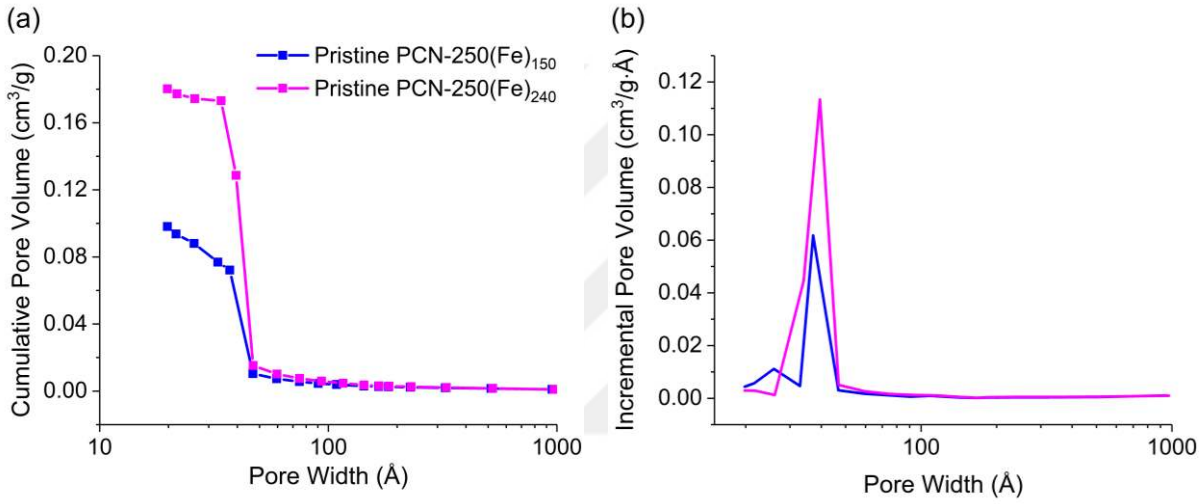

Figure 6.2.3.3. (a) Cumulative and (b) incremental pore volumes of pristine $PCN\text{-}250(Fe)_{150}$ and pristine $PCN\text{-}250(Fe)_{240}$ with respect to the pore width of the porous materials. Pore widths are given in logarithmic scale.

In the case of composite samples, a dramatic decrease in the surface areas of IL/MOF composites were observed upon the incorporation of $[P_{6,6,6,14}][DCA]$ consistent with our previous reports.[2, 41, 90, 229] Such a substantial decrease in the surface areas can be given as a direct evidence of the successful incorporation of IL onto/into the cages of MOF.[228] In addition, pore volume analysis of IL/MOF composites could not be determined due to inadequacy of obtained data points. This phenomenon is associated with the poor solubility of the probe gas, N_2, in used IL, $[P_{6,6,6,14}][DCA]$ at the measurement temperature. Hence, the BET analysis can be quantitatively misleading due to the extremely poor N_2 solubility of $[P_{6,6,6,14}][DCA]$ at liquid nitrogen temperature as presented in **Figure 6.2.3.4**, as suggested by the results of COSMO-RS calculations. Formed $[P_{6,6,6,14}][DCA]$ layer occupying the pore openings of pristine PCN-

250(Fe) can obstruct the passage of probe gas N_2, which leads to insufficient analysis of the actual surface area and pore volume of the samples.

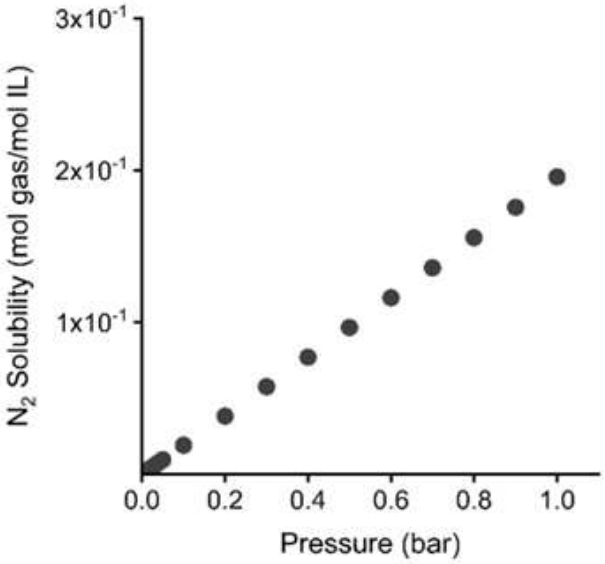

Figure 6.2.3.4. Solubility of N_2 in bulk $[P_{6,6,6,14}][DCA]$ computed by COSMO-RS calculations in the range of 0.001-1 bar at -196 °C.

Integrity of the crystalline structure was investigated by using the XRD analysis as given in **Figure 6.2.3.5**. The effect of heat treatment and IL-incorporation on the crystal structure of PCN-250(Fe) were examined to ensure that the crystal structure of parent MOF is still intact without any distortion. PCN-250(Fe) has cubic crystal system with $P\bar{4}3n$ symmetry and six characteristic peaks, located approximately at 8.0º, 9.8º, 11.35º, 12.7º, 13.9º, and 14.5º corresponding to (200), (211), (220), (310), (222), and (320), respectively. Location of the characteristic peaks and corresponding lattice constants of 22.02 and 22.05 Å for PCN-$250(Fe)_{150}$ and PCN-$250(Fe)_{240}$, respectively, were in good agreement with simulated theoretical data as given in **Figure 6.2.3.6(a-b)**.[238] Upon heat treatment, no change was observed in the characteristic diffraction peaks of pristine PCN-250(Fe) as given in **Figure 6.2.3.6(b)**, indicating the integrity of the crystal structure was preserved and structural stability maintained under high temperature conditions.

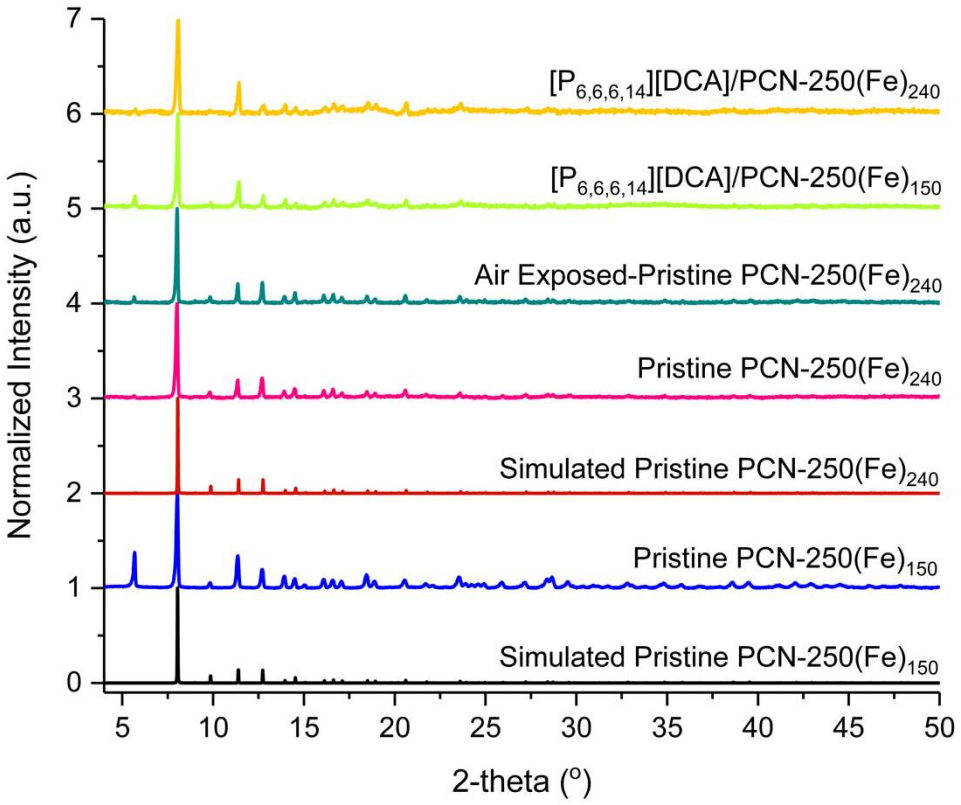

Figure 6.2.3.5. Experimental and simulated X-ray diffraction patterns of pristine PCN-250(Fe), and $[P_{6,6,6,14}][DCA]$/PCN-250(Fe) composites in 2θ range of 5-50º.

Moreover, data presented in **Figure 6.2.3.5** illustrated that the characteristic peaks of pristine PCN-250(Fe) were preserved upon the deposition of $[P_{6,6,6,14}][DCA]$ layer demonstrating that the crystal structure is not distorted or collapsed during the IL layer formation. However, it was observed that the characteristic diffraction peaks slightly shifted to higher 2θ values, as presented in **Figure 6.2.3.6(c-d)**, while lattice constants decreased to 21.93 and 21.90 Å, respectively for $[P_{6,6,6,14}][DCA]/PCN\text{-}250(Fe)_{150}$, and $[P_{6,6,6,14}][DCA]/PCN\text{-}250(Fe)_{240}$, compared to those of the pristine $PCN\text{-}250(Fe)_{150}$ and $PCN\text{-}250(Fe)_{240}$. This result can be attributed to the layer formation and increasing electron density on the surface of the MOF cage leading to a decrease in the dimensions of the MOF's crystallite unit cell. Reverse phenomenon was observed in the case of pore filling with IL, where an increase was identified implying an expansion of the MOF's crystallite unit cell.[90] On the contrary, an increase in the crystallite lateral size was observed upon both heat treatment and IL-incorporation. Crystallite lateral size of pristine $PCN\text{-}250(Fe)_{150}$ was increased from 11.07 to 13.47 Å upon heat treating

at 240 °C whereas a substantial increase was observed from 11.07 to 17.22 Å upon IL-incorporation. Similar trend was observed upon IL-incorporation on pristine PCN-250(Fe)$_{240}$, from 12.47 to 17.22 Å, implying an increase in the crystallite size of parent MOF with the IL-layer formation. Nonetheless, IL-incorporation can be further identified with the newly formed shoulder peaks and decreased intensities of the characteristic diffraction peaks suggesting a decreased crystallinity for the IL/MOF composites. This can be attributed to the newly formed defects in the structure of the parent MOF upon the incorporation of IL consistent with the previous observations regarding SEM images.

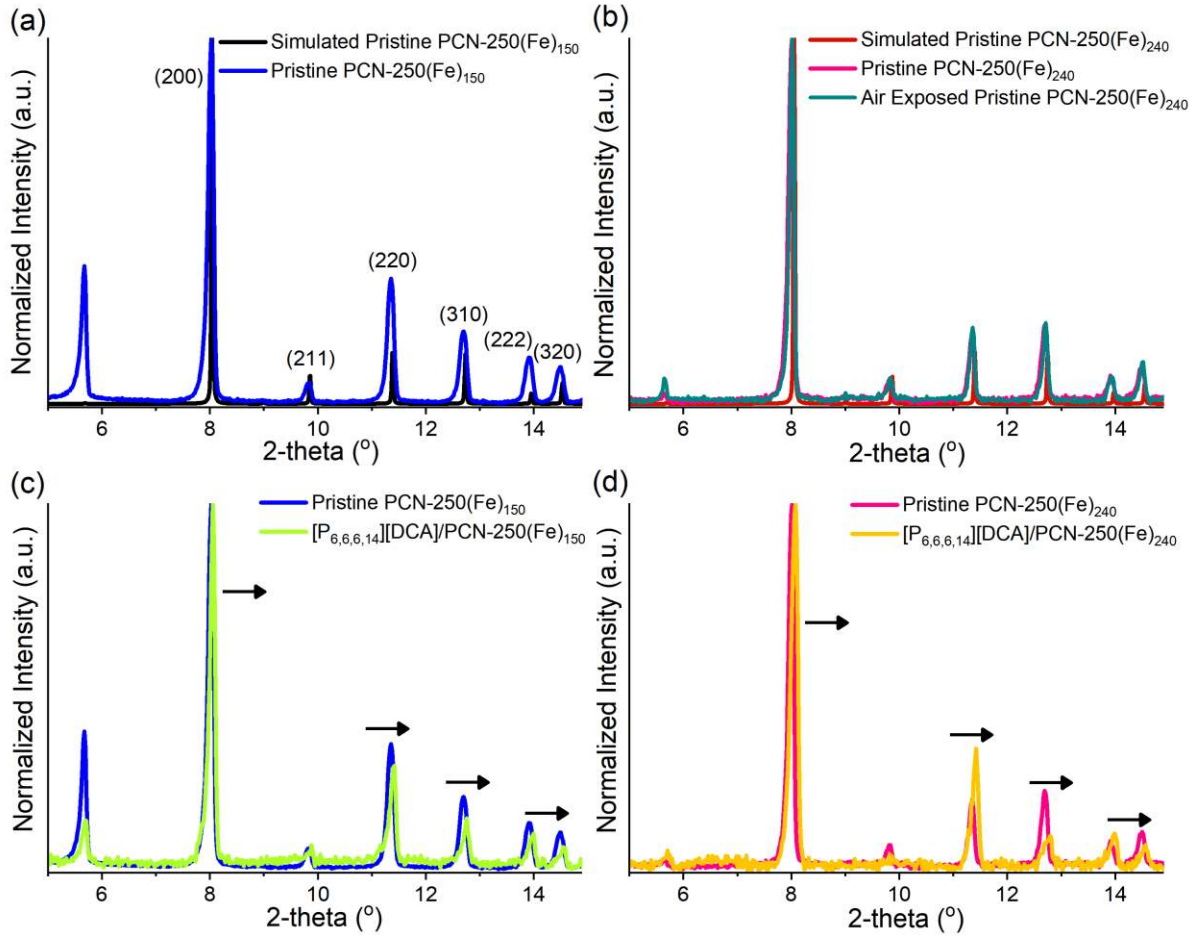

Figure 6.2.3.6. (a) X-ray diffraction pattern of simulated and pristine PCN-250(Fe)$_{150}$, (b) X-ray diffraction pattern of simulated and air exposed pristine PCN-250(Fe)$_{240}$, (c) X-ray diffraction pattern of pristine and IL-incorporated PCN-250(Fe)$_{150}$, and (d) X-ray diffraction pattern of pristine and $[P_{6,6,6,14}][DCA]$-incorporated PCN-250(Fe)$_{240}$ in 2θ range of 5-15º.

To elucidate the thermal stability of pristine PCN-250(Fe)$_{150}$, pristine PCN-250(Fe)$_{240}$, bulk $[P_{6,6,6,14}][DCA]$, $[P_{6,6,6,14}][DCA]$/PCN-250(Fe)$_{150}$, and $[P_{6,6,6,14}][DCA]$/PCN-250(Fe)$_{240}$ composites, thermogravimetric analyses were performed under an inert atmosphere. Thermal stability limits, T'_{onset}, of each sample was estimated from the data presented in **Figure 6.2.3.7** and identified as the point where the DTG curve is non-zero. T'_{onset} represents the maximum allowable temperature point before the decomposition of the structure starts to happen. Accordingly, data demonstrated that the pristine PCN-250(Fe) has approximately the same T'_{onset} value, 400 ± 15 °C, regardless of the temperature it was isothermally pre-treated. Moreover, a three-stage decomposition mechanism was observed for both pristine PCN-250(Fe)$_{150}$ and PCN-250(Fe)$_{240}$ composites with an only difference in the isothermal first stage happening at 150 and 240 °C, respectively. Accordingly, stages of decomposition mechanism associated with (i) vaporization of volatile compounds, (ii) decomposition of organic ligand, (iii) decomposition of the framework for pristine PCN-250(Fe)$_{150,}$ and (i) decarboxylation mechanism happening at 240°C, (ii) decomposition of organic ligand, (iii) decomposition of the framework for pristine PCN-250(Fe)$_{240}$, consistent with the reported literature.[230]

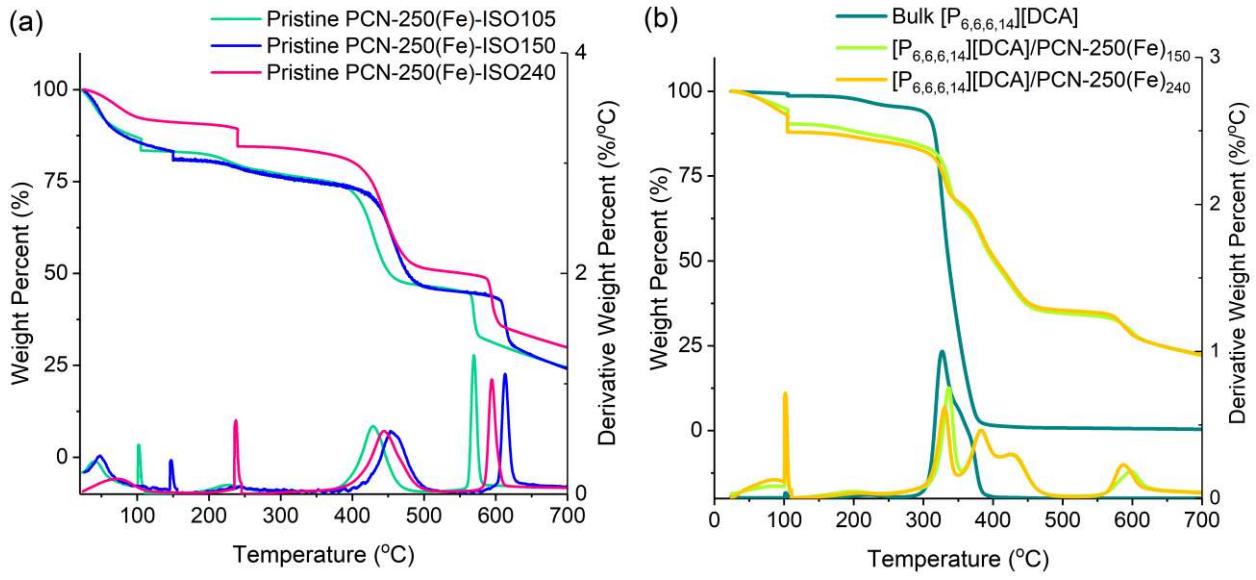

Figure 6.2.3.7. TGA and DTG curves of (a) pristine PCN-250(Fe) isothermal at 105, 150, 240 °C and (b) Bulk $[P_{6,6,6,14}][DCA]$ and $[P_{6,6,6,14}][DCA]$/PCN-250(Fe) composites isothermal at 105 °C.

In the case of $[P_{6,6,6,14}][DCA]$/PCN-250(Fe) composites, obtained decomposition mechanism resembled to the that of bulk $[P_{6,6,6,14}][DCA]$ showing the significant impact of IL layer formation on the thermal stability of the prepared core-shell type IL/MOF composites. Similarly, T'_{onset} values of the composites (tabulated in **Table 6.2.3.3**), estimated as 312 ± 7 and 307 ± 7 °C respectively for $[P_{6,6,6,14}][DCA]$/PCN-250(Fe)$_{150}$ and $[P_{6,6,6,14}][DCA]$/PCN-250(Fe)$_{240}$, were nearly same as the that of bulk $[P_{6,6,6,14}][DCA]$, 305±7 °C. Moreover, it was observed that the DTG curve appeared at 300-400 °C of bulk $[P_{6,6,6,14}][DCA]$ splited into two curves and right-shifted to the higher temperatures in the cases of both $[P_{6,6,6,14}][DCA]$/PCN-250(Fe)$_{150}$ and $[P_{6,6,6,14}][DCA]$/PCN-250(Fe)$_{240}$ composites. This can be attributed to possible direct interactions between the $[P_{6,6,6,14}][DCA]$ molecules and the surface of PCN-250(Fe).

Table 6.2.3.3. Estimated T'_{onset} values of pristine PCN-250(Fe), bulk $[P_{6,6,6,14}][DCA]$ and $[P_{6,6,6,14}][DCA]$/PCN-250(Fe) composites. Error bar determined according to the deviation of three consecutive estimations.

Sample	T'_{onset} **(°C)**
PCN-250(Fe)$_{105}$	389 ± 7
PCN-250(Fe)$_{150}$	407 ± 7
PCN-250(Fe)$_{240}$	400 ± 7
Bulk $[P_{6,6,6,14}][DCA]$	305 ± 7
$[P_{6,6,6,14}][DCA]$/PCN-250(Fe)$_{150}$	312 ± 7
$[P_{6,6,6,14}][DCA]$/PCN-250(Fe)$_{240}$	307 ± 7

FTIR analysis was performed on each sample (i) to confirm the integrity of the chemical structure and, (ii) to analyze the changes in the molecular bond structure upon the deposition of IL molecules. Characteristic peaks observed at approximately 533 and 611 cm^{-1} in the IR spectra of PCN-250(Fe)$_{150}$ attributed to the stretching vibrations of Fe–O bond in the monometallic Fe_3 clusters and observed to be red-shifted to lower energies upon the applied heat treatment at 240 °C, as given in **Figure 6.2.3.8**.[239, 240] This can be attributed to the change in electronic environment of Fe_3 clusters due to the decarboxylation of ABTC ligand. Nonetheless, presence of these characteristic Fe–O bands in the IR spectra of PCN-250(Fe)$_{240}$ further confirmed the structural integrity of Fe_3 clusters upon heat treatment at 240 °C. Similarly, characteristic C─H bending vibrations located in the vibrational range of 1000-650 cm^{-1} and characteristic N=N stretching vibrations of azobenzene located at approximately 1501

and 1437 cm^{-1} red-shifted upon heat treatment suggesting a possible bond weakening in the structure of ABTC organic ligand, consistent with the previous observations. Furthermore, disappearance of the characteristic IR peaks of CO_2H group located in the range of 3000-2800 cm^{-1} validated the successful decarboxylation of the framework structure as shown in **Figure 6.2.3.8**.[241]

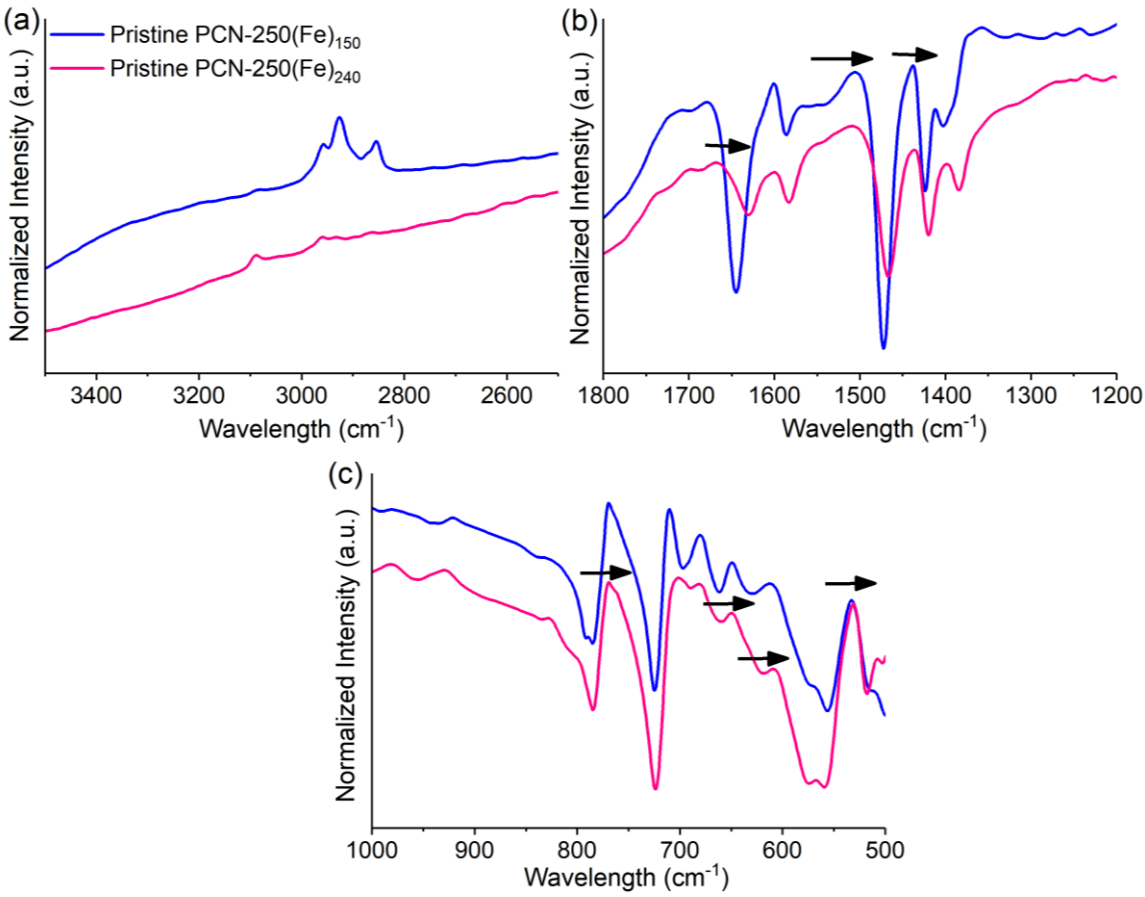

Figure 6.2.3.8. IR spectra of pristine PCN-250(Fe)$_{150}$ and pristine PCN-250(Fe)$_{240}$ between the spectral ranges of (a) 3500-2500 cm^{-1}, (b) 1800-1200 cm^{-1}, and (c) 1000-500 cm^{-1}.

In the case of $[P_{6,6,6,14}][DCA]$-incorporated PCN-250(Fe)$_{150}$ and PCN-250(Fe)$_{240}$, the characteristic peaks related with the pristine PCN-250(Fe) overlapped with the strong bond vibrations of deposited bulk $[P_{6,6,6,14}][DCA]$ layer and subsequently, composites exhibited IR spectra which are similar to the that of bulk $[P_{6,6,6,14}][DCA]$, as given in **Figure 6.2.3.9**. This resemblance can be directly correlated with the formation of IL layer on the surface of pristine MOF consistent with the previously reported studies. Accordingly, characteristic IR peaks of

$[P_{6,6,6,14}][DCA]$, located at approximately 2224, 2187, 2126 cm^{-1} corresponding to C≡N stretching vibration and 2957, 2926, 2854 cm^{-1} corresponding to C–H stretching of phosphonium cation, can be easily observed in the IR spectra of $[P_{6,6,6,14}][DCA]$/PCN-250(Fe)$_{150}$ and $[P_{6,6,6,14}][DCA]$/PCN-250(Fe)$_{240}$ validating the successful deposition of IL layer on the surface of pristine PCN-250(Fe).[242]

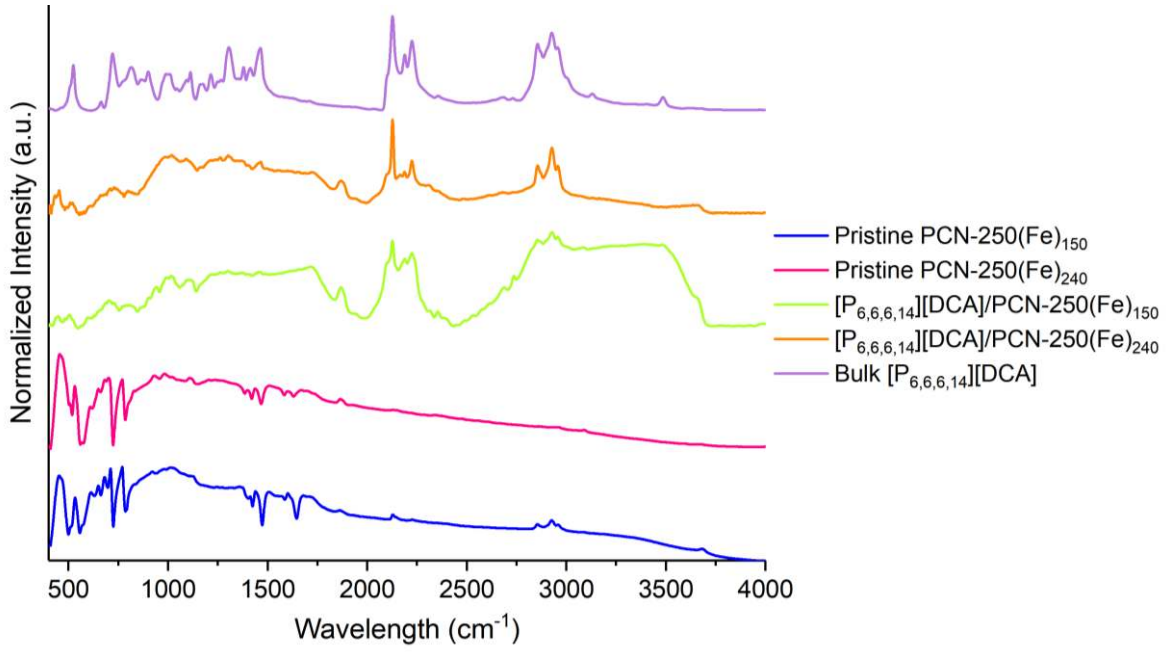

Figure 6.2.3.9. FTIR spectra of bulk $[P_{6,6,6,14}][DCA]$, pristine PCN-250(Fe)$_{150}$, pristine PCN-250(Fe)$_{240}$, $[P_{6,6,6,14}][DCA]$/PCN-250(Fe)$_{150}$, and $[P_{6,6,6,14}][DCA]$/PCN-250(Fe)$_{240}$ composites in the spectral range of 4000-400 cm^{-1}.

As expected, there were no characteristic peak shifts in the IR spectra of $[P_{6,6,6,14}][DCA]$/PCN-250(Fe)$_{150}$ and $[P_{6,6,6,14}][DCA]$/PCN-250(Fe)$_{240}$, as shown in **Figure 6.2.3.10**, further confirming the presence of bulk like IL layer electrostatically attached on the surface of pristine PCN-250(Fe) consistent with the previously made SEM, EDX, and XRD analysis. This observation on the IR spectra of core-shell type composites was shown previously by our group[2] and explained further in recently published review article[228] by comparing with the significant changes observed in the IR spectra of IL/MOF composites having IL confined inside the cages of MOF. However, a significant difference in the peak sharpness of the characteristic peaks of bulk IL in the IR spectra of $[P_{6,6,6,14}][DCA]$/PCN-

$250(Fe)_{150}$ and $[P_{6,6,6,14}][DCA]/PCN\text{-}250(Fe)_{240}$ was observed. In the spectra of $[P_{6,6,6,14}][DCA]/PCN\text{-}250(Fe)_{240}$ composite, nearly identical IR peaks with sharp peak formations were observed indicating the presence of more bulk-like IL molecules on the surface, whereas, an opposite statement can be made for $[P_{6,6,6,14}][DCA]/PCN\text{-}250(Fe)_{150}$ composite where comparably broader peaks were detected. This can be attributed to the change in intermolecular interaction strength between the PCN-250(Fe) surface and IL molecules leading to a different preservation state of IL's bulk like properties. Basically, when the strength of the attraction between the IL molecules and MOFs surface is higher, less amount of IL molecules will preserve their bulk-like vibrations leading to a decrease in the density of characteristic bond vibrations, consequently, sharpness of that particular peak. Mentioned phenomenon was also observed in Chapter 7 where the similarity between the IR spectra of IL/AC composites and bulk [BMIM][OAC] increased with increasing IL loading, in other words, increasing density of the IL molecules having bulk-like intermolecular interactions.

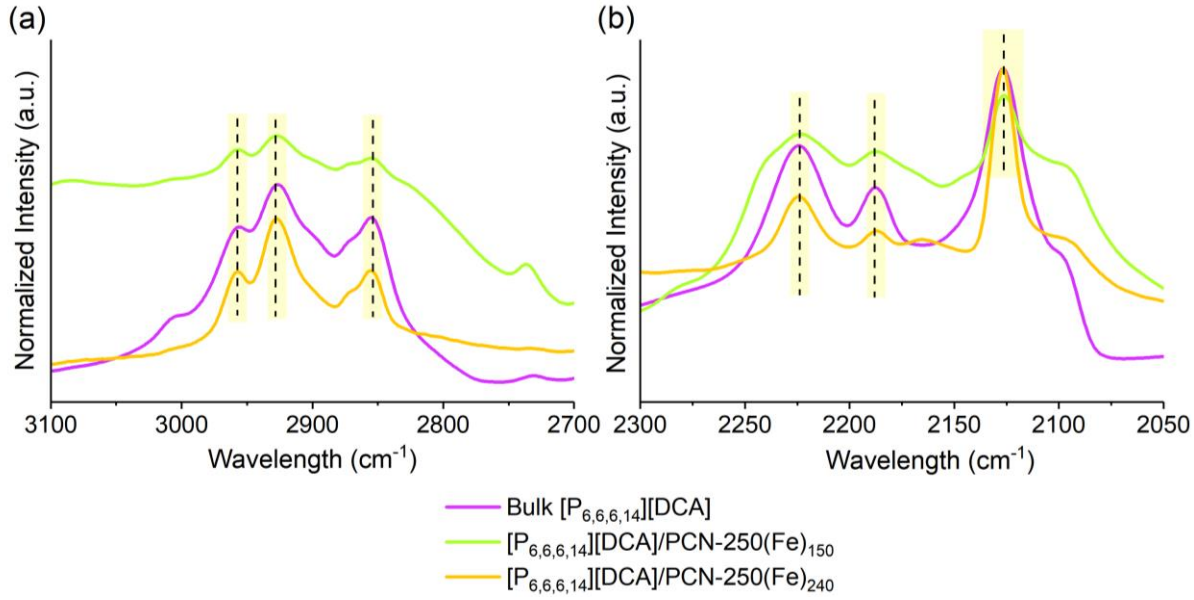

Figure 6.2.3.10. FTIR spectra of bulk $[P_{6,6,6,14}][DCA]$, $[P_{6,6,6,14}][DCA]/PCN\text{-}250(Fe)_{150}$, and $[P_{6,6,6,14}][DCA]/PCN\text{-}250(Fe)_{240}$ composites in the spectral range of (a) 3100-2700 cm^{-1} and (b) 2300-2050 cm^{-1}.

6.2.4 Effect of Heat Treatment on Gas Adsorption and Separation Performance

Volumetric O_2 and N_2 gas adsorption measurements were performed on pristine PCN-250(Fe)$_{150}$, pristine PCN-250(Fe)$_{240}$, $[P_{6,6,6,14}][DCA]$/PCN-250(Fe)$_{150}$, and $[P_{6,6,6,14}][DCA]$/PCN-250(Fe)$_{240}$ composites to assess the influence of IL incorporation on the gas adsorption performance of heat-treated PCN-250(Fe)$_{150}$ and PCN-250(Fe)$_{240}$. Gas adsorption measurements were conducted at three different temperatures (10, 25, and 40 °C) within the pressure range of 0.001 to 1 bar and the corresponding isotherm fitting parameters were tabulated in **Figure B.3.1** in Appendix C. Data shown in **Figure 6.2.4.1(a-b)** illustrated that both O_2 and N_2 uptakes of pristine PCN-250(Fe) were increased with an increase in the heat treatment temperature, from 150 to 240 °C, indicating an enhancement in the O_2 and N_2 gas adsorption capacity upon decarboxylation of the framework. Results were also validated by GCMC simulations conducted at 25 °C and 0.1-1 bar to evaluate the structural uniformity of the pristine material subjected to heat treatment. Data shown in **Figure B.4.1** illustrated that the experimental uptakes and the simulated uptakes were in a good agreement.

In the case of IL-incorporated composites, two different trends were observed in **Figure 6.2.4.1(c)**. $[P_{6,6,6,14}][DCA]$/PCN-250(Fe)$_{150}$ composite showed significantly reduced O_2 and N_2 uptakes implying a possible pore blockage on the pore openings of PCN-250(Fe)$_{150}$ framework upon the incorporation of IL. On the other hand, $[P_{6,6,6,14}][DCA]$/PCN-250(Fe)$_{240}$ composite exhibited a remarkable enhancement in the O_2 uptake compared to the that of pristine PCN-250(Fe)$_{240}$ upon the incorporation of IL; whereas, an opposite trend was observed for the adsorption of N_2. Upon IL deposition on the surface of decarboxylated framework structure, volumetric O_2 adsorption of pristine PCN-250(Fe)$_{240}$ increased by 2.5-times, from 6.4 to 16.2 cc/g, while the volumetric N_2 adsorption decreased by 7.6-times, from 6.9 to 0.9 cc/g, at 1 bar and 25 °C. Moreover, similar trends were observed for each temperature demonstrating the stable performance of synthesized $[P_{6,6,6,14}][DCA]$/PCN-250(Fe)$_{240}$ composite. Results attributed to the newly formed surface sorption sites upon the deposition of $[P_{6,6,6,14}][DCA]$ molecules consistent with the DFT calculations showing O_2 and N_2 interactions with bulk $[P_{6,6,6,14}][DCA]$ reported in Section 6.2.

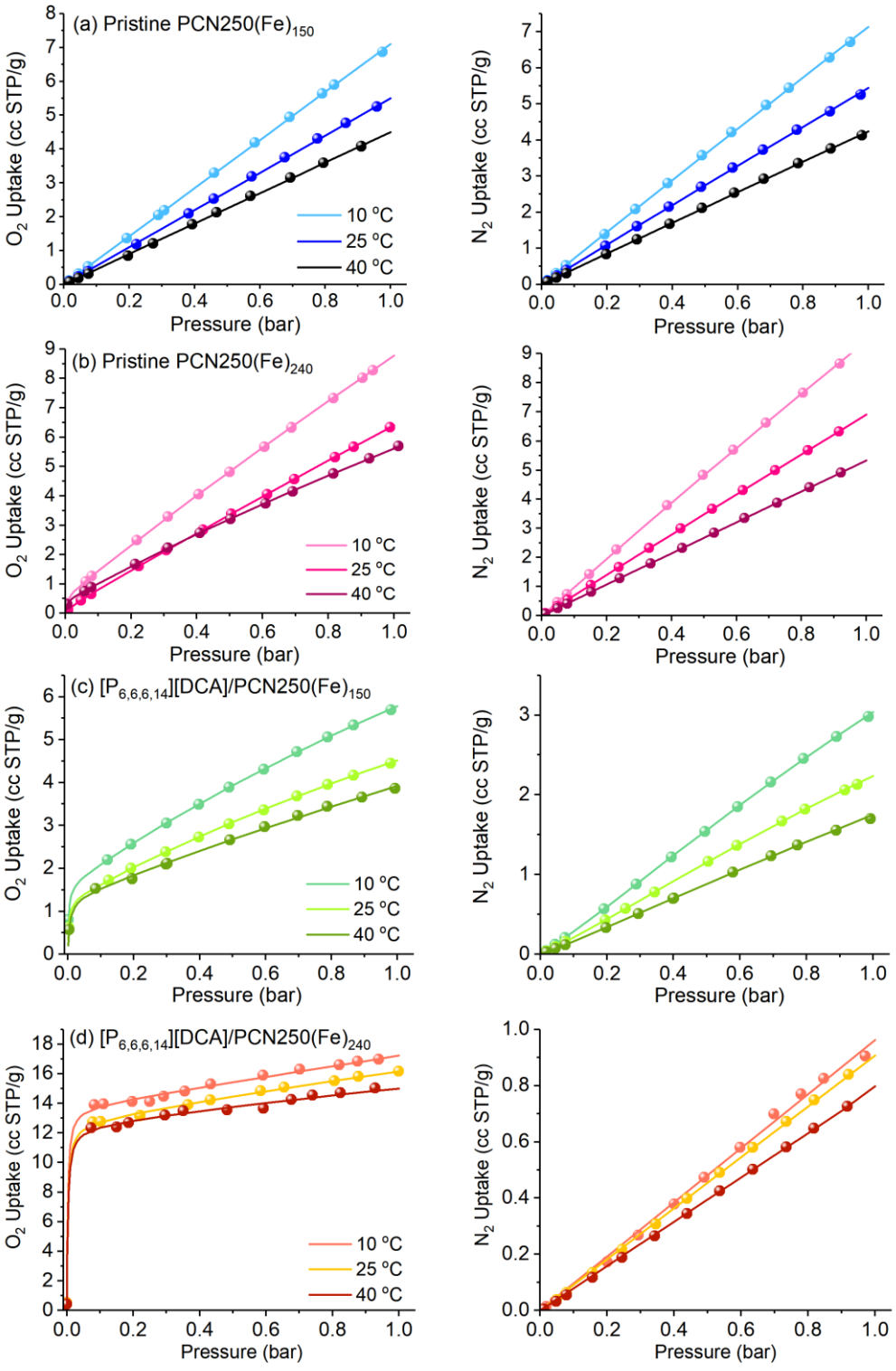

Figure 6.2.4.1. Single-component O_2 and N_2 gas adsorption isotherms of (a) pristine PCN-250(Fe)$_{150}$, (b) pristine PCN-250(Fe)$_{240}$, (c) $[P_{6,6,6,14}][DCA]$/PCN-250(Fe)$_{150}$, and (d) $[P_{6,6,6,14}][DCA]$/PCN-250(Fe)$_{240}$ in the pressure range of 0.001 to 1 bar at 10, 25, and 40 °C. Circle represents the experimental data whereas straight line represents isotherm fittings.

Assessment of O_2 purification and corresponding air separation potential of IL-incorporated composites were conducted by calculating O_2/N_2 selectivity of each sample from the measured single-component gas sorption data. Ideal O_2/N_2 selectivities showed a significant enhancement compared to the that of pristine material for both composites, $[P_{6,6,6,14}][DCA]$/PCN-250(Fe)$_{150}$ and $[P_{6,6,6,14}][DCA]$/PCN-250(Fe)$_{240}$, as illustrated in **Figure 6.2.4.2**. Upon IL incorporation, ideal O_2/N_2 selectivity of PCN-250(Fe)$_{150}$ increased from 1 to 2 at 1 bar and 25 °C, whereas a significant improvement of 19-times from 0.9 to 17.8 was observed in the case of PCN-250(Fe)$_{240}$ reaching a benchmark value among previously reported MOF studies, as tabulated in **Table B.1.1**. A remarkable O_2/N_2 selectivity were obtained in the low-pressure region. An ideal O_2/N_2 selectivity of 6824 (1094), boosting from 3.9 (1.9), was observed for $[P_{6,6,6,14}][DCA]$/PCN-250(Fe)$_{240}$ composite at 0.001 (0.01) bar and 25 °C corresponding to a substantial 1739 (565)-times improvement. It is noteworthy to mention that obtained O_2/N_2 selectivity results were highly comparable in each analysis temperature which can be associated with the trivial effect of temperature change on the solubility of O_2 and N_2 in $[P_{6,6,6,14}][DCA]$, as reported in Section 6.2.

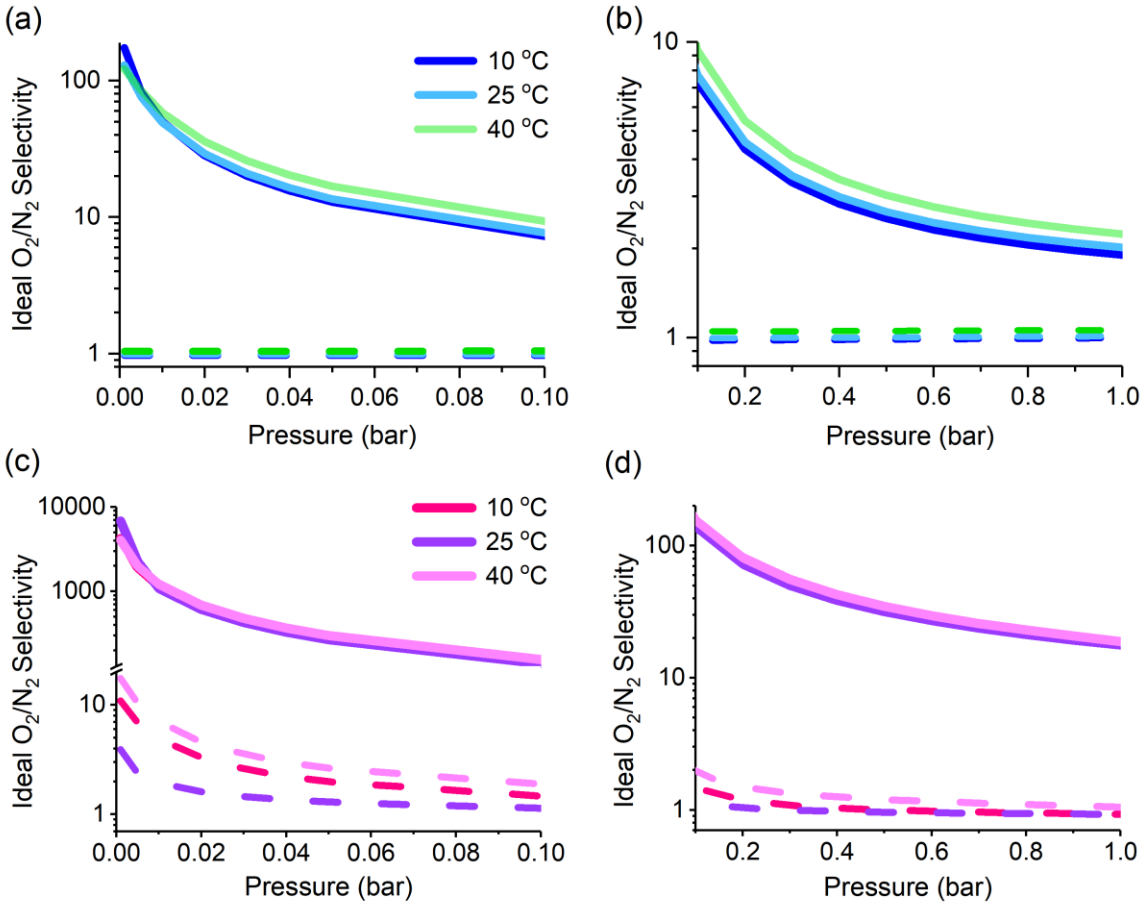

Figure 6.2.4.2. Ideal O_2/N_2 selectivity of (a-b) pristine PCN-250(Fe)$_{150}$ and $[P_{6,6,6,14}][DCA]$/PCN-250(Fe)$_{150}$ composite, and (b-c) pristine PCN-250(Fe)$_{240}$, and $[P_{6,6,6,14}][DCA]$/PCN-250(Fe)$_{240}$ composites in the pressure range of (a-c) 0.001 to 0.1 bar and (b-d) 0.1 to 1 bar at 10, 25, and 40 °C. Straight line represents IL-incorporated composite, and the dashed line represents pristine material.

Mixture gas adsorption behavior of the best-performing $[P_{6,6,6,14}][DCA]$/PCN-250(Fe)$_{240}$ composite having exceptional O_2/N_2 selectivity was investigated by utilizing IAST calculations to evaluate the corresponding direct O_2 purification performance under O_2/N_2:21/79 mixture. IAST selectivity results demonstrated greater improvement at atmospheric pressure compared to the calculated ideal selectivity, highlighting the promising potential of synthesized $[P_{6,6,6,14}][DCA]$/PCN-250(Fe)$_{240}$ composite for superior air separation applications. O_2/N_2 mixture selectivity results given in **Figure 6.2.4.3** highlighted that $[P_{6,6,6,14}][DCA]$/PCN-250(Fe)$_{240}$ composite has a selectivity of 362 at 1 bar and 25°C which further demonstrates the exceptionally high O_2 separation performance of $[P_{6,6,6,14}][DCA]$/PCN-250(Fe)$_{240}$.

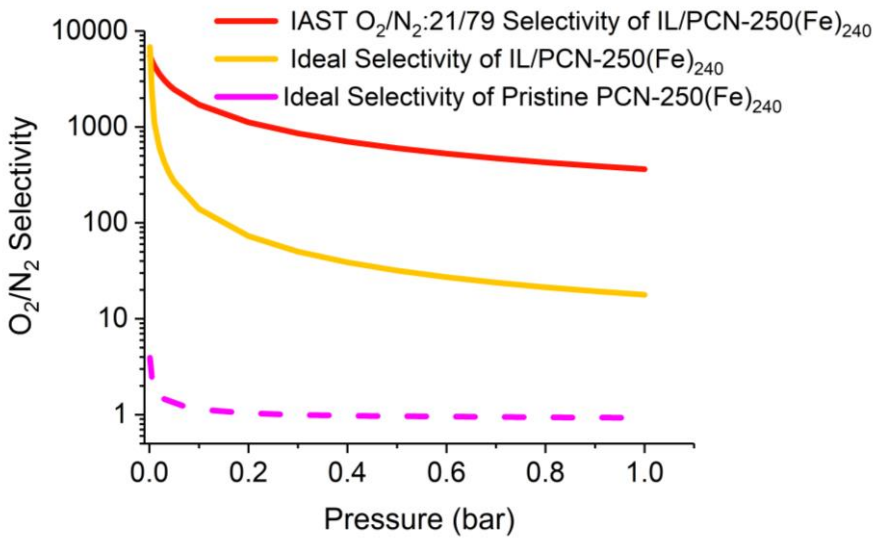

Figure 6.2.4.3. Ideal O_2/N_2 selectivities of pristine PCN-250(Fe)$_{240}$ and $[P_{6,6,6,14}][DCA]$/PCN-250(Fe)$_{240}$ composite and IAST O_2/N_2:21/79 selectivity of $[P_{6,6,6,14}][DCA]$/PCN-250(Fe)$_{240}$ composite. Straight curve represents IL-incorporated composite, and the dashed curve represents pristine material.

To further validate the exceptional improvement of O_2/N_2 separation performance, breakthrough adsorption measurements were performed with a column packed with pristine PCN-250(Fe)$_{240}$ and $[P_{6,6,6,14}][DCA]$/PCN-250(Fe)$_{240}$ composite under continuous 10 ml/min flow of O_2/N_2:21/79 mixture (using He as the carrier gas) at 25 °C and 1 bar. Corresponding schematic representation of breakthrough experimental set-up can be found in Chapter 3. Obtained breakthrough curves given in **Figure 6.2.4.4** confirmed the preferential sorption of O_2 molecules over N_2 under gas mixture conditions in the case of $[P_{6,6,6,14}][DCA]$/PCN-250(Fe)$_{240}$ composite. As expected, simultaneously appeared O_2 and N_2 peaks with equal retention time was observed for pristine PCN-250(Fe)$_{240}$ implying the similar affinities towards O_2 and N_2 molecules leading to poor selective separation performance consistent with the previous single-component sorption results. However, $[P_{6,6,6,14}][DCA]$/PCN-250(Fe)$_{240}$ composite showed 3-times improved O_2 retention time compared to the that of N_2 justifying the preferential sorption of O_2 molecules on novel $[P_{6,6,6,14}][DCA]$/PCN-250(Fe)$_{240}$ composite owing to the enhanced molecular affinity towards O_2 molecules upon the deposition of IL layer.

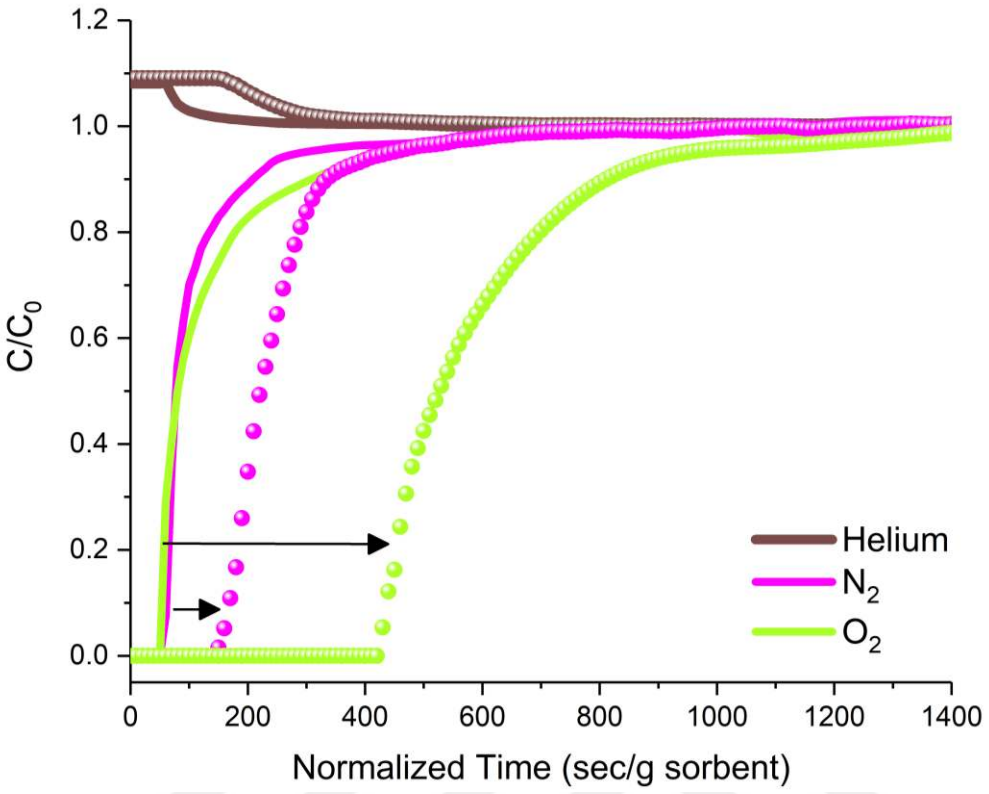

Figure 6.2.4.4. Adsorption column breakthrough experiments for pristine $PCN-250(Fe)_{240}$ and $[P_{6,6,6,14}][DCA]/PCN-250(Fe)_{240}$ composite with O_2/N_2:21/79 mixture (10 ml/min flow rate) at 25 °C and 1 bar. Straight curve represents pristine $PCN-250(Fe)_{240}$ and filled circles represent $[P_{6,6,6,14}][DCA]/PCN-250(Fe)_{240}$ composite.

Moreover, isosteric heat of sorption (Q_{st}) of O_2 and N_2 were calculated for each sample and corresponding Clausius-Clapeyron equation fittings are presented in **Figures B.4.1-2**. In the case of N_2 sorption, data given in **Figure 6.2.4.5(a)** illustrated a linear trend in between 20-23 kJ/mol for all samples, namely pristine $PCN-250(Fe)_{150}$, pristine $PCN-250(Fe)_{240}$, $[P_{6,6,6,14}][DCA]/PCN-250(Fe)_{150}$, and $[P_{6,6,6,14}][DCA]/PCN-250(Fe)_{240}$ composites, highlighting the physisorption nature of N_2 sorption on each sample. Moreover, observed linear trend can be attributed to the existing physisorption sites with similar energies. On the other hand, in the case of O_2 sorption, a decreasing trend was observed in **Figure 6.2.4.5(b)** for pristine $PCN-250(Fe)_{240}$, $[P_{6,6,6,14}][DCA]/PCN-250(Fe)_{150}$, and $[P_{6,6,6,14}][DCA]/PCN-250(Fe)_{240}$ composites confirming the heterogeneity of the existing sorption sites where both physisorption and chemisorption sites exist consistent with the previous findings. Therefore, it can be concluded that pristine $PCN-250(Fe)_{240}$, $[P_{6,6,6,14}][DCA]/PCN-250(Fe)_{150}$, and

$[P_{6,6,6,14}][DCA]$/PCN-250$(Fe)_{240}$ samples have sorption sites with different energies owing to having decarboxylated framework structure, as in the case of pristine PCN-250$(Fe)_{240}$, or deposited IL layering on the surface, as in the cases of $[P_{6,6,6,14}][DCA]$/PCN-250$(Fe)_{150}$ and $[P_{6,6,6,14}][DCA]$/PCN-250$(Fe)_{240}$ composites, which induced the formation of newly available sorption sites for O_2 molecules.

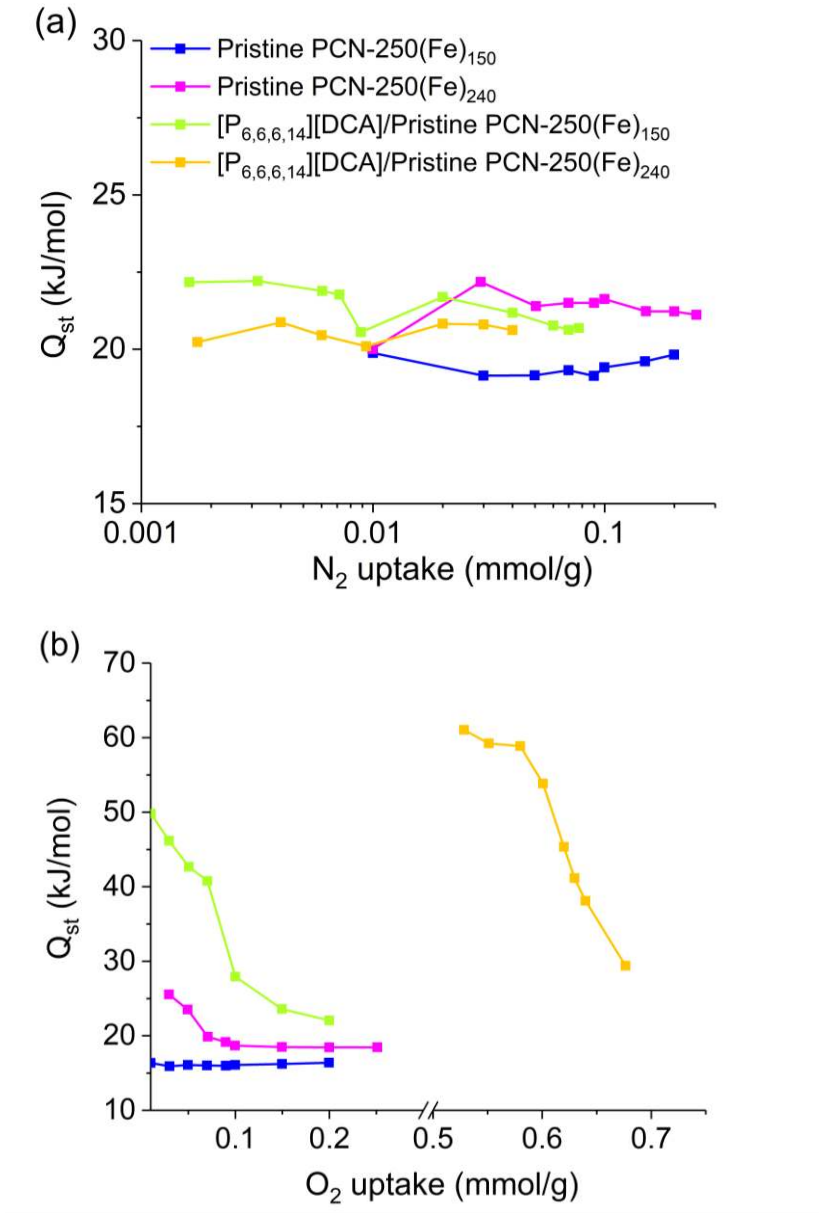

Figure 6.2.4.5. Calculated Q_{st} values obtained from (a) N_2 and (b) O_2 gas sorption measurements at 10, 25, 40 °C.

6.2.5 Effect of Dispersion on Gas Adsorption and Separation Performance of $[P_{6,6,6,14}][DCA]/PCN\text{-}250(Fe)_{240}$

Possible structural modifications of pristine PCN-250(Fe), prior to the incorporation of IL particles, were also evaluated for the $[P_{6,6,6,14}][DCA]/PCN\text{-}250(Fe)_{240}$ composite by investigating the dispersion effect and resulting change in particle size. Dispersion effect was examined by using two different particle dispersion techniques, namely, sonication and ultrasound sonication, to change the particle size of PCN-250(Fe) powder for improved IL incorporation. The change in particle size of PCN-250(Fe) was aimed to improve the IL layer thickness deposited on the surface.

Pristine PCN-250(Fe) was dispersed in several solvents, namely acetone, chloroform, and DMF, by sonication or ultrasound sonication techniques before the incorporation of IL molecules. Samples dispersed with sonication (ultrasound sonication) in selected solvent was labeled as $[P_{6,6,6,14}][DCA]/PCN\text{-}250(Fe)_{240\text{-}S,Solvent}$ ($[P_{6,6,6,14}][DCA]/PCN\text{-}250(Fe)_{240\text{-}US,Solvent}$). Volumetric O_2 and N_2 adsorption results of $[P_{6,6,6,14}][DCA]/PCN\text{-}250(Fe)_{240\text{-}S,Acetone}$ demonstrated a significant increase in O_2 sorption capacity, from 16.2 to 21.5 cc/g, together with a substantial decrease in N_2 sorption capacity, from 0.9 to 0.8 cc/g, compared to the that of $[P_{6,6,6,14}][DCA]/PCN\text{-}250(Fe)_{240}$ composite, which was synthesized without applying any dispersion techniques, as shown in **Figure 6.2.5.1(a)**. However, sample dispersed with ultrasound sonication technique having acetone as its solvent illustrated a different trend. Lowered uptake results were obtained for both O_2 and N_2 gas sorption compared to the that of sonication case indicating a possible damage and defect formation in the framework structure due to the applied ultrasound sonication technique. Nonetheless, ideal O_2/N_2 selectivity of the $[P_{6,6,6,14}][DCA]/PCN\text{-}250(Fe)_{240}$ composite increased in both cases, from 17.8 to 26.1 and 22, respectively, for the samples prepared with sonication and ultrasound sonication techniques, as illustrated in **Figure 6.2.5.2**. Meanwhile, composites prepared by dispersing in chloroform and DMF (both sonication and ultrasound sonication techniques) exhibited substantially decreased uptakes for both the O_2 and N_2 volumetric sorption measurements, as presented in **Figure 6.2.5.1**, together with decreased ideal O_2/N_2 selectivity results.

Volumetric O_2 and N_2 sorption results presented in this section highlights the significance aftermath of the alterations in the synthesis route and shows the potential performance losses due to the interactions formed by used synthesis solvent. Therefore, a rational selection of the

synthesis solvent and investigation of the dispersion effect must be made prior to the synthesis of IL/MOF composites.

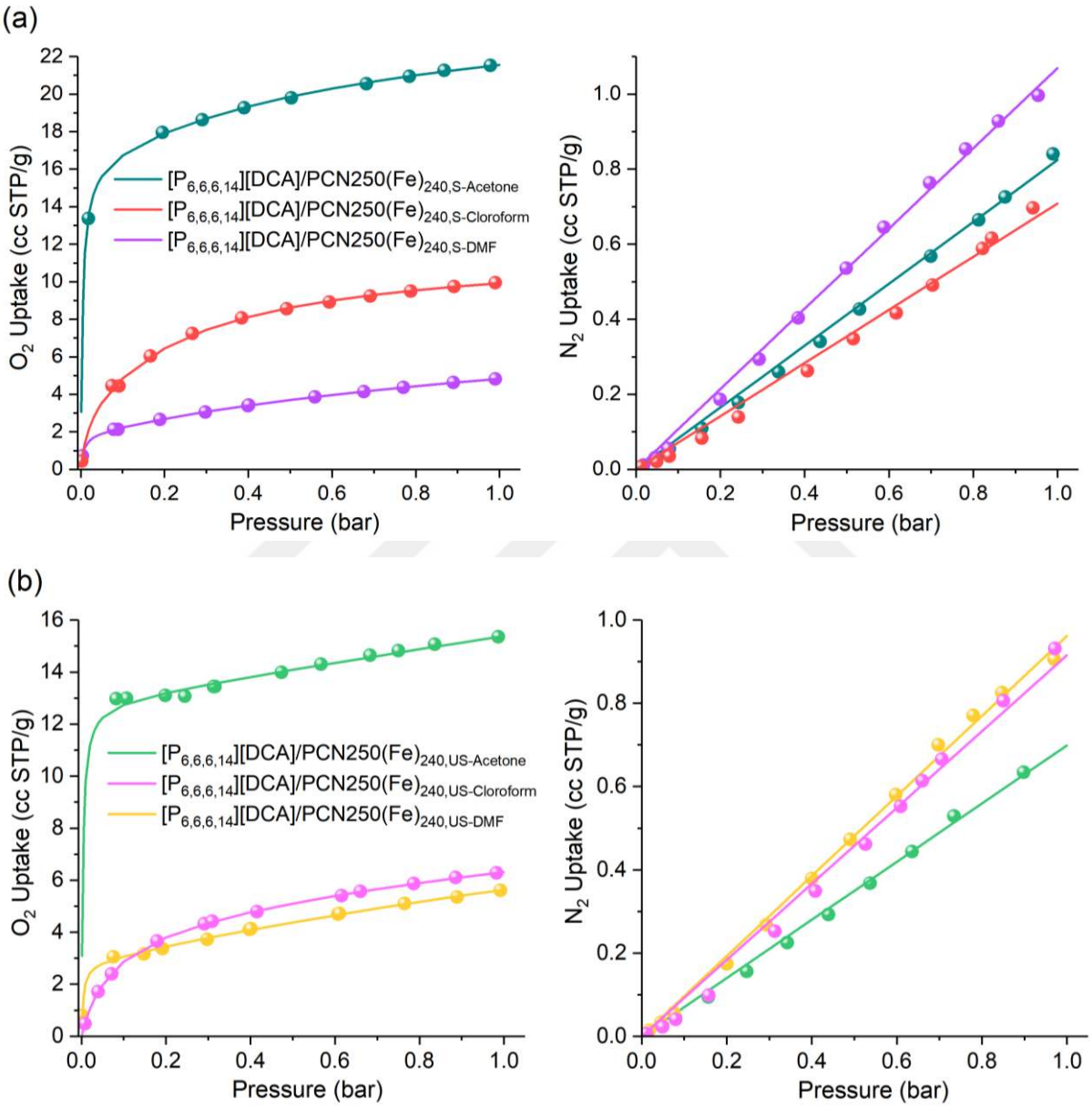

Figure 7.3.5.1. Single-component O_2 and N_2 gas adsorption isotherms of [$P_{6,6,6,14}$][DCA]/PCN-250(Fe)$_{240}$ samples treated with (a) sonication or (b) ultrasound sonication techniques prior to IL incorporation. Gas adsorption isotherms collected in the pressure range of 0.001 to 1 bar at 25 °C. Circle represents the experimental data whereas straight line represents isotherm fittings.

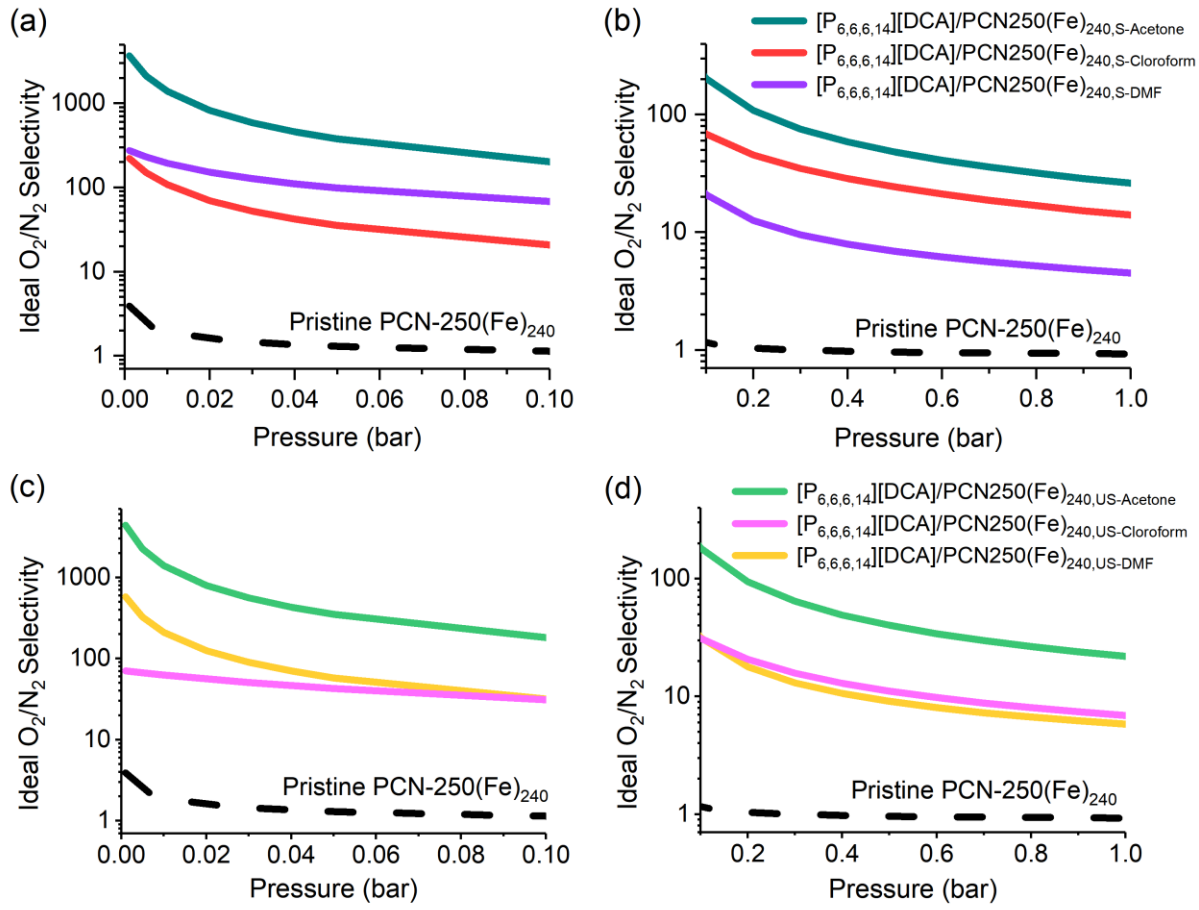

Figure 7.3.5.2. Ideal O_2/N_2 selectivity of (a-b) $[P_{6,6,6,14}][DCA]$/PCN-250(Fe)$_{240}$ prepared by sonication technique in acetone, chloroform, and DMF, (c-d) $[P_{6,6,6,14}][DCA]$/PCN-250(Fe)$_{240}$ prepared by ultrasound sonication technique in acetone, chloroform, and DMF in the pressure range of (a-c) 0.001 to 0.1 bar and (b-d) 0.1 to 1 bar at 25 °C. Straight line represents IL-incorporated composite, and the dashed line represents pristine material.

In conclusion, a core-shell type IL/MOF composite consisting of a phosphonium-based IL, $[P_{6,6,6,14}][DCA]$, and iron-based MOF, PCN-250(Fe), was computationally designed and experimentally synthesized. Considering the unlimited number of IL-MOF pairs, different computational tools, COSMO-RS calculations, DFT calculations and GCMC simulations were used to predict the best $[P_{6,6,6,14}][DCA]$/PCN-250(Fe) composite for improved O_2/N_2 selectivity. Characterization of synthesized $[P_{6,6,6,14}][DCA]$/PCN-250(Fe) composites confirmed the formation of a core-shell type structure and the successful deposition of $[P_{6,6,6,14}][DCA]$ molecules via various characterization techniques as XRD, BET, SEM/EDX,

TGA, and FTIR analysis. The O_2 adsorption capacity and O_2/N_2 selectivity of synthesized composites were investigated by systematic changes in the heat treatment and dispersion of the pristine PCN-250(Fe). A remarkable 19-times improvement in ideal O_2/N_2 selectivity, from 0.9 to 17.8, was observed at 1 bar and 25 °C in the case of $[P_{6,6,6,14}][DCA/PCN\text{-}250(Fe)_{240}$ reaching a benchmark value among previously reported MOF studies. Similarly, IAST O_2/N_2:21/79 mixture selectivity of $[P_{6,6,6,14}][DCA/PCN\text{-}250(Fe)_{240}$ was calculated as 329 at 1 bar and 25 °C indicating a promising potential of direct O_2 capture from air. These selectivity improvements were further increased with systematic changes in the dispersion agent. Results illustrated a remarkable 29-times improvement in the ideal O_2/N_2 selectivity together with 3.4-times increase in O_2 adsorption capacity for $[P_{6,6,6,14}][DCA]/PCN\text{-}250(Fe)_{240\text{-}S,Acetone}$ composite, synthesized with pristine PCN-250(Fe) treated at 240 °C and dispersed in acetone by sonication. This study highlights the significance of both the usage of computational methods as designing tools and the structural optimization of synthesized IL/MOF composites.

Chapter 7: [BMIM][OAc] Coating Layer Makes Activated Carbon Almost Completely Selective for CO_2*

*This chapter has been published as a research article in *Chemical Engineering Journal 437 135436 (2022)* by authors Özce Durak, Muhammad Zeeshan, Seda Keskin, and Alper Uzun. The original manuscript has been rearranged to conform to the format requirements of the thesis.

Tuning the molecular affinity of porous materials towards desired gases is important to achieve superior selectivity for a target separation. Herein, we report a novel composite, prepared by coating an ordinary AC with an IL (1-butyl-3-methylimidazolium acetate, [BMIM][OAc]) offering an almost complete CO_2 selectivity over N_2 and CH_4. Data indicated that pore blockage by the IL accompanied with the enhancement in polarity and reduction in the hydrophobic character of the surface hindered the sorption of N_2 and CH_4. For CO_2, on the other hand, new chemisorption and physisorption sites became available associated with the IL layer on the surface making the composite material significantly selective. Newly formed chemisorption sites attributed to cation's acidic C2H sites which become available with bi-layer formation. Presence of multiple competitive sorption sites with different energies further proven with thermal analysis and detailed spectroscopic analysis. Data showed that CO_2/CH_4 and CO_2/N_2 ideal selectivities boosted from 3.3 to 688.3 (2.3 to 54.7) and from 15.6 to 903.7 (7.1 to 74.3) at 0.1 (1) bar and 25 °C, respectively, upon the deposition of the IL layer. At lower pressures, the IL/AC material became almost fully selective for CO_2 offering ideal selectivities in the order of several tens of thousands. To the best of our knowledge, the remarkable enhancement in the ideal CO_2 selectivity by a straightforward post-synthesis modification of an ordinary AC as reported here sets a new benchmark in high-performance and efficient gas separation for similar porous materials.

Results discussed in this chapter were published in the *Chemical Engineering Journal*. I would like to express my gratitude to co-author Dr. Muhammad Zeeshan for his contribution in sample characterization and validation, nonetheless, for his support through this research study.

7.1 Background

With increasing industrial growth, CO_2 emitted into the atmosphere has reached to an alarming level, posing risks to both environment and human health by causing various global contagions, such as climate change, rising of sea levels, and ocean acidification.[243, 244] In the path of selectively capturing anthropogenic CO_2 emitted into the atmosphere, adsorption-based gas separation processes gained considerable interest among the other techniques, such as absorption and membrane-based separation processes, due to its energy efficiency and environmentally friendly nature.[245, 246] Porous adsorbent materials, such as MOFs,[85, 247] zeolites,[248, 249] porous carbons,[250, 251] graphene-based materials,[4, 252] carbon nanotubes (CNTs),[253] ACs,[254-256] and clays[257] have been intensively studied for the selective CO_2 capture, and promising adsorption capacity and selectivity results were reported.[258, 259]

Among various adsorbent materials, ACs have attracted a significant attention in CO_2 adsorption and separation applications with their highly tunable nature in addition to high surface area, low cost, and high thermal/chemical stability limits.[93, 260] However, ACs fall short of providing a good separation performance because of their poor affinity towards CO_2, even though they are considered as excellent adsorbents owing to their robust nature, high surface area, and low cost.[261, 262] For effective CO_2 separation, an adsorbent has to provide CO_2 selectivities in the order of thousands and should be easily recycled for reuse.[263] Therefore, discovery of new adsorbents materials that are highly efficient, environmentally friendly, chemically robust, and cost-efficient are strongly needed and can be achieved with the help of newly synthesized task-specific hybrid materials from cost-efficient porous materials as ACs.

Recently, post-synthesis modifications of various porous materials with ILs were introduced as a prominent technique to enhance the CO_2 selectivity.[5, 227, 264-269] ILs are molten salts, which compose of an organic cation and an inorganic/organic anion, offering high thermal stability, non-volatility, and high solubility of CO_2.[1] There exists several studies showing exceptional CO_2 absorption capabilities of ILs, particularly, for ILs having highly acidic nature.[270-273] However, in terms of application, their liquid and highly viscous physical state, toxicity, availability, and cost issues can be considered as main drawbacks for process implementation scenarios.[274, 275] Accordingly, Yang and

co-workers confined [BMIM][Tf_2N] inside the nanocages of ZIF-8 and reported approximately 5-times higher ideal selectivities calculated from the Henry region of the gas adsorption isotherms where selectivities increased from 7.5 to 41 and 19 to 100 for CO_2/CH_4 and CO_2/N_2, respectively.[276] Later, our group demonstrated a MOF can be externally coated with an IL layer forming a core-shell type material, where the IL shell works as a smart gate for controlling the passage of different guest molecules. This study demonstrated that the CO_2/CH_4 ideal selectivity of ZIF-8 at very low pressures can be boosted 45-times, from 2.4 to 110, upon coating it with [HEMIM][DCA].[2] Recently, this concept was extended to the reduced graphene aerogels.[4] Data showed an approximately 20-times increase in CO_2/CH_4 selectivity, reaching 120, under 0.1 bar at 25 °C compared to that of pristine aerogel. Even though IL incorporation approach was shown to be very promising for boosting the CO_2 separation performance, in all these cases the resulting materials' ideal CO_2 selectivity over CH_4 and N_2 was still limited with only in the order of hundreds, far from desired levels.

Herein, we report a simple modification strategy, which makes the AC almost completely selective towards CO_2 with ideal selectivity values exceeding several tens of thousands at low pressures. An IL, 1-butyl-3-methylimidazolium acetate, [BMIM][OAc], selected based on its exceptionally high affinity towards CO_2 and relatively low cost, was deposited on the surface of AC by impregnation. Detailed characterization and volumetric gas uptake data demonstrated that [BMIM][OAc] layer electrostatically attached on the AC surface enhances the sorption of CO_2 molecules by offering an additional sorption mechanism, chemisorption.[84, 277-281] These newly formed sorption sites increased the polarity of the surface to hinder the physisorption of CH_4 molecules while blocking the adsorbent's pores to eliminate the N_2 physisorption. The composite showed exceptionally high ideal CO_2/CH_4 and CO_2/N_2 selectivities, especially at low pressures, outperforming those of carbon-based materials, zeolites, and MOFs reported to date as given in **Table C.1.1**, Appendix C.

7.2 Results and Discussion

Carbon surface functionalities (CSFs) of pristine AC (DESOREX© K33), as given in **Figure C.2.1**, were characterized by applying the Boehm titration method. Results presented in **Figures C.2.2 and C.2.3** (and as summarized in **Table C.2.1**) illustrated that AC contains a total of 485±24 µmol/g CSFs, corresponding to a relatively low surface polarity, and thus, high capability for the adsorption of non-polar molecules.

Surface areas and pore volumes of the pristine and [BMIM][OAc]-coated AC samples were presented in **Table C.3.1**, and corresponding N_2 sorption-desorption isotherms at -196 °C were given in **Figure 7.2.1**. Compared to the pristine material, data showed a decreasing trend in these quantities with increasing IL loading. However, BET analysis can be quantitatively misleading in terms of providing reliable data for IL-coated composites because the solubility of N_2 gas in bulk IL plays a crucial role during the measurement.[53, 145] Accordingly, N_2 solubility in bulk [BMIM][OAc] calculated by COSMO-RS calculations indicated poor solubility levels as given in **Figure C.3.1(a)**. Due to the low N_2 solubility of [BMIM][OAc], especially at the BET measurement conditions, the pores of AC can be mostly unavailable for the probe molecule; thus, the BET technique is not sufficient to precisely determine the surface areas and pore volumes of the prepared IL/AC composites. However, the successful incorporation of IL can be validated by the obtained results. Consistently, the corresponding pore size distribution of pristine AC (**Figure C.3.1(b)**) confirmed that the mesopores, as small as 20 Å, can easily accommodate the [BMIM][OAc] molecules.

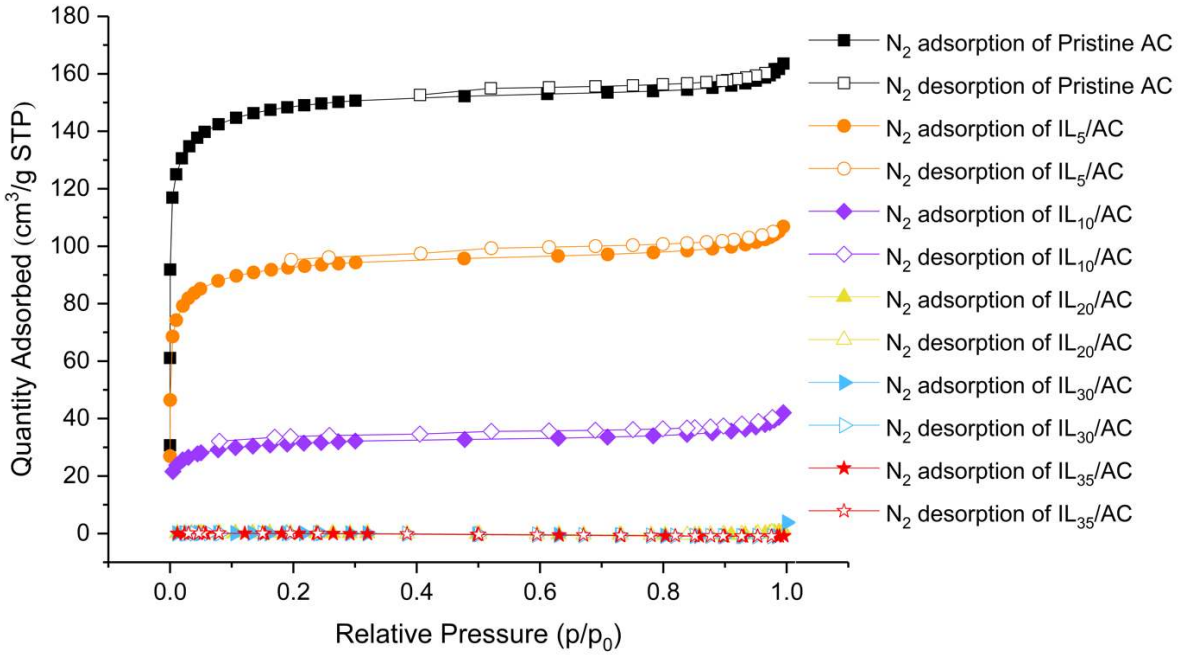

Figure 7.2.1. N_2 sorption and desorption isotherms at -196 °C for pristine AC and IL/AC composites with 5, 10, 20, 30, and 35 wt.% IL loadings.

The SEM images of pristine AC, IL_{10}/AC, and IL_{35}/AC samples presented in **Figure 7.2.2(a-c-e)** demonstrated that surface of the pristine AC was covered with IL molecules, while the surface morphology remained mostly intact upon the incorporation of [BMIM][OAc]. The EDX results obtained at different locations on pristine AC, IL_{10}/AC and IL_{35}/AC samples given in **Figure 7.2.2(b-d-f)** showed that the IL molecules were uniformly distributed on the surface of AC. Complementary SEM images and EDX mapping results showing carbon, nitrogen, and oxygen atoms can be found in **Figures C.4.1-2**, respectively.

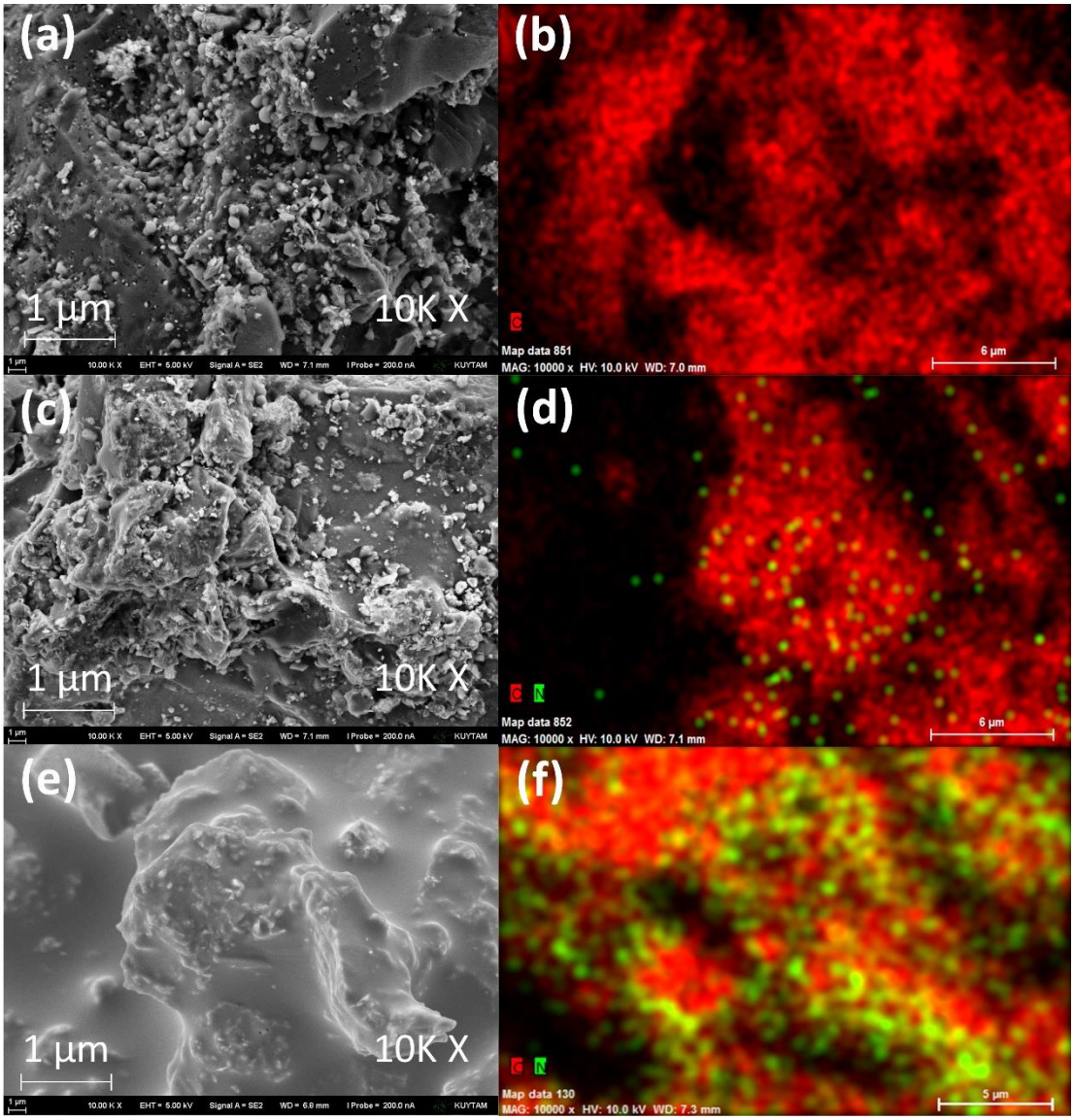

Figure 7.2.2. SEM/EDX images of (a-b) pristine AC, (c-d) IL_{10}/AC, (e-f) IL_{35}/AC at 10 k× magnification.

The XRD patterns given in **Figures C.5.1-2** showed that there were no noticeable shifts in the (002) and (004) characteristic diffraction peaks of AC located in a 2-theta range of 20-30° and 40-50°, respectively. These weak broad peaks were attributed to the amorphous carbon composed of randomly oriented aromatic carbon sheets in the structure.[282] Moreover, the sharp peak located at 26.4° can be ascribed to the (002) graphitic plane and can be associated with the graphitized carbon structure of the pristine AC.[283] However, the intensity of this peak decreased with an increase in the IL loading, indicating a highly amorphous carbon-based structure for IL/AC composites compared

to that of pristine AC.[284] Moreover, crystallite lateral size, height, and d-spacing values were calculated by deconvolution of the XRD data as provided in **Figure C.5.3** and tabulated in **Table C.5.1**. Data showed an increase in both lateral size and height, while d-spacing remained almost constant. These results indicated the deposition of the IL layer on the surface of the highly amorphous AC without disturbing the crystal structure.

To further evaluate the structural changes, Raman spectra of all samples, as given in **Figure C.6.1**, were analysed by deconvoluting the spectra in the range of 2000 to 1000 cm^{-1} into five different defect bands. Deconvolution using these defect bands (as defined in **Table C.6.1**), called *G*, *D*, *D2*, *D3*, and *D4,* were illustrated in **Figure C.6.2** and tabulated in **Table C.6.2**, respectively.[285] Data showed that the position and intensity of the *G* band, representing ideal graphitic lattice order, decreased with increasing IL loading up to 20 wt.%, however, samples with an IL loading exceeding 20 wt.%, showed an opposite trend indicating a possible change in the structure with impregnated [BMIM][OAc] molecules. Consistently, the same trend was obtained for the *D3* and *D* bands, representing amorphous carbon phases and the degree of disordered graphitic lattice, respectively. In addition, the I_D/I_G and A_D/A_G ratios, representing the degree of disorder, showed a similar trend, further indicating the change in the surface structure with the IL loading exceeding 20 wt.%.

Data given in **Figure C.7.1** and **Table C.7.1** illustrated that the T'_{onset} values of IL/AC composites were lower than that of pristine AC (<700 °C) but comparable with that of bulk IL (184±3 °C). It was observed that T'_{onset} values approach to that of bulk IL with increasing IL loading, from 162±3 °C to 179±3 °C, respectively for IL_5/AC to IL_{35}/AC. This change further demonstrates the impact of the molecular-level interactions, especially for low IL loadings, on the thermal stability limits.[155]

Molecular-level interactions between the pristine AC and the IL molecules were further analysed by infrared (IR) and XP spectroscopies. As presented in **Figure 7.2.3(a)**, the IR spectra of the samples, with an IL loading exceeding 20 wt.%, resembled more to that of bulk IL, compared to those with lower IL loadings. In the spectra of the samples with 5, 10, and 20 wt.% IL loading, a red-shift was observed on the characteristic ν(C=C) bands of pristine AC located at 1568 and 1440 cm^{-1}, whereas blue shifts were observed for ν(C–H_n), ν(C=O), and ν(C–O) bands located at approximately 2938, 1667, and 1150-990 cm^{-1}, as given in **Figure C.8.1(a-b)** and summarized in **Table**

C.8.1. As the majority of these shifts involve stretching features associated with the skeletal C=C, the nature of these interactions is identified as π–interactions.[286, 287] A slight red-shift in the energy of C=C bond can be expected due to the sharing of free π-electrons as having a relatively lower amount of oxygen-containing surface functional groups (485 μmol for pristine AC) provides a higher density of free π-electrons for π–interactions.[288] However, to create π-interactions, there are two possible alignments of IL's cation with the surface of AC, as illustrated in **Figure C.8.2**. Therefore, characteristic IR peaks of the cation were investigated to understand the nature of this alignment. The analysis indicated a dramatic change occurred in the case of ν(C2H) of heterocyclic ring located at 3089 cm^{-1} as given in **Figure 7.2.3(b-c)** and **Table C.8.2**. Red-shift observed on the ν(C2H) attributed to the vertical-to-face alignment of the cation with the surface of AC via CH–π interactions up to an IL loading of 20 wt.%.[289] However, this significant red-shift reduced gradually and became undetectable (from -19 cm^{-1} to almost no observable shift within a spectral resolution of 2 cm^{-1}) with increasing IL loading up to 35 wt.%. This change indicates a possible alteration in the interionic interactions of IL with increasing IL loading. Similar phenomena were observed in the case of acetate anion. Red-shifts, which were slightly above the spectral resolution, were observed for the characteristic IR peaks of carboxylate anion, ν(C=O) and ν(C–O), located at 1561 and 1389 cm^{-1}, respectively, indicating a possible change in the electron density distributions of IL due to the newly formed interactions between cation and the surface as shown in **Figure 7.2.4(a)**. However, with increasing IL loading, these shifts observed on the position of ν(C–O) and ν(C=O) almost disappeared and returned to their bulk IL vibrational frequencies. Thus, we inferred that for IL loadings exceeding 20 wt.%, IL molecules on the multilayers act as their bulk state and preserve their initial interionic interactions as given in **Figure C.8.3** (more detailed discussion is provided in the Appendix A). Based on these, it can be inferred that there are two different interaction layers on the surface of AC, namely wetting layer and bi-layer, formed with increasing IL loading.[290, 291]

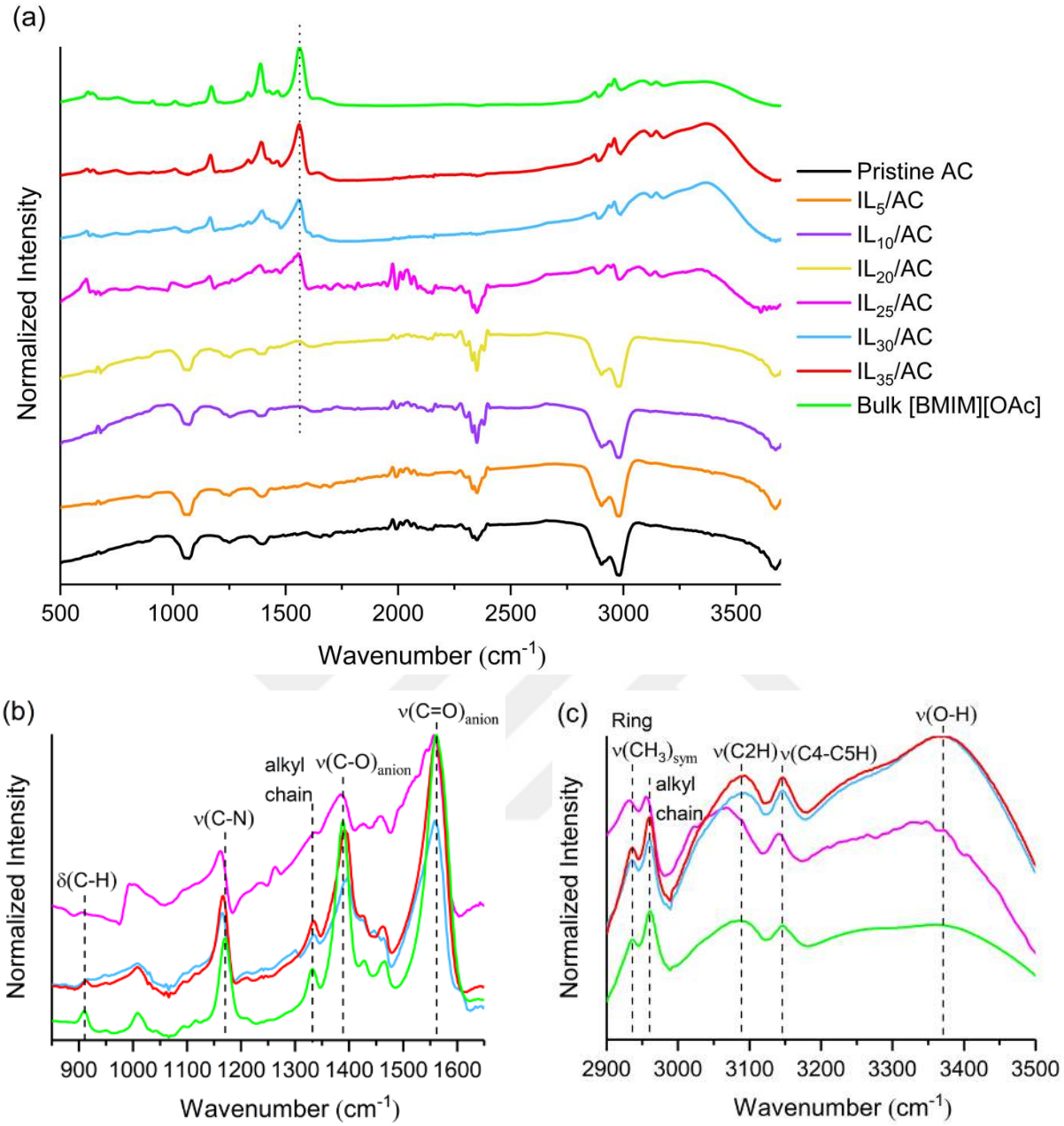

Figure 7.2.3. (a) FTIR spectra of pristine AC, bulk IL, and IL/AC with 5, 10, 20, 25, 30, and 35 wt.% IL loadings between the region 3700-500 cm^{-1}; (b) FTIR peak shifts of bulk [BMIM][OAc] and IL/AC composites with 25, 30, and 35 wt.% IL loading between the region 1650-850 cm^{-1}; (c) FTIR peak shifts of bulk [BMIM][OAc] and IL/AC composites with 25, 30, and 35 wt.% IL loading between the region 3500-2900 cm^{-1}.

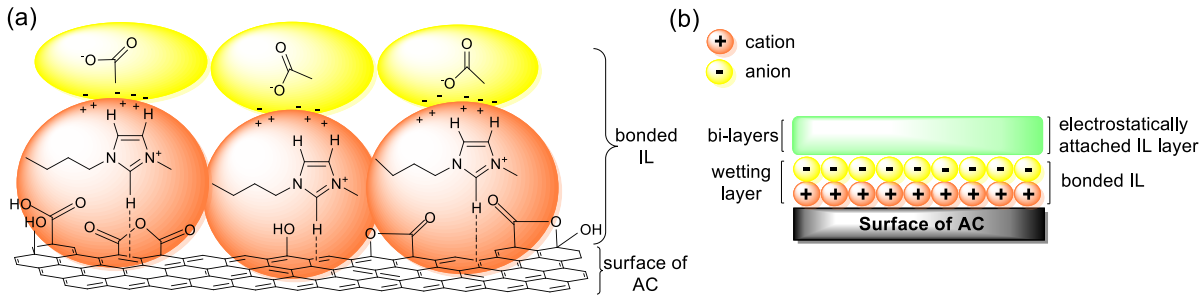

Figure 7.2.4. (a) Proposed cation-surface interaction mechanism and (b) resulting IL layer formation of IL/AC composites for IL loadings exceeding 20 wt.%.

In addition to these IR results, a blue shift of approximately 3 eV in the (π–π^*) satellite peak of C 1s was observed in the XP spectra of the IL_{20}/AC, IL_{30}/AC, and IL_{35}/AC composites (**Figure C.9.1-2** and **Table C.9.1**). This shift indicates the presence of π–interactions with delocalized π-electrons in the structure of IL/AC composites.[292] Also, the proportion of C–O/C–N (highlighted as green in **Table C.9.1**) increased with increasing IL loading proving the presence of IL molecules impregnated onto the pristine AC. Moreover, the proportion of the main C–C/C=C peak (highlighted as yellow in **Table C.9.1**) showed a decreasing trend indicating a decrease in the number of C=C bonds on the surface of AC. This can be interpreted as the surface covering of the IL molecules consistent with SEM/EDX images and Raman spectra. Contribution of this peak is important in evaluating the degree of graphitized carbon on the surface of the samples. It was already known from XRD data that the crystal structure of pristine AC was not altered upon IL impregnation. Therefore, this decrease of the graphitized carbon on the surface can be associated with the IL layer formation covering the surface. Consistent with our findings, only one peak appeared in N 1s XP spectra of the IL_{30}/AC and IL_{35}/AC where cation and anion of IL interact as in their bulk state.[293] Further discussion of XP spectra is provided in the Appendix A. Thus, based on these IR and XPS data, we inferred that the IL structure is distorted at low loadings, where the IL molecules can directly interact with the surface; however, as the IL loading increases above 20 wt.%, charged surface induces electrostatic interactions between IL molecules and electrostatically attached IL layer formed on the surface of AC, acting like bulk IL, as illustrated in **Figure 7.2.4(b)**.[294, 295]

To investigate the effect of IL impregnation on the gas sorption and separation performance of AC, volumetric sorption measurements were performed for CO_2, CH_4, and N_2 between 0.001 and 1 bar at 25 °C using both the pristine AC and IL/AC composites. Results were fitted to the Langmuir-Freundlich, dual-site Langmuir, and dual-site Langmuir-Freundlich models as presented in **Figure C.10.1**, and the corresponding fitting parameters were given in **Table C.10.1**. The ideal selectivities of CO_2/CH_4 and CO_2/N_2 were calculated from the fitted single-component gas sorption data for given total pressures and presented in **Figure 7.2.5**. Results illustrated that upon IL impregnation, the sorption capacity of AC decreases for CH_4, CO_2, and N_2 compared to that of pristine AC with increasing IL loading. However, in the case of CO_2 sorption, we observed an increase in the uptakes of IL_{30}/AC and IL_{35}/AC compared to that of IL_{20}/AC.

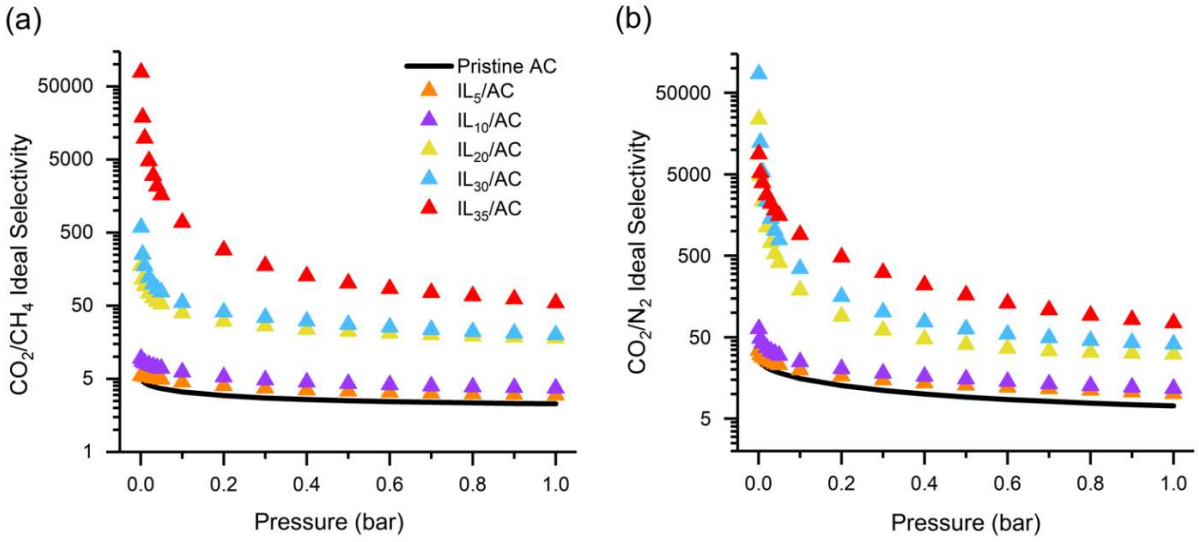

Figure 7.2.5. Ideal (a) CO_2/CH_4 and (b) CO_2/N_2 selectivities of pristine AC and IL/AC composites with 5, 10, 20, 30, and 35 wt.% IL loading at 25 °C. Selectivities are given in logarithmic scale.

Moreover, data illustrated that the ideal selectivities were remarkably enhanced for all IL-impregnated composites. Especially, IL_{35}/AC showed the highest selectivity enhancement among all composites. CO_2/CH_4 and CO_2/N_2 selectivities increased from 3.3 to 688.3 (2.3 to 54.7) and 15.6 to 903.7 (7.1 to 74.3) at 0.1 (1) bar and 25 °C, respectively. At lower pressures, the corresponding CO_2/CH_4 and CO_2/N_2 selectivities were significantly higher, 77390.4 (9781.8) and 8853.4 (3916.5) at 0.001 (0.01) bar and

25 °C, respectively. Such remarkably high selectivities indicate that the pristine material becomes almost completely selective for CO_2 upon coating its surface with the deposited IL layer. To the best of our knowledge, these ideal selectivity results, especially obtained at lower pressures, were higher than those of other post-synthesis functionalized porous materials reported to date, as given in **Table C.1.1**.

Furthermore, the thermodynamic analysis demonstrated that the sorption mechanism changed from exothermic to endothermic for each gas when the IL loading exceeds 20 wt.% (**Figure C.11.1-3**). It was obtained that up to 20 wt.% IL loading, sorption mechanism was controlled by temperature and proceeded exothermically similar to what we obtained for pristine AC, indicating the presence of physisorption. However, after 20 wt.% IL loading, the process became endothermic. This change might be associated with the newly formed IL bi-layers (as shown in **Figure 7.2.4(b)**), in which CO_2 is absorbed. Thus, for such high IL loadings, we infer that CO_2 absorption in the newly formed IL layer might also play a role along with the existing CO_2 adsorption sites.

In the case of CH_4 and N_2 sorption, the magnitudes of obtained ΔH_{sorp} values (at all uptakes) were below 30-40 kJ/mol, indicating the physisorption nature of their sorption as presented in **Figure 7.2.6(a-c)** (please refer to **Figure C.12.1-3** for Clausius-Clapeyron equation fittings). In both cases, the obtained ΔH_{sorp} values followed the same trend with the increasing gas uptake. However, in the case of CO_2, we observed a different trend compared to that of CH_4 and N_2. For the composites with 30 and 35 wt.% IL loadings, data illustrated a decreasing trend with increasing CO_2 uptake. The corresponding ΔH_{sorp} values decreased sharply, from 114.1 and 139.1 kJ/mol to 18.9 and 27.4 kJ/mol, with an increase in the CO_2 uptake for IL_{30}/AC and IL_{35}/AC, respectively. Such a substantial decrease in ΔH_{sorp} indicates the heterogeneity of the existing sorption sites, offering different affinities towards CO_2 molecules.[296] Accordingly, the ΔH_{sorp} values higher than 30-40 kJ/mol are associated with the available chemisorption sites present in the newly formed IL layer.[297] Thus, it can be inferred that the CO_2 sorption mechanism changes from chemisorption to physisorption with increasing coverage in the cases of IL_{30}/AC and IL_{35}/AC composites. In this respect, the available sites for chemisorption are limited in number, and as they get saturated with the chemisorbed CO_2, the sorption mechanism switches to physisorption.

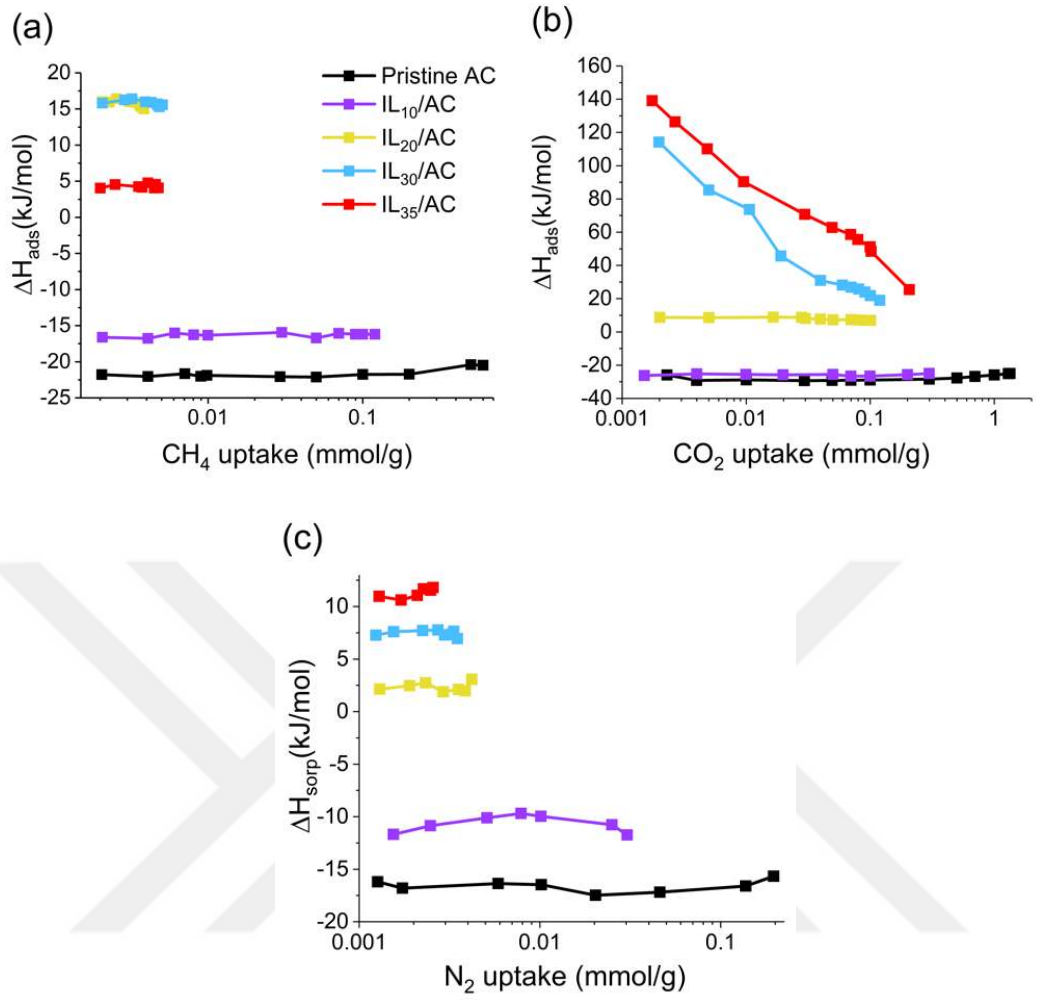

Figure 7.2.6. ΔH_{sorp} results obtained from (a) CH_4, (b) CO_2, and (c) N_2 gas sorption experiments conducted at three different temperatures as 15, 25, and 35 °C.

Next, we investigated the interactions between CH_4, CO_2, and N_2 molecules with the bulk [BMIM][OAc], pristine AC, and IL/AC composites in more detail by IR and liquid-state NMR spectroscopies. In the case of CH_4 sorption, IR analysis (**Figure C.13.1**) of the pristine AC and IL/AC composites did not provide any evidence on the formation of a new peak, confirming that the sorption mostly involves physisorption. It was observed that the characteristic peaks of ν(C–O) and ν(C=C) red-shifted to lower energy levels for pristine AC, IL_{10}/AC, and IL_{20}/AC, indicating a possible hydrophobic interaction between non-polar CH_4 molecules and the surface of AC. Moreover, IR analysis of the CH_4-saturated bulk [BMIM][OAc] (**Figure C.14.1**) complemented with the liquid-state NMR data (**Figure C.15.1** and **Table C.15.1**) provided similar evidence

confirming the presence of physisorption, and more detailed discussion is provided in the Appendix B. Therefore, it was concluded that the surface hydrophobicity and polarity of AC control the sorption of non-polar CH_4 molecules.[298] Hence, decreasing CH_4 uptake of IL/AC composites can be attributed to the newly attached cation molecules on the surface, which enhance the surface polarity by creating repulsive dipole moment for non-polar molecules. Accordingly, upon the deposition of IL, enhanced polarity and decreased hydrophobic character of the surface unfavoured the sorption of non-polar CH_4 molecules.

In the case of CO_2, carboxylate formation was observed in the IR and NMR spectra of the CO_2-saturated bulk [BMIM][OAc] (**Figure C.16.1**, **Table C.16.1** and **Figure C.17.1**, **Table C.17.1**, presenting the IR and NMR spectra, respectively). Detailed discussion on these results is provided in the Appendix A. These results are consistent with the previous reports demonstrating the chemical interaction of CO_2 with [BMIM][OAc] as shown in **Figure C.17.2**.[84, 270, 277, 279] On the contrary, for pristine AC, CO_2 physisorption through surface functional groups was expected, as found in **Figure C.18.1(a)**. Presence of adsorbed CO_2 molecules were verified from newly appeared peaks located between the region of 2400-2300 cm^{-1} consistent with the literature. Furthermore, a red-shift was observed in ν(C–O) band of pristine AC, as given in **Figure C.18.1(a)**, which can be attributed to the interactions between oxygen-containing functional groups and CO_2 molecules. Consistent with our findings, it was previously reported that oxygen atom of the highly electronegative functional groups, such as carboxylic and phenolic, can act as a basic site during CO_2 sorption.[299] In the case of composites with 10 and 20 wt.% IL loadings, a similar pattern was observed for ν(C–O) band as given in **Figure C.18.1(b-c)**. Moreover, the effect of adsorbed CO_2 molecules on the IL vibrations can be observed from the newly formed peak located at 1259 cm^{-1}, which corresponds to C–H bending vibrations of C2H of cation.[85] Based on these results, it can be inferred that the interaction mechanism for the sorption process was not altered significantly for the composites with IL loading up to 20 wt.%, compared to that of pristine AC. Therefore, decreasing CO_2 uptake can be attributed to the pore occupation of pristine AC by impregnated [BMIM][OAc] molecules. Consistently, several studies have reported lower uptake values due to pore occupation or blockage of AC.[300, 301] On the other hand, a new phenomenon was observed for IL loadings exceeding 20 wt.%, where new chemisorption sites for CO_2 molecules become available. As previously discussed, acidic C2H sites become available with bi-layer formation,

consistent with remarkably high ΔH_{sorp} values measured at low coverages. For the case of 35 wt.% IL loading, FTIR results yielded similar peak formations with CO_2-saturated bulk [BMIM][OAc], indicating a direct interaction between CO_2 molecules and formed IL layer through additional absorption mechanism. It was found that there exist two possible interaction mechanisms between CO_2 and [BMIM][OAc] layer; chemisorption through the cation part or physisorption through anion/cation part.[279, 302] Hence, each possible interaction type is analyzed one by one, considering the possibility of competitive multiple sorption sites. Accordingly, newly formed peaks upon CO_2 sorption can be seen in **Figure C.18.2(a)** with their corresponding locations. Two major results were obtained from the FTIR spectra given in **Figure C.18.2(a-b)**: i) carboxylate formation occurs during CO_2 sorption similar to the case of bulk [BMIM][OAc]; ii) physisorption sites exist in the structure of newly prepared IL_{35}/AC. First, the difference in the peaks related to chemisorption sites was analyzed. In **Figure C.18.2**, spectra of CO_2-saturated IL_{35}/AC and IL_{35}/AC were given together with the CO_2-saturated bulk [BMIM][OAc] to understand the interaction mechanism through already proposed various chemisorption paths for bulk [BMIM][OAc] (**Figure C.17.2**). Similar with the case of bulk [BMIM][OAc], we observed a red-shift and a dramatic decrease in the intensity of the characteristic ν(C2H) peak upon CO_2 sorption as tabulated in **Table C.18.1**. Moreover, the characteristic peak ν(COO) of formed carboxylate was observed at a lower wavenumber for CO_2-saturated IL_{35}/AC composite compared to that of CO_2-saturated bulk [BMIM][OAc], possibly indicating the presence of weaker interactions between CO_2 and carbon located at the C2 position of the cation. This result can be attributed to the formation of a transition complex, containing both hydrogen and CO_2 molecules bonded at C2 location as proposed in **Figure C.17.2(c)**. This proposed mechanism can also be supported with the lack of any acetic acid related IR peaks, which should be formed after the hydrogen substitution between C2H and acetate anion. As a second step, newly observed peak shifts in the spectra of CO_2-saturated IL_{35}/AC were investigated. Several peak shifts in the spectra of CO_2-saturated IL_{35}/AC can be attributed to the newly formed physisorption interactions between CO_2 molecules and IL layer on the IL_{35}/AC composite. Different from what we observed in the case of CO_2-saturated bulk [BMIM][OAc], a newly occurring red-shift on the ν(C4-C5H) peak of cation and an increased red-shift on the ν(C–O) peak of anion were observed as tabulated in **Table C.18.1**. These shifts are evidence of the existence of the competing chemisorption and physisorption sites. Hence, it can be inferred that multiple sorption sites exist in the structure of newly prepared IL_{35}/AC

composite.[303] These sites offer different mechanisms for sorption, such as chemisorption through C2H sites, physisorption through acetate anion, and physisorption through C4-C5H sites. This inference is consistent with previous reports demonstrating [BMIM][OAc] can interact with CO_2 molecules through multiple hydrogen bonding sites with changing structural conformations.[304] Consequently, increased CO_2 uptake after 20 wt.% IL loading can be attributed to these new sorption sites, which become available with [BMIM][OAc] bi-layer formation.

The IR results further indicated that the sorption occurs through physisorption for N_2 (**Figure C.19.1**), and detailed discussion is provided in the SI. Both N_2 and CO_2 are non-polar molecules; however, CO_2 consists of an electron-deficient carbon, which increases its affinity towards electronegative species on the surface.[305] In our case, when acidic C2H sites become available with bi-layer formation, it creates electronegative species on the surface, which favour the sorption of CO_2 over N_2 because a change in electronegativity does not affect N_2 sorption.[305] As a result, decreasing N_2 uptake was observed owing to the pore blockage by the deposition of [BMIM][OAc], in which N_2 has a poor solubility (**Figure C.3.1(a)**). Thus, we infer that the IL coating layer on the surface acts as a smart layer for the selective sorption of CO_2 by significantly blocking the passage of CH_4 and N_2 molecules.

Reusability is another crucial performance indicator for the adsorbents in terms of both stability and applicability. Hence, cyclic sorption experiments were conducted with two different batches of the best performing IL_{35}/AC composite to evaluate the regenerability and reusability of the composites. **Figure 7.2.7** demonstrates an excellent reproducibility of the data. Besides, the cyclic performance measurements, given in **Figure C.20.1-2**, showed that both batches of IL_{35}/AC were stable for at least ten CO_2 sorption/vacuum cycles without any significant performance loss. Such regeneration ability demonstrates the reversible nature of the chemisorption reaction between CO_2 and IL bi-layer.

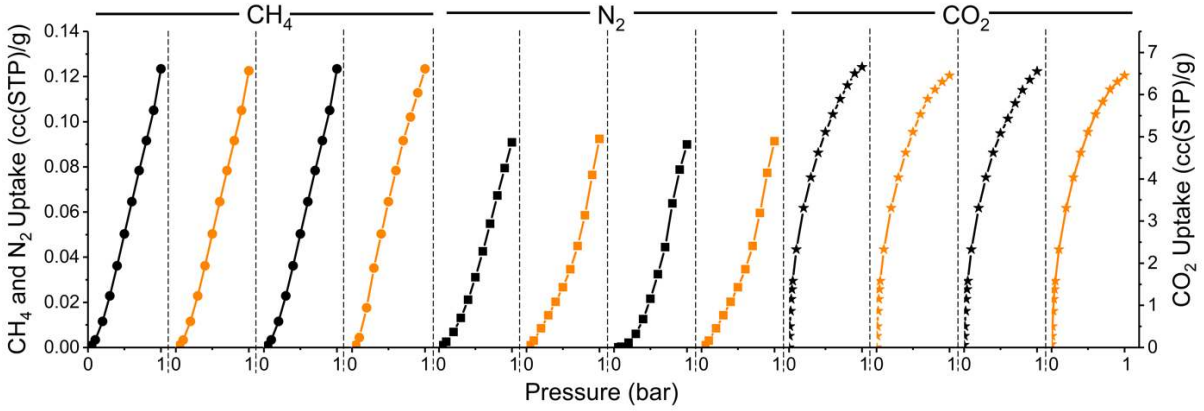

Figure 7.2.7. CH_4 (circle), N_2 (square), and CO_2 (star) gas sorption results for cyclic performance with two different batches, 1st batch (black) and 2nd batch (orange), of IL_{35}/AC up to two cycles between 0.001-1 bar at 25 °C.

To conclude, we reported a new IL-impregnated AC composite having practically complete selectivity for CO_2 over CH_4 and N_2. Among all composites, IL_{35}/AC showed the highest selectivity enhancement, where CO_2/CH_4 and CO_2/N_2 selectivities increased from 3.3 to 688.3 (2.3 to 54.7) and 15.6 to 903.7 (7.1 to 74.3) at 0.1 (1) bar and 25 °C, respectively. At lower pressures, the corresponding CO_2/CH_4 and CO_2/N_2 selectivities were significantly higher, 77390.4 (9781.8) and 8853.4 (3916.5) at 0.001 (0.01) bar and 25 °C, respectively. These results were attributed to IL layer formation on the surface of AC, which provides new chemisorption and physisorption sites for CO_2 and acts as a smart layer by preferentially blocking the sorption of CH_4 and N_2 molecules. Our data demonstrated a significant improvement in the CO_2 separation performance of AC upon the deposition of the IL layer, however, this benefit comes with an inevitable additional cost of required adsorber volume due to the decrease in the gas uptake values. This study presents a simple way of converting an ordinary AC into a completely selective material and provides opportunities for the design of cost-effective materials with exceptional gas separation performance.

Chapter 8: Conclusion and Outlook*

*This chapter is a section of Review article published in *Microporous and Mesoporous Materials 332, 111703 (2022)* by authors Özce Durak, Muhammad Zeeshan, Nitasha Habib, Hasan Can Gülbalkan, Ala Abdulalem Abdo Moqbel Alsuhile, Hatice Pelin Çağlayan, Samira F. Kurtoğlu-Öztulum, Yuxin Zhao, Zeynep Pınar Haşlak, Alper Uzun, and Seda Keskin. The related part presented here was written mainly by the author of this thesis.

ILs are one of the promising agents to modify the physicochemical properties of a pristine porous host material. In this thesis, the promising aspects of IL/porous material composites was highlighted where the structural dynamics of pristine material are tuned by the addition of ILs. The field of IL/porous material composites was examined, where we focused different types of MOFs and AC, in terms of synthesis methodologies, characterization techniques, and application scope. IL incorporation enhances the performance of pristine materials in various applications, including gas adsorption and separation, catalysis, liquid-phase adsorption and separation, and ionic conductivity. These enhanced performances were explained by the interactions between IL and porous materials. Both experimental and computational tools were utilized to gain more in-depth insight into the possibilities for different types of IL/porous material composites, specifically, IL/MOFs and IL/ACs.

In Chapter 1 to 3, a detailed literature survey on IL/porous material composites was conducted and the recent advances of the field was given together with the in-depth explanations of various synthesis and characterization techniques to create a background knowledge on the field. In chapter 4, a hydrophilic IL, [BMIM][$MeSO_4$], was incorporated into the cages of UiO-66 and its ligand functionalized counterpart, NH_2-UiO-66. Corresponding changes on thermal and chemical stability limits were analyzed to obtain a fundamental-level understanding of the importance of porous material functionalization. Results illustrated that the composite with the ligand-functionalized MOF, NH_2-UiO-66, exhibited a lower degree of decrease in the thermal stability limits compared to the those containing non-functionalized UiO-66. When the IL is hydrophilic, its hydrogen bonding ability can be utilized to designate an interaction site on MOF's ligand structure which will lead to a lower reduction in thermal stability limits. Then, these systematic changes in the structure of MOF were further investigated in Chapter 5 by incorporating the same IL, [BMIM][$C(CN)_3$], into the cages of three different Zr-MOFs, UiO-66, UiO-67, and MOF-801. Extraordinary performance improvements in the selective gas separation of CO_2, C_2H_4, and C_2H_2 from CH_4 and N_2 were achieved for the [BMIM][$C(CN)_3$]/UiO-66 composite emphasizing the significance of MOF selection on the resulting gas separation performance. Motivated from the superior performance obtained through the deposited IL layer on the surface of MOF, a core-shell type IL/MOF composite was designed in Chapter 7 by an integrated computational-experimental hierarchical approach for enhanced air separation. A bulky phosphonium-based IL, [$P_{6,6,6,14}$][DCA], and an iron-based MOF with open redox-active metal sites, PCN-250(Fe),

were selected after a detailed computational investigation for experimental trials. During the computational selection of the most promising IL-MOF pair having superior O_2/N_2 selectivity, GCMC simulations, quantum chemistry based COSMO-RS calculations, and DFT calculations was utilized. Synthesized $[P_{6,6,6,14}][DCA]$/PCN-250 composite was systematically optimized by investigating the effect of heat treatment and solvent dispersion of the porous host material, pristine PCN-250(Fe). Results illustrated a remarkable improvement (in the order of almost 20-times) in ideal O_2/N_2 selectivity, from 0.9 to 17.8, at 1 bar and 25 °C in the case of $[P_{6,6,6,14}][DCA/PCN\text{-}250(Fe)_{240}$ reaching a benchmark value among previously reported MOF studies. Moreover, O_2/N_2 selectivity under mixture gas conditions was determined by IAST selectivity calculations to evaluate the direct O_2 purification performance of $[P_{6,6,6,14}][DCA]/PCN\text{-}250(Fe)_{240}$ composite under air. $[P_{6,6,6,14}][DCA]/PCN\text{-}250(Fe)_{240}$ composite showed extraordinary O_2/N_2 selectivity of 362 at 1 bar and 25°C which complemented with the dynamic breakthrough measurements under continues air. Preferential O_2 sorption on $[P_{6,6,6,14}][DCA]/PCN\text{-}250(Fe)_{240}$ composite was further validated with the performed breakthrough experiments. Furthermore, obtained ideal O_2/N_2 selectivity results were improved with systematic changes in the dispersion of pristine PCN-250(Fe) during the synthesis of the composite. $[P_{6,6,6,14}][DCA]/PCN\text{-}250(Fe)_{240\text{-}S,Acetone}$ composite, which was synthesized with pristine PCN-250(Fe) treated at 240 °C and dispersed in acetone by sonication, showed almost 30-times improvement in the ideal O_2/N_2 selectivity together with a 3.4-times increase in O_2 adsorption capacity at 1 bar and 25 °C . In Chapter 7, an ordinary AC was modified with [BMIM][OAc] to enhance the scope of the field by utilizing a cost-effective and chemically robust porous material. Upon the deposition of [BMIM][OAc] layer on the surface of pristine AC, IL/AC composite became almost completely selective towards CO_2 with ideal selectivity values exceeding several tens of thousands at low pressure outperforming those of carbon-based materials, zeolites, and MOFs reported to date.

Besides the discussed current advances, there are many aspects of the IL-incorporated hybrid composites field which need to be improved in the future. Therefore, together with the potential limitations that affect the performance of IL/porous material composites, several suggestions associated with each chapter were discussed below to guide the future directions.

Selecting appropriate preparation technique: There are various *in-situ* and post-synthesis modification techniques to prepare IL/porous material composites. Hence, choosing a task-specific preparation technique is significant. The mechanism and strength of the molecular

interactions between IL and porous materials dramatically change with different *in-situ*/post-synthesis techniques, resulting in completely different IL/porous material composites in terms of both characteristic and performance measures. For instance, due to steric hindrance, relatively large ILs may not enter the zeolite cages, which requires an in-situ synthesis method, such as ship-in-a-bottle, to encapsulate IL molecules in the cages. Moreover, during ionothermal synthesis of IL-based hybrid MOFs, several studies reported structures with only one constituent of IL while the other constituent remained in the solution to maintain surface neutrality of the resulting hybrid material.[33, 42, 48] For this synthesis technique, ILs' desired properties cannot be produced within the hybrid material due to the lack of control over the final structural design. Therefore, in the case of MOFs, the usage of post-synthesis techniques to incorporate IL will be more beneficial and flexible in terms of taking advantage of IL's desired properties, such as gas solubility and ion mobility. In contrast, for negatively charged zeolite structures, post-synthesis techniques yield composites containing only the cation part of IL where the anion part remains in the solution.[306] Thus, the structural integrity of the ILs is generally lost in such materials. Accordingly, a detailed evaluation of the advantages and disadvantages of the preparation techniques is crucial for further research studies as evidenced in Chapter 6. Preparation techniques of $[P_{6,6,6,14}][DCA]/PCN\text{-}250(Fe)_{240}$ composites demonstrated a significant difference in the gas separation performance highlighting the vital importance of selecting the appropriate preparation technique. Accordingly, diversity of the synthesis techniques can be improved in the future studies or the number of research studies only focusing on the synthesis techniques of IL/porous material composites can be increased.

Rational design of IL-porous material composites: There are limitless combinations for IL/porous material composites owing to the high number of ILs available. In the case of rational design, the determination of newly formed interactions and their effects on the performance should be elucidated in detail. By understanding the effect of the specific functionalization on desired performance measures, appropriate IL and porous material combinations can be made. For example, the selectivity of materials towards a particular molecule can be directly adjusted and enhanced by the rational selection of IL-porous material combination. Many IL/porous material composites have been examined so far, but it is still not quite sufficient compared to the theoretical number of IL-porous material combinations. In this aspect, computational studies can provide opportunities for large-scale screening for IL-containing porous hybrid materials and their performance of desired applications. In Chapter 6, selection of the most

promising IL-MOF pair was conducted by computational tools and superior O_2 separation performance was achieved without synthesizing thousands of IL/MOF composites. Similarly, this approach can be extended to each chapter, especially to Chapter 7 where a different type of robust porous material was utilized. Computational tools can be used to predict the performance of thousands of IL/AC composites for various gas separation applications to design a cost-efficient hybrid material in comparably much smaller time and experimental effort.

Thermal and chemical stability of IL/porous material composites: Another aspect to be considered for future research is the thermal and chemical stability limits at elevated temperatures/pressures. In most cases, IL/porous material composites have new characteristics than their parent constituents, resulting in lower thermal stability limits due to newly formed interactions between IL and porous material. However, most industrial processes require moderately high temperature and/or pressure conditions. Hence, developing porous material composites with adequate stability limits is crucial for their usage and should be investigated further by taking different IL/porous material composites into account. Moreover, corresponding recyclability or reusability concept of these materials is mostly overlooked in the literature. It is crucial to understand the effect of the application on structural integrity of the composite as it will be important while evaluating the performance measures. Therefore, reported performance data on IL-incorporated composites should also include reusability of these materials at least up to multiple cycles. Consistently, Chapter 4, 6, and 7 emphasize the structural stability of studied composites and corresponding reusability performance was investigated.

Fundamental understanding of the structural effects of the individual constituents of the composites on performance measures: Structural properties of IL containing hybrid materials, such as pore size and shape, porosity, surface area, stability, flexibility, crystallinity, and morphology are directly related to the those of IL and porous material, which can be altered by functionalization methods. Various studies focused on these structural effects by modifying the porous materials or ILs by functional group addition, thermal treatments, change of the metal nodes or linkers, polarity, and hydrophobicity/hydrophilicity. For each case, the structural change affects the performance measures, either causing a different interaction mechanism between the IL and porous material or a change in the position of IL in the resulting hybrid material. In gas-phase/liquid-phase adsorption and separation applications, performance

efficiencies are changing with newly formed interactions between IL and porous material due to the blockage of the existing adsorption sites or the opening of the new ones. Hence, to benefit from the IL incorporation, a fundamental level understanding of the interaction mechanism in composites and investigating the resulting effect on the performance measures are of great importance. Chapter 4, focusing on ligand functionalization of MOFs, and Chapter 5, focusing on organic linker selection of MOFs, can be given as an example to highlight this concept. Accordingly, further experimental research on the functionalization of AC in Chapter 7 can be made to improve the analysis of IL/AC composites.

Testing IL-porous material composites for other gas separations: Currently, experimental studies of IL-porous material composites mostly focus on flue gas separation and natural gas purification (CO_2/N_2 and CO_2/CH_4) processes. However, it would be of great interest to explore the potential of these versatile materials in industrially important gas separation processes such as hydrocarbon separation (C_2H_2/C_2H_4, C_2H_2/CO_2, C_2H_4/C_2C_6), hydrogen separation (H_2/CO_2, H_2/CH_4, H_2/O_2, H_2/N_2, H_2/CH_4, H_2/CO), sulfur separation (H_2S/CH_4), and most importantly oxygen separation due to ongoing COVID-19 pandemic as of August 2021 (O_2/N_2). In accordance with mentioned suggestions, several different gas separation studies were included in the thesis to emphasize the importance of the diversity of gas separation applications.

Applicability into real-life processes: The behavior of IL/porous material composites should be evaluated under various temperature, pressure, and humidity conditions with the exposure of different chemical environments mimicking the realistic application conditions to assess their applicability. Lack of investigations on different process conditions generates an important drawback for their real-life usage. Going from lab-scale to industrial pilot-scale is also required to assess the real-life efficiency of the process parameters. Therefore, the number of studies on the applicability, especially for the best-performing IL/porous material composites, should be extended for future usage. For instance, in the case of gas-phase adsorption and separation, most of the research in the field focuses on single-component gas adsorption experiments rather than mixture gas. However, in real-life processes, almost all process streams consist of gas mixtures having impurities. Therefore, the focus should be on mixture-gas experiments under industrial conditions. Accordingly, more research on potential adsorption processes, such as PSA, PVSA and TSA systems, is needed to widen the scope of investigation related with the applicability of composite materials. In this regard, dynamic

breakthrough measurements were performed on the synthesized IL/MOF composite in Chapter 6 to evaluate the gas separation performance under gas mixture conditions (air) together with the obtained single-component gas separation results. Similarly, dynamic breakthrough experiments can be conducted in Chapter 5 and 7 to further validate the obtained superior separation performance and to investigate the performance measures under real-life conditions.

Operational cost of hybrid composites: Moreover, from operational cost perspective, superior selectivity performance of IL-incorporated adsorbents can provide the opportunities for lowering the cost. Currently, there are several case studies available on the operation costs of CO_2 and H_2 separation processes, which highlight the benefits of using highly selective "ideal" adsorbents, where "ideal" refers to the materials with high gas recovery, selectivity, energy penalty and productivity measures.[307] The lowest possible CO_2 avoided costs are reported for the adsorbents with superior CO_2 selectivity over specified gasses which further demonstrates the promising process implementation aspect of IL-incorporated composites.[307, 308] For instance, in a case study, the cost of CO_2 capture was shown to reduce from US$49 per ton CO_2 avoided to US$30 with a hypothetical adsorbent which provides 3-times higher CO_2/N_2 selectivity compared to conventional adsorbent.[309] Consequently, the improved selectivity offered by IL-incorporated composites provides opportunities for decreasing the operation cost. In addition to these, the subject of material cost is highly overlooked in IL/porous material composites and should be carefully evaluated. Performance measures increase with increasing IL loadings for most applications, such as gas-phase separation. However, the cost of ILs and porous materials, especially for the conventionally expensive MOFs, creates a significant limitation for future large-scale industrial usage. Thereby, further investigation on loading effect and task-specific modifications for IL and porous material is extremely important to obtain highly efficient IL/porous material composites with lower IL loading and lower material cost. In this respect, material cost point of view can be stated as the prominent shortcoming of the thesis and further economic analysis can be added into each chapter to improve the applicability aspect of the novel IL/porous material composites reported in this thesis.

Future advances in experimental and computational methodologies will provide a more in-depth insight into the great potential of IL-containing hybrid materials, and with time, we believe that these advantageous hybrid materials will evolve as alternative materials for various applications than their conventional counterparts.

APPENDIX A: Supplementary Information of Chapter 5

A.1 Isotherm Fittings

Table A.1.1. Fitted isotherm parameters of Dual-Site Langmuir Model, Dual-Site Langmuir-Freundlich Model, and Langmuir-Freundlich Model for pristine Zr-MOFs and IL/Zr-MOF composites.

Adsorbent	Gas	Dual-Site Langmuir Model					Dual-Site Langmuir-Freundlich Model							Langmuir-Freundlich Model			
		q_1 (cc/g)	k_1 (1/mbar)	q_2 (cc/g)	k_2 (1/mbar)	R^2	q_1 (cc/g)	k_1 (1/mbar)	n_1^*	q_2 (cc/g)	k_2 (1/mbar)	n_2^*	R^2	q (cc/g)	k (1/mbar)	n*	R^2
Pristine UiO-66	CH_4	74.1	0.125	20.5	0.125	0.99											
	CO_2	707.6	0.021	47.4	1.22	0.99											
	N_2						8.29	0.389	1.03	38.16	0.085	1.47	0.99				
	C_2H_4	165.9	0.239	19.4	4.23	0.99											
	C_2H_2	156.7	0.527	3.11	10.4	0.99											
Pristine UiO-67	CH_4	28.2	0.123	110.6	0.0181	0.99											
	CO_2	173.1	0.082	5.70	2.25	0.99											
	N_2	18.8	0.021	54.5	0.021	0.99											
	C_2H_4	4.09	5.94	111.5	0.241	0.99											
	C_2H_2	5.06	9.80	143.4	0.201	0.99											
Pristine MOF-801	CH_4	20.4	0.387	244.1	0.008	0.99											
	CO_2						109.7	0.246	0.866	7.53	5.73	0.994	0.99				
	N_2	27.3	0.057	11.8	0.057	0.99											
	C_2H_4						62.1	0.458	0.828	11.3	8.29	1.01	0.99				
	C_2H_2	9.90	25.4	69.3	0.896	0.99											

[BMIM][C(CN)$_3$]/UiO-66	CH_4													1.73	0.216	1.66	0.99
	CO_2	915.5	0.0008	0.981	0.766	0.99											
	N_2																
	C_2H_4						28.7	0.017	0.97	1.78	2.77	1.78	0.99				
	C_2H_2	0.634	2.876	27.6	0.098	0.99											
[BMIM][C(CN)$_3$]/UiO-67	CH_4	0.00001	2.46	4.56	0.068	0.99											
	CO_2	260.4	0.0038	1.13	1.15	0.99											
	N_2													7.01	0.014	1.03	0.99
	C_2H_4	1.06	1.54	441.7	0.0013	0.99											
	C_2H_2	28.6	0.122	0.416	9.31	0.99											
[BMIM][C(CN)$_3$]/MOF-801	CH_4	0.896	0.451	32.1	0.007	0.99											
	CO_2	1.35	4.28	19.7	0.128	0.99											
	N_2													0.746	0.411	1.51	0.99
	C_2H_4	8.88	0.142	1.34	5.57	0.99											
	C_2H_2	21.2	0.234	1.98	13.3	0.99											

APPENDIX B: Supplementary Information of Chapter 6

B.1 Literature Overview

Table B.1.1. Literature overview for O_2/N_2 gas separation performance.

Material	O_2/N_2	Conditions	
		Pressure (bar)	Temperature (K)
$[P_{6,6,6,14}][DCA]/PCN\text{-}250(Fe)_{240}$	**6824**	0.001	298
	1093	0.01	298
	140	0.1	298
	17.8	1	298
$[P_{6,6,6,14}][DCA]/PCN\text{-}250(Fe)_{240,S\text{-}Acetone}$	**3699**	0.001	
	1393	0.01	
	202.8	0.1	
	26.1	1	
$[P_{6,6,6,14}][DCA]/PCN\text{-}250(Fe)_{240}$ (IAST 21/79)	**5533**	0.001	298
	4323	0.01	298
	1705	0.1	
	362	1	298
Ideal Selectivity*			
CuBTC[310]	0.9	1	298
Fe/CuBTC[310]	1.1	1	298
$MIL\text{-}53(Al)_{solht}$[311]	0.6	1	303
$K_{1.09}Fe_2(bdp)_3$[217]	6.2	1	298
1 ● $2O_2$[225]	2.3	1	298
$Cu(Qc)_2$[224]	3.6	5	298
	4.62	50	298
$Co_2(OH)_2(BBTA)$[218]	5.2	1	298
MOF-177[226]	1.8	1	298
Mixture (21/79) Selectivity			
$Cr_3(BTC)_2$[219]	22	1	298
1 ● $2O_2$[225]	38	1	298
IAST (21/79) Selectivity			
Fe-BTTri[223]	27	1	195.15
$Fe_2(dobdc)$[221]	11	1	201
$Co_2(OH)_2(BBTA)$[218]	49	1	298
Co-BTTri[222]	13	1	243
	41	1	195
Co-BDTriP[222]	40	1	243
3a (Co(II) carborane-based)[312]	3	1	298
4a (Co(II) carborane-based)[312]	2.4	1	298
4b (Co(II) carborane-based)[312]	1.3	1	298
IAST (20/80) Selectivity			
Cr-BTT[220]	2570	1	298

B.2 EDX Analysis

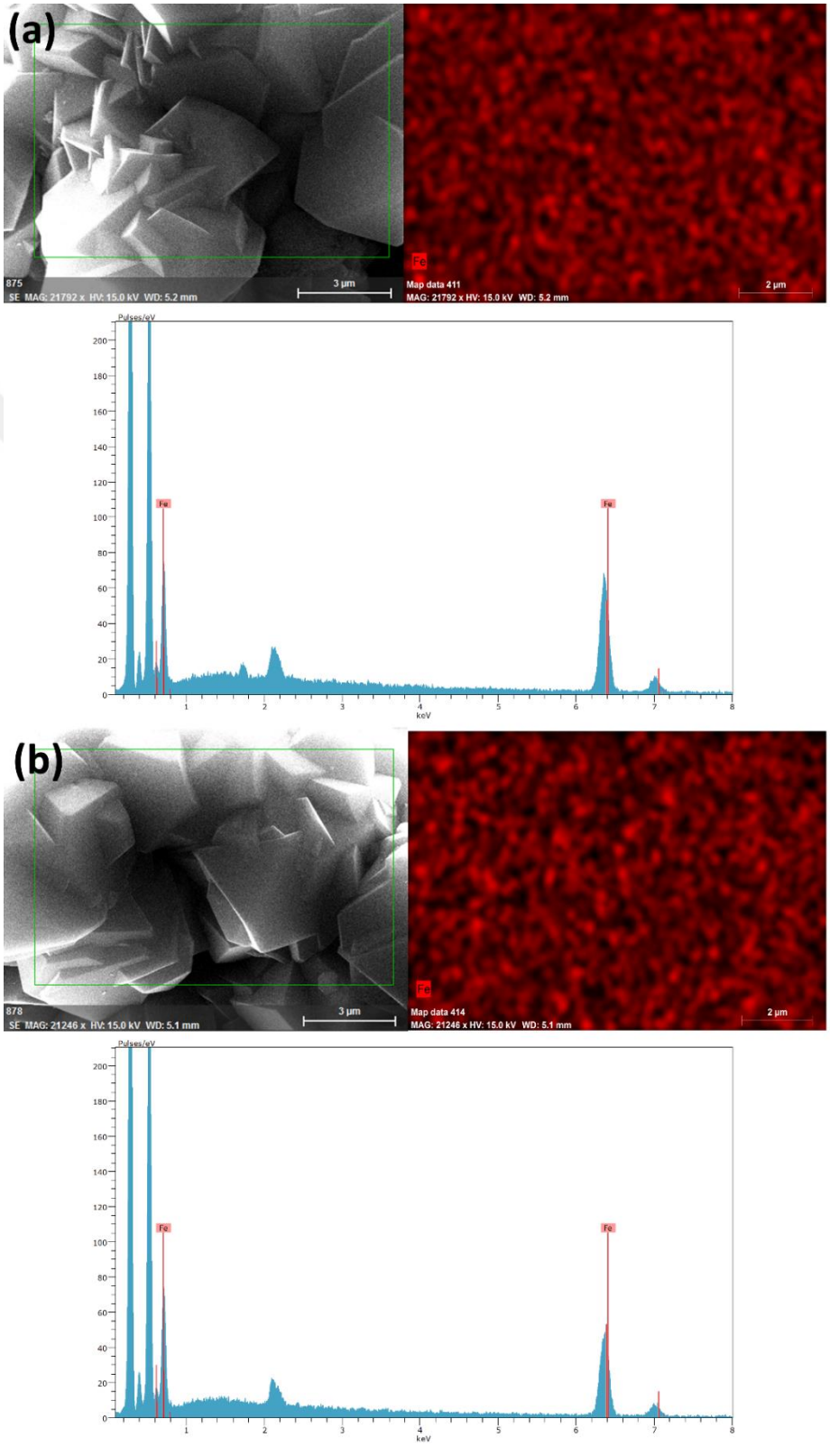

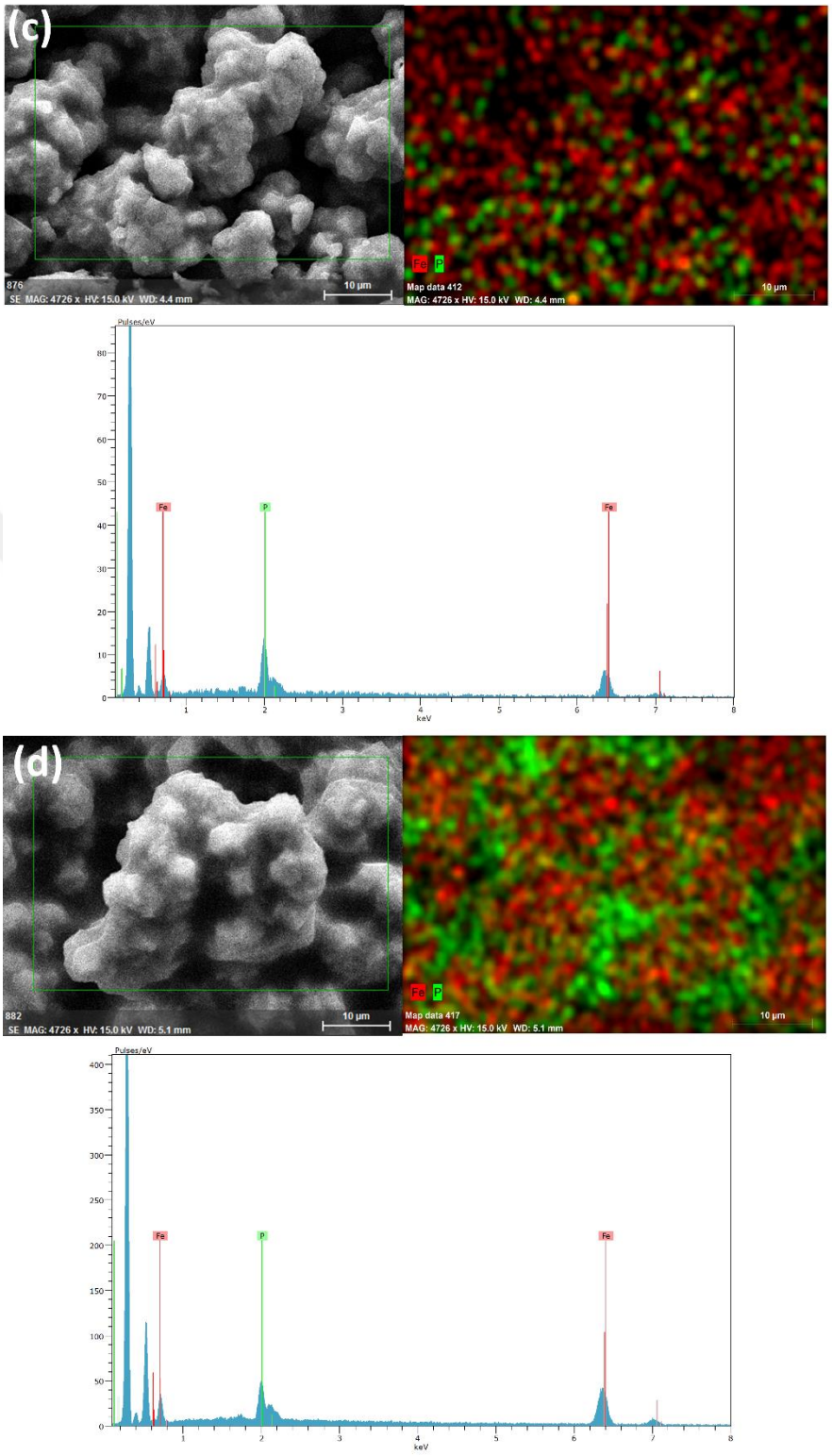

Figure B.2.1. EDX mapping of (a) pristine PCN-250(Fe)$_{150}$, (b) pristine PCN-250(Fe)240, (c) [P$_{6,6,6,14}$][DCA]/PCN-250(Fe)$_{150}$, and (d) [P$_{6,6,6,14}$][DCA]/PCN-250(Fe)$_{240}$

B.3 Isotherm Fittings

Table B.3.1. Fitted isotherm parameters of Dual-Site Langmuir Model for pristine and composite samples.

Adsorbent	Gas	10 °C Dual-Site Langmuir Model					25 °C Dual-Site Langmuir Model					40 °C Dual-Site Langmuir Model				
		q_1 (cc/g)	k_1 (1/mbar)	q_2 (cc/g)	k_2 (1/mbar)	R^2	q_1 (cc/g)	k_1 (1/mbar)	q_2 (cc/g)	k_2 (1/mbar)	R^2	q_1 (cc/g)	k_1 (1/mbar)	q_2 (cc/g)	k_2 (1/mbar)	R^2
Pristine PCN-250(Fe)$_{150}$	O_2	0.002	0.0041	2260	0.0031	0.99	8454	0.00037	9565.9	0.00024	0.99	4209	0.0003	5851	0.00055	0.99
	N_2	181.6	0.026	97.6	0.027	0.99	285.5	0.016	44.8	0.017	0.99	239.9	0.013	78.7	0.0134	0.99
Pristine PCN-250(Fe)$_{240}$	O_2	0.592	200.83	111.3	0.079	0.99	123.5	0.053	0.157	86.3	0.99	38.9	0.153	0.443	259.7	0.99
	N_2	197.1	0.045	20.04	0.045	0.99	359.4	0.019	0.0001	0.0087	0.99	734.3	0.0073	0.056	0.0073	0.99
[$P_{6,6,6,14}$][DCA]/ PCN-250(Fe)$_{150}$	O_2	1.62	417.7	20.8	0.249	0.99	1.2	360.3	15.5	0.265	0.99	1.3	186.2	24.5	0.119	0.99
	N_2	5.4	0.498	0.355	6.07	0.99	1.3	0.338	7.2	0.431	0.99	1.08	0.0089	12.4	0.190	0.99
[$P_{6,6,6,14}$][DCA]/ PCN-250(Fe)$_{240}$	O_2	13.7	420.9	971.6	0.00366	0.99	12.6	356.7	41.8	0.0916	0.99	12.3	350.1	18.0	0.173	0.99
	N_2	1817	0.0009	0.001	0.000002	0.99	0.0002	0.00006	426.4	0.0021	0.99	336.2	0.0023	0.004	10000	0.99
[$P_{6,6,6,14}$][DCA]/ PCN-250(Fe)$_{240,S\text{-}Acetone}$	O_2						16.3	228.1	9.5	1.2	0.99					
	N_2						2628.3	0.00031	0.0002	0.286	0.99					
[$P_{6,6,6,14}$][DCA]/ PCN-250(Fe)$_{240,S\text{-}DMF}$	O_2						1.9	139.1	7.5	0.636	0.99					
	N_2						1954	0.00054	0.0002	0.0006	0.99					
[$P_{6,6,6,14}$][DCA]/ PCN-250(Fe)$_{240,S\text{-}Cloroform}$	O_2						2.8	61.3	9.1	3.6	0.99					
	N_2						2937	0.00024	0.0006	841.3	0.99					
[$P_{6,6,6,14}$][DCA]/ PCN-250(Fe)$_{240,US\text{-}Acetone}$	O_2						12.8	315.4	158.2	0.0163	0.99					
	N_2						0.0174	0.001	3439	0.00021	0.99					
[$P_{6,6,6,14}$][DCA]/ PCN-250(Fe)$_{240,US\text{-}DMF}$	O_2						2.8	244.5	13.6	0.261	0.99					
	N_2						2.1	0.000007	1223	0.00078	0.99					
[$P_{6,6,6,14}$][DCA]/ PCN-250(Fe)$_{240,US\text{-}Cloroform}$	O_2						4.3	14.3	9.6	0.298	0.99					
	N_2						530.4	0.0017	0.0003	10000	0.99					

B.4 GCMC Simulations of Pristine PCN-250(Fe)

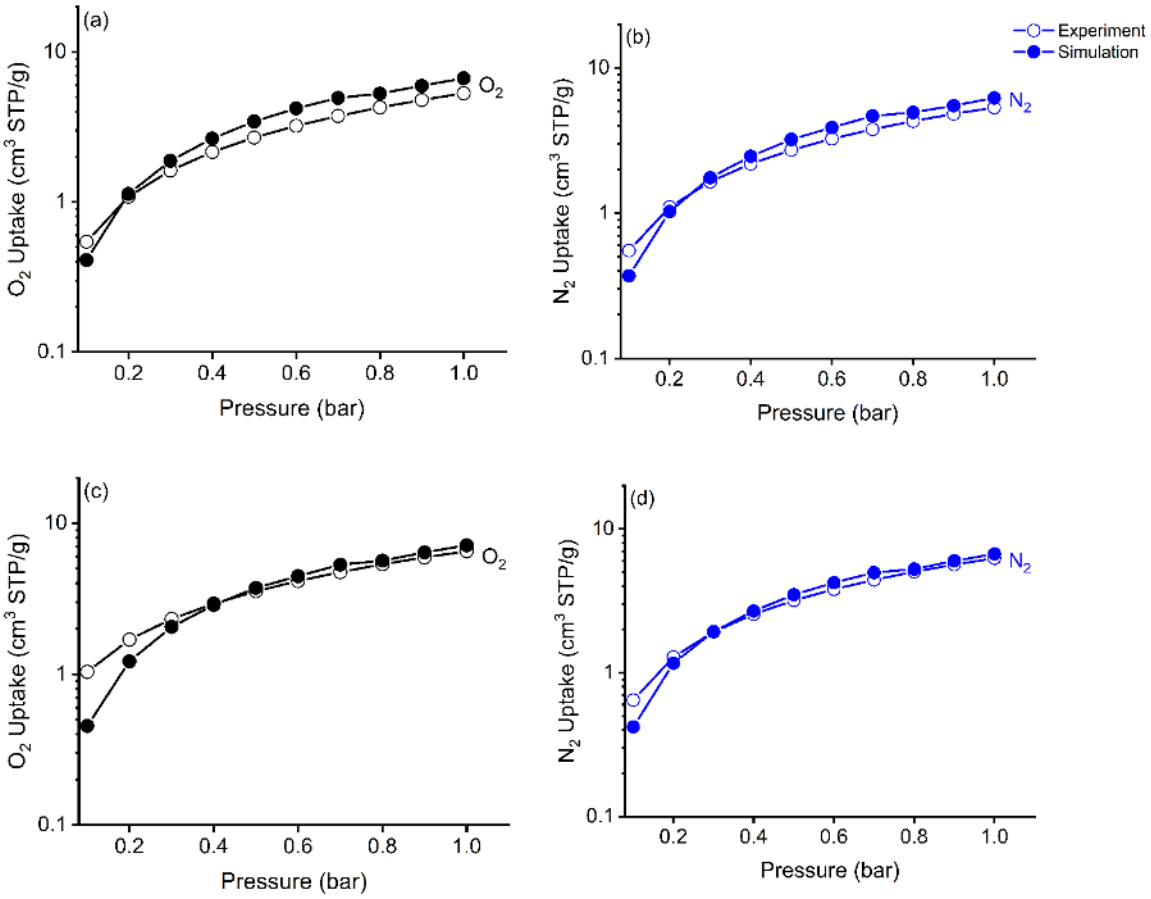

Figure B.4.1. Comparison of experimental (empty circles) and simulation (filled circles) single component adsorption isotherms of O_2 and N_2 as a function of pressure at 25 °C for (a-b) pristine PCN-250(Fe)$_{150}$ and (c-d) pristine PCN-250(Fe)$_{240}$ in the pressure range of 0.1 to 1 bar.

B.5 Q_{st} Fittings

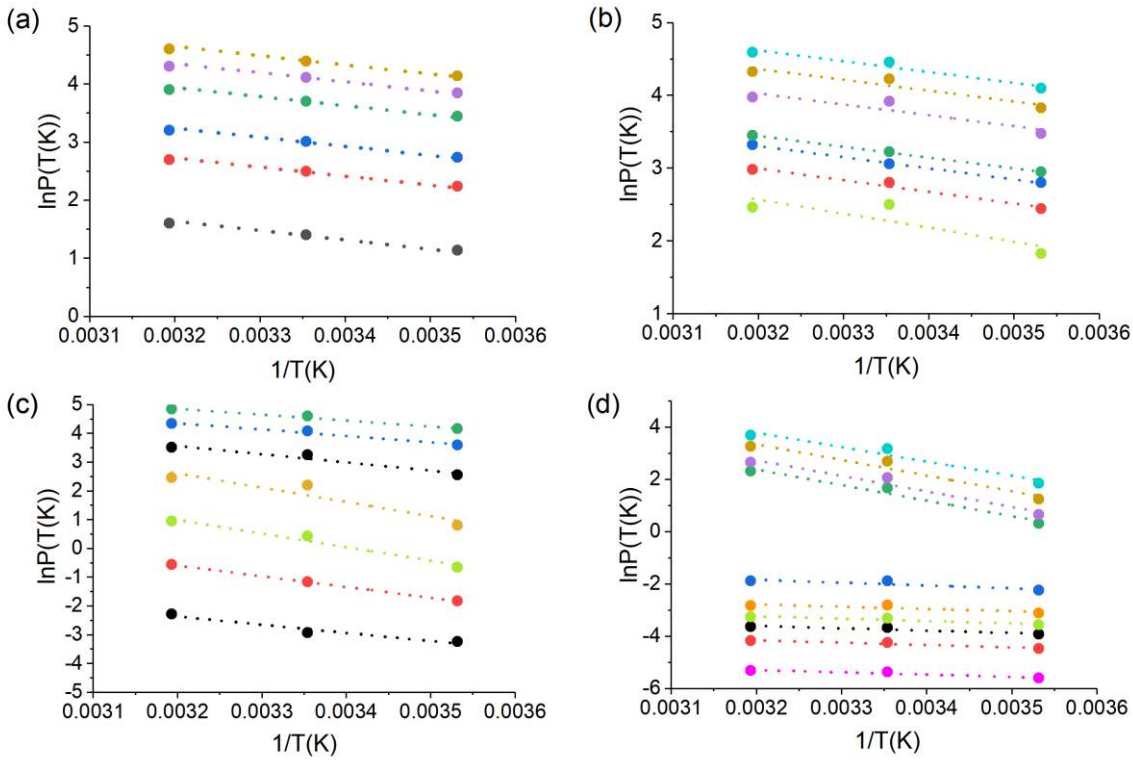

Figure B.5.1. LnP(T(K)) vs 1/T(K) linear fittings of ΔH_{ads} calculations for O_2 gas sorption of (a) pristine PCN-250(Fe)$_{150}$ (between 0.001-0.2 mmol O_2 uptake), (b) PCN-250(Fe)$_{240}$ (between 0.001-0.3 mmol O_2 uptake), (c) [$P_{6,6,6,14}$][DCA]/PCN-250(Fe)$_{150}$ (between 0.001-0.2 mmol O_2 uptake), and (d) [$P_{6,6,6,14}$][DCA]/PCN-250(Fe)$_{240}$ (between 0.001-0.7 mmol O_2 uptake) obtained from Clausius-Clapeyron equation.

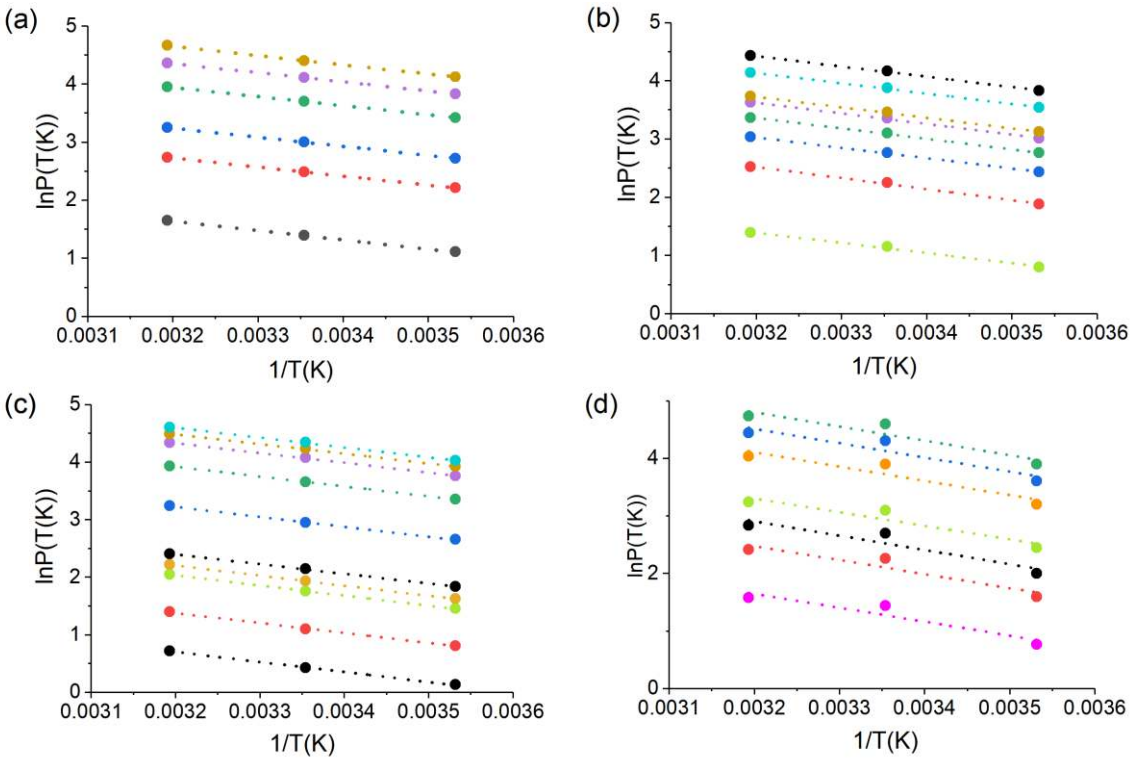

Figure B.5.1. LnP(T(K)) vs 1/T(K) linear fittings of ΔH_{ads} calculations for N_2 gas sorption of (a) pristine PCN-250(Fe)$_{150}$ (between 0.001-0.2 mmol N_2 uptake), (b) PCN-250(Fe)$_{240}$ (between 0.001-0.25 mmol N_2 uptake), (c) [$P_{6,6,6,14}$][DCA]/PCN-250(Fe)$_{150}$ (between 0.001-0.08 mmol N_2 uptake), and (d) [$P_{6,6,6,14}$][DCA]/PCN-250(Fe)$_{240}$ (between 0.001-0.04 mmol N_2 uptake) obtained from Clausius-Clapeyron equation.

APPENDIX C: Supplementary Information of Chapter 7

C.1 Literature Overview

Table C.1.1. Literature overview of ideal selectivity values of various materials at given total pressures.

Adsorbent Material	Conditions		Ideal Selectivity	
	Pressure (bar)	Temperature (K)	CO_2/CH_4[a]	CO_2/N_2[a]
Carbon-based				
Activated Carbon, Desorex K33 (This work)	**0.001**	**298**	**5.3**	**28.2**
	0.01	**298**	**4.4**	**22.9**
	0.1	**298**	**3.3**	**15.6**
	1	**298**	**2.3**	**7.1**
[b]IL/AC, [BMIM][OAc]$_{35}$/AC (This work)	**0.001**	**298**	**77390.4**	**8853.4**
	0.01	**298**	**9781.8**	**3916.5**
	0.1	**298**	**688.3**	**903.7**
	1	**298**	**54.7**	**74.3**
Reduced Graphene Aerogel, rGA[4]	1	298	3.1	-
IL$_{50}$/rGA[4]	0.01	298	120	-
	0.1	298	8.6	-
	1	298	2.3	-
Porous Carbon, oaC-AO1[313]	1	273	-	24.1
Activated Carbon, RHC-399[254]	1	293	-	26.9
Activated Carbon, WV1050[260]	1	283	8.6	-
Activated Carbon, mAC[255]	1	298	22.7	-
Activated Carbon, K4-60@700-150-5[314]	1	298	-	9.3
Activated Carbon, IPT-AC-2[93]	1	273	-	30
Graphene Aerogel, NGA[252]	1	298	3.8	12
Porous Carbon, a-GDC-2[250]	1	298	1.4	-
Activated Carbon, AC[315]	1	298	1.2	-
Porous Carbon, SA-1-600[316]	1	298	3.1	10.1
Mesoporous Carbon, sOMC[317]	1	298	2.9	10
Graphene, NG7[318]	1	298	2.7	9

Porous Carbon,WAPC[251]	1	298	4.4	8
Porous Carbon, N-WAPC[251]	1	298	2.9	22.3
Activated Carbon, Norit R1 Extra[256]	1	298	1.9	-
Activated Carbon, BPL[256]	1	298	2	-
Activated Carbon, Maxsorb[256]	1	298	2.5	-
Activated Carbon, A10[256]	1	298	2	-
Activated Carbon A[256]	1	298	1.9	-
Porous Carbon, C-N950[319]	1	298	-	4.2
Carbon, CMK-13[320]	1	298	2	-
Activated Carbon, Maxsorb[321]	1	298	2	-
Activated Carbon, Norit[321]	1	298	2	-
Graphene, GrO@Cu-BTC[322]	1	303	2.7	-
Horn-shaped carbon nanotubes[253]	1	298	2.7	8.8
Activated Carbon, Cu(I)-4/AC[323]	1	298	3	12
Activated Carbon, BPL[249]	1	298	2.3	7
N-doped Microporous Carbon, NMC-700[324]	1	273	30	-
Porous carbon, OAC-2[325]	1	298	4.6	26.5
Other Materials				
Zeolite, NaY-MAE[326]	1	298	2.2	-
Zeolite, Zeolite-13X[249]	1	298	4.3	8.5
Zeolite, ZSM-5[248]	1	313	1.6	3.7
[c]MOM, SIFSIX-2-Cu-i[327]	1	298	51	72
[d]MOF, 1-C' [328]	1	296	2	-
MOF, 1-M' [328]	1	296	2	-
MOF, ZnDABCO[329]	1	294	2.5	5.5
Metal Organic Coordination Polymer[330]	1	298	5	-
Silica Molecular Sieve, SBA-14-413K2d[331]	5	298	4.2	9.9
Silica Molecular Sieve, SBA-15[320]	1	298	7	-
Silica, MCM-41[332]	1	298	4	-
Clay, PILC (Al_w)[257]	10	298	4.5	11
Clay, PILC (Zr_w)[257]	10	298	9	25.2
Clay, PILC (Al_B)[257]	10	298	3.3	7.6
Clay, PILC (Zr_B)[257]	10	298	4.2	6.1
MOF, HNUST-3[333]	20	298	7.9	26.1
MOF, HNUST-4[334]	1	273	6.3	29.9
MOF, HNUST-5[335]	1	273	7.3	32.5
MOF, HNUST-6[336]	1	273	6.6	30.3
MOF, UiO-66-$(OH)_2$-NO_2[247]	1	298	3.5	-

MOF, UiO-66-NO_2[337]	1	298	8	18
MOF, UiO-66-NH_2[337]	1	298	10	18
MOF, UiO-66-Br[337]	1	298	10	18
MOF, UiO-66[337]	1	298	8.5	20
MOF, ZIF-8[85]	1	298	2.7	7.5
IL/MOF, [BMIM][PF_6]$_{24}$/ZIF-8[85]	1	298	5.1	13.2
IL/MOF, [BMIM][BF_4]$_{28}$/ZIF-8[12]	1	298	3.5	11.6
MOF, CuBTC[5]	1	298	5.6	15.8
IL/MOF, [BMIM][BF_4]$_{30}$/CuBTC[5]	1	298	3.6	11.5
IL/MOF, [HEMIM][DCA]/ZIF-8[2]	1	298	11	-
IL/MOF, [BMIM][PF_6]/MIL-53(Al)[338]	1	298	8.6	24.2
IL/MOF, [BMIM][$MeSO_4$]/MIL-53(Al)[13]	1	298	8	24
IL/MOF, [BMIM][SCN]/ZIF-8[191]	1	298	5.2	11.5
IL/MOF, [BMIM][OAc]/ZIF-8[86]	1	323	-	30
IL/MOF, [EMIM][OAc]/ZIF-8[86]	1	323	-	22
Ni-BDP-CHO[339]	1	293	3.3	14.5
Ni-BDP-CN[339]	1	293	3.6	12.3
Ni-BDP-COOH[339]	1	293	3.6	15.7
NH_2-MIL-53(Al)[340]	30	283	3.3	12.5
PI-UiO/GO-1[341]	30	298	-	64.7

C.2 Carbon Surface Functionality Analysis

Surface functionality of pristine AC was investigated by using Boehm titration method as described in the experimental procedure section. Investigated surface acidic groups are presented in **Figure C.2.1**. The amount of NaOH titrant to reach endpoint (pH=7) was found from obtained titration curves for all three reaction bases and given in **Figure C.2.2**. Moles of oxygen-containing functional groups were calculated by using equations (4), (5), (6), (7), and (8) as given in Chapter 3 and reported in **Table C.2.1** and **Figure C.2.3** consistent with reported values in literature.[342, 343]

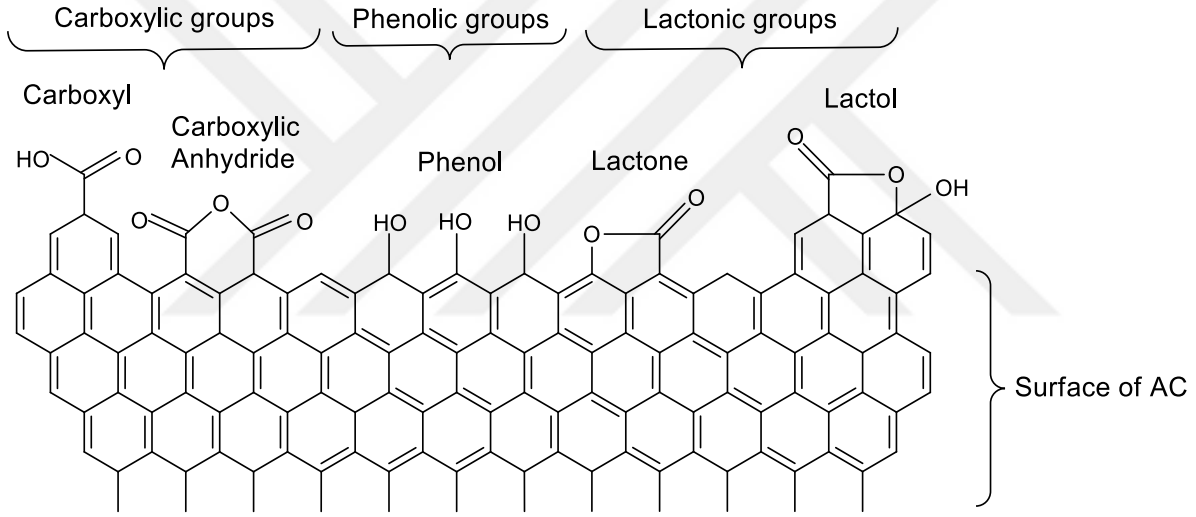

Figure C.2.1. Representation of oxygen-containing acidic surface functional groups of AC.

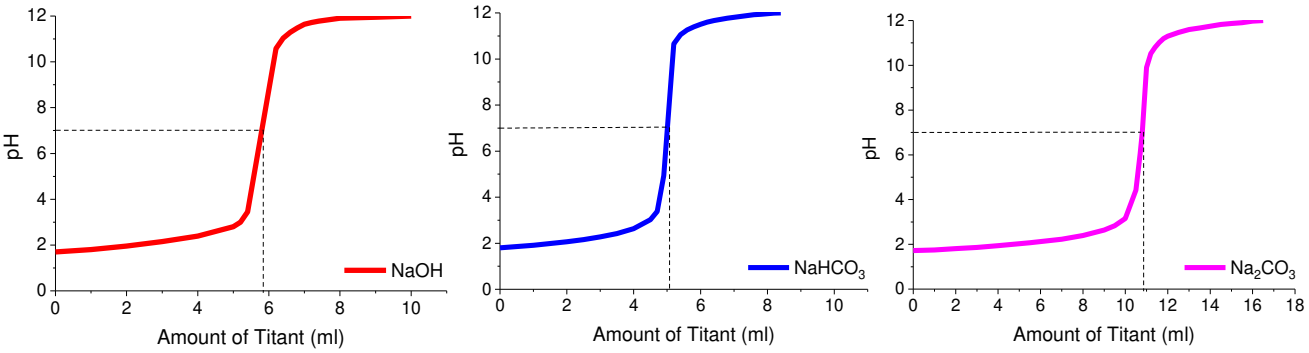

Figure C.2.2. Titration curves obtained from Boehm titration method using reaction bases, NaOH, $NaHCO_3$, and Na_2CO_3.

Table C.2.1. Mole of carbon surface functionality per gram

	n_{csf}(NaOH) (µmol/g)	n_{csf}(Na_2CO_3) (µmol/g)	n_{csf}($NaHCO_3$) (µmol/g)
Pristine AC	485±24	325±16	145±15

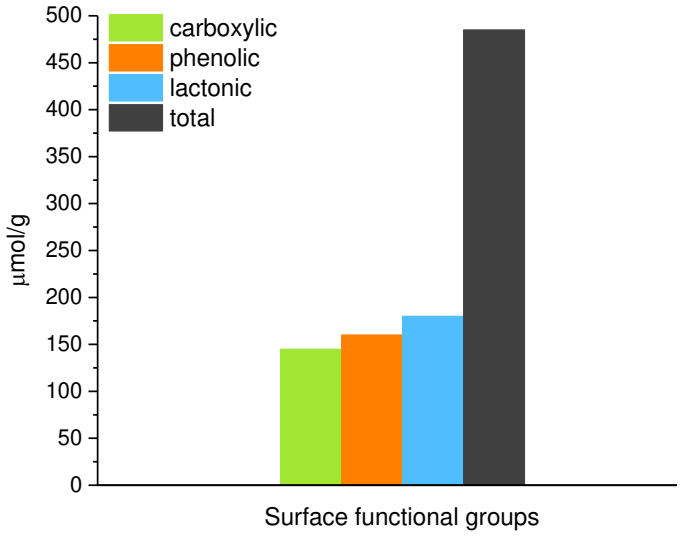

Figure C.2.3. Calculated moles of oxygen-containing surface acidic functional groups of pristine AC.

C.3 BET Surface Area and Pore Size Analysis

BET analysis was conducted for pristine AC and IL/AC composites in order to understand the change in the surface area and pore volume upon IL impregnation. However, BET analysis can be quantitatively misleading in terms of providing reliable data for the composites with IL coating because solubility of N_2 in bulk IL plays an important role for BET analysis of IL/AC composites. Hence, N_2 solubility of bulk [BMIM][OAc] was calculated using COSMO-RS calculations as given in **Figure C.3.1(a)**. COSMO-RS calculations were used to approximate CH_4, CO_2, and N_2 gas solubilities in bulk [BMIM][OAc], and data illustrated that the solubility of CO_2 gas in bulk IL is higher than that of CH_4 and N_2. Due to low N_2 solubility of [BMIM][OAc], which plugs the pores of AC, BET is not sufficient to determine precise surface areas and pore volumes of prepared IL/AC composites, however, successful incorporation of IL can be validated with obtained results.[145]

Pore size distribution of pristine AC was reported in terms of cumulative pore size vs pore width rather than calculated differential values with the aim of analyzing the real data obtained from BET analysis compared to the that of calculated differential values.[344] According to the pore size distribution of pristine AC given in **Figure C.3.1(b)**, it was expected to observe IL molecules inside the pores due to mesoporous nature of AC, 20 Å, compared to the small molecular size of [BMIM][OAc]. However, due to IL layer formation on the surface after 20 wt.% IL loading and low solubility of used BET analysis gas (N_2) in bulk [BMIM][OAc], results yielded lower surface area and pore volume values for the composites with 20, 30, and 35 wt.% IL loading as given in **Table C.3.1**.[53, 145] Both chemical and physical evidence for layer formation were discussed detailly in the later sections by providing SEM/EDX images, Raman, FTIR, NMR, and XPS results.

Table C.3.1. BET surface areas and pore volume analysis of pristine AC and IL_x/AC composites where x represents loading.

Sample	S_{BET} (m^2/g)	V_{pore} (cm^3/g)
Pristine AC	581.1	0.1909
IL_5/AC	358.7	0.1175
IL_{10}/AC	120.1	0.036049
IL_{20}/AC	0.4	0.000785
IL_{30}/AC	0.3	0.000571
IL_{35}/AC	0.1	0.000178

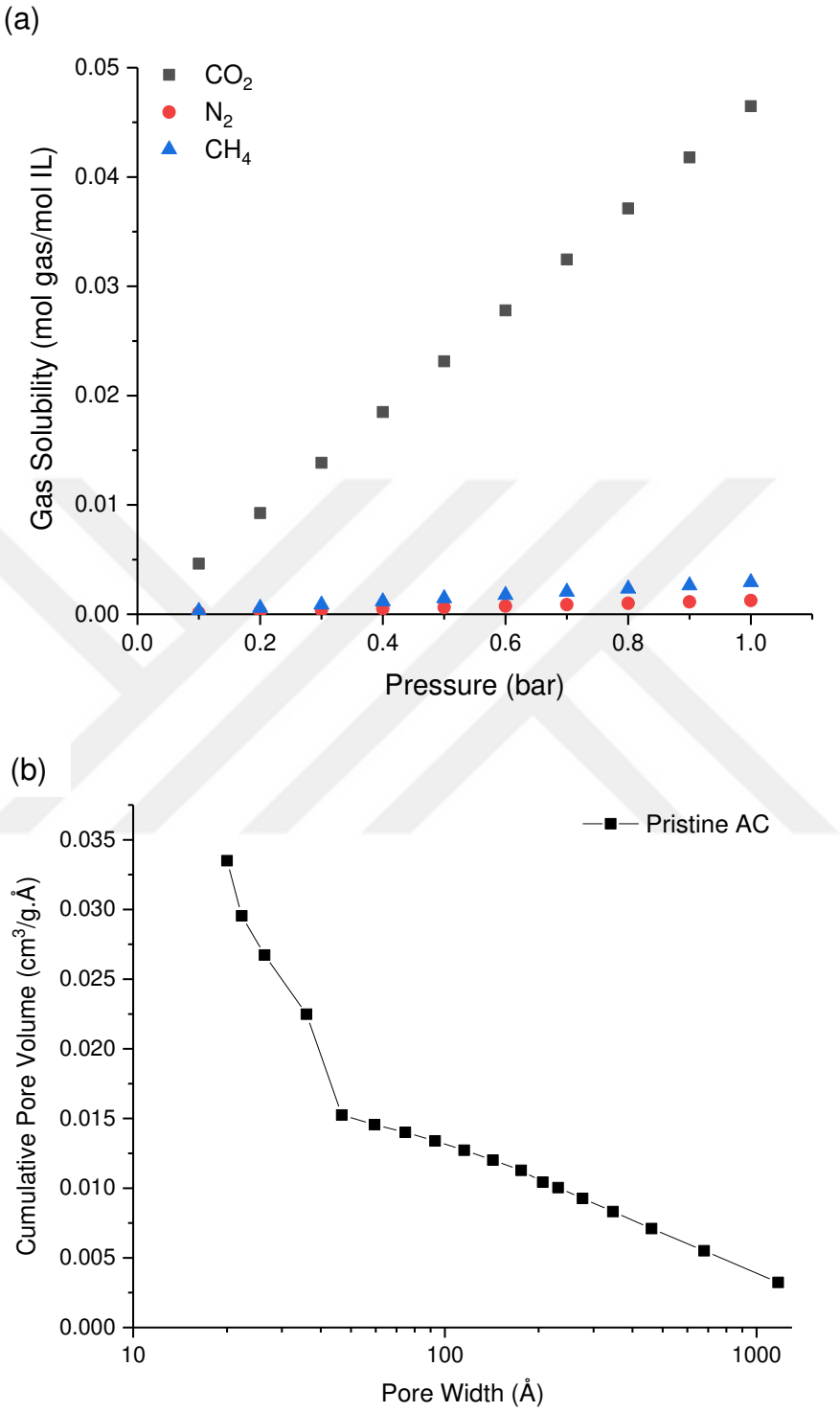

Figure C.3.1. (a) The gas solubilities of CH_4, CO_2, and N_2 in bulk [BMIM][OAc] obtained by using COSMO-RS calculations. (b) Cumulative volume vs pore width of pristine AC.

C.4 SEM Images and EDX Mapping Analysis

SEM images of IL_5/AC, IL_{20}/AC, and IL_{30}/AC were given below in **Figure C.4.1**. Complementary EDX mapping of all materials was done to show successful impregnation of IL on the surface of the pristine AC as shown in **Figure C.4.2**. Data illustrated data IL, [BMIM][OAc], was successfully impregnated to the pristine AC.

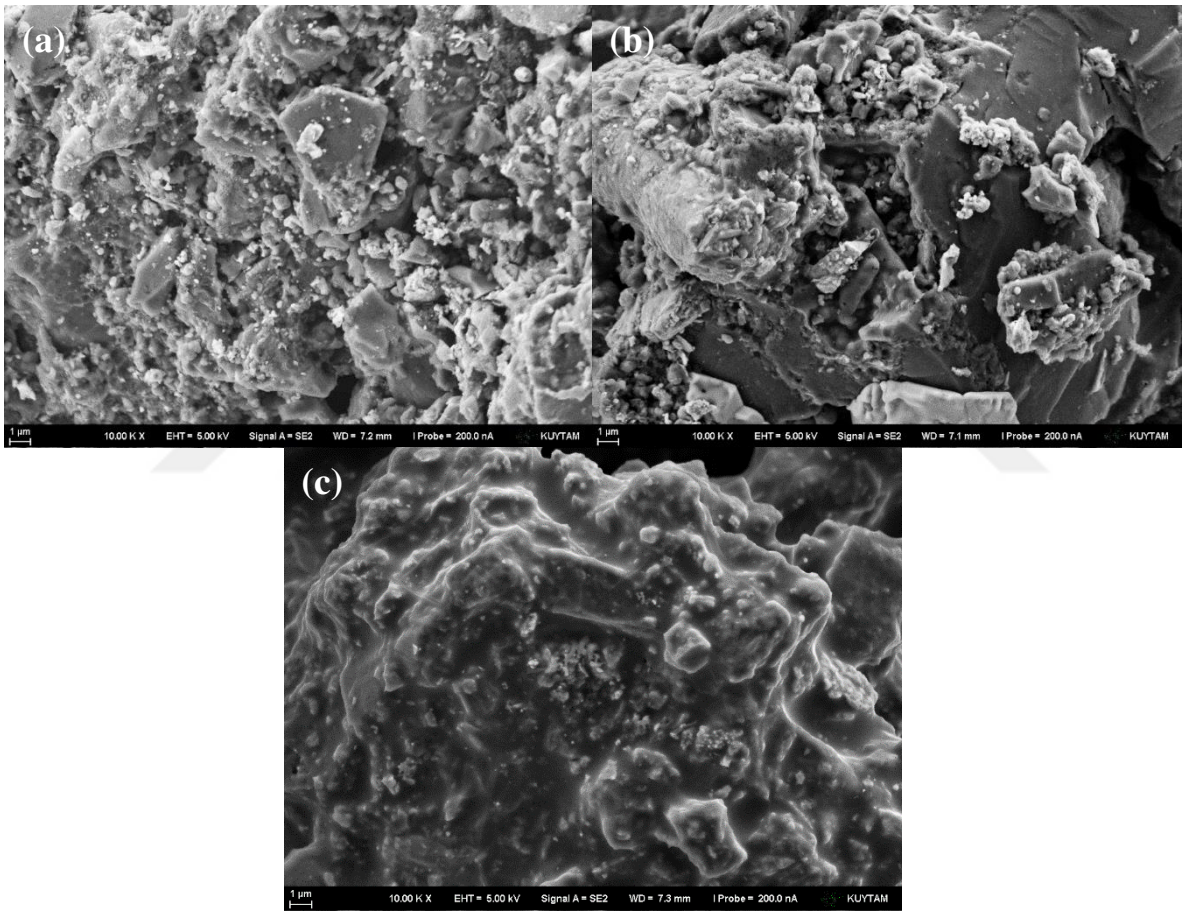

Figure C.4.1. Complementary SEM images of (a) IL_5/AC, (b) IL_{10}/AC, and (c) IL_{30}/AC at 10 k× magnification.

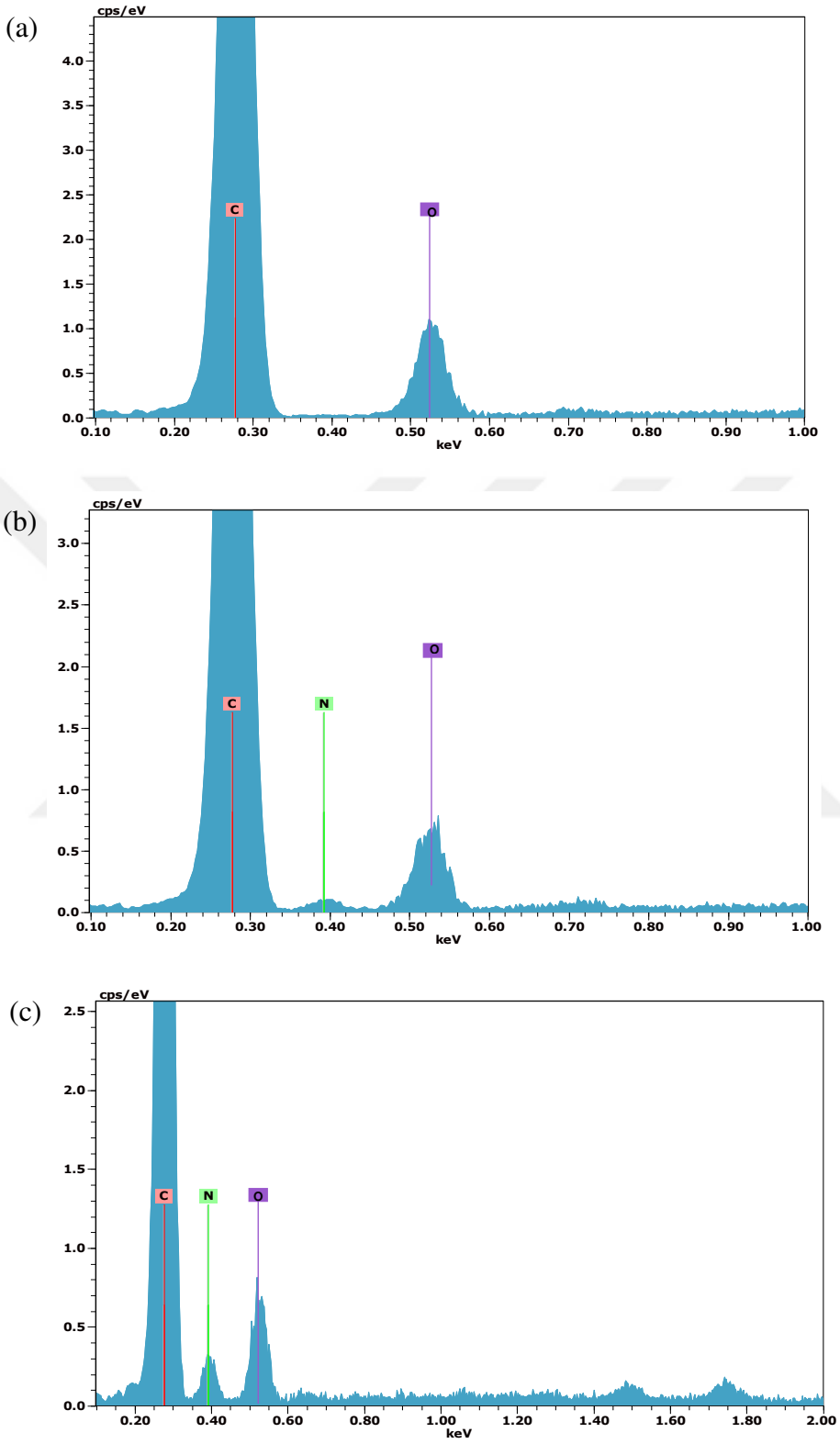

Figure C.4.2. EDX mapping results of (a) pristine AC, (b) IL_{10}/AC, and (c) IL_{35}/AC showing carbon, nitrogen, and oxygen atoms.

C.5 XRD Analysis

Crystal structure of pristine AC and IL/AC composites were analyzed by using obtained XRD spectra given in **Figure C.5.1**. Two broad peaks were detected in the XRD spectra of pristine AC and IL impregnated composites. These broad peaks located at approximately 2θ = 24° and 2θ = 43° designated as (002) and (004), respectively.[285, 345, 346] Data illustrated no significant change in the peak locations of both peaks upon IL impregnation as presented in **Figure C.5.2**. Obtained peaks were deconvoluted in **Figure C.5.3** and crystallite lateral size (L_a) and lateral height (L_c) were calculated by using Scherrer Equation.[99] Parameters for calculation were obtained from used XRD method, λ, and peak deconvolution, β and θ. For the calculation of L_a, Scherrer constant, k_a, was taken as 0.9 and (002) diffraction peak was used, whereas for L_c, Scherrer constant, k_c, was taken as 1.84 and (004) diffraction peak was used.[99, 347, 348] Full width half maximum (FWHM) and θ of both diffraction peaks were found from deconvolution as given in **Table C.5.1** and changed to radian unit before the calculations. Lateral size and lateral height results were summarized in **Table C.5.1**. Increases in both lateral size and lateral height were observed upon IL impregnation and can be interpreted as the IL molecules present on the surface of AC.

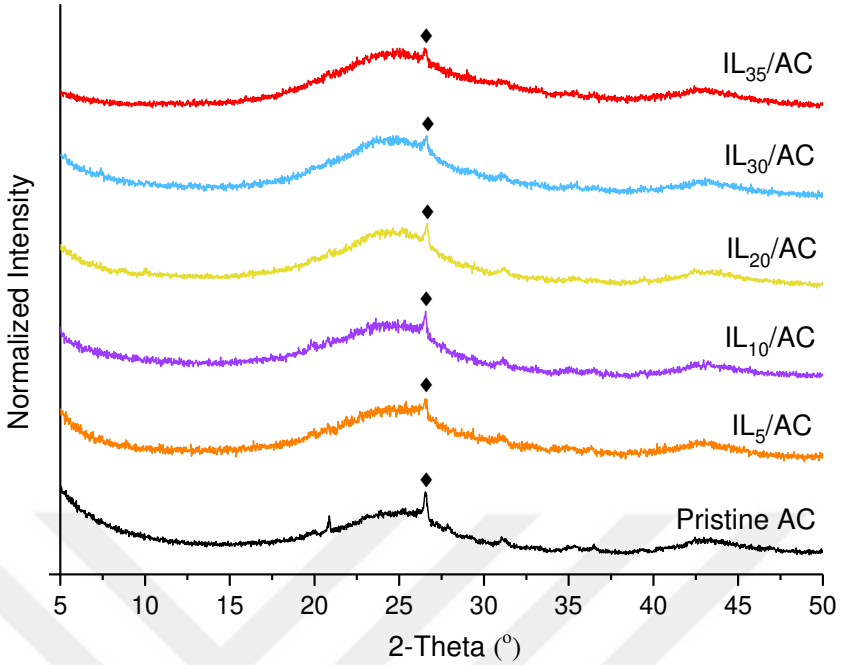

Figure C.5.1. XRD patterns of pristine AC and IL/AC composites with 5, 10, 20, 30, and 35 wt.% IL loadings.

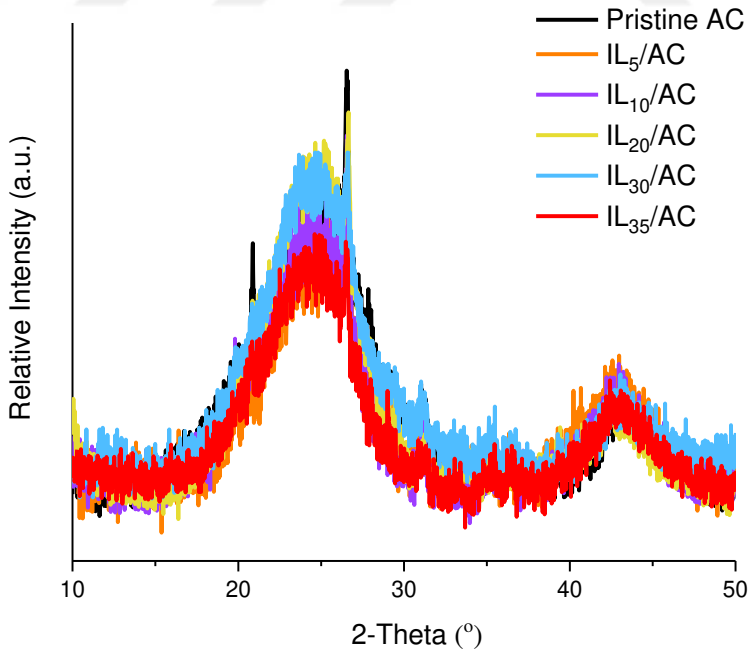

Figure C.5.2. (002) and (004) XRD peaks of pristine AC and IL/AC composites with 5, 10, 20, 30, and 35 wt.% IL loadings.

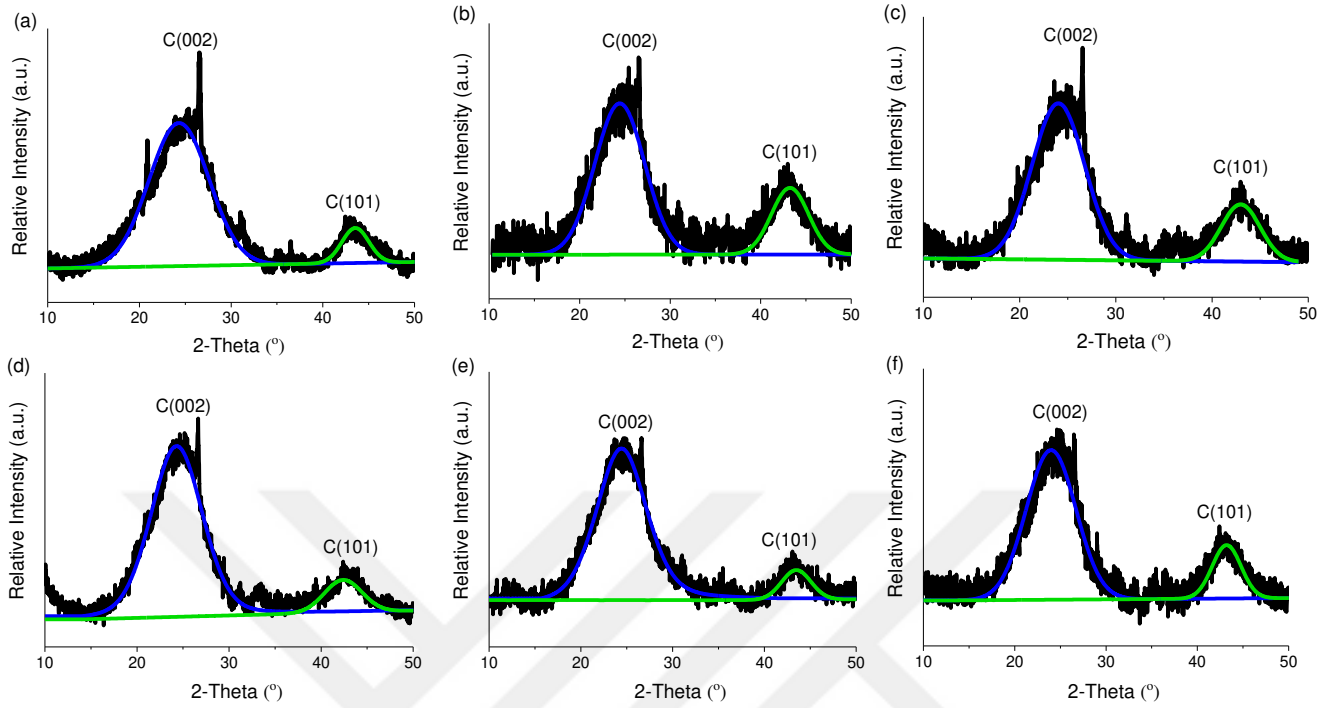

Figure C.5.3. XRD peak deconvolution of (a) pristine AC, (b) IL_5/AC, (c) IL_{10}/AC, (d) IL_{20}/AC, (e) IL_{30}/AC, and (f) IL_{35}/AC.

Table C.5.1. Calculated values of crystallite lateral size, lateral height, and d spacing with related parameters obtained from XRD peak deconvolution for pristine AC and IL/AC composites with 5, 10, 20, 30 and 35 wt.% IL loadings.

Sample	FWHM(202)	FWHM(101)	2θ(202) (°)	2θ(101) (°)	Lc (nm)	La (nm)	d(002) (nm)	d(101) (nm)
Pristine AC	7.7	3.4	24.3	43.5	1.05	5.05	0.36	0.21
IL_5/AC	6.5	4.8	24.6	43.5	1.24	3.62	0.36	0.21
IL_{10}/AC	6.5	4.8	24.0	43	1.25	3.66	0.36	0.21
IL_{20}/AC	6.4	4.6	24.3	43.1	1.26	3.75	0.36	0.21
IL_{30}/AC	6.4	3.7	24.4	43.4	1.27	4.66	0.36	0.21
IL_{35}/AC	6.3	3.7	24.6	43.2	1.28	4.70	0.36	0.21

C.6 Raman Analysis

Raman analysis was conducted for pristine AC and IL impregnated composites and corresponding Raman spectra of each sample can be found in **Figure C.6.1**. Raman peak deconvolution of the samples were done according to the defined deconvolution peaks for carbon-based materials.[285, 349-352] Location designation of the peaks and their related meanings can be found in **Table C.6.1**. Raman band of each sample deconvoluted into five different bands. Gaussian, Lorentzian, Pseudo-Voigt, and Breit-Wigner-Fano functions are commonly used as fitting curve functions for carbon-based materials; however, there is no well-established decision on a specific curve type in the literature. In this study, beside D3 band, which is Gaussian, all bands have the line shape of Lorentzian curve due to obtained lowest goodness-of-fit, χ^2, results. Deconvolution of the Raman bands can be seen in **Figure C.6.2**, and the parameters related with each band were summarized in **Table C.6.2**. Obtained χ^2 values of each optimization, where $\chi^2 = 1$ represents ideal fit and $\chi^2 < 3$ represents convergence,[285] can also be found in Table S6. All χ^2 results were in acceptable range of < 3. Moreover, change in structural defects was investigated by calculating I_D/I_G ratio, representing disorder degree of the structure, for each sample. I_D/I_G ratio was calculated by using relative intensities of two main D and G Raman bands from their respective raw data. Moreover, A_D/A_G ratio was calculated by using areas of D and G band which obtained from deconvolution.

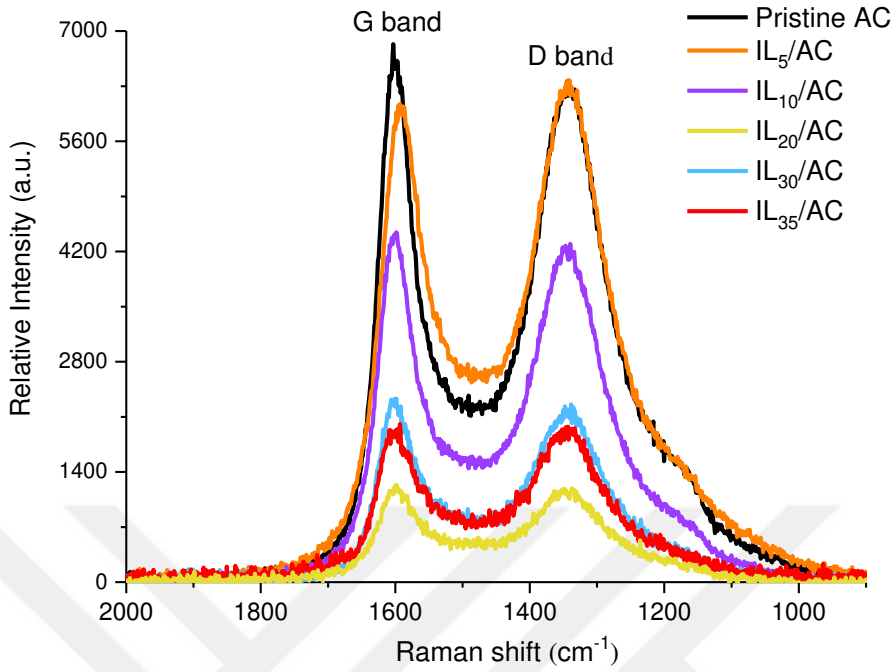

Figure C.6.1. Raman spectra of pristine AC and IL_x/AC composites with 5, 10, 20, 30, and 35 wt.% IL loadings.

Table C.6.1. Deconvoluted Raman bands and their respective vibration modes.

Peak	**Raman shift (cm^{-1})**	**Assignment of vibrational mode**
D (D1)	~1350	Disordered graphitic lattice, graphene layer edges
D2 (D')	~1610	Disordered graphitic lattice, surface graphene layers
D3 (D", A)	~1500	Amorphous carbon
D4 (I, D^*)	~1200	Disordered graphitic lattice, impurities in the graphite lattice
G	~1580	Ideal graphitic lattice order

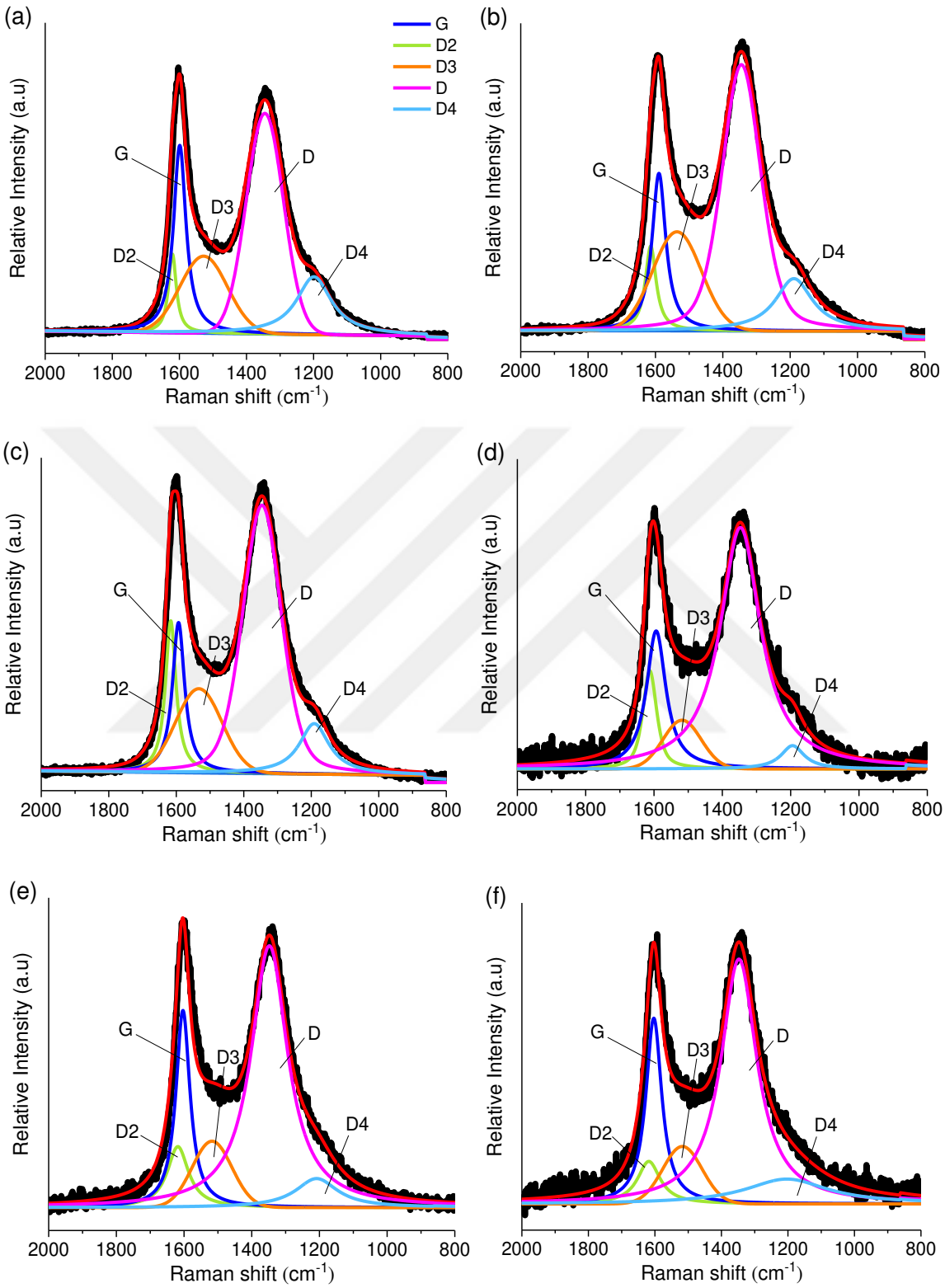

Figure C.6.2. Raman peak deconvolutions of (a) pristine AC, (b) IL_5/AC, (c) IL_{10}/AC, (d) IL_{20}/AC, (e) IL_{30}/AC, and (f) IL_{35}/AC.

Table C.6.2. Related parameters of deconvoluted Raman bands and their respective goodness-of-fit (χ^2) results.

Sample	Peak	Position (cm^{-1})	Area	FWHM	χ^2	I_D/I_G	A_D/A_G
Pristine AC	G	1595	339228.2	44.7			
	D	1341	788530.6	130.6			
	D2	1617	90125.2	28.3	1.7	0.93	2.32
	D3	1524	352013.2	166.9			
	D4	1195	295152.1	126.3			
IL_5/AC	G	1587	266291.7	49.1			
	D	1341	986027.6	136.6			
	D2	1610	114300.9	39.1	1.8	1.03	3.7
	D3	1532	394811.8	170.8			
	D4	1185	241367.4	133.7			
IL_{10}/AC	G	1587	153930.2	43.4			
	D	1342	598446.9	134.9			
	D2	1613	135052.1	37.7	1.7	1.05	3.9
	D3	1529	217368.0	161.6			
	D4	1187	127595.5	107.2			
IL_{20}/AC	G	1590	72108.1	68.7			
	D	1343	262210.5	142.8			
	D2	1609	32620.6	48.3	1.3	0.98	3.63
	D3	1514	33087.1	131.8			
	D4	1190	14565.6	82.2			
IL_{30}/AC	G	1600	134585.0	50.2			
	D	1344	470975.2	131.3			
	D2	1615	63429.6	73.4	1.1	0.96	3.49
	D3	1514	86559.2	140.0			
	D4	1203	57471.3	146.7			
IL_{35}/AC	G	1600	128783.9	57.7			
	D	1344	384353.2	130.8			
	D2	1615	42275.0	82.8	1.1	0.96	2.98
	D3	1514	65452.0	140.0			
	D4	1201	89980.4	301.3			

C.7 TGA Analysis

TGA analysis was conducted to obtain thermal stability limits of the pristine AC and IL/AC composites. Obtained TGA and DTG curves were given in **Figure C.7.1**. By utilizing high thermal stability of pristine AC (above 700 °C), corresponding IL loadings of each composite were calculated from TGA and DTG curves as summarized in **Table C.7.1**. Moreover, T'_{onset} value of each sample was determined to analyze thermal stability of prepared composites. T'_{onset} temperature represents the point where decomposition of the material is initiated, hence, respective to changes in T'_{onset} value, it can be inferred that the thermal stability limits are altering for that material. Determination of T'_{onset} values for each sample was made by making sure of the decomposition temperature of pristine AC which is above 700 °C. Moreover, respective approximate IL loadings were calculated through TGA weight loss by subtracting the moisture/solvent content (weight loss at 120 °C for 9-h) that was coming from impregnation process.

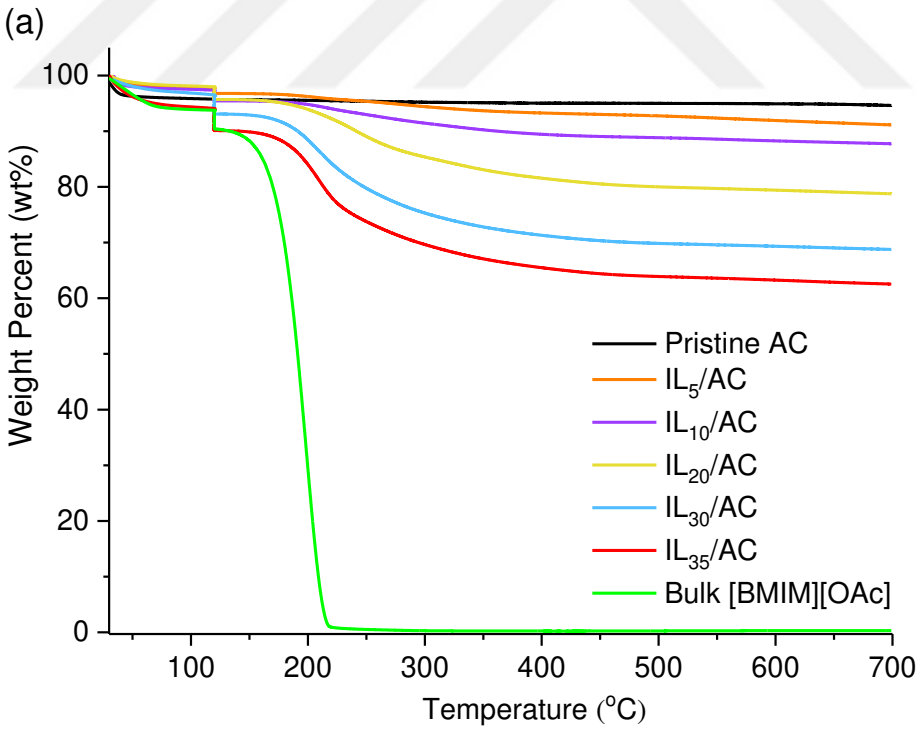

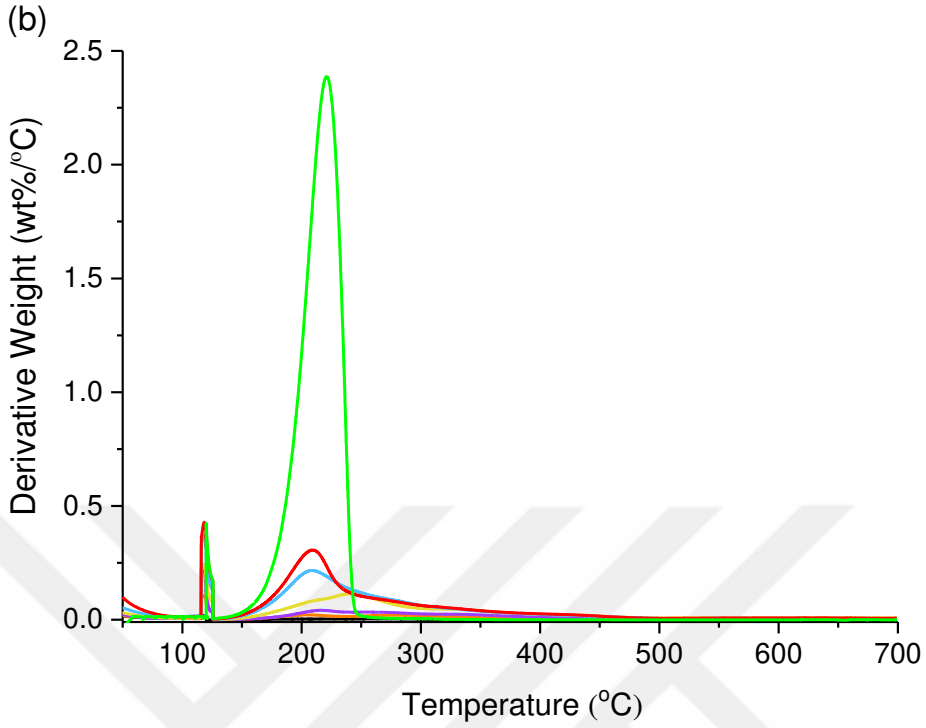

Figure C.7.1. (a) TGA and (b) DTG curves of pristine AC, bulk IL, and IL_x/AC composites with 5, 10, 20, 30, and 35 wt.% IL loading.

Table C.7.1. Derivative onset temperatures (T'_{onset}) and % weight loss at 700 °C of pristine AC, bulk [BMIM][OAc], and IL_x/AC composites with 5, 10, 20, 30, and 35 wt.% IL loading.

Sample	**T'_{onset} (°C)**	**Weight loss at 700 °C (wt.%)**	**Calculated approximate IL loading (wt.%)**
Bulk [BMIM][OAc]	184 ± 3	0.3	-
Pristine AC	> 700	96.6	-
IL_5/AC	162 ± 3	91.4	4.2
IL_{10}/AC	165 ± 3	87.2	9.3
IL_{20}/AC	166 ± 3	76.9	18.7
IL_{30}/AC	176 ± 3	65.8	30.8
IL_{35}/AC	179 ± 3	61.7	34.5

C.8 FTIR Analysis of IL/AC Composites

Interactions between AC and IL molecules were investigated by using FTIR analysis. As it can be seen in **Figure C.8.1(a)**, the FTIR spectra of 5, 10, and 20 wt.% IL-loaded composites resembled the FTIR spectra of pristine AC and an opposite trend was valid for 30 wt.% and 35 wt.% IL-loaded composites, where their FTIR spectra were similar to that of bulk IL, [BMIM][OAc]. This change in the FTIR spectra can be interpreted as an indication of the IL layer formation on the surface of AC with increasing loading. It is proposed that IL loadings exceeding 20 wt.%, IL molecules form layers covering the surface of AC and these layers act like bulk IL. Hence, a detailed FTIR investigation regarding their interactions was conducted to verify the proposed structure. To understand the transition from first layer to bilayers, one extra data set of IL/AC composite which contains 25 wt.% IL was prepared and added for FTIR analysis. For that sample, IL content was calculated approximately as 24.5 according to TGA results as same as other samples. FTIR spectra of this sample was used to obtain higher accuracy in the investigation by adding another point between 20 and 30 wt.% and to see the transition.

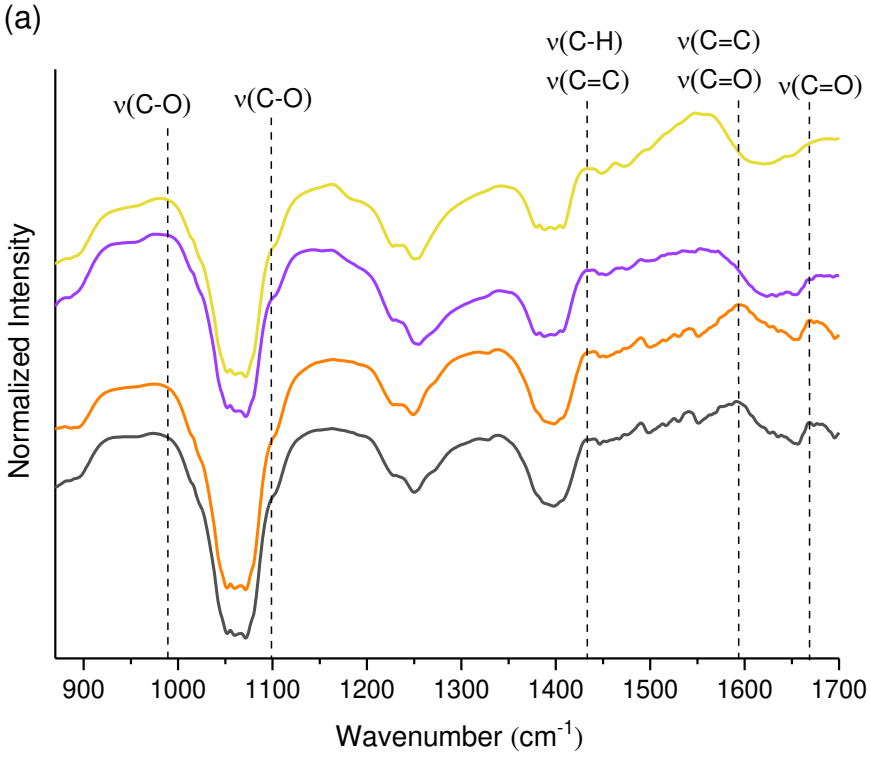

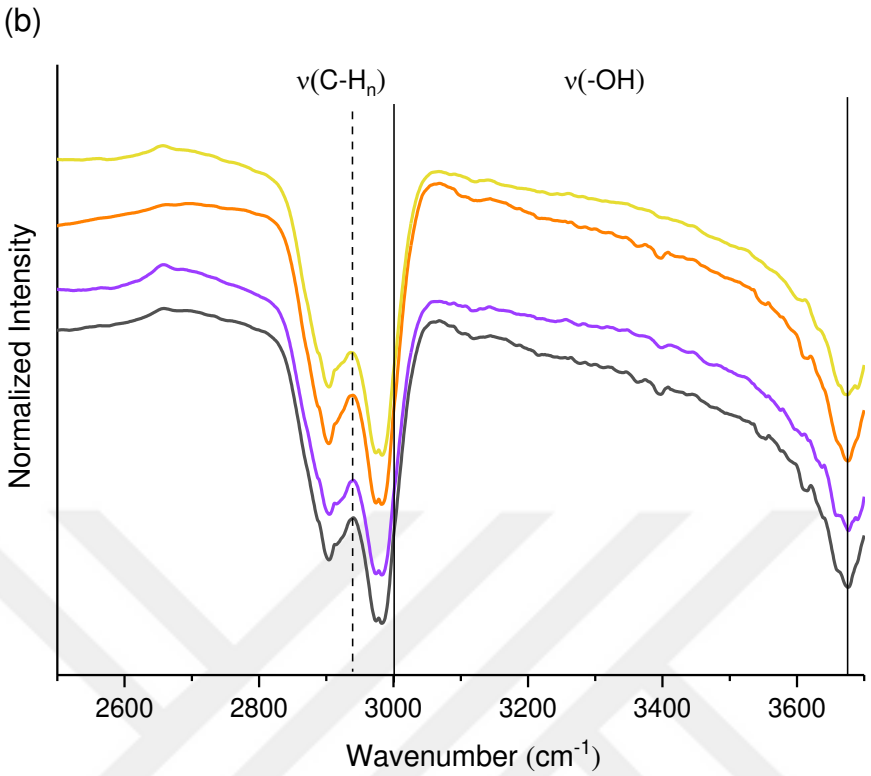

Figure C.8.1. (a) FTIR peak shifts of pristine AC and IL/AC composites with 5, 10, and 20 wt.% IL loading between the region 1700-800 cm^{-1} (b) FTIR peak shifts of pristine AC and IL/AC composites with 5, 10, and 20 wt.% IL loading between the region 3700-2500 cm^{-1}.

In the spectrum of the samples with 5, 10, and 20 wt.% IL loading, characteristic peaks of pristine AC were identified as ν(–OH), ν(C–H_n), ν(C=O), ν(C=C), ν(C–H), and ν(C–O), respectively, at approximately 3600-3500, 2938, 1667, 1586, 1440, and 1150-990 cm^{-1} as given in **Figure C.8.1** and summarized in **Table C.8.1**. [353-356] In the IR spectra of pristine AC, a significant red shift was observed for ν(C=C) band, located at 1586 and 1440 cm^{-1} with increasing IL loading, while blue-shifts were observed for the characteristic peaks of ν(C–H_n), ν(C=O), and ν(C–O) which are near the spectral resolution. Based on the obtained peak shifts, it can be inferred that the surface of AC interacting with IL molecules through carbon skeleton, possibly via π–interactions.[286, 287, 357, 358] Having a relatively small amount of oxygen containing surface functional groups (485 µmol for pristine AC) provides higher density of free π-electrons for π–interactions.[288, 359] Therefore, a red-shift in the energy of C=C bond can be expected due to the sharing of free π-electrons. The π–interactions are highly common between the compounds with heterocyclic ring and carbon-based materials, such as CNT, AC, and

graphene.[287, 360, 361] To create π–interactions, there are two possible alignments of IL's cation with the surface of AC as given in **Figure C.8.2**. Cation of the IL can be aligned face-to-face by forming cation-π interactions through its heterocyclic ring or it can be aligned vertical-to-face by forming CH–π interactions through its C2 hydrogen atom.

Table C.8.1. Characteristic FTIR peak assignment of pristine AC and corresponding peak shifts of IL/AC composites with respect to pristine AC.

Characteristic Peaks of Pristine AC		Corresponding Peak Shifts on IL/AC Composites					
Peak Assignment	Location (cm^{-1})	IL_5/AC	IL_{10}/AC	IL_{20}/AC	IL_{25}/AC	IL_{30}/AC	IL_{35}/AC
ν(–OH)	3600	-5	-4	-4	n.d.	n.d.	n.d.
ν(C–H_n)	2938	3	3	2	n.d.	n.d.	n.d.
ν(C=O)	1667	2	3	3	n.d.	n.d.	n.d.
ν(C–C)	1500	-2	-2	-3	n.d.	n.d.	n.d.
ν(C=C)	1440	-2	-2	-4	n.d.	n.d.	n.d.
ν(C–O)	1084-1056	4	5	4	n.d.	n.d.	n.d.

n.d. = not detected.

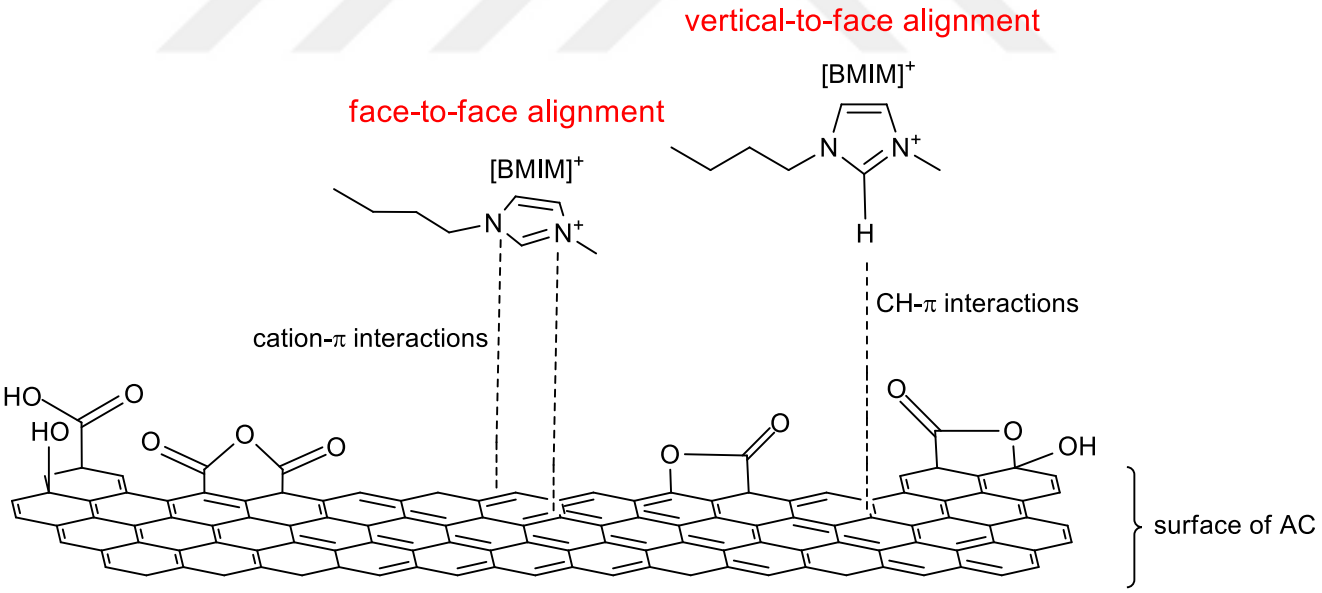

Figure C.8.2. Possible π–interaction mechanisms between the $[BMIM]^+$ cation and surface of AC.

To analyze intermolecular interactions of 30 and 35 wt.% IL loaded composites, characteristic peaks of IL were investigated and transition from 20 wt.% IL loading to 30 wt.% IL loading was analyzed by adding 25 wt.% IL loaded composite, IL_{20}/AC. Change in peak positions of 25, 30, and 35 wt.% IL loaded composites with respect to bulk IL and corresponding shift amounts can be seen in **Figure 7.3(b-c)** and summarized in **Table C.8.2**. During the analysis, the changes in these interactions were investigated to understand the newly formed interaction mechanism between IL and AC. In the case of bulk [BMIM][OAc], cation and anion interact via electrostatic interactions and hydrogen bonding between the hydrogen atom of cation located at C2 and oxygen of acetate anion as illustrated in **Figure C.8.3**.

Table C.8.2. Characteristic FTIR peak assignment of bulk [BMIM][OAc] and corresponding peak shifts of IL/AC composites with respect to bulk [BMIM][OAc].

Characteristic Peaks of bulk [BMIM][OAc]		Corresponding Peak Shifts on IL/AC Composites					
Peak Assignment	Location (cm^{-1})	IL_5/AC	IL_{10}/AC	IL_{20}/AC	IL_{25}/AC	IL_{30}/AC	IL_{35}/AC
ν(—OH)	3375	n.d.	n.d.	n.d.	-20	-6	-3
ν(C4—C5H)	3146	n.d.	n.d.	n.d.	-6	0	0
ν(C2H)	3089	n.d.	n.d.	n.d.	-19	2	2
$\nu(N-CH_3)_{sym}$	3030	n.d.	n.d.	n.d.	0	0	0
$\nu(N-CH_3)_{asym}$	2995	n.d.	n.d.	n.d.	0	0	0
ν(C=O) (anion)	1561	n.d.	n.d.	n.d.	-4	-2	-2
ν(C—O) (anion)	1389	n.d.	n.d.	n.d.	-4	2	2
ν(C=C)	1333	n.d.	n.d.	n.d.	4	2	2
ν(C—N)	1171	n.d.	n.d.	n.d.	-4	-2	-2
ν(C—O)	1009	n.d.	n.d.	n.d.	-16	0	0

n.d. = not detected.
sym = symmetrical stretching
asym = asymmetrical stretching

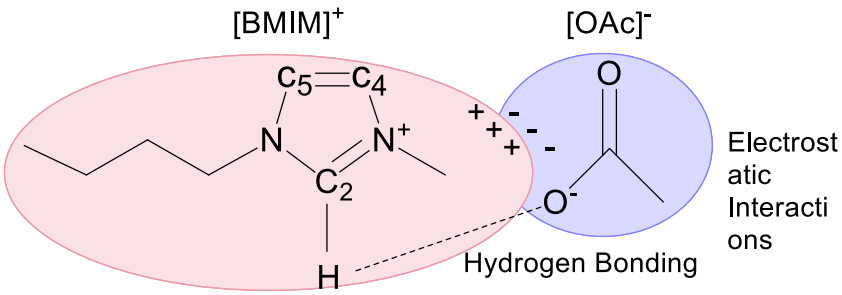

Figure C.8.3. Intermolecular interactions of bulk [BMIM][OAc].

To understand the nature of the alignment, characteristic FTIR peaks of cation, ν(C4–C5H), ν(C2H), ν(N–CH_3)$_{sym}$, ν(N–CH_3)$_{asym}$, butyl ν(C1H)$_{sym}$/ν(C2H)$_{asym}$, ring ν(CH_3)$_{sym}$, ν(C=C)/alkyl chain, ν(C–N), ν(C–O), and δ(C–H) located at 3146, 3089, 3030, 2995, 2961, 2935, 1333, 1171, 1009, and 910 cm^{-1} were investigated.[86, 362] For this investigation, FTIR spectra of 25, 30, and 35 wt.% IL-loaded composites were considered. A dramatic shift was observed in the case of ν(C2H), while heterocyclic ring related other peaks did not show a comparable amount of change in their peak positions as tabulated in **Table C.8.2**. Therefore, the presence of cation–π interactions was ruled out due to the lack of change in the IR spectra of imidazolium ring related peaks, which should be observed in the case of this type of interactions. In the case of cation–π interactions, electrons are shifted to the electron deficient imidazolium ring of cation, which significantly affect the characteristic ring peaks, such as ring ν(CH_3)$_{sym}$ and ν(C–N).[290, 363] However, we only observed slight red-shifts for these bonds, indicating the change in the electrostatic environment of the cation, which cannot be given as evidence for a direct interaction between the IL's cation and the surface of AC. Moreover, a possible cation–π interaction mechanism via charge transfer will induce a significant change in the Raman spectra.[364] However, we did not observe any significant peak shifts or shape changes in the Raman spectra of the composites compared to that of pristine AC, which further demonstrates the conservation of electrostatic structure of the surface up to 20 wt.% IL loading.[290, 363] Therefore, dramatic red-shift of (C2H) can be attributed to vertical-to-face alignment of cation with the surface of AC via newly formed CH–π hydrogen bonding interactions. Moreover, the bending vibration of heterocyclic C–H bond located at 910 cm^{-1} weakened in the case of 25 wt.%, which also supports the proposed interaction mechanism.[290] However, red-shift which we observed in the characteristic peak of ν(C2H) become a slight blue shift (around the spectral resolution of 2 cm^{-1}) with increasing IL loading, which can be interpreted as a change in the interaction mechanism with increasing IL loading.[289, 365, 366] It can be said that with increasing IL loading, the energy of C2H bond also tends to increase, which demonstrates the formation of a state similar to that of bulk IL. Hence, we infer that this bond becomes available with increasing IL loading due to IL layer formation on the surface of AC.
In the case of anion, characteristic FTIR peaks of carboxylate anion, ν(C=O) and ν(C–O) located at 1561 and 1389 cm^{-1}, were investigated. A similar trend, which was observed for cation, was obtained for anion as well. Red-shifts, which are slightly above the resolution, were observed for both peaks indicating a change in the electrostatic environment of anion as a result

of decreasing hydrogen bonding interactions between anion and cation with newly formed interactions between the cation and the surface of AC. These changes which were slightly above resolution cannot be interpreted as a direct interaction between the anion and the surface of AC. A possible anion–π interaction between acetate anion and the surface of AC should induce more dramatic shifts in the characteristic peaks of anion due to higher electron density of surface π-bonds compared to existing hydrogen bonding between anion and cation. Moreover, with increasing IL loading, ν(C–O) shows a slight blue shift indicating a change in the interionic interactions consistent with our findings for cation. In addition to these, ν(–OH) band located approximately at 3375 cm^{-1} red-shifted upon IL impregnation, however, the observed amount of red-shift decreased with increasing IL loading similar with characteristics peaks of cation and anion. This further indicates a dramatic change in the structure of IL at lower loadings due to the newly formed interactions between $[BMIM]^+$ cation and the surface of AC.

These changes in the interaction mechanism attributed to the layer formation on the surface of AC for IL loadings exceeding 20 wt.% consistent with our first observation of obtained FTIR spectra, where the FTIR spectra of composites with 30 and 35 wt.% IL loading resembles to that of bulk IL. Based on these results, it can be proposed that there are two different interaction layers on the surface of AC.[290, 291, 367] Up to 20 wt.% IL loading, mostly C2H of $[BMIM]^+$ cation interacts with C=C skeleton of AC through CH–π hydrogen bonding creating a vertical alignment of cation on the surface of AC. IL loadings exceeding 20 wt.%, charged surface induces electrostatic interactions between IL molecules and comparably loosely attached IL layer formed on the surface of AC which acts like bulk IL.

C.9 XPS Analysis

XPS analysis was conducted for pristine AC and its composites with IL to further investigate the interaction mechanism. XPS peaks of C1s, N1s, and O1s are deconvoluted into 5, 2, and 3 peaks, respectively. For deconvolution of C1s, peaks located around, 284.8, 285.2, 286, 288.6, and 290 eV defined as C–C/C=C, C–OH, C–O/C–N, C=O, and π–π^* satellite, respectively.[368-372] For deconvolution of N1s, peaks located at approximately 400 and slight below 400 eV defined as N^0 and N^+, respectively.[293, 373-375] Similarly, for deconvolution of O1s, peaks located around 531.5, 532.9, and 533.3 eV defined as C=O, C–O, and C–OH, respectively.[368, 371] Full XP spectra and deconvoluted XP spectra peaks of pristine AC and IL/AC composites were presented in **Figure C.9.1** and **Figure C.9.2**, respectively.

Deconvolution of C1s uncovers that with increasing IL loadings, peak defined as π–π^* satellite shifted to higher energy levels by 3 eV with a shape change from broad to sharp peak. Moreover, its proportion increases dramatically as given in **Table C.9.1** (highlighted as red). These results are interpreted as an indication of the delocalized (π–π^*) electrons in the prepared composites.[292] Moreover, for C–OH peak exists in both C 1s and O 1s peaks, a red-shift to lower energy levels was observed for 5 wt.%, 10 wt.% and 20 wt.% IL loaded IL/AC samples compared to pristine AC. However, for 30 wt.% and 35 wt.%, C–OH peak was blue-shifted to higher energy levels compared to that of 20 wt.%. This can be interpreted as an indication of decreasing hydrogen bonding effect with increasing IL loading consistent with FTIR findings. To investigate the surface interactions of IL, N1s peak was deconvoluted into two separate peaks, representing N^0 and N^+. With increasing IL loading, the peak defined as N^0 convoluted into the main N^+ peak at higher energy levels. For 30 and 35 wt.% IL-loaded samples, only one peak appeared in the XPS spectra. This one peak represents the bulk N1s peak of [BMIM][OAc] and indicates the conformation where cation and anion of IL interacting as in their bulk state.[293, 373] Therefore, we inferred that IL acts as in bulk form on the surface of 30 and 35 wt.% IL-loaded samples, which also proves that there is two different interaction mechanism of IL on the composite. First IL layer, formed until 20 wt.% loading, bonded to surface by altering the intermolecular interactions of its bulk form, however, IL loadings exceeding 20 wt.%, IL molecules were attached to the surface by electrostatic interactions and π–π interactions which enable them to maintain their bulk state. Consequently, it is interpreted that at higher IL loadings (higher than 20 wt.%) the IL molecules interact with the surface of

AC statically (electrostatic interactions) and π–π interactions then create a layer on the surface consistent with the visible coverage of the surface in SEM images.

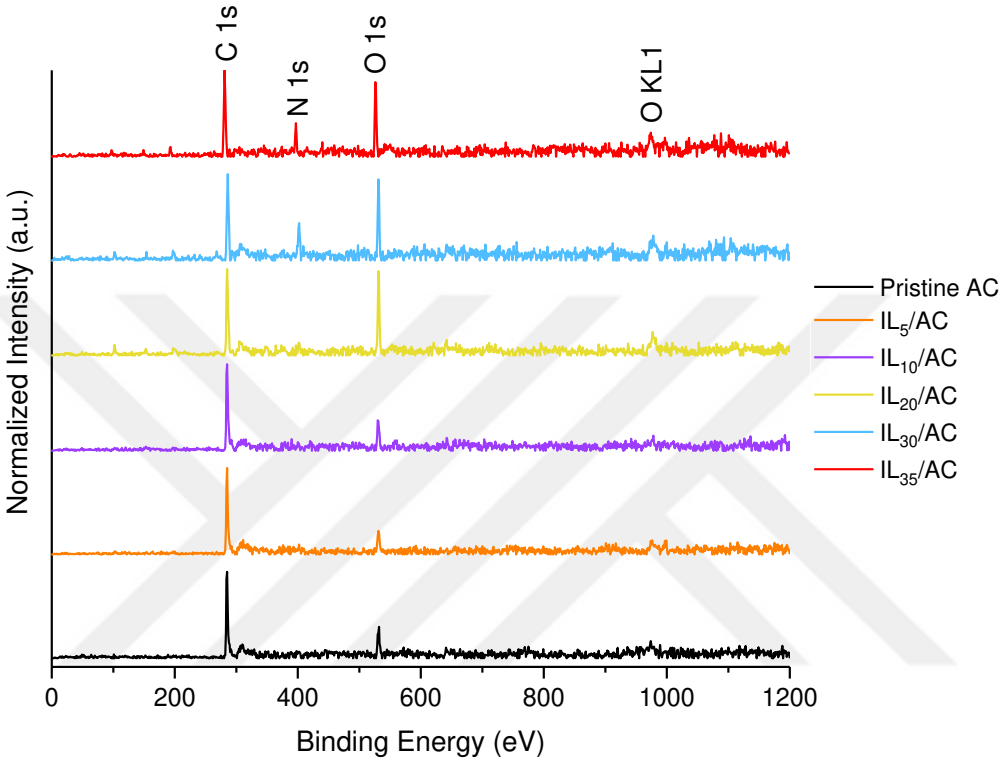

Figure C.9.1. Full XPS spectra of pristine AC and IL/AC composites with 5, 10, 20, 30 and 35 wt.% IL loading.

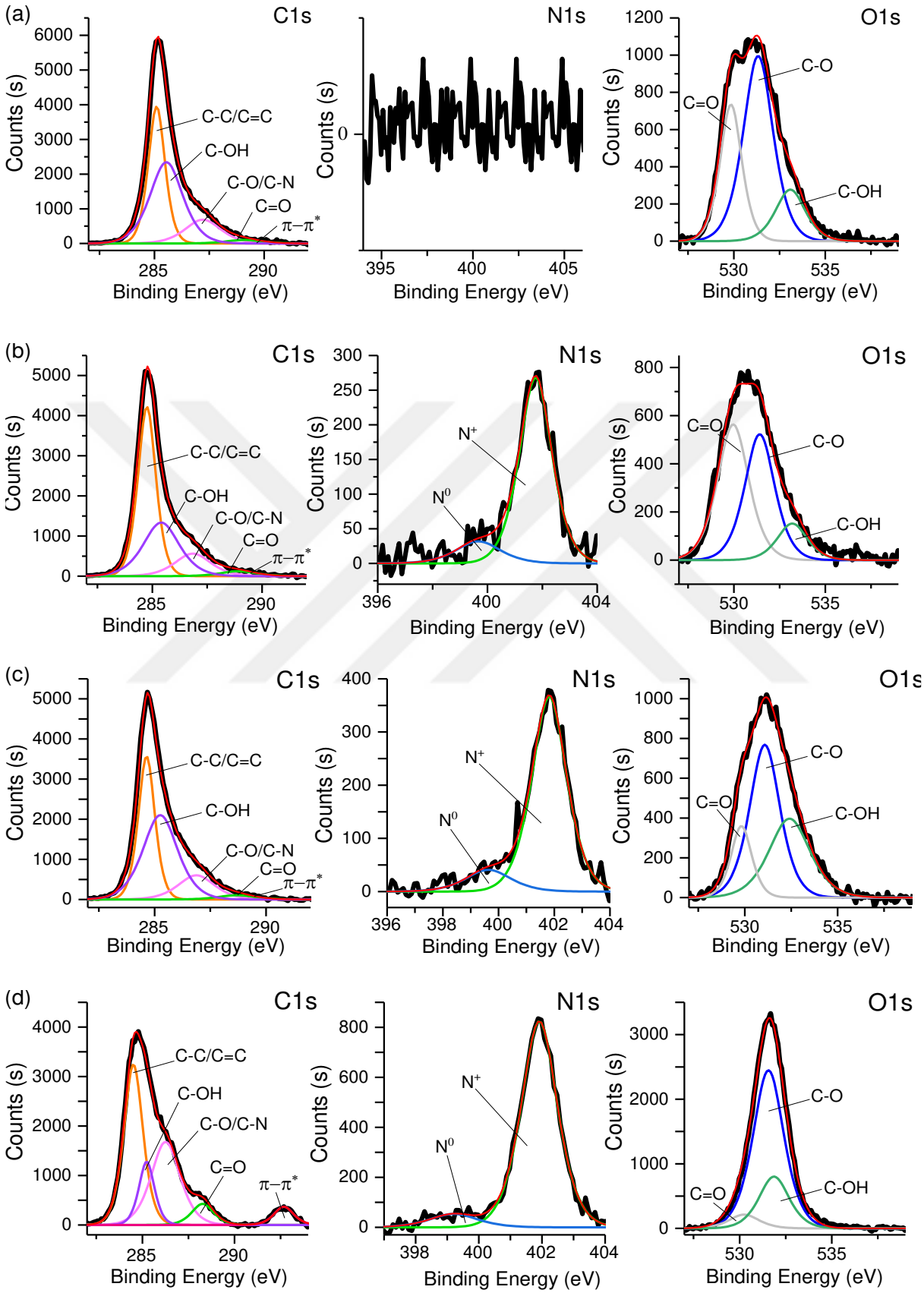
(a)
C1s
N1s
O1s
Counts (s)
Binding Energy (eV)
C-C/C=C
C-OH
C-O/C-N
C=O
π–π*
C-O
C=O
C-OH
(b)
N+
N0
(c)
(d)

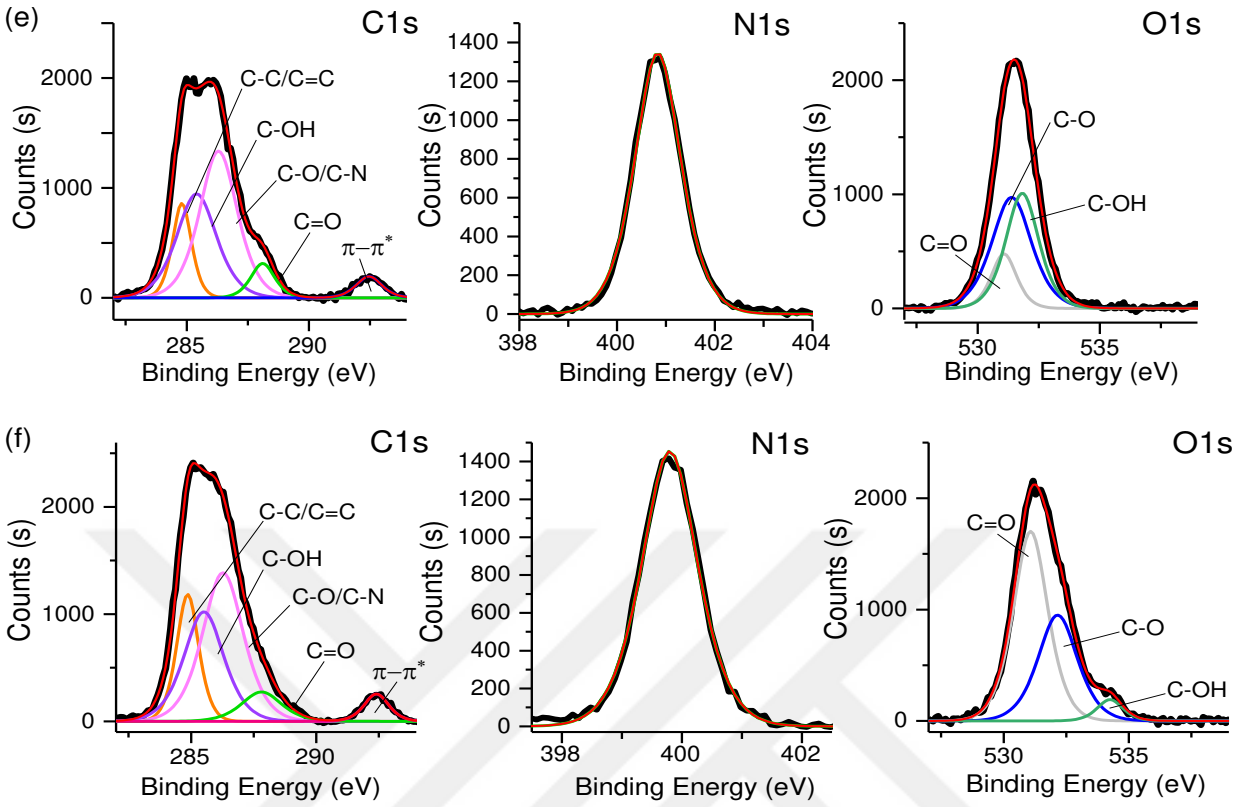

Figure C.9.2. Deconvolution of C1s, N1s and O1s XPS peaks of (a) pristine AC, (b) IL_5/AC, (c) IL_{10}/AC, (d) IL_{20}/AC, (e) IL_{30}/AC, and (f) IL_{35}/AC.

Table C.9.1. Proportions of deconvoluted peaks of C1s and O1s for IL/AC samples with 5, 10, 20, 30, and 35 wt.% loading.

Sample	Deconvolution of C1s Peak					Deconvolution of O1s Peak		
	C–C/C=C (wt.%)	C–OH (wt.%)	C–O/C–N (wt.%)	C=O (wt.%)	π-π* (wt.%)	C=O (wt.%)	C–O (wt.%)	C–OH (wt.%)
Pristine AC	44.7	41.2	11.3	2.2	0.6	29.3	55.5	15.2
IL_5/AC	51.1	32.5	12.6	3	0.8	41.3	46.7	12.0
IL_{10}/AC	39.5	43.3	13.2	2.4	1.6	15.8	49.6	34.6
IL_{20}/AC	32.4	25.4	32.7	4.2	4.3	3.5	71.6	24.9
IL_{30}/AC	17.6	32.9	38.8	5.7	5.0	14.4	46	39.6
IL_{35}/AC	14.5	29.6	42.4	8.3	5.2	58.1	37.0	4.9

C.10 Gas Sorption Studies

CH_4, CO_2, and N_2 gas sorption studies were conducted for pristine AC and IL/AC composites and corresponding results of each gas were given in below as **Figure C.10.1(a-c)** where filled symbols represent obtained experimental data and straight line represents the data obtained after isotherm fitting. Moreover, respective parameters obtained from isotherm fitting were given in **Table C.10.1**.

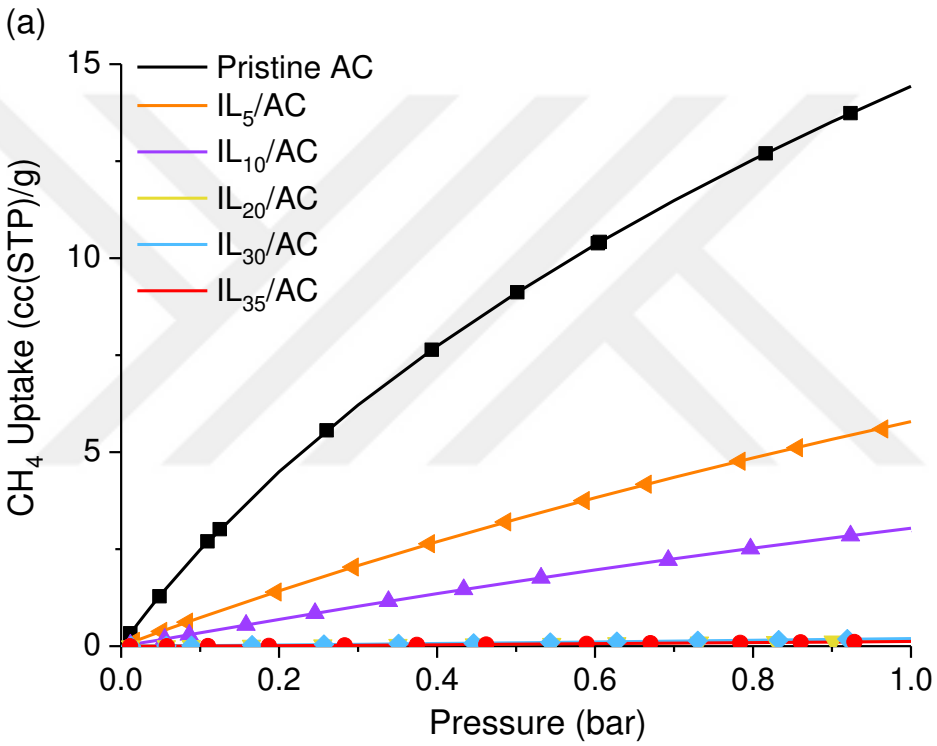

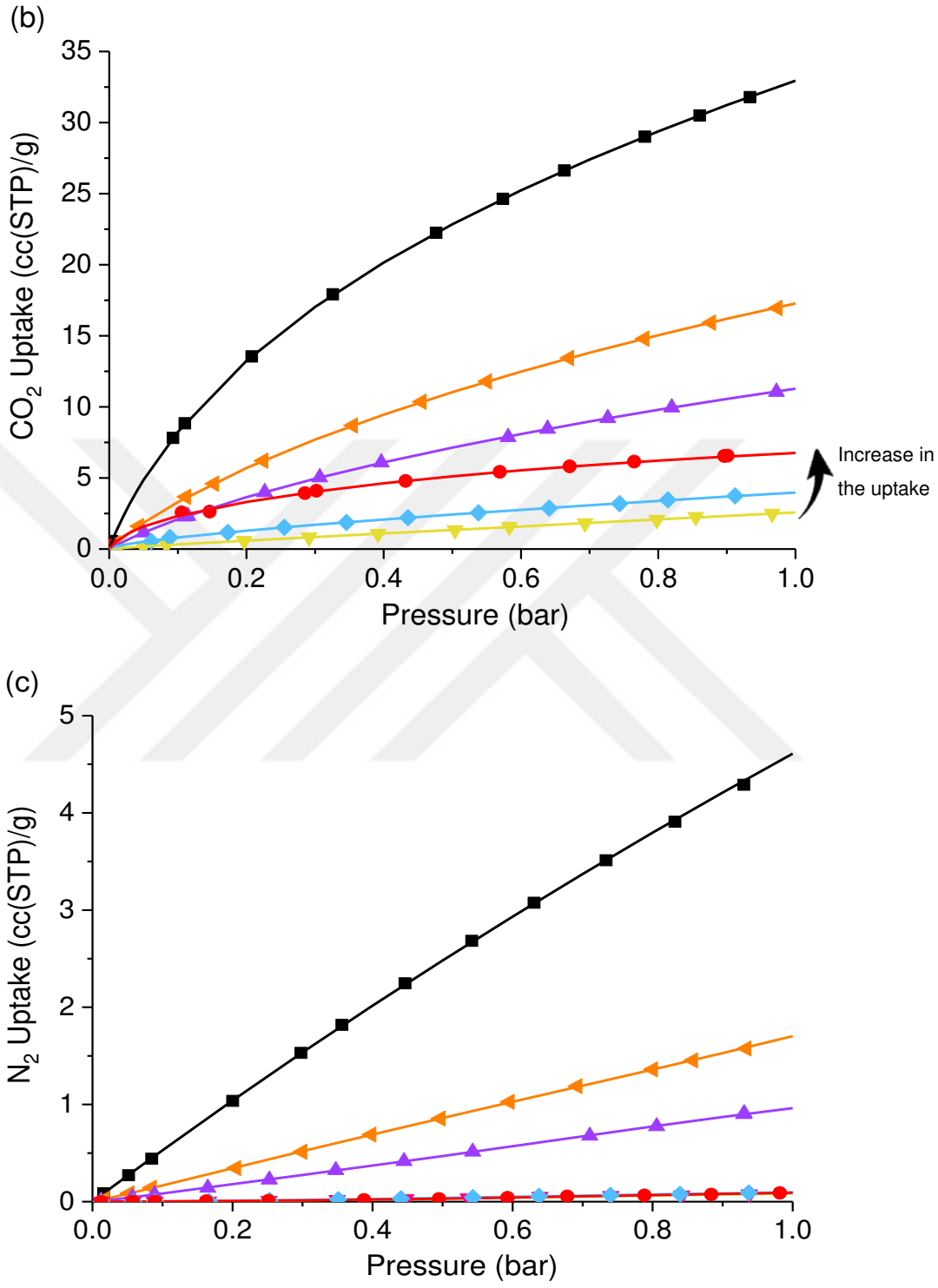

Figure C.10.1. Experimental and fitted gas sorption results of (a) CH_4, (b) CO_2, and (c) N_2 for pristine AC and corresponding IL/AC composites with 5, 10, 20, 30, and 35 wt.% IL loading. Filled symbols represent experimental data whereas the solid lines represent isotherm fitting results.

Table C.10.1. Fitted isotherm parameters of Dual-Site Langmuir Model, Dual-Site Langmuir-Freundlich Model, and Langmuir-Freundlich Model for pristine AC and IL/AC composites with 5, 10, 20, 30, and 35 wt.% IL loading.

		Dual-Site Langmuir Model					**Dual-Site Langmuir-Freundlich Model**							**Langmuir-Freundlich Model**			
Adsorbent	**Gas**	**q_1 (cc/g)**	**k_1 (1/mbar)**	**q_2 (cc/g)**	**k_2 (1/mbar)**	**R^2**	**q_1 (cc/g)**	**k_1 (1/mbar)**	**n_1^***	**q_2 (cc/g)**	**k_2 (1/mbar)**	**n_2^***	**R^2**	**q (cc/g)**	**k (1/mbar)**	**n***	**R^2**
Pristine AC	CH_4	38.87	0.43	3.54	3.31	0.99											
	CO_2						80.98	0.26	1.01	20.80	3.89	0.91	0.99				
	N_2	16.53	0.18	14.05	0.18	0.99											
IL_5/AC	CH_4	63.89	0.02	17.45	0.37	0.99											
	CO_2	47.97	0.42	3.63	6.13	0.99											
	N_2						2.30	0.45	0.92	4.15	0.42	1.44	0.99				
IL_{10}/AC	CH_4													13.17	0.32	1.05	0.99
	CO_2	2.41	5.68	33.34	0.38	0.99											
	N_2						2.84	0.41	1.09	12.54	0.15	2.15	0.99				
IL_{20}/AC	CH_4													58.56	0.01	1.24	0.99
	CO_2	89.44	0.01	0.12	18.04	0.99											
	N_2						0.01	1.06	50.28	0.16	1.01	1.97	0.99				
IL_{30}/AC	CH_4						0.22	0.85	2.85	0.21	1.09	1.17	0.99				
	CO_2						47.31	0.071	1.24	6.06	0.46	0.65	0.99				
	N_2													0.23	0.83	1.84	0.99
IL_{35}/AC	CH_4						16.39	1.00	118.30	0.23	1.02	1.84	0.99				
	CO_2	1.93	26.14	9.31	1.11	0.99											
	N_2						0.09	1.07	2.87	0.31	0.23	1.28	0.99				

C.11 Thermal Analysis for CH_4, CO_2, and N_2 sorption

To understand the sorption kinetics of CH_4, CO_2, and N_2 gasses, a thermal analysis was made by conducting gas sorption experiments at three different temperatures, as 15, 25, and 35 °C, for each gas. Results were illustrated in **Figure C.11.1-3**.

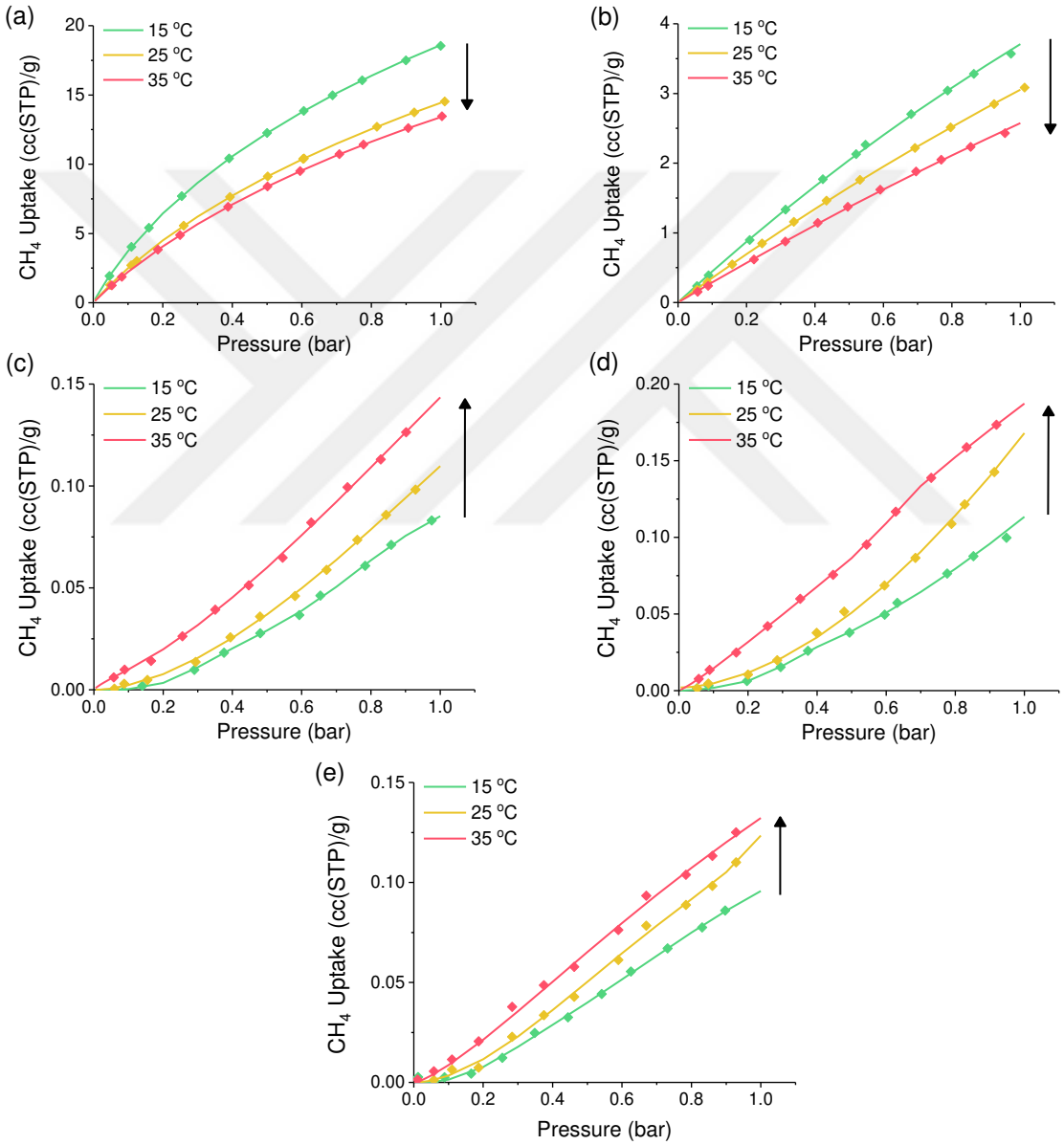

Figure C.11.1. Experimental (squares) and fitted (straight line) CH4 gas sorption results of (a) Pristine AC, (b) IL_{10}/AC, (c) IL_{20}/AC, (d) IL_{30}/AC, and (e) IL_{35}/AC at 15, 25, and 35 °C. Arrow indicates the direction of increasing temperature.

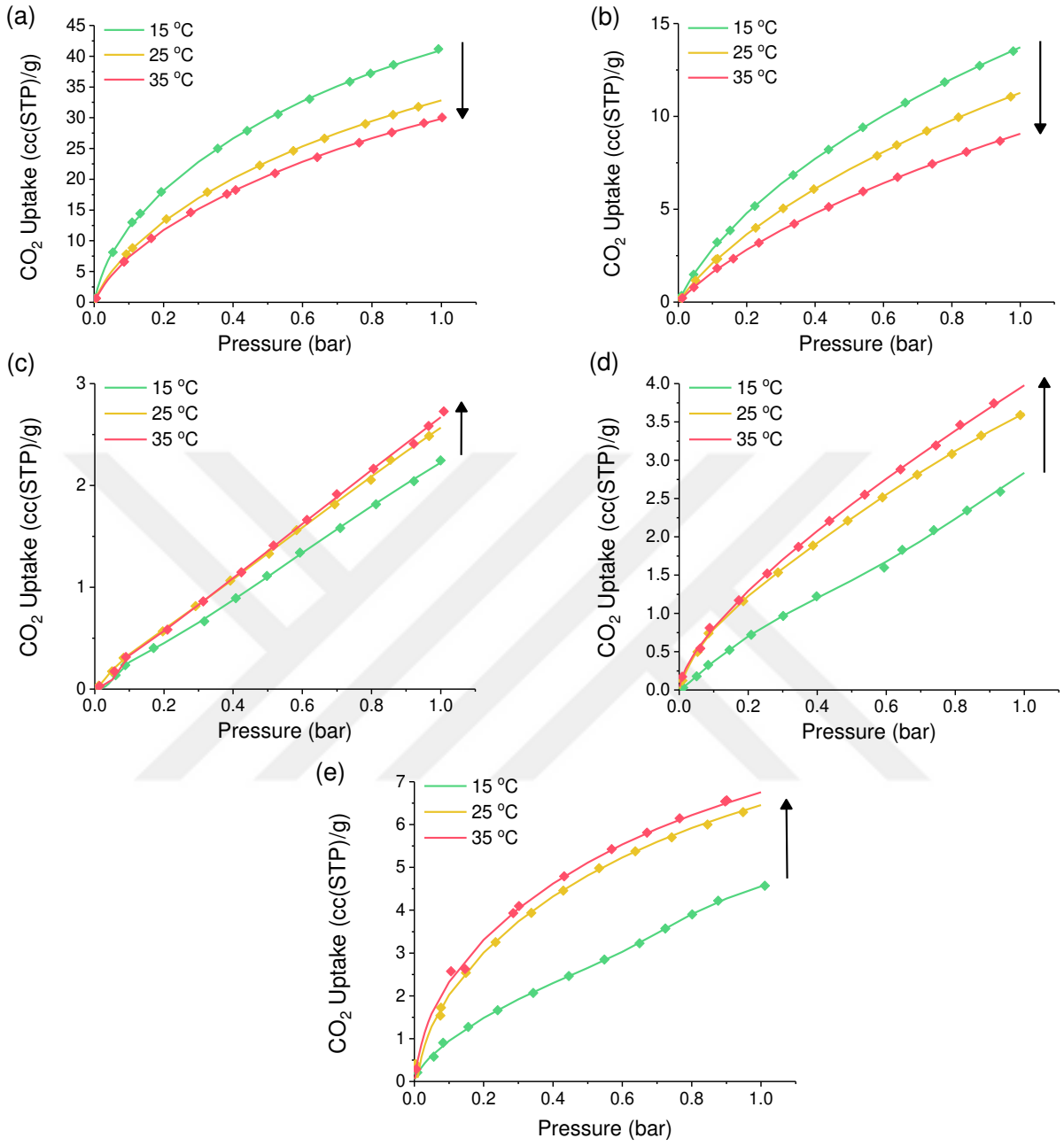

Figure C.11.2. Experimental (squares) and fitted (straight line) CO_2 gas sorption results of (a) Pristine AC, (b) IL_{10}/AC, (c) IL_{20}/AC, (d) IL_{30}/AC, and (e) IL_{35}/AC at 15, 25 and 35 °C. Arrow indicates the direction of increasing temperature.

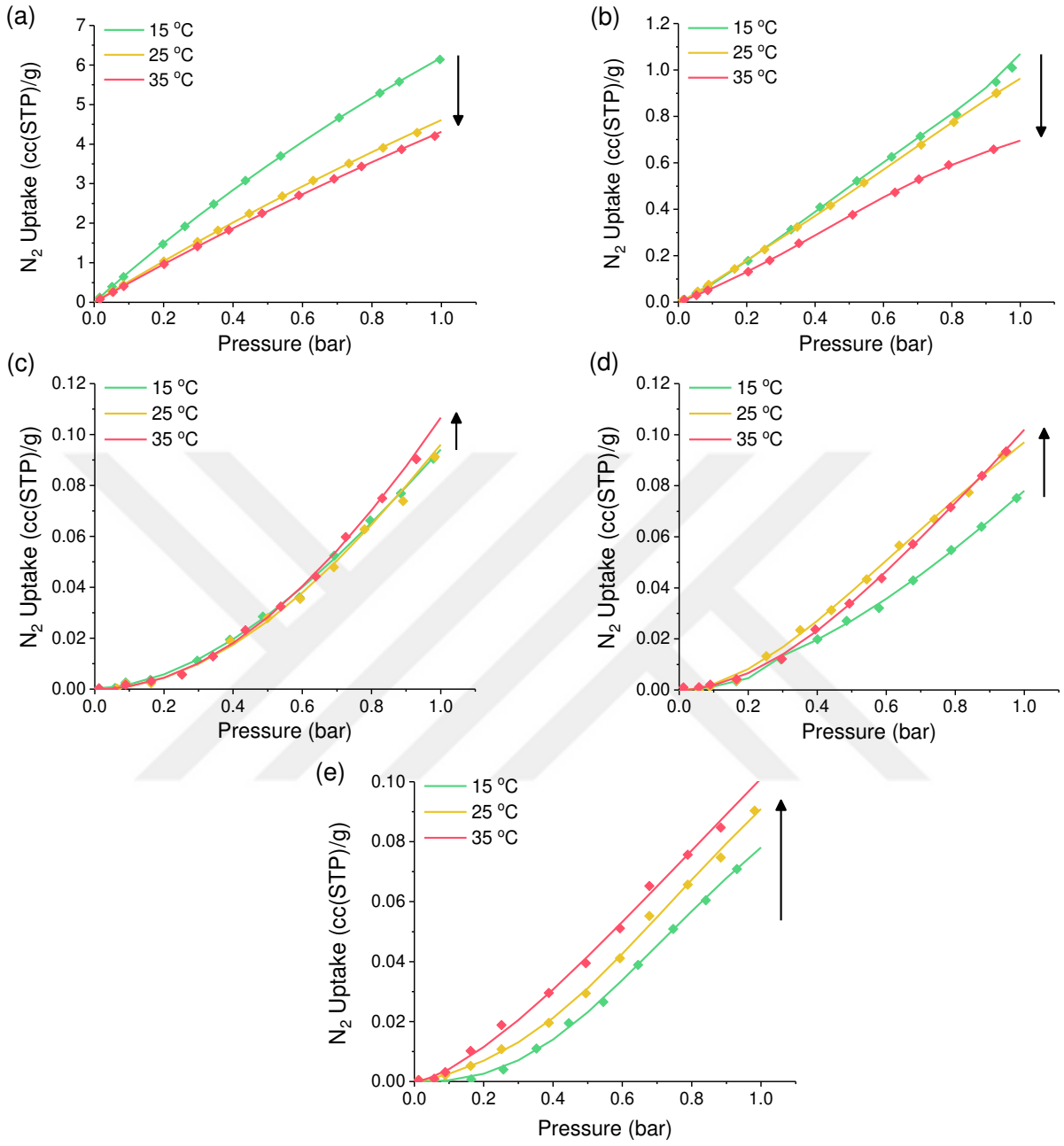

Figure C.11.3. Experimental (squares) and fitted (straight line) N_2 gas sorption results of (a) Pristine AC, (b) IL_{10}/AC, (c) IL_{20}/AC, (d) IL_{30}/AC, and (e) IL_{35}/AC at 15, 25, and 35 °C. Arrow indicates the direction of increasing temperature.

C.12 Entalphy of sorption (ΔH_{sorp}) analysis for CH_4, CO_2, and N_2 sorption

The ΔH_{sorp} values, which are also equal to the negative of isosteric heat of sorption values ($-Q_{st}$), with respect to gas uptake in mmol/g and linear fittings of Clausius-Clapeyron equation were given in **Figure 7.4** and **Figure C.12.1-3**, respectively, for each of CH_4, CO_2, and N_2 gasses. It is generally known that ΔH_{sorp} values below 30-40 kJ/mol indicates physisorption, whereas values above 30-40 kJ/mol indicates chemisorption.[376, 377]

Moreover, with increasing IL loading, trend observed in Figure 6 becomes steeper. The slope of this trend can be associated with the degree of heterogeneity of the surface.[296] For our samples with 30 and 35 wt.% IL loadings, linear fittings yielded negative slopes of -49.8±1.9 and -52.6±3.0 with the corresponding R^2 values of 0.986 and 0.981, respectively. Hence, the slope and the loading showed a proportional relationship illustrating an increase in the degree of surface heterogeneity of the samples. Therefore, increase in the CO_2 uptake after 20 wt.% IL loading can be associated with increasing surface heterogeneity and consequently, with the increasing number of high energy chemisorption sites coming from newly formed IL layer.

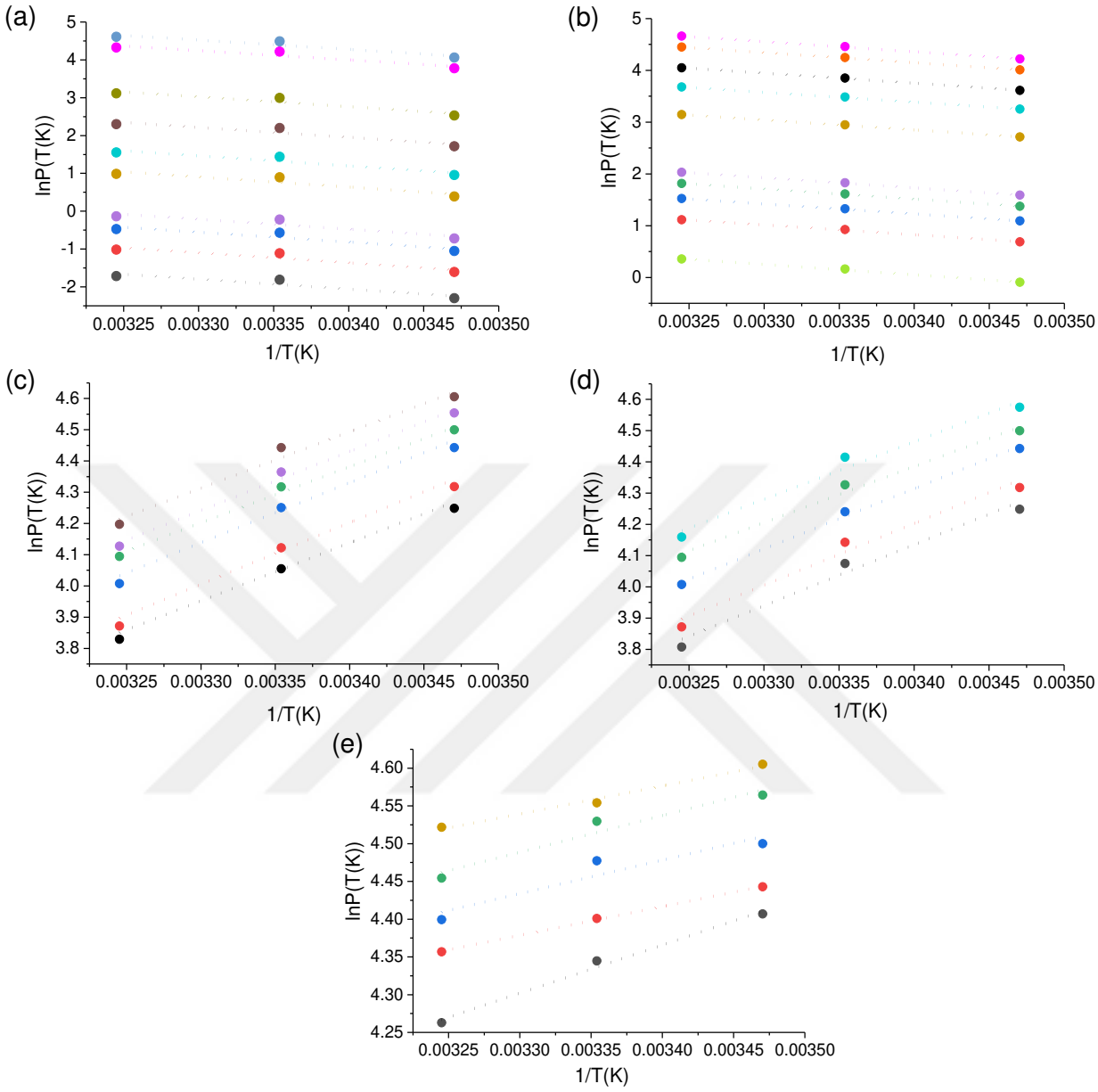

Figure C.12.1. LnP(T(K)) vs 1/T(K) linear fittings of ΔH_{ads} calculations for CH_4 gas sorption of (a) pristine AC (between 0.002-0.5 mmol CH_4 uptake), (b) IL_{10}/AC (between 0.002-0.12 mmol CH_4 uptake), (c) IL_{20}/AC (between 0.002-0.005 mmol CH_4 uptake), (d) IL_{30}/AC (between 0.002-0.005 mmol CH_4 uptake), and (e) IL_{35}/AC (between 0.002-0.005 mmol CH_4 uptake) obtained from Clausius-Clapeyron equation.

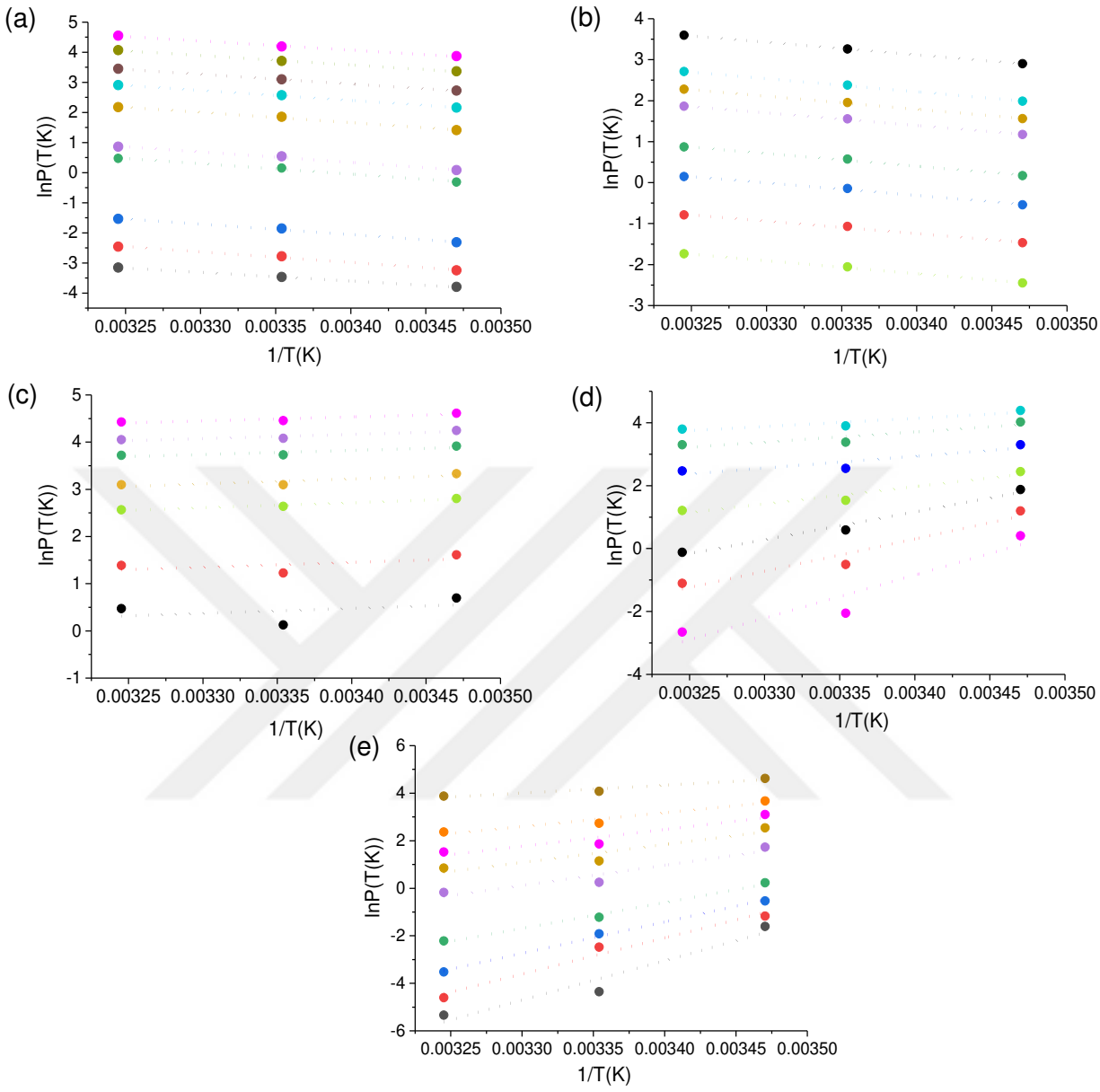

Figure C.12.2. LnP(T(K)) vs 1/T(K) linear fittings of ΔH_{ads} calculations for CO_2 gas sorption of (a) pristine AC (between 0.002-1.35 mmol CO_2 uptake), (b) IL_{10}/AC (between 0.002-0.4 mmol CO_2 uptake), (c) IL_{20}/AC (between 0.002-0.1 mmol CO_2 uptake), (d) IL_{30}/AC (between 0.002-0.15 mmol CO_2 uptake), and (e) IL_{35}/AC (between 0.002-0.25 mmol CO_2 uptake) obtained from Clausius-Clapeyron equation.

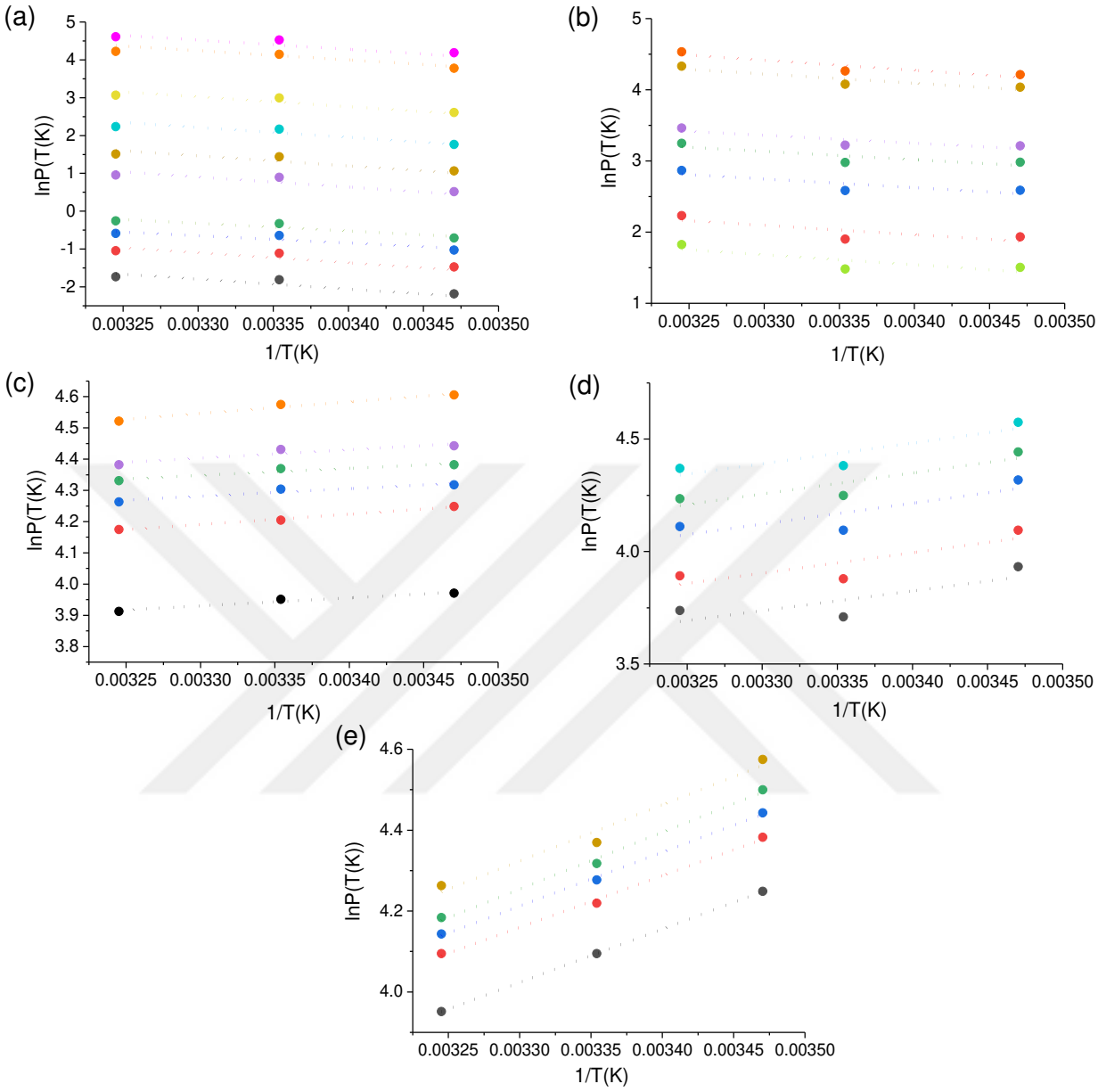

Figure C.12.3. LnP(T(K)) vs 1/T(K) linear fittings of ΔH_{ads} calculations for N_2 gas sorption of (a) pristine AC (between 0.002-0.2 mmol N_2 uptake), (b) IL_{10}/AC (between 0.002-0.03 mmol N_2 uptake), (c) IL_{20}/AC (between 0.002-0.004 mmol N_2 uptake), (d) IL_{30}/AC (between 0.002-0.0035 mmol N_2 uptake), and (e) IL_{35}/AC (between 0.002-0.0025 mmol N_2 uptake) obtained from Clausius-Clapeyron equation.

C.13 FTIR Analysis of CH_4-saturated Pristine AC and IL/AC Composites

Interactions between CH_4 molecules and the composites were investigated by analyzing FTIR spectra of CH_4-saturated pristine AC and CH_4-saturated composites as given in **Figure C.13.1**. As a first step, interactions between CH_4 molecules and pristine AC were analyzed to create a ground understanding of the sorption process. Presence of sorbed CH_4 molecules were verified from newly appeared peaks located at 2982, 2893, and 1323 cm^{-1} as given in **Figure C.13.1(a)**. The peak located at 2982 cm^{-1} was assigned to asymmetric stretching of C–H bond, while the peak at 2893 cm^{-1} was assigned to symmetric stretching of C–H bond.[378] For free CH_4 molecules, these peaks correspond to 3020 and 2914 cm^{-1}, respectively, however, both were red-shifted to lower energy levels indicating a perturbation of their vibrations inside the pores of the adsorbent. Formation of these peaks were also observed in the spectra of IL_{10}/AC and IL_{20}/AC as given in **Figure C.13.1(b-c)**. Similarly, two newly formed peaks were observed in the spectra of CH_4-saturated IL_{35}/AC, as given in **Figure C.13.1(d)**, which were attributed to the vibrations of CH_4 molecules similar with the case of bulk [BMIM][OAc]. Furthermore, it was observed that the characteristic peaks of ν(C–O) and ν(C=C) red shifted to lower energy levels for pristine AC, IL_{10}/AC, and IL_{20}/AC indicating a possible hydrophobic interaction between non-polar CH_4 molecules and the surface of AC (mainly through oxygen containing surface functional groups). In literature, it was shown that CH_4 sorption of carbon-based materials was directly related to the hydrophobic character and polarity of the surface.[298, 342, 379-382] Therefore, decreased CH_4 uptake can be attributed to increasing surface polarity of the composites due to newly formed interactions between the surface of AC and IL, as explained in detail in the previous sections. Newly attached cation molecules of IL enhance the polarity of the surface which creates a repulsive dipole moment for non-polar methane molecules. Enhanced polarity and decreased hydrophobic character of the surface unfavored the sorption of methane molecules due to their non-polar nature. As a result, IL layer on the surface of pristine AC acts as a smart layer for selective sorption of CH_4 molecules by blocking the sorption of non-polar CH_4 with enhanced polarity of the surface.

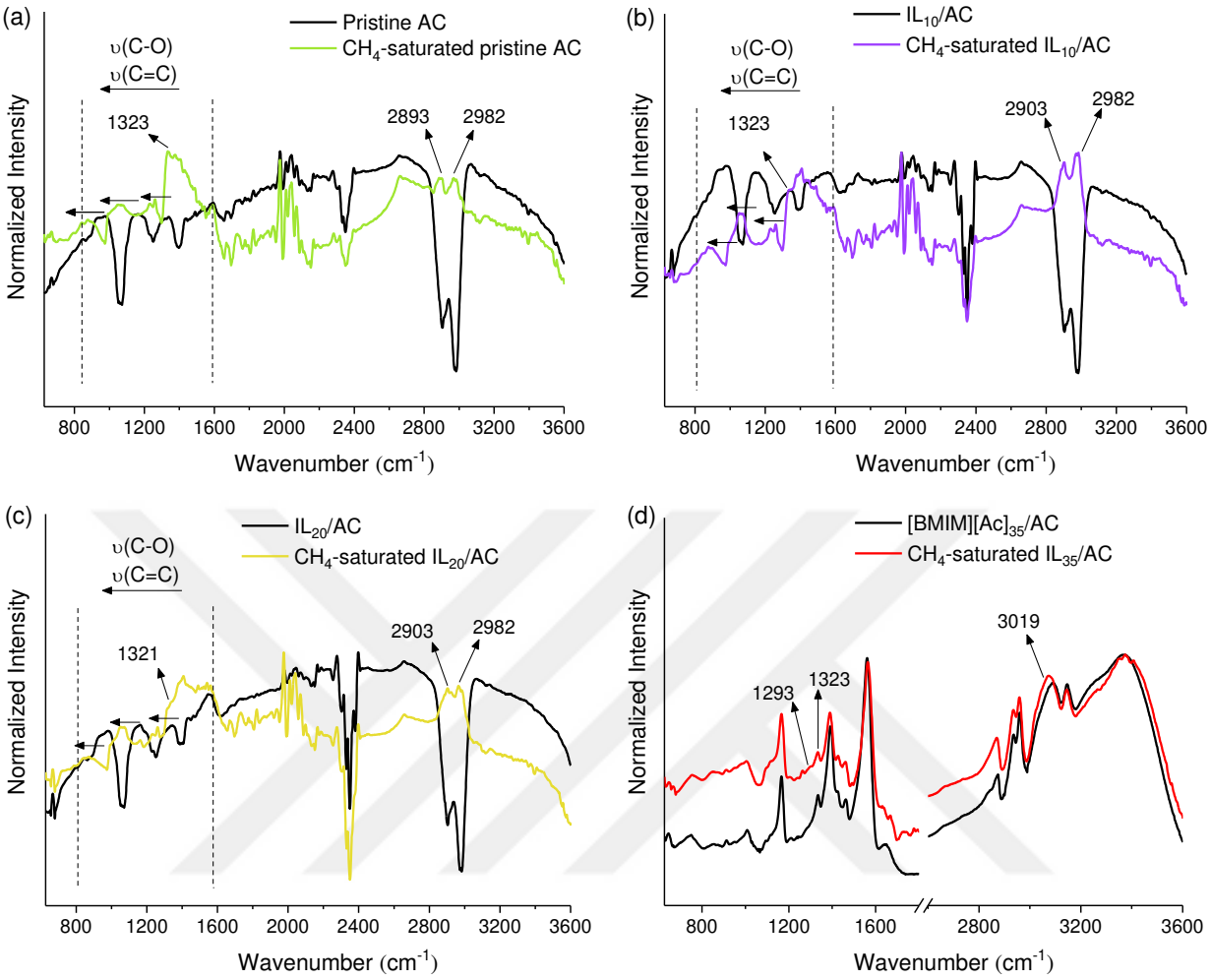

Figure C.13.1. FTIR spectra of (a) pristine AC and CH_4-saturated pristine AC, (b) IL_{10}/AC and CH_4-saturated IL_{10}/AC, (c) IL_{20}/AC and CH_4-saturated IL_{20}/AC, and (d) IL_{35}/AC and CH_4-saturated IL_{35}/AC between the region 3600-600 cm^{-1}.

C.14 FTIR Analysis of CH_4-saturated Bulk [BMIM][OAc]

CH_4 absorption nature of bulk [BMIM][OAc] investigated by comparing FTIR spectra of bulk [BMIM][OAc], CH_4-saturated [BMIM][OAc] and CH_4-saturated [BMIM][OAc] after drying. Obtained FTIR spectra were given as **Figure C.14.1**. Data illustrated that upon CH_4 absorption, two new peaks appeared in the spectra of bulk [BMIM][OAc] located at 3019 and 1324 cm^{-1}. The peak located at 3019 cm^{-1} is observable on the spectra, however, the peak located at 1324 cm^{-1} convoluted into an existing peak at 1325 cm^{-1}. These two peaks were attributed to adsorbed CH_4 molecules consistent with the FTIR spectra of pure CH_4 molecules.[383-385] In order to investigate the nature of these interactions, CH_4-saturated sample was dried overnight at 80 °C to remove physiosorbed CH_4 molecules. As a result, new peaks appeared in the spectra upon CH_4 absorption, which were disappeared after drying indicating the removal of physiosorbed CH_4 molecules and further prove the physisorption nature of CH_4 absorption.

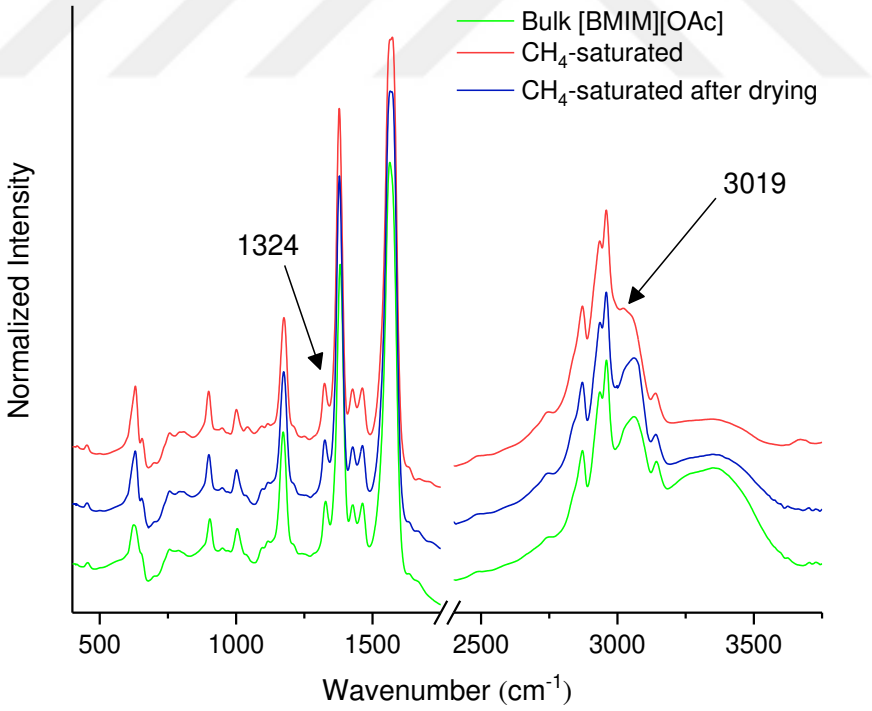

Figure C.14.1. FTIR spectra of bulk [BMIM][OAc], CH_4-saturated [BMIM][OAc] and CH_4-saturated [BMIM][OAc] after drying.

C.15 NMR Analysis of CH_4-saturated Bulk [BMIM][OAc]

^1H and ^{13}C NMR spectra of both bulk [BMIM][OAc] and its CH_4-saturated counterpart were obtained for comparison and presented as **Figure C.15.1** together with corresponding signals in **Table C.15.1**. Obtained ^1H and ^{13}C NMR spectra of bulk [BMIM][OAc] were consistent with the literature.[277, 278, 386] Data illustrated that there is no chemical shift occurred for primary signals and no new signal appeared after saturating the IL with CH_4. This result indicates that there is no chemical bonding or complex formation during the absorption of CH_4 molecules. Thus, it can be inferred that the nature of CH_4 absorption of bulk [BMIM][OAc] is physisorption.

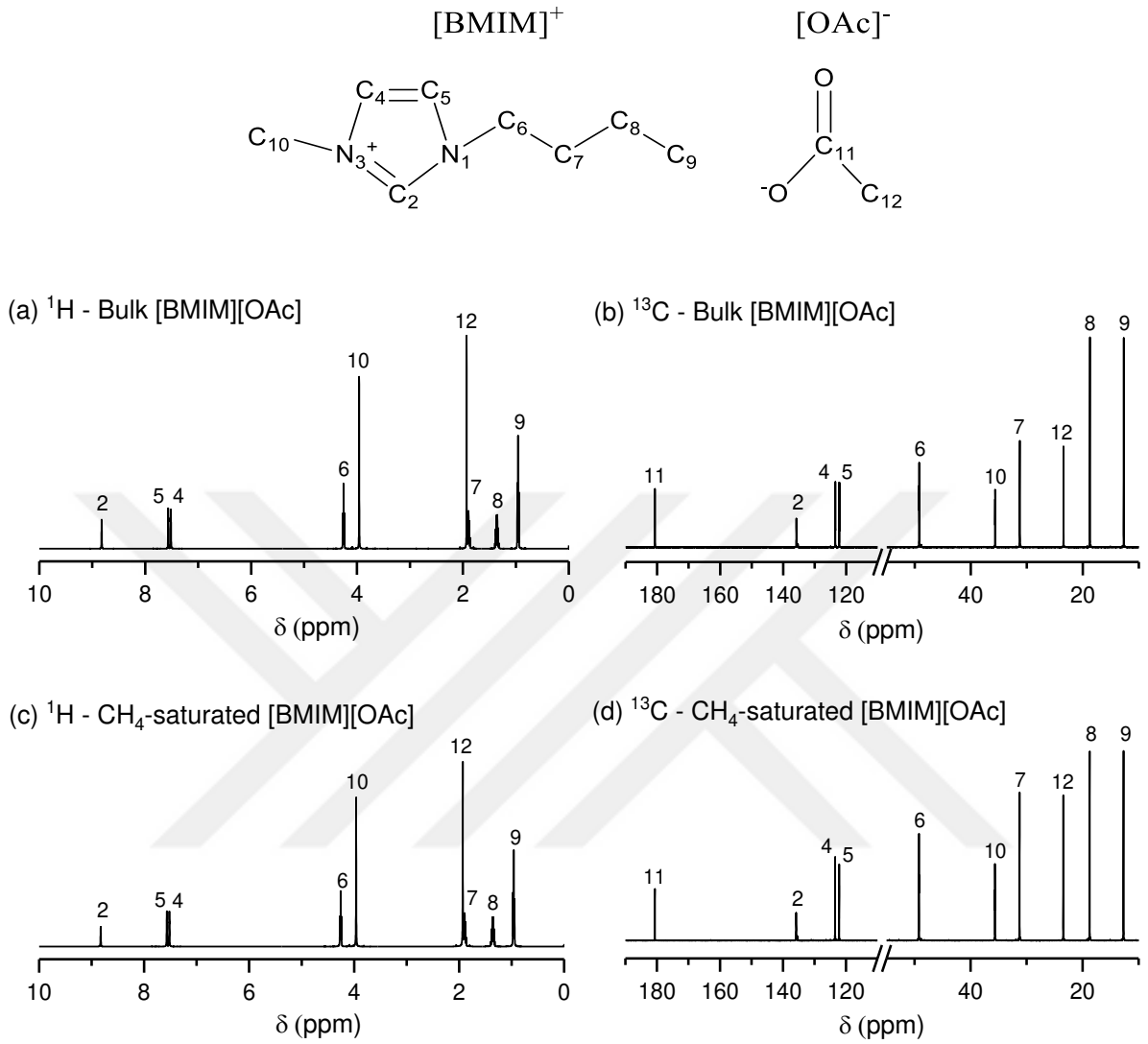

Figure C.15.1. (a) ^{1}H NMR spectra of bulk [BMIM][OAc], (b) ^{13}C NMR spectra of bulk [BMIM][OAc], (c) ^{1}H NMR spectra of CH_4-saturated [BMIM][OAc], (d) ^{13}C NMR spectra of CH_4-saturated [BMIM][OAc].

Table C.15.1. ^{1}H and ^{13}C NMR signal designation of bulk [BMIM][OAc] and CH_4-saturated counterpart. Signal locations were given as ppm in units.

Atom	Bulk [BMIM][OAc]				CH_4-saturated [BMIM][OAc]			
	^{1}H	**Secondary lines**	**^{13}C**	**Secondary lines**	**^{1}H**	**Secondary lines**	**^{13}C**	**Secondary lines**
2	8.82		135.81		8.82		135.81	
4	7.51		123.45	123.49	7.51		123.45	123.50
5	7.56		122.17	122.21	7.56		122.17	122.21
6	4.25	4.24 4.26	49.18	49.21	4.25	4.24 4.27	49.19	49.21
7	1.89	1.87 1.90	31.24		1.89	1.87 1.90	31.24	
8	1.35	1.34 1.38	18.73		1.35	1.34 1.38	18.74	
9	0.95	0.94 0.97	12.69		0.95	0.94 0.97	12.69	
10	3.95		35.62	35.65	3.96		35.63	35.66
11			180.67				180.67	
12	1.92		23.44		1.92		23.45	

C.16 FTIR Analysis of CO_2-saturated Bulk [BMIM][OAc]

CO_2 absorption nature of bulk [BMIM][OAc] investigated by comparing FTIR spectra of bulk [BMIM][OAc], CO_2-saturated [BMIM][OAc] and CO_2-saturated [BMIM][OAc] after drying. Obtained FTIR spectra are given in **Figure C.16.1**. Data illustrated that upon CO_2 absorption, five new peaks appeared in the spectra of bulk [BMIM][OAc] located at 1665, 1508, 1323, 1254, and 794 cm^{-1}. These peaks were in accordance with the characteristic peaks reported for 1-butyl-3-methylimidazolium carboxylate, which further proves the occurrence of the carboxylate formation reaction.[84, 277, 280, 387, 388] New peaks and their corresponding assignments can be found in **Table C.16.1**. A red-shift in the characteristic peak of cation, ν(C2H), was observed which can be related with the substitution between CO_2 molecule and hydrogen atom linked to the carbon located at C2. Moreover, red-shift of ν(C–O) and blue shift of ν(C=O) was observed which can be related to with substitution of hydrogen atom or a possible interaction with CO_2 molecules. Due to the lack of any IR features related to acetic acid formation, this change can be inferred to the interactions with CO_2 molecules. Furthermore, to investigate the nature of absorption, CO_2-saturated [BMIM][OAc] was dried overnight at 80 °C and it was observed that the characteristic peaks located at 1665, 1323, and 1254 cm^{-1} can still be seen. This result can be attributed to a chemical change happening upon CO_2 absorption indicating chemisorption type of absorption consistent with NMR findings.

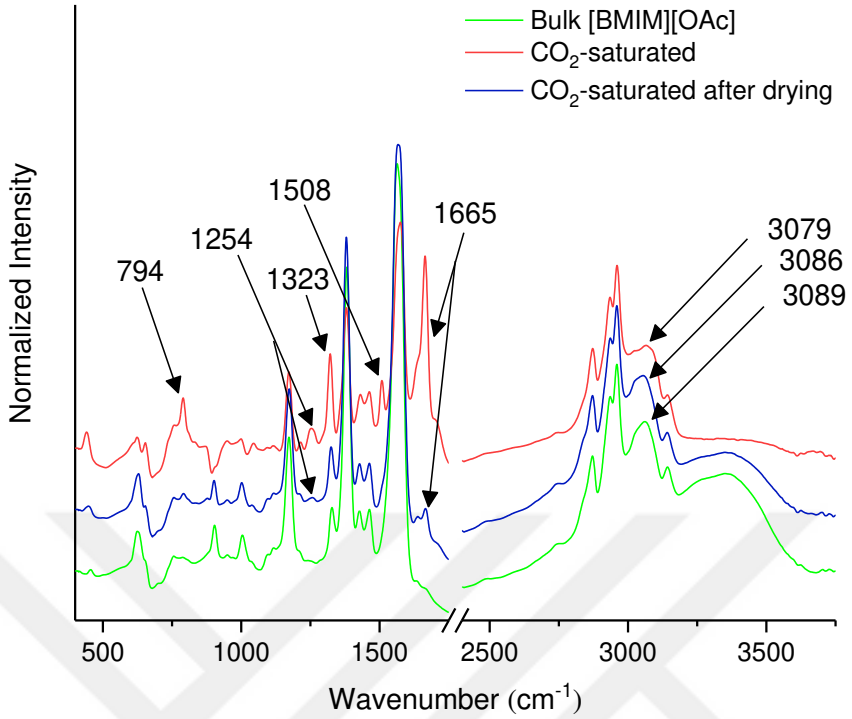

Figure C.16.1. FTIR spectra of bulk [BMIM][OAc], CO_2-saturated [BMIM][OAc] and CO_2-saturated [BMIM][OAc] after drying.

Table C.16.1. Peak assignments for newly appeared peaks in the FTIR spectra of CO_2-saturated bulk [BMIM][OAc]

Peak Location (cm^{-1})	**Assignment**
1665	*v*(COO)asym
1508	*v*(C=C–C)
1323	*v*(COO)sym
1254	δ(C–H), *v*(C–C), *v*(C–O)
794	δ(COO)

C.17 Liquid-state NMR Analysis of CO_2-saturated Bulk [BMIM][OAc]

^{1}H and ^{13}C NMR spectra of both bulk [BMIM][OAc] and its CO_2-saturated counterpart were obtained for comparison and presented as **Figure C.17.1** together with corresponding signals in Table S14. Data illustrated multiple new signals and secondary lines in the ^{1}H and ^{13}C NMR spectra of CO_2-saturated [BMIM][OAc] compared with the that of bulk. Therefore, it can be said that there is a chemical bonding or complex formation occurred during the absorption of CO_2 and it can be associated with chemisorption. There are various detailed studies on this subject proving that the CO_2 molecules are chemisorbed on bulk [BMIM][OAc].[277-279, 281] As a result of these studies, several different interaction mechanisms were proposed for the chemisorption of CO_2 into [BMIM][OAc]. In 2005, Maginn[270] proposed a two-step reaction mechanism for the chemisorption of CO_2 by the cation of [BMIM][OAc] as illustrated in **Figure C.17.2(a)**. As the first step of the reaction, acetate anion abstracts the hydrogen atom located at C2 of cation and as a result, a carbane species and acetic acid are formed. The mechanism proceeds with the second step as imidazolium-2-carboxylate formation due to the reaction between carbane and CO_2. However, they did not observe any evidence regarding the formation of acetic acid which was criticized by another study.[280] Later on, the formation of 1-ethyl-3-methylimidazolium carboxylate was proven by obtained crystallite product after the introduction of CO_2 into [EMIM][OAc]. A second reaction mechanism was proposed by a series of publications by Besnard et al.[84, 277, 278] as illustrated in **Figure C.17.2(b)**. In this reaction mechanism, they confirmed the formation of 1-butyl-3-methylimidazolium carboxylate via NMR, Raman, FTIR and DFT analysis, however, they excluded the carbane formation step by stating that the presence of acetic acid is only detected after some time upon the introduction of CO_2 into the [BMIM][OAc]. They obtained the characteristic acetic acid ^{1}H NMR peak (belongs to –COOH of acetic acid and located around 10 ppm) 3 days after the mixture preparation, which demonstrates the slow stabilization of the reaction system with the late formation of acetic acid. Similarly, another reaction mechanism was proposed by Mao et. al[279] as illustrated in **Figure C.17.2(c)**. After a detailed DFT study, they proposed a new transition state complex for a solvated model which was proven to be more stable than carbane formation. In this mechanism, a transition complex was formed where both CO_2 and hydrogen bonded to the same C2 location, and the structure was stabilized by surrounding bulky solvent molecules. Upon this complex formation, reaction proceeds with the same resulting step which

is imidazolium-2-carboxylate and acetic acid. Accordingly, we obtained consistent ^{1}H and ^{13}C NMR results with the literature proving the formation of carboxylate for bulk [BMIM][OAc]. Isolated free CO_2 molecule has a ^{13}C NMR resonance line located at 125.4 ppm, therefore, the new peaks in ^{13}C NMR spectra which are located at 139.98 and 158.03 ppm can be associated with newly formed structure, in this case imidazolium-2-carboxylate structure.[389] Moreover, newly appeared ^{1}H NMR secondary line located at 4.03 ppm can be associated with a transition state complex, CO_2-carbane complex, during the formation of imidazolium-2-carboxylate structure via the reaction between CO_2 and the cation.[278]

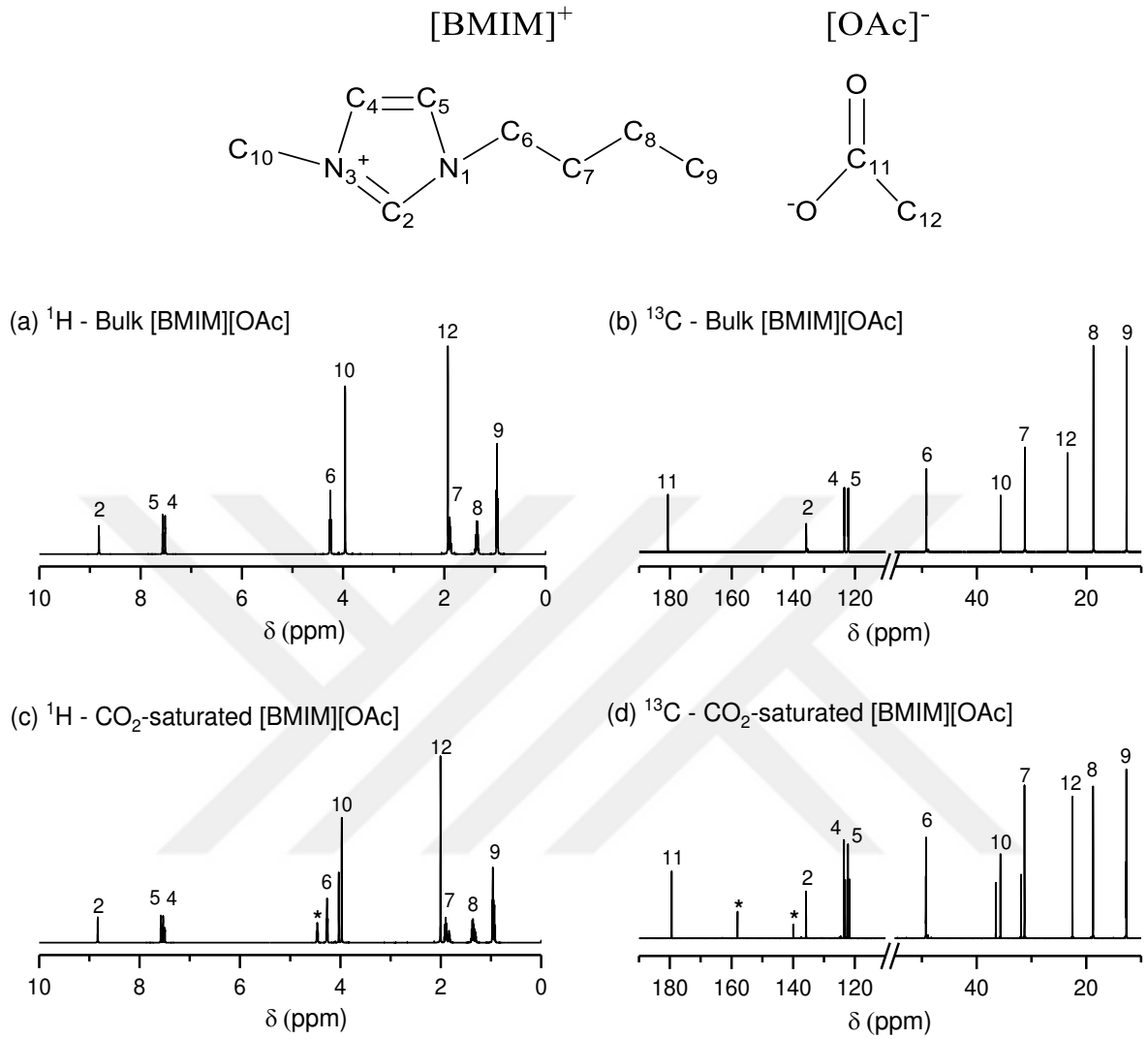

Figure C.17.1. (a) ^{1}H NMR spectra of bulk [BMIM][OAc], (b) ^{13}C NMR spectra of bulk [BMIM][OAc], (c) ^{1}H NMR spectra of CO_2-saturated [BMIM][OAc], (d) ^{13}C NMR spectra of CO_2-saturated [BMIM][OAc].

Table C.17.1. ^{1}H and ^{13}C NMR signal designation of bulk [BMIM][OAc] and CO_2-saturated counterpart. Signal locations were given as ppm in units.

Atom	Bulk [BMIM][OAc]				CO_2-saturated [BMIM][OAc]			
	^{1}H	**Secondary lines**	**^{13}C**	**Secondary lines**	**^{1}H**	**Secondary lines**	**^{13}C**	**Secondary lines**
2	8.82		135.81		8.83		135.81	135.81
4	7.51		123.45	123.49	7.53	7.49	123.50	123.11
5	7.56		122.17	122.21	7.57		122.21	122.75
6	4.25	4.24 4.26	49.18	49.21	4.26	4.25 4.27	49.22	49.26
7	1.89	1.87 1.90	31.24		1.90	1.88 1.92	31.21	31.9
8	1.35	1.34 1.38	18.73		1.35	1.34 1.38	18.74	18.8
9	0.95	0.94 0.97	12.69		0.96	0.94 0.97	12.67	12.71
10	3.95		35.62	35.65	3.97	4.03*	35.66	35.67 36.50
11			180.67				179.39	
12	1.92		23.44		2.00		22.51	
New peak*							139.98*	
New peak*							158.03*	

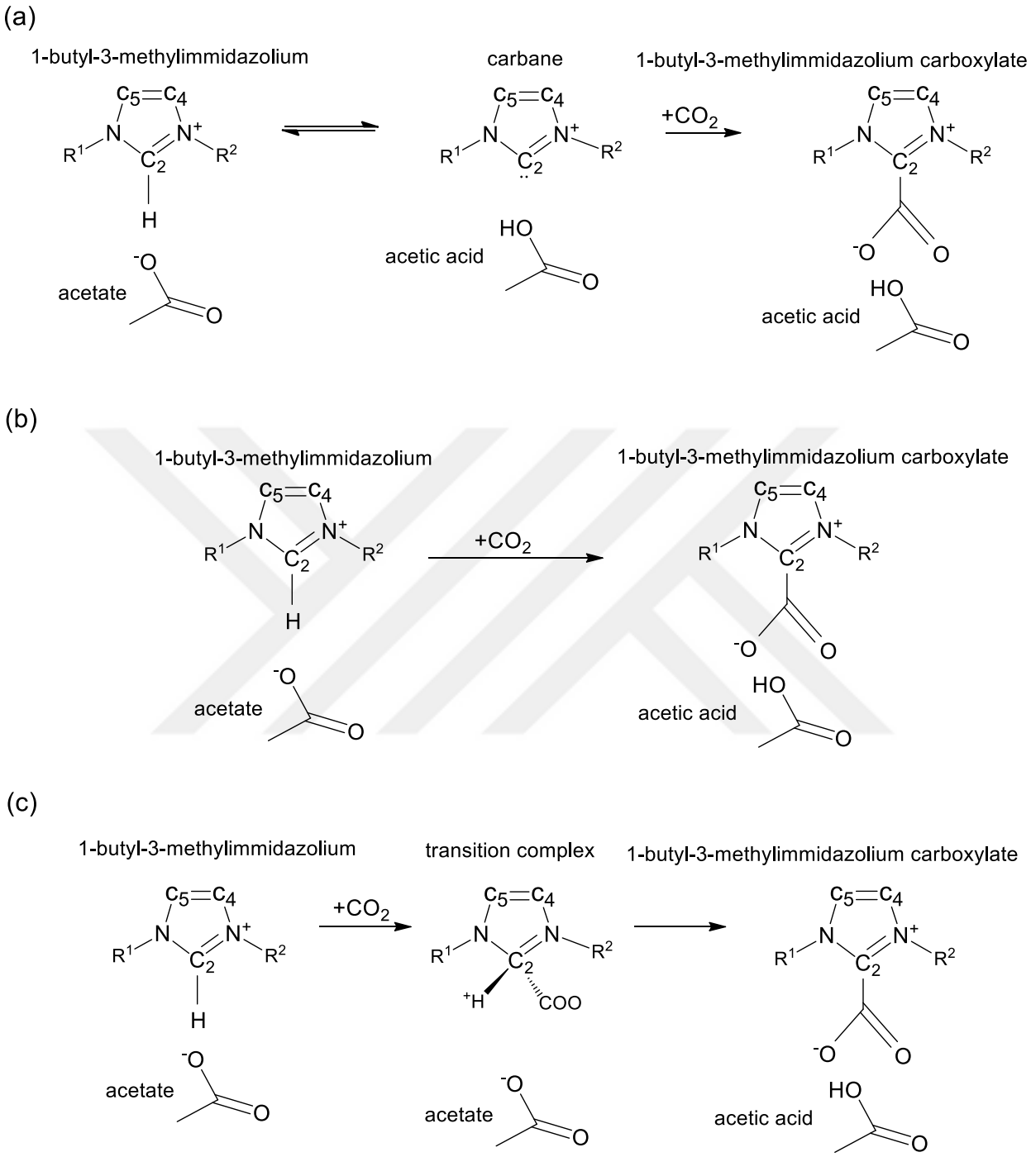

Figure C.17.2. Proposed reaction mechanisms for CO_2 chemisorption of imidazolium acetate by (a) Maginn[270], (b) Besnard et al.[84, 277, 278], (c) Mao et al.[279].

C.18 FTIR Analysis of CO_2-saturated Pristine AC and IL/AC Composites

Interactions between CO_2 molecules and the composites were investigated by analyzing FTIR spectra of CO_2-saturated pristine AC, CO_2-saturated IL_{10}/AC and CO_2-saturated IL_{20}/AC composites as presented in **Figure C.18.1**. Moreover, FTIR spectra of IL_{35}/AC, CO_2-saturated IL_{35}/AC, and CO_2-saturated bulk [BMIM][OAc] can be found in **Figure C.18.2** with the respective peak shifts tabulated in **Table C.18.1**.

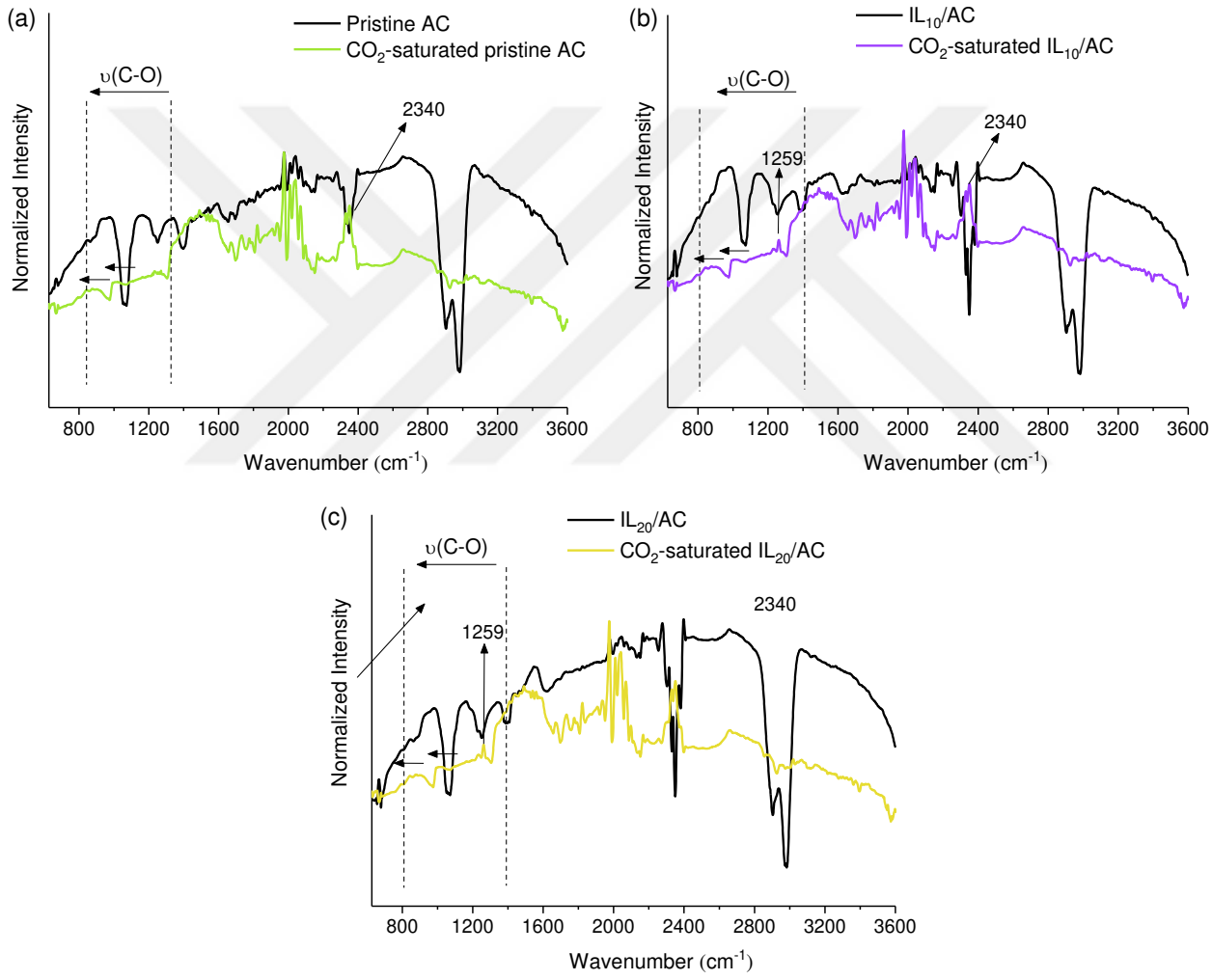

Figure C.18.1. FTIR spectra of (a) pristine AC and CO_2-saturated pristine AC, (b) IL_{10}/AC and CO_2-saturated IL_{10}/AC, (c) IL_{20}/AC and CO_2-saturated IL_{20}/AC between the region 3600-600 cm^{-1}.

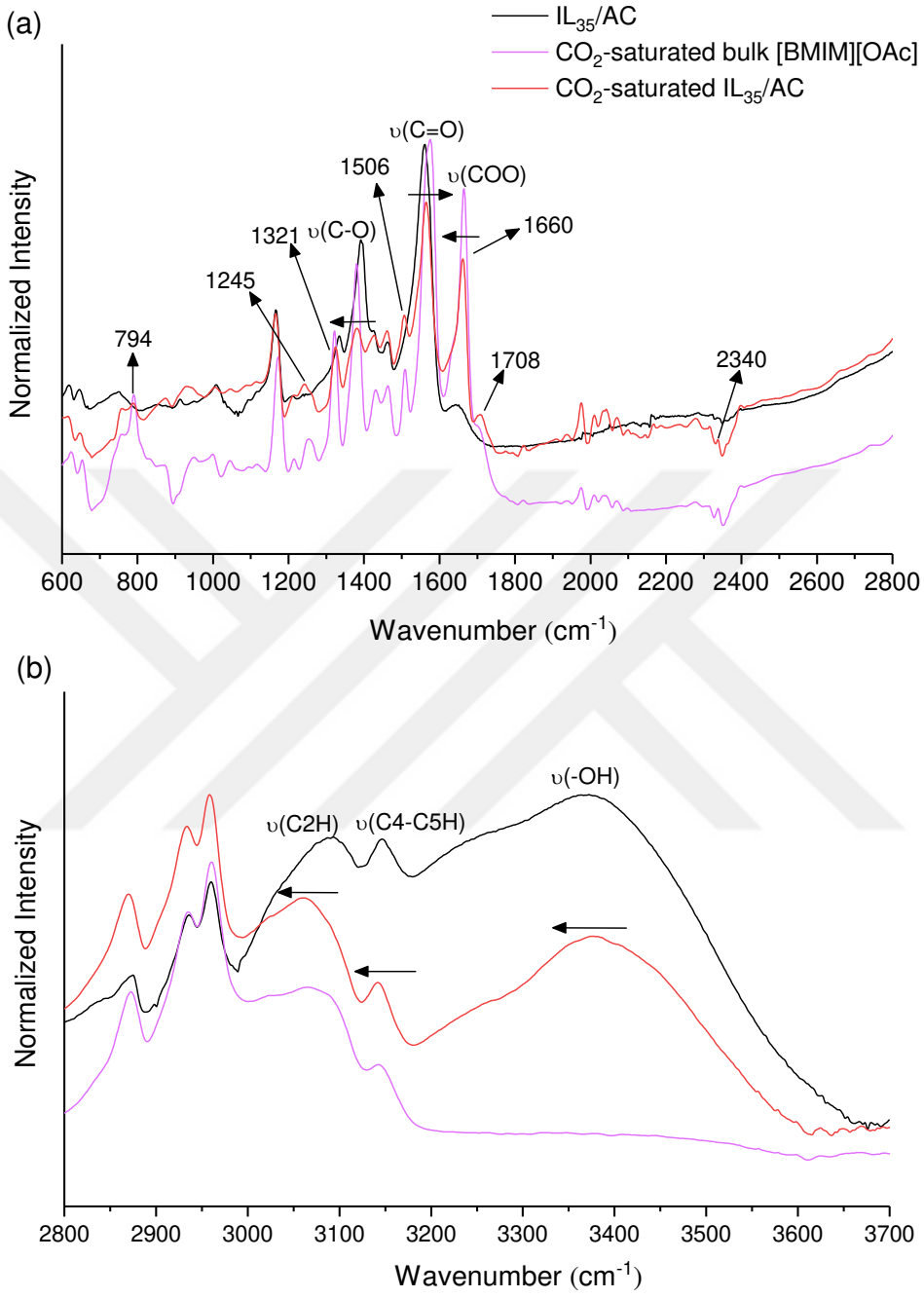

Figure C.18.2. FTIR spectra of IL_{35}/AC, CO_2-saturated IL_{35}/AC, and CO_2-saturated [BMIM][OAc] between the region (a) 600-2800 cm^{-1} and (b) 2800-3600 cm^{-1}.

Table C.18.1. FTIR peak assignments and locations of IL_{35}/AC, CO_2-saturated IL_{35}/AC and CO_2-saturated [BMIM][OAc].

Peak Assignments	Corresponding peak locations (cm^{-1})			
	[BMIM][OAc]$_{35}$/AC	**CO_2-saturated [BMIM][OAc]$_{35}$/AC**	**Bulk [BMIM][OAc]**	**CO_2-saturated bulk [BMIM][OAc]**
ν(–OH)	3375	3369	3375	3374
ν(C4-C5H)	3146	3142	3146	3146
ν(C2H)	3093	3083	3089	3079
ν(COO)	-	1661	-	1665
ν(C=O)	1559	1564	1561	1572
ν(C–O)	1394	1383	1389	1385

C.19 FTIR Analysis of N_2-saturated Pristine AC and IL/AC Composites

Interactions between N_2 molecules and the composite were investigated by analyzing FTIR spectra of N_2-saturated pristine AC and N_2-saturated composites as given in **Figure C.19.1**. N_2 and CH_4 have similar physicochemical properties, hence, similar with CH_4 sorption, it was expected to observe physisorption type of sorption for N_2 molecules. Similarly, noise formation and intensity changes in the skeletal peaks of AC located between 1400-800 cm^{-1} were attributed to the effect of physiosorbed N_2 molecules as shown in **Figure C.19.1**. However, presence of adsorbed N_2 molecules cannot be detected through FTIR because of the constant dipole moment of N_2 molecules. Free N_2 molecules have an inactive FTIR band located at 2359 cm^{-1} which cannot be detected in the spectra.[390] Similar to CO_2, N_2 is a non-polar molecule, however, their kinetic diameters (3.30 and 3.64 Å, respectively for CO_2 and N_2), quadrupole moments (2.85 and 1, respectively for CO_2 and N_2) and polarizabilities (1.5 and 1, respectively for CO_2 and N_2) are different.[391] Moreover, CO_2 has an electron deficient carbon in its structure which increase its affinity towards electronegative species on the surfaces, whereas in the case of N_2, electronegativity of the surface does not affect its sorption.[305] In our case, releasing acidic C2H sites of cation creates electronegative species on the surface which will favor CO_2 sorption over N_2. As a result, decreasing N_2 sorption can be directly related to the pore blockage of the adsorbent, AC, by IL, [BMIM][OAc], and the low solubility of N_2 inside bulk [BMIM][OAc] (**Figure C.3.1(a)**) as it is explained above that the N_2 sorption will not be affected by the change in the surface characteristics.

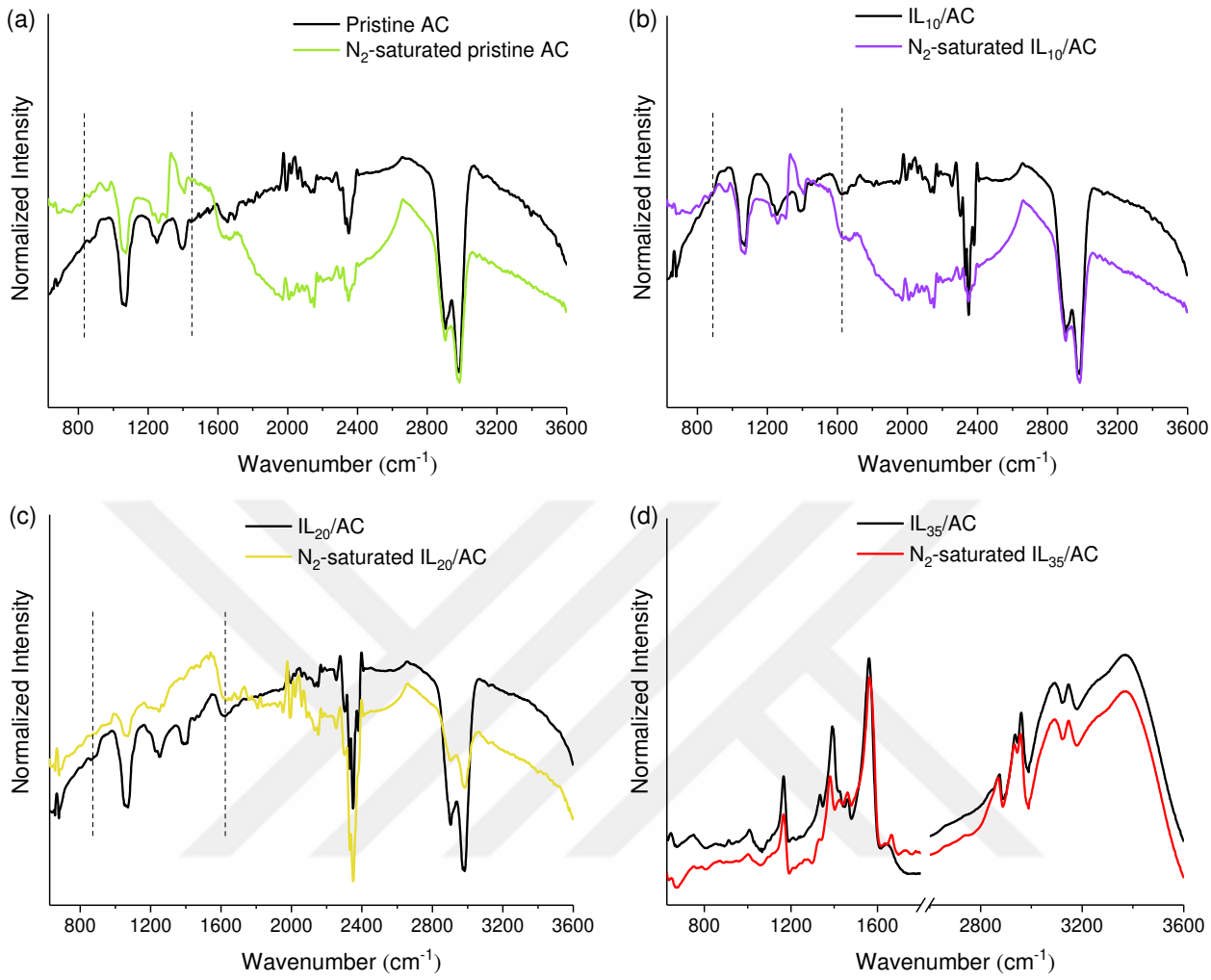

Figure C.19.1. FTIR spectra of (a) pristine AC and N_2-saturated pristine AC, (b) IL_{10}/AC and N_2-saturated IL_{10}/AC, (c) IL_{20}/AC and N_2-saturated IL_{20}/AC, and (d) IL_{35}/AC and N_2-saturated $[BMIM][OAc]_{35}$/AC between the region 3600-600 cm^{-1}.

C.20 Cyclic Gas Sorption Studies (Regeneration Studies)

Cyclic gas sorption studies were conducted to investigate the regeneration of best-performing adsorbent material among all prepared composites, IL_{35}/AC, as given in **Figure C.20.1-2**. In the case of both physiosorbed and chemisorbed CO_2 molecules, ten cycles were performed with two different batches of the composite. It was concluded that no significant performance decrease was observed after ten cyclic indicating a successful regeneration.

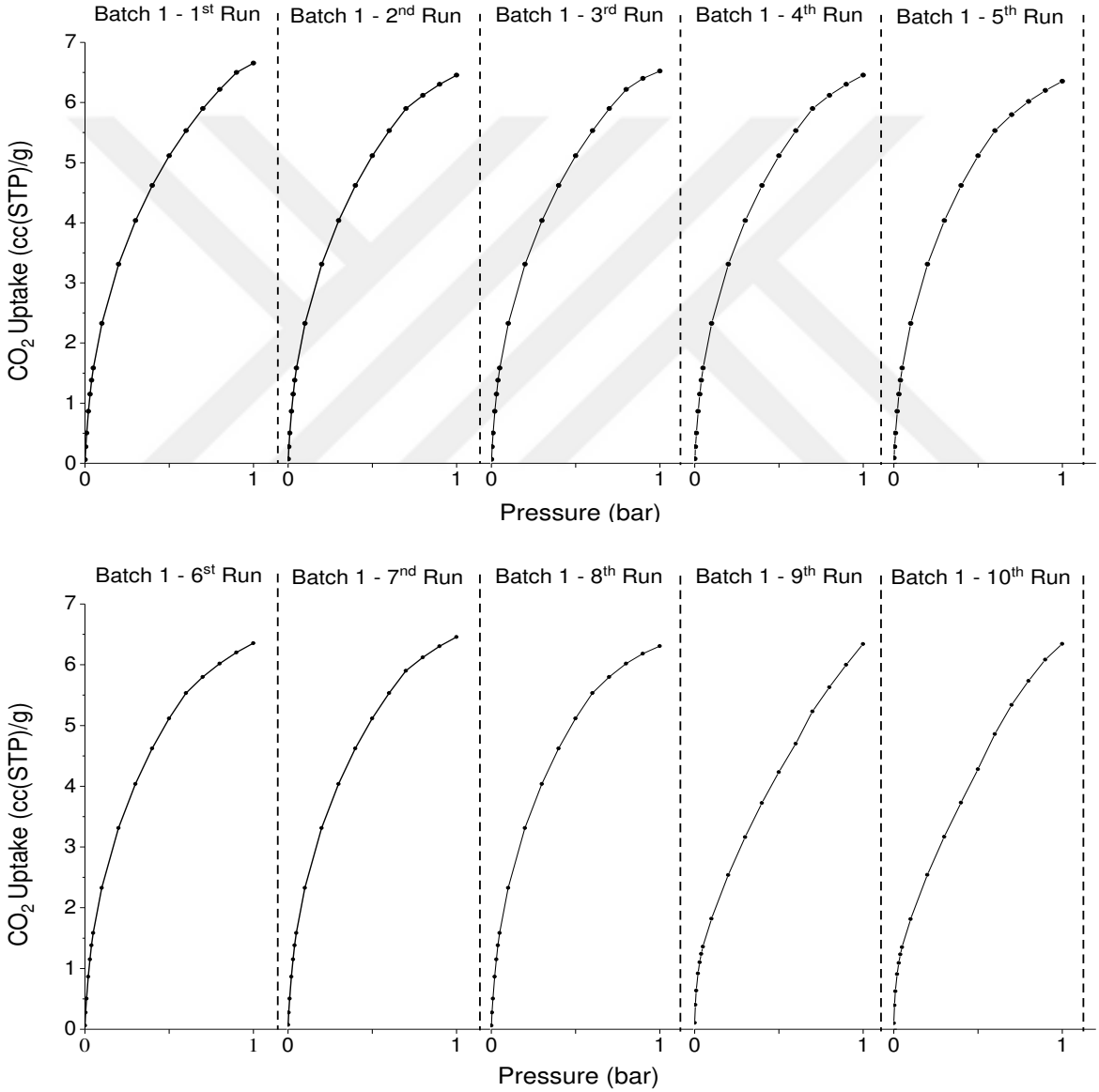

Figure C.20.1. CO_2 gas sorption results for cyclic performance with 1st batch of IL_{35}/AC up to ten cycles.

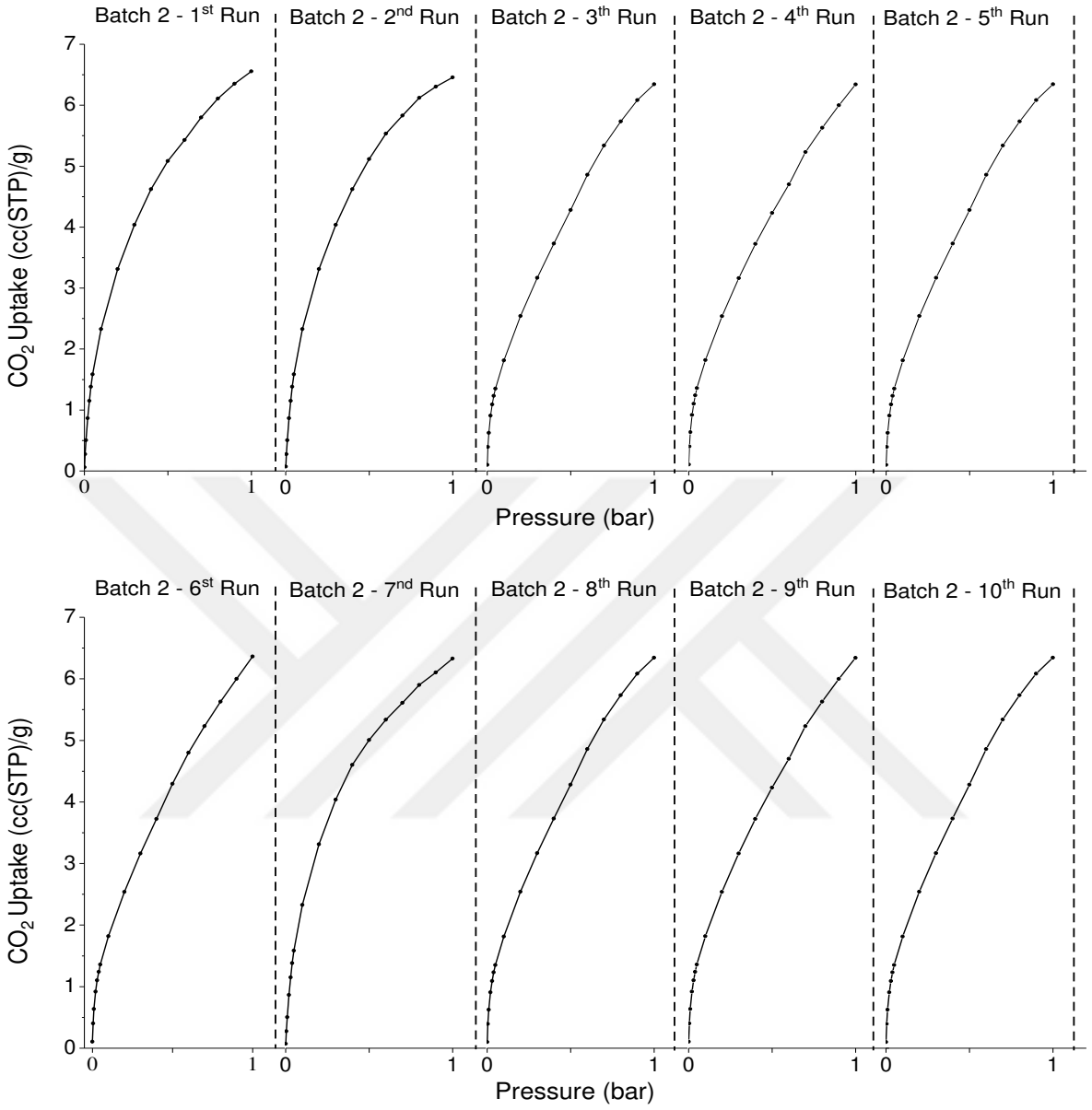

Figure C.20.2. CO_2 gas sorption results for cyclic performance with 2nd batch of IL_{35}/AC up to ten cycles.

BIBLIOGRAPHY

1. Marsh, K. N.; Boxall, J. A.; Lichtenthaler, R., Room temperature ionic liquids and their mixtures—a review. *Fluid Phase Equilib.* **2004,** *219* (1), 93-98.
2. Zeeshan, M.; Nozari, V.; Yagci, M. B.; Isık, T.; Unal, U.; Ortalan, V.; Keskin, S.; Uzun, A., Core–Shell Type Ionic Liquid/Metal Organic Framework Composite: An Exceptionally High CO_2/CH_4 Selectivity. *Journal of the American Chemical Society* **2018,** *140* (32), 10113-10116.
3. Yusuf, N. Y. M.; Masdar, M. S.; Isahak, W. N. R. W.; Nordin, D.; Husaini, T.; Majlan, E. H.; Wu, S. Y.; Rejab, S. A. M.; Lye, C. C., Impregnated carbon–ionic liquid as innovative adsorbent for H_2/CO_2 separation from biohydrogen. *Int. J. Hydrogen Energy* **2019,** *44* (6), 3414-3424.
4. Zeeshan, M.; Yalcin, K.; Sarac Oztuna, F. E.; Unal, U.; Keskin, S.; Uzun, A., A new class of porous materials for efficient CO_2 separation: Ionic liquid/graphene aerogel composites. *Carbon* **2021,** *171*, 79-87.
5. Sezginel, K. B.; Keskin, S.; Uzun, A., Tuning the Gas Separation Performance of CuBTC by Ionic Liquid Incorporation. *Langmuir* **2016,** *32* (4), 1139-1147.
6. Gupta, K. M.; Chen, Y.; Hu, Z.; Jiang, J., Metal–organic framework supported ionic liquid membranes for CO_2 capture: anion effects. *Phys. Chem. Chem. Phys.* **2012,** *14* (16), 5785-5794.
7. Wang, Z.; Zhou, H.; Meng, C.; Xiong, W.; Cai, Y.; Hu, P.; Pang, H.; Yuan, A., Enhancing Ion Transport: Function of Ionic Liquid Decorated MOFs in Polymer Electrolytes for All-Solid-State Lithium Batteries. *ACS Appl. Energy Mater.* **2020,** *3* (5), 4265-4274.
8. Kavak, S.; Kulak, H.; Polat, H. M.; Keskin, S.; Uzun, A., Fast and Selective Adsorption of Methylene Blue from Water Using [BMIM][PF_6]-Incorporated UiO-66 and NH_2-UiO-66. *Cryst. Growth Des.* **2020,** *20* (6), 3590-3595.
9. Luo, Q.-x.; An, B.-w.; Ji, M.; Zhang, J., Hybridization of metal–organic frameworks and task-specific ionic liquids: fundamentals and challenges. *Mater. Chem. Front* **2018,** *2* (2), 219-234.
10. Silva, F. W. M. d.; Magalhães, G. M.; Jardim, E. O.; Silvestre-Albero, J.; Sepúlveda-Escribano, A.; de Azevedo, D. C. S.; de Lucena, S. M. P., CO_2 Adsorption on Ionic Liquid—Modified Cu-BTC: Experimental and Simulation Study. *Adsorpt. Sci. Technol.* **2015,** *33* (2), 223-242.
11. Kinik, F. P.; Altintas, C.; Balci, V.; Koyuturk, B.; Uzun, A.; Keskin, S., [BMIM][PF_6] Incorporation Doubles CO_2 Selectivity of ZIF-8: Elucidation of Interactions and Their Consequences on Performance. *ACS Appl. Mater. Interfaces* **2016,** *8* (45), 30992-31005.
12. Koyuturk, B.; Altintas, C.; Kinik, F. P.; Keskin, S.; Uzun, A., Improving Gas Separation Performance of ZIF-8 by [BMIM][BF_4] Incorporation: Interactions and Their Consequences on Performance. *The Journal of Physical Chemistry C* **2017,** *121* (19), 10370-10381.
13. Kulak, H.; Polat, H. M.; Kavak, S.; Keskin, S.; Uzun, A., Improving CO_2 Separation Performance of MIL-53(Al) by Incorporating 1-n-Butyl-3-Methylimidazolium Methyl Sulfate. *Energy Technol.* **2019,** *7* (7), 1900157.
14. Xin, Y.; Wang, C.; Wang, Y.; Sun, J.; Gao, Y., Encapsulation of an ionic liquid into the nanopores of a 3D covalent organic framework. *RSC Advances* **2017,** *7* (3), 1697-1700.
15. Ding, L.-G.; Yao, B.-J.; Li, F.; Shi, S.-C.; Huang, N.; Yin, H.-B.; Guan, Q.; Dong, Y.-B., Ionic liquid-decorated COF and its covalent composite aerogel for selective CO_2 adsorption and catalytic conversion. *J. Mater. Chem. A* **2019,** *7* (9), 4689-4698.
16. Yu, Y.; Mai, J.; Wang, L.; Li, X.; Jiang, Z.; Wang, F., Ship-in-a-bottle synthesis of amine-functionalized ionic liquids in NaY zeolite for CO_2 capture. *Sci. Rep.* **2014,** *4* (1), 5997.
17. Li, H.; Zhang, T.; Yuan, S.; Tang, S., MCM-36 zeolites tailored with acidic ionic liquid to regulate adsorption properties of isobutane and 1-butene. *Chin. J. Chem. Eng.* **2016,** *24* (12), 1703-1711.
18. Tamilarasan, P.; Ramaprabhu, S., Integration of polymerized ionic liquid with graphene for enhanced CO_2 adsorption. *J. Mater. Chem. A* **2015,** *3* (1), 101-108.
19. Guo, C. X.; Lu, Z. S.; Lei, Y.; Li, C. M., Ionic liquid–graphene composite for ultratrace explosive trinitrotoluene detection. *Electrochem. Commun.* **2010,** *12* (9), 1237-1240.

20. Althuluth, M.; Overbeek, J. P.; Van Wees, H. J.; Zubeir, L. F.; Haije, W. G.; Berrouk, A.; Peters, C. J.; Kroon, M. C., Natural gas purification using supported ionic liquid membrane. *J. Membr. Sci.* **2015,** *484*, 80-86.
21. Halder, K.; Khan, M. M.; Grünauer, J.; Shishatskiy, S.; Abetz, C.; Filiz, V.; Abetz, V., Blend membranes of ionic liquid and polymers of intrinsic microporosity with improved gas separation characteristics. *J. Membr. Sci.* **2017,** *539*, 368-382.
22. Vu, M.-T.; Lin, R.; Diao, H.; Zhu, Z.; Bhatia, S. K.; Smart, S., Effect of ionic liquids (ILs) on MOFs/polymer interfacial enhancement in mixed matrix membranes. *J. Membr. Sci.* **2019,** *587*, 117157.
23. Ban, Y.; Li, Z.; Li, Y.; Peng, Y.; Jin, H.; Jiao, W.; Guo, A.; Wang, P.; Yang, Q.; Zhong, C.; Yang, W., Confinement of Ionic Liquids in Nanocages: Tailoring the Molecular Sieving Properties of ZIF-8 for Membrane-Based CO_2 Capture. *Angew. Chem. Int. Ed. Engl.* **2015,** *54* (51), 15483-7.
24. Ma, J.; Ying, Y.; Guo, X.; Huang, H.; Liu, D.; Zhong, C., Fabrication of mixed-matrix membrane containing metal–organic framework composite with task-specific ionic liquid for efficient CO_2 separation. *Journal of Materials Chemistry A* **2016,** *4* (19), 7281-7288.
25. Hudiono, Y. C.; Carlisle, T. K.; LaFrate, A. L.; Gin, D. L.; Noble, R. D., Novel mixed matrix membranes based on polymerizable room-temperature ionic liquids and SAPO-34 particles to improve CO_2 separation. *J. Membr. Sci.* **2011,** *370* (1-2), 141-148.
26. Rodriguez-Perez, L.; Teuma, E.; Falqui, A.; Gomez, M.; Serp, P., Supported ionic liquid phase catalysis on functionalized carbon nanotubes. *Chem. Commun.* **2008,** (35), 4201-3.
27. Luo, Q.-x.; Ji, M.; Lu, M.-h.; Hao, C.; Qiu, J.-s.; Li, Y.-q., Organic electron-rich N-heterocyclic compound as a chemical bridge: building a Brönsted acidic ionic liquid confined in MIL-101 nanocages. *J. Mater. Chem. A* **2013,** *1* (22), 6530-6534.
28. Nasrollahpour, A.; Moradi, S. E., Hexavalent chromium removal from water by ionic liquid modified metal-organic frameworks adsorbent. *Microporous Mesoporous Mater.* **2017,** *243*, 47-55.
29. Fujie, K.; Otsubo, K.; Ikeda, R.; Yamada, T.; Kitagawa, H., Low temperature ionic conductor: ionic liquid incorporated within a metal–organic framework. *Chem. Sci.* **2015,** *6* (7), 4306-4310.
30. Wang, Z.; Tan, R.; Wang, H.; Yang, L.; Hu, J.; Chen, H.; Pan, F., A Metal–Organic-Framework-Based Electrolyte with Nanowetted Interfaces for High-Energy-Density Solid-State Lithium Battery. *Adv. Mater.* **2018,** *30* (2), 1704436.
31. Kinik, F. P.; Uzun, A.; Keskin, S., Ionic Liquid/Metal-Organic Framework Composites: From Synthesis to Applications. *ChemSusChem* **2017,** *10* (14), 2842-2863.
32. Fuller, J.; Breda, A. C.; Carlin, R. T., Ionic Liquid-Polymer Gel Electrolytes. *J. Electrochem. Soc.* **1997,** *144* (4), L67-L70.
33. Jin, K.; Huang, X.; Pang, L.; Li, J.; Appel, A.; Wherland, S., $[Cu(i)(bpp)]BF_4$: the first extended coordination network prepared solvothermally in an ionic liquid solvent. *Chem. Commun.* **2002,** (23), 2872-2873.
34. Morris, R. E., Ionothermal synthesis—ionic liquids as functional solvents in the preparation of crystalline materials. *Chem. Commun.* **2009,** (21), 2990-2998.
35. Ji, Q.; Honma, I.; Paek, S.-M.; Akada, M.; Hill, J. P.; Vinu, A.; Ariga, K., Layer-by-Layer Films of Graphene and Ionic Liquids for Highly Selective Gas Sensing. *Angew. Chem. Int. Ed.* **2010,** *49* (50), 9737-9739.
36. Cooper, E. R.; Andrews, C. D.; Wheatley, P. S.; Webb, P. B.; Wormald, P.; Morris, R. E., Ionic liquids and eutectic mixtures as solvent and template in synthesis of zeolite analogues. *Nature* **2004,** *430* (7003), 1012-1016.
37. Chen, Y.; Hu, Z.; Gupta, K. M.; Jiang, J., Ionic Liquid/Metal–Organic Framework Composite for CO_2 Capture: A Computational Investigation. *J. Phys. Chem. C* **2011,** *115* (44), 21736-21742.
38. Khan, N. A.; Hasan, Z.; Jhung, S. H., Ionic Liquids Supported on Metal-Organic Frameworks: Remarkable Adsorbents for Adsorptive Desulfurization. *Chem. - Eur. J.* **2014,** *20* (2), 376-380.
39. Hu, Z.; Zhang, X.; Chen, S., A graphene oxide and ionic liquid assisted anion-immobilized polymer electrolyte with high ionic conductivity for dendrite-free lithium metal batteries. *J. of Power Sources* **2020,** *477*, 228754.

40. Chen, S.; Yuan, B.; Liu, G.; Zhang, D., Electrochemical Sensors Based on Covalent Organic Frameworks: A Critical Review. *Front. Chem.* **2020,** *8* (1082).
41. Zeeshan, M.; Kulak, H.; Kavak, S.; Polat, H. M.; Durak, O.; Keskin, S.; Uzun, A., Influence of anion size and electronic structure on the gas separation performance of ionic liquid/ZIF-8 composites. *Microporous and Mesoporous Materials* **2020,** *306*, 110446.
42. Parnham, E. R.; Morris, R. E., Ionothermal Synthesis of Zeolites, Metal–Organic Frameworks, and Inorganic–Organic Hybrids. *Acc. Chem. Res.* **2007,** *40* (10), 1005-1013.
43. Guan, X.; Ma, Y.; Li, H.; Yusran, Y.; Xue, M.; Fang, Q.; Yan, Y.; Valtchev, V.; Qiu, S., Fast, Ambient Temperature and Pressure Ionothermal Synthesis of Three-Dimensional Covalent Organic Frameworks. *J. Am. Chem. Soc.* **2018,** *140* (13), 4494-4498.
44. Zdolšek, N.; Rocha, R. P.; Krstić, J.; Trtić-Petrović, T.; Šljukić, B.; Figueiredo, J. L.; Vujković, M. J., Electrochemical investigation of ionic liquid-derived porous carbon materials for supercapacitors: pseudocapacitance versus electrical double layer. *Electrochim. Acta* **2019,** *298*, 541-551.
45. Antonietti, M.; Kuang, D.; Smarsly, B.; Zhou, Y., Ionic liquids for the convenient synthesis of functional nanoparticles and other inorganic nanostructures. *Angew. Chem. Int. Ed. Engl.* **2004,** *43* (38), 4988-92.
46. Taubert, A.; Li, Z., Inorganic materials from ionic liquids. *Dalton Transactions* **2007,** (7), 723-727.
47. Thomas, A.; Ahamed, R.; Prakash, M., Selection of a suitable ZIF-8/ionic liquid (IL) based composite for selective CO_2 capture: the role of anions at the interface. *RSC Advances* **2020,** *10* (64), 39160-39170.
48. Dybtsev, D. N.; Chun, H.; Kim, K., Three-dimensional metal–organic framework with (3,4)-connected net, synthesized from an ionic liquid medium. *Chem. Commun.* **2004,** (14), 1594-1595.
49. Zhang, J.; Chen, S.; Bu, X., Multiple functions of ionic liquids in the synthesis of three-dimensional low-connectivity homochiral and achiral frameworks. *Angewandte Chemie (International ed. in English)* **2008,** *47* (29), 5434-5437.
50. Xiao, W.; Sun, Z.; Chen, S.; Zhang, H.; Zhao, Y.; Huang, C.; Liu, Z., Ionic liquid-stabilized graphene and its use in immobilizing a metal nanocatalyst. *RSC Advances* **2012,** *2* (21), 8189-8193.
51. Zawada Donato, K.; Matějka, L.; Mauler, R.; Donato, R., Recent Applications of Ionic Liquids in the Sol-Gel Process for Polymer–Silica Nanocomposites with Ionic Interfaces. *Colloids and Interfaces* **2017,** *1*, 5.
52. Vioux, A.; Viau, L.; Volland, S.; Le Bideau, J., Use of ionic liquids in sol-gel; ionogels and applications. *Comptes Rendus Chimie* **2010,** *13* (1), 242-255.
53. Durak, Ö.; Kulak, H.; Kavak, S.; Polat, H. M.; Keskin, S.; Uzun, A., Towards complete elucidation of structural factors controlling thermal stability of IL/MOF composites: effects of ligand functionalization on MOFs. *J. Phys.: Condens. Matter* **2020,** *32* (48), 484001.
54. Li, M.; Pham, P. J.; Pittman Jr, C. U.; Li, T., Selective solid-phase extraction of α-tocopherol by functionalized ionic liquid-modified mesoporous SBA-15 adsorbent. *Anal. Sci.* **2008,** *24* (10), 1245-1250.
55. Vangeli, O. C.; Romanos, G. E.; Beltsios, K. G.; Fokas, D.; Kouvelos, E. P.; Stefanopoulos, K. L.; Kanellopoulos, N. K., Grafting of Imidazolium Based Ionic Liquid on the Pore Surface of Nanoporous Materials—Study of Physicochemical and Thermodynamic Properties. *The Journal of Physical Chemistry B* **2010,** *114* (19), 6480-6491.
56. Han, M.; Gu, Z.; Chen, C.; Wu, Z.; Que, Y.; Wang, Q.; Wan, H.; Guan, G., Efficient confinement of ionic liquids in MIL-100(Fe) frameworks by the "impregnation-reaction-encapsulation" strategy for biodiesel production. *RSC Advances* **2016,** *6* (43), 37110-37117.
57. Li, H.; Tuo, L.; Yang, K.; Jeong, H.-K.; Dai, Y.; He, G.; Zhao, W., Simultaneous enhancement of mechanical properties and CO_2 selectivity of ZIF-8 mixed matrix membranes: Interfacial toughening effect of ionic liquid. *J. Membr. Sci.* **2016,** *511*, 130-142.
58. Chen, C.; Wu, Z.; Que, Y.; Li, B.; Guo, Q.; Li, Z.; Wang, L.; Wan, H.; Guan, G., Immobilization of a thiol-functionalized ionic liquid onto HKUST-1 through thiol compounds as the chemical bridge. *RSC Advances* **2016,** *6* (59), 54119-54128.

59. Hassan, H. M. A.; Betiha, M. A.; Mohamed, S. K.; El-Sharkawy, E. A.; Ahmed, E. A., Stable and recyclable MIL-101(Cr)–Ionic liquid based hybrid nanomaterials as heterogeneous catalyst. *J. Mol. Liq.* **2017,** *236*, 385-394.
60. Abednatanzi, S.; Abbasi, A.; Masteri-Farahani, M., Immobilization of catalytically active polyoxotungstate into ionic liquid-modified MIL-100(Fe): A recyclable catalyst for selective oxidation of benzyl alcohol. *Catal. Commun.* **2017,** *96*, 6-10.
61. Wu, J.; Gao, Y.; Zhang, W.; Tan, Y.; Tang, A.; Men, Y.; Tang, B., Deep desulfurization by oxidation using an active ionic liquid-supported Zr metal–organic framework as catalyst. *Applied Organometallic Chemistry* **2015,** *29* (2), 96-100.
62. Luo, Q.-x.; Song, X.-d.; Ji, M.; Park, S.-E.; Hao, C.; Li, Y.-q., Molecular size- and shape-selective Knoevenagel condensation over microporous Cu3(BTC)2 immobilized amino-functionalized basic ionic liquid catalyst. *Appl. Catal., A* **2014,** *478*, 81-90.
63. Wan, H.; Chen, C.; Wu, Z.; Que, Y.; Feng, Y.; Wang, W.; Wang, L.; Guan, G.; Liu, X., Encapsulation of Heteropolyanion-Based Ionic Liquid within the Metal–Organic Framework MIL-100(Fe) for Biodiesel Production. *ChemCatChem* **2015,** *7* (3), 441-449.
64. Nasrollahpour, A.; Moradi, S. E.; Baniamerian, M. J., Vortex-Assisted Dispersive Solid-Phase Microextraction Using Ionic Liquid-Modified Metal-Organic Frameworks of PAHs from Environmental Water, Vegetable, and Fruit Juice Samples. *Food Anal. Methods* **2017,** *10* (8), 2815-2826.
65. Abednatanzi, S.; Leus, K.; Derakhshandeh, P. G.; Nahra, F.; De Keukeleere, K.; Van Hecke, K.; Van Driessche, I.; Abbasi, A.; Nolan, S. P.; Der Voort, P. V., POM@IL-MOFs – inclusion of POMs in ionic liquid modified MOFs to produce recyclable oxidation catalysts. *Catal. Sci. Technol.* **2017,** *7* (7), 1478-1487.
66. Fujie, K.; Yamada, T.; Ikeda, R.; Kitagawa, H., Introduction of an Ionic Liquid into the Micropores of a Metal–Organic Framework and Its Anomalous Phase Behavior. *Angew. Chem. Int. Ed.* **2014,** *53* (42), 11302-11305.
67. Li, M.; Pham, P. J.; Wang, T.; Li, T. In *Synthesis of ionic liquids immobilized mesoporous adsorbents with silver salts and applications in concentration of polyunsaturated fatty acid methyl esters*, ACS National Meeting Book of Abstracts, 2007.
68. Dhumal, N. R.; Singh, M. P.; Anderson, J. A.; Kiefer, J.; Kim, H. J., Molecular Interactions of a Cu-Based Metal–Organic Framework with a Confined Imidazolium-Based Ionic Liquid: A Combined Density Functional Theory and Experimental Vibrational Spectroscopy Study. *J. Phys. Chem. C* **2016,** *120* (6), 3295-3304.
69. Sun, X.-L.; Deng, W.-H.; Chen, H.; Han, H.-L.; Taylor, J. M.; Wan, C.-Q.; Xu, G., A Metal–Organic Framework Impregnated with a Binary Ionic Liquid for Safe Proton Conduction above 100 °C. *Chem. Eur. J.* **2017,** *23* (6), 1248-1252.
70. Khan, N. A.; Hasan, Z.; Jhung, S. H., Ionic liquid@MIL-101 prepared via the ship-in-bottle technique: remarkable adsorbents for the removal of benzothiophene from liquid fuel. *Chem. Commun.* **2016,** *52* (12), 2561-2564.
71. Park, S.; Jeong, H.-K., Highly H_2O permeable ionic liquid encapsulated metal–organic framework membranes for energy-efficient air-dehumidification. *J. Mater. Chem. A* **2020,** *8* (44), 23645-23653.
72. Li, Z.; Wang, W.; Chen, Y.; Xiong, C.; He, G.; Cao, Y.; Wu, H.; Guiver, M. D.; Jiang, Z., Constructing efficient ion nanochannels in alkaline anion exchange membranes by the in situ assembly of a poly(ionic liquid) in metal–organic frameworks. *J. Mater. Chem. A* **2016,** *4* (6), 2340-2348.
73. Macchione, M. A.; Biglione, C.; Strumia, M., Design, Synthesis and Architectures of Hybrid Nanomaterials for Therapy and Diagnosis Applications. *Polymers* **2018,** *10* (5).
74. Pizzoccaro-Zilamy, M. A.; Piña, S. M.; Rebiere, B.; Daniel, C.; Farrusseng, D.; Drobek, M.; Silly, G.; Julbe, A.; Guerrero, G., Controlled grafting of dialkylphosphonate-based ionic liquids on γ-alumina: design of hybrid materials with high potential for CO_2 separation applications. *RSC Advances* **2019,** *9* (35), 19882-19894.
75. Tamilarasan, P.; Ramaprabhu, S., Amine-rich ionic liquid grafted graphene for sub-ambient carbon dioxide adsorption. *RSC Advances* **2016,** *6* (4), 3032-3040.

76. Han, L.; Li, H.; Choi, S.-J.; Park, M.-S.; Lee, S.-M.; Kim, Y.-J.; Park, D.-W., Ionic liquids grafted on carbon nanotubes as highly efficient heterogeneous catalysts for the synthesis of cyclic carbonates. *Appl. Catal., A* **2012,** *429-430*, 67-72.
77. Le, C. M. Q.; Cao, X. T.; Bach, L. G.; Lee, W.-K.; Kang, I.; Lim, K. T., Direct grafting imidazolium-based poly(ionic liquid) onto multiwalled carbon nanotubes via Diels-Alder "click" reaction. *Molecular Crystals and Liquid Crystals* **2018,** *660* (1), 143-149.
78. Soengas, R.; Navarro, Y.; Iglesias, M. J.; López-Ortiz, F., Immobilized Gold Nanoparticles Prepared from Gold(III)-Containing Ionic Liquids on Silica: Application to the Sustainable Synthesis of Propargylamines. *Molecules* **2018,** *23* (11).
79. Zeeshan, M.; Nozari, V.; Keskin, S.; Uzun, A., Structural Factors Determining Thermal Stability Limits of Ionic Liquid/MOF Composites: Imidazolium Ionic Liquids Combined with CuBTC and ZIF-8. *Ind. Eng. Chem. Res.* **2019,** *58* (31), 14124-14138.
80. Bowers, C., Matrix Effect Corrections in X-ray Fluorescence Spectrometry. *J. Chem. Educ.* **2019,** *96* (11), 2597-2599.
81. Ferreira, T. J.; Ribeiro, R. P.; Mota, J. P.; Rebelo, L. P.; Esperança, J. M.; Esteves, I. A., Ionic Liquid-Impregnated Metal–Organic Frameworks for CO_2/CH_4 Separation. *ACS Appl. Nano Mater.* **2019,** *2* (12), 7933-7950.
82. Torralba-Calleja, E.; Skinner, J.; Gutiérrez-Tauste, D., CO_2 Capture in Ionic Liquids: A Review of Solubilities and Experimental Methods. *Journal of Chemistry* **2013,** *2013*, 473584.
83. Lei, Z.; Dai, C.; Chen, B., Gas Solubility in Ionic Liquids. *Chem. Rev.* **2014,** *114* (2), 1289-1326.
84. Cabaço, M. I.; Besnard, M.; Danten, Y.; Coutinho, J. A. P., Carbon Dioxide in 1-Butyl-3-methylimidazolium Acetate. I. Unusual Solubility Investigated by Raman Spectroscopy and DFT Calculations. *The Journal of Physical Chemistry A* **2012,** *116* (6), 1605-1620.
85. Kinik, F. P.; Altintas, C.; Balci, V.; Koyuturk, B.; Uzun, A.; Keskin, S., [BMIM][PF_6] Incorporation Doubles CO_2 Selectivity of ZIF-8: Elucidation of Interactions and Their Consequences on Performance. *ACS Applied Materials & Interfaces* **2016,** *8* (45), 30992-31005.
86. Mohamedali, M.; Ibrahim, H.; Henni, A., Incorporation of acetate-based ionic liquids into a zeolitic imidazolate framework (ZIF-8) as efficient sorbents for carbon dioxide capture. *Chem. Eng. J.* **2018,** *334*, 817-828.
87. Ferreira, T. J.; Ribeiro, R. P.; Mota, J. P.; Rebelo, L. P.; Esperança, J. M.; Esteves, I. A. J. A. A. N. M., Ionic Liquid-Impregnated Metal–Organic Frameworks for CO_2/CH_4 Separation. **2019,** *2* (12), 7933-7950.
88. Ding, M.; Jiang, H.-L., Incorporation of Imidazolium-Based Poly(ionic liquid)s into a Metal–Organic Framework for CO_2 Capture and Conversion. *ACS Catalysis* **2018,** *8* (4), 3194-3201.
89. Kavak, S.; Polat, H. M.; Kulak, H.; Keskin, S.; Uzun, A., MIL-53(Al) as a Versatile Platform for Ionic-Liquid/MOF Composites to Enhance CO_2 Selectivity over CH_4 and N_2. *Chem Asian J* **2019,** *14* (20), 3655-3667.
90. Zeeshan, M.; Gulbalkan, H. C.; Durak, O.; Haslak, Z. P.; Unal, U.; Keskin, S.; Uzun, A., An Integrated Computational–Experimental Hierarchical Approach for the Rational Design of an IL/UiO-66 Composite Offering Infinite CO_2 Selectivity. *Advanced Functional Materials* **2022,** *n/a* (n/a), 2204149.
91. Erto, A.; Silvestre-Albero, A.; Silvestre-Albero, J.; Rodríguez-Reinoso, F.; Balsamo, M.; Lancia, A.; Montagnaro, F., Carbon-supported ionic liquids as innovative adsorbents for CO_2 separation from synthetic flue-gas. *J. Colloid Interface Sci.* **2015,** *448*, 41-50.
92. Raja Shahrom, M. S.; Nordin, A. R.; Wilfred, C. D., The improvement of activated carbon as CO_2 adsorbent with supported amine functionalized ionic liquids. *J. Environ. Eng. Technol.* **2019,** *7* (5), 103319.
93. He, X.; Zhu, J.; Wang, H.; Zhou, M.; Zhang, S., Surface Functionalization of Activated Carbon with Phosphonium Ionic Liquid for CO_2 Adsorption. *Coatings* **2019,** *9* (9).
94. Abbas, T.; Gonfa, G.; Lethesh, K. C.; Mutalib, M. I. A.; Abai, M. b.; Cheun, K. Y.; Khan, E., Mercury capture from natural gas by carbon supported ionic liquids: Synthesis, evaluation and molecular mechanism. *Fuel* **2016,** *177*, 296-303.

95. Severa, G.; Bethune, K.; Rocheleau, R.; Higgins, S., SO_2 sorption by activated carbon supported ionic liquids under simulated atmospheric conditions. *Chem. Eng. J.* **2015,** *265*, 249-258.
96. Tamilarasan, P.; Ramaprabhu, S., Ionic liquid functionalization – an effective way to tune carbon dioxide adsorption properties of carbon nanotubes. *RSC Advances* **2015,** *5* (44), 35098-35106.
97. Ghosh, S.; Ramaprabhu, S., High-pressure investigation of ionic functionalized graphitic carbon nitride nanostructures for CO_2 capture. *J.* CO_2 *Util.* **2017,** *21*, 89-99.
98. Groom, C. R.; Bruno, I. J.; Lightfoot, M. P.; Ward, S. C., The Cambridge Structural Database. *Acta Crystallographica Section B* **2016,** *72* (2), 171-179.
99. Warren, B. E., X-Ray Diffraction in Random Layer Lattices. *Physical Review* **1941,** *59* (9), 693-698.
100. Momma, K.; Izumi, F., VESTA 3 for three-dimensional visualization of crystal, volumetric and morphology data. *Journal of Applied Crystallography* **2011,** *44* (6), 1272-1276.
101. Wojdyr, M., Fityk: a general-purpose peak fitting program. *J. Appl. Crystallogr.* **2010,** *43* (5 Part 1), 1126-1128.
102. Boehm, H. P., Surface oxides on carbon and their analysis: a critical assessment. *Carbon* **2002,** *40* (2), 145-149.
103. Goertzen, S. L.; Thériault, K. D.; Oickle, A. M.; Tarasuk, A. C.; Andreas, H. A., Standardization of the Boehm titration. Part I. CO_2 expulsion and endpoint determination. *Carbon* **2010,** *48* (4), 1252-1261.
104. Klamt, A., The COSMO and COSMO-RS solvation models. *WIREs Computational Molecular Science* **2018,** *8* (1), e1338.
105. Anantharaj, R.; Banerjee, T., COSMO-RS-Based Screening of Ionic Liquids as Green Solvents in Denitrification Studies. *Industrial & Engineering Chemistry Research* **2010,** *49* (18), 8705-8725.
106. Sistla, Y. S.; Khanna, A., Validation and Prediction of the Temperature-Dependent Henry's Constant for CO_2–Ionic Liquid Systems Using the Conductor-like Screening Model for Realistic Solvation (COSMO-RS). *Journal of Chemical & Engineering Data* **2011,** *56* (11), 4045-4060.
107. Paduszyński, K., An overview of the performance of the COSMO-RS approach in predicting the activity coefficients of molecular solutes in ionic liquids and derived properties at infinite dilution. *Physical Chemistry Chemical Physics* **2017,** *19* (19), 11835-11850.
108. Lee, S.; Lee, J. H.; Kim, J., User-friendly graphical user interface software for ideal adsorbed solution theory calculations. *Korean Journal of Chemical Engineering* **2018,** *35* (1), 214-221.
109. Myers, A. L.; Prausnitz, J. M., Thermodynamics of mixed-gas adsorption. *AIChE Journal* **1965,** *11* (1), 121-127.
110. Walton, K. S.; Sholl, D. S., Predicting multicomponent adsorption: 50 years of the ideal adsorbed solution theory. *AIChE Journal* **2015,** *61* (9), 2757-2762.
111. Sumida, K.; Rogow, D. L.; Mason, J. A.; McDonald, T. M.; Bloch, E. D.; Herm, Z. R.; Bae, T. H.; Long, J. R., Carbon dioxide capture in metal-organic frameworks. *Chem Rev* **2012,** *112* (2), 724-81.
112. Herm, Z. R.; Swisher, J. A.; Smit, B.; Krishna, R.; Long, J. R., Metal−Organic Frameworks as Adsorbents for Hydrogen Purification and Precombustion Carbon Dioxide Capture. *Journal of the American Chemical Society* **2011,** *133* (15), 5664-5667.
113. Furukawa, H.; Cordova, K. E.; O'Keeffe, M.; Yaghi, O. M., The chemistry and applications of metal-organic frameworks. *Science* **2013,** *341* (6149), 1230444.
114. Li, J. R.; Kuppler, R. J.; Zhou, H. C., Selective gas adsorption and separation in metal-organic frameworks. *Chem Soc Rev* **2009,** *38* (5), 1477-504.
115. Horcajada, P.; Gref, R.; Baati, T.; Allan, P. K.; Maurin, G.; Couvreur, P.; Férey, G.; Morris, R. E.; Serre, C., Metal-organic frameworks in biomedicine. *Chemical Reviews* **2012,** *112* (2), 1232-1268.
116. Della Rocca, J.; Liu, D.; Lin, W., Nanoscale metal-organic frameworks for biomedical imaging and drug delivery. *Accounts of Chemical Research* **2011,** *44* (10), 957-968.
117. An, J.; Geib, S. J.; Rosi, N. L., Cation-triggered drug release from a porous zinc-adeninate metal-organic framework. *Journal of the American Chemical Society* **2009,** *131* (24), 8376-8377.

118. Burtch, N. C.; Jasuja, H.; Walton, K. S., Water stability and adsorption in metal-organic frameworks. *Chemical Reviews* **2014,** *114* (20), 10575-10612.
119. Kavak, S.; Kulak, H.; Polat, H. M.; Keskin, S.; Uzun, A., Fast and Selective Adsorption of Methylene Blue from Water Using [BMIM][PF6]-Incorporated UiO-66 and NH_2-UiO-66. *Crystal Growth & Design* **2020**.
120. Haque, E.; Jun, J. W.; Jhung, S. H., Adsorptive removal of methyl orange and methylene blue from aqueous solution with a metal-organic framework material, iron terephthalate (MOF-235). *Journal of Hazardous Materials* **2011,** *185* (1), 507-511.
121. Yang, D.; Gaggioli, C. A.; Conley, E.; Babucci, M.; Gagliardi, L.; Gates, B. C., Synthesis and characterization of tetrairidium clusters in the metal organic framework UiO-67: Catalyst for ethylene hydrogenation. *Journal of Catalysis* **2020,** *382*, 165-172.
122. Jiang, H.; Wang, Q.; Wang, H.; Chen, Y.; Zhang, M., MOF-74 as an Efficient Catalyst for the Low-Temperature Selective Catalytic Reduction of NOx with NH3. *ACS Applied Materials & Interfaces* **2016,** *8* (40), 26817-26826.
123. Trickett, C. A.; Osborn Popp, T. M.; Su, J.; Yan, C.; Weisberg, J.; Huq, A.; Urban, P.; Jiang, J.; Kalmutzki, M. J.; Liu, Q.; Baek, J.; Head-Gordon, M. P.; Somorjai, G. A.; Reimer, J. A.; Yaghi, O. M., Identification of the strong Brønsted acid site in a metal–organic framework solid acid catalyst. *Nature Chemistry* **2019,** *11* (2), 170-176.
124. Lustig, W. P.; Mukherjee, S.; Rudd, N. D.; Desai, A. V.; Li, J.; Ghosh, S. K., Metal-organic frameworks: Functional luminescent and photonic materials for sensing applications. *Chemical Society Reviews* **2017,** *46* (11), 3242-3285.
125. Kreno, L. E.; Leong, K.; Farha, O. K.; Allendorf, M.; Van Duyne, R. P.; Hupp, J. T., Metal-organic framework materials as chemical sensors. *Chemical Reviews* **2012,** *112* (2), 1105-1125.
126. Wang, C.; Zhang, T.; Lin, W., Rational synthesis of noncentrosymmetric metal-organic frameworks for second-order nonlinear optics. *Chemical Reviews* **2012,** *112* (2), 1084-1104.
127. Kim, S. H.; Lee, Y. J.; Kim, D. H.; Lee, Y. J., Bimetallic Metal-Organic Frameworks as Efficient Cathode Catalysts for Li-O_2 Batteries. *ACS Applied Materials and Interfaces* **2018,** *10* (1), 660-667.
128. Han, Y.; Qi, P.; Zhou, J.; Feng, X.; Li, S.; Fu, X.; Zhao, J.; Yu, D.; Wang, B., Metal-organic frameworks (MOFs) as sandwich coating cushion for silicon anode in lithium ion batteries. *ACS Applied Materials and Interfaces* **2015,** *7* (48), 26608-26613.
129. Li, M.; Wan, Y.; Huang, J. K.; Assen, A. H.; Hsiung, C. E.; Jiang, H.; Han, Y.; Eddaoudi, M.; Lai, Z.; Ming, J.; Li, L. J., Metal-Organic Framework-Based Separators for Enhancing Li-S Battery Stability: Mechanism of Mitigating Polysulfide Diffusion. *ACS Energy Letters* **2017,** *2* (10), 2362-2367.
130. Furukawa, H.; Cordova, K. E.; O'Keeffe, M.; Yaghi, O. M., The Chemistry and Applications of Metal-Organic Frameworks. *Science* **2013,** *341* (6149), 1230444.
131. Rowsell, J. L. C.; Yaghi, O. M., Effects of Functionalization, Catenation, and Variation of the Metal Oxide and Organic Linking Units on the Low-Pressure Hydrogen Adsorption Properties of Metal−Organic Frameworks. *Journal of the American Chemical Society* **2006,** *128* (4), 1304-1315.
132. Maurin, G.; Serre, C.; Cooper, A.; Férey, G., The new age of MOFs and of their porous-related solids. *Chemical Society Reviews* **2017,** *46* (11), 3104-3107.
133. Yaghi, O. M.; O'Keeffe, M.; Ockwig, N. W.; Chae, H. K.; Eddaoudi, M.; Kim, J., Reticular synthesis and the design of new materials. *Nature* **2003,** *423* (6941), 705-14.
134. Chen, Z.; Xiang, S.; Arman, H. D.; Mondal, J. U.; Li, P.; Zhao, D.; Chen, B., Three-Dimensional Pillar-Layered Copper(II) Metal−Organic Framework with Immobilized Functional OH Groups on Pore Surfaces for Highly Selective CO_2/CH_4 and C_2H_2/CH_4 Gas Sorption at Room Temperature. *Inorganic Chemistry* **2011,** *50* (8), 3442-3446.
135. Sun, D.; Sun, F.; Deng, X.; Li, Z., Mixed-Metal Strategy on Metal–Organic Frameworks (MOFs) for Functionalities Expansion: Co Substitution Induces Aerobic Oxidation of Cyclohexene over Inactive Ni-MOF-74. *Inorganic Chemistry* **2015,** *54* (17), 8639-8643.
136. Wang, N.; Mundstock, A.; Liu, Y.; Huang, A.; Caro, J., Amine-modified Mg-MOF-74/CPO-27-Mg membrane with enhanced H_2/CO_2 separation. *Chemical Engineering Science* **2015,** *124*, 27-36.

137. Fang, Z.; Bueken, B.; De Vos, D. E.; Fischer, R. A., Defect-Engineered Metal-Organic Frameworks. *Angew Chem Int Ed Engl* **2015,** *54* (25), 7234-54.
138. Kavak, S.; Polat, H. M.; Kulak, H.; Keskin, S.; Uzun, A., MIL-53(Al) as a Versatile Platform for Ionic-Liquid/MOF Composites to Enhance CO_2 Selectivity over CH_4 and N_2. *Chem Asian J* **2019,** *14* (20), 3655-3667.
139. Babucci, M.; Fang, C.-Y.; Hoffman, A. S.; Bare, S. R.; Gates, B. C.; Uzun, A., Tuning the Selectivity of Single-Site Supported Metal Catalysts with Ionic Liquids. *ACS Catalysis* **2017,** *7* (10), 6969-6972.
140. Babucci, M.; Hoffman, A. S.; Debefve, L. M.; Fatma Kurtoglu, S.; Bare, S. R.; Gates, B. C.; Uzun, A., Unraveling the Individual Influences of Supports and Ionic Liquid Coatings on the Catalytic Properties of Supported Iridium Complexes and Iridium Clusters. *Journal of Catalysis* **2020**.
141. Babucci, M.; Fang, C.-Y.; Perez-Aguilar, J. E.; Hoffman, A. S.; Boubnov, A.; Guan, E.; Bare, S. R.; Gates, B. C.; Uzun, A., Controlling catalytic activity and selectivity for partial hydrogenation by tuning the environment around active sites in iridium complexes bonded to supports. *Chemical Science* **2019,** *10* (9), 2623-2632.
142. Chen, C.; Feng, N.; Guo, Q.; Li, Z.; Li, X.; Ding, J.; Wang, L.; Wan, H.; Guan, G., Surface engineering of a chromium metal-organic framework with bifunctional ionic liquids for selective CO_2 adsorption: Synergistic effect between multiple active sites. *J Colloid Interface Sci* **2018,** *521*, 91-101.
143. Mohamedali, M.; Henni, A.; Ibrahim, H., Investigation of CO_2 capture using acetate-based ionic liquids incorporated into exceptionally porous metal–organic frameworks. *Adsorption* **2019,** *25* (4), 675-692.
144. Xia, X.; Hu, G.; Li, W.; Li, S., Understanding Reduced CO_2 Uptake of Ionic Liquid/Metal-Organic Framework (IL/MOF) Composites. *ACS Applied Nano Materials* **2019,** *2* (9), 6022-6029.
145. Nozari, V.; Keskin, S.; Uzun, A., Toward Rational Design of Ionic Liquid/Metal–Organic Framework Composites: Effects of Interionic Interaction Energy. *ACS Omega* **2017,** *2* (10), 6613-6618.
146. Nozari, V.; Zeeshan, M.; Keskin, S.; Uzun, A., Effect of methylation of ionic liquids on the gas separation performance of ionic liquid/metal–organic framework composites. *CrystEngComm* **2018,** *20* (44), 7137-7143.
147. Kandiah, M.; Nilsen, M. H.; Usseglio, S.; Jakobsen, S.; Olsbye, U.; Tilset, M.; Larabi, C.; Quadrelli, E. A.; Bonino, F.; Lillerud, K. P., Synthesis and Stability of Tagged UiO-66 Zr-MOFs. *Chemistry of Materials* **2010,** *22* (24), 6632-6640.
148. DeCoste, J. B.; Peterson, G. W.; Jasuja, H.; Glover, T. G.; Huang, Y.-g.; Walton, K. S., Stability and degradation mechanisms of metal–organic frameworks containing the Zr6O4(OH)4 secondary building unit. *Journal of Materials Chemistry A* **2013,** *1* (18), 5642-5650.
149. Adamová, G.; Gardas, R. L.; Nieuwenhuyzen, M.; Puga, A. V.; Rebelo, L. P. N.; Robertson, A. J.; Seddon, K. R., Alkyltributylphosphonium chloride ionic liquids: synthesis, physicochemical properties and crystal structure. *Dalton Transactions* **2012,** *41* (27), 8316-8332.
150. Kulak, H.; Polat, H. M.; Kavak, S.; Keskin, S.; Uzun, A., Improving CO_2 Separation Performance of MIL-53(Al) by Incorporating 1-n-Butyl-3-Methylimidazolium Methyl Sulfate. *Energy Technol (Weinh)* **2019,** *7* (7), 1900157.
151. Mohamedali, M.; Henni, A.; Ibrahim, H., Markedly improved CO_2 uptake using imidazolium-based ionic liquids confined into HKUST-1 frameworks. *Microporous and Mesoporous Materials* **2019,** *284*, 98-110.
152. Zhang, Q.-G.; Wang, N.-N.; Yu, Z.-W., The Hydrogen Bonding Interactions between the Ionic Liquid 1-Ethyl-3-Methylimidazolium Ethyl Sulfate and Water. *The Journal of Physical Chemistry B* **2010,** *114* (14), 4747-4754.
153. Andanson, J.-m.; Traïkia, M.; Husson, P., Ionic association and interactions in aqueous methylsulfate alkyl-imidazolium-based ionic liquids. *The Journal of Chemical Thermodynamics* **2014,** *77*, 214-221.
154. Singh, T.; Kumar, A., Cation–anion–water interactions in aqueous mixtures of imidazolium based ionic liquids. *Vibrational Spectroscopy - VIB SPECTROSC* **2011,** *55*, 119-125.
155. Babucci, M.; Akçay, A.; Balci, V.; Uzun, A., Thermal Stability Limits of Imidazolium Ionic Liquids Immobilized on Metal-Oxides. *Langmuir* **2015,** *31* (33), 9163-9176.

156. Akçay, A.; Balci, V.; Uzun, A., Structural factors controlling thermal stability of imidazolium ionic liquids with 1-n-butyl-3-methylimidazolium cation on γ-Al_2O_3. *Thermochimica Acta* **2014,** *589*, 131-136.
157. Wulf, A.; Fumino, K.; Ludwig, R., Spectroscopic Evidence for an Enhanced Anion–Cation Interaction from Hydrogen Bonding in Pure Imidazolium Ionic Liquids. *Angewandte Chemie International Edition* **2010,** *49* (2), 449-453.
158. Chavan, S.; Vitillo, J. G.; Gianolio, D.; Zavorotynska, O.; Civalleri, B.; Jakobsen, S.; Nilsen, M. H.; Valenzano, L.; Lamberti, C.; Lillerud, K. P.; Bordiga, S., H_2 storage in isostructural UiO-67 and UiO-66 MOFs. *Physical Chemistry Chemical Physics* **2012,** *14* (5), 1614-1626.
159. Valenzano, L.; Civalleri, B.; Chavan, S.; Bordiga, S.; Nilsen, M. H.; Jakobsen, S.; Lillerud, K. P.; Lamberti, C., Disclosing the Complex Structure of UiO-66 Metal Organic Framework: A Synergic Combination of Experiment and Theory. *Chemistry of Materials* **2011,** *23* (7), 1700-1718.
160. Yang, P.; Liu, Q.; Liu, J.; Zhang, H.; Li, Z.; Li, R.; Liu, L.; Wang, J., Interfacial growth of a metal–organic framework (UiO-66) on functionalized graphene oxide (GO) as a suitable seawater adsorbent for extraction of uranium(vi). *Journal of Materials Chemistry A* **2017,** *5* (34), 17933-17942.
161. Vellingiri, K.; Kumar, P.; Deep, A.; Kim, K.-H., Metal-organic frameworks for the adsorption of gaseous toluene under ambient temperature and pressure. *Chemical Engineering Journal* **2017,** *307*, 1116-1126.
162. Shen, L.; Liang, S.; Wu, W.; Liang, R.; Wu, L., Multifunctional NH_2-mediated zirconium metal-organic framework as an efficient visible-light-driven photocatalyst for selective oxidation of alcohols and reduction of aqueous Cr(VI). *Dalton Trans* **2013,** *42* (37), 13649-57.
163. Cavka, J. H.; Jakobsen, S.; Olsbye, U.; Guillou, N.; Lamberti, C.; Bordiga, S.; Lillerud, K. P., A New Zirconium Inorganic Building Brick Forming Metal Organic Frameworks with Exceptional Stability. *Journal of the American Chemical Society* **2008,** *130* (42), 13850-13851.
164. Zhu, J.; Wu, L.; Bu, Z.; Jie, S.; Li, B.-G., Polyethyleneimine-Modified UiO-66-NH_2(Zr) Metal–Organic Frameworks: Preparation and Enhanced CO_2 Selective Adsorption. *ACS Omega* **2019,** *4* (2), 3188-3197.
165. Abid, H. R.; Rada, Z. H.; Shang, J.; Wang, S., Synthesis, characterization, and CO_2 adsorption of three metal-organic frameworks (MOFs): MIL-53, MIL-96, and amino-MIL-53. *Polyhedron* **2016,** *120*, 103-111.
166. Kandiah, M.; Usseglio, S.; Svelle, S.; Olsbye, U.; Lillerud, K. P.; Tilset, M., Post-synthetic modification of the metal–organic framework compound UiO-66. *Journal of Materials Chemistry* **2010,** *20* (44), 9848-9851.
167. Liang, Q.; Zhang, M.; Zhang, Z.; Liu, C.; Xu, S.; Li, Z.-Y., Zinc phthalocyanine coupled with UIO-66 (NH 2) via a facile condensation process for enhanced visible-light-driven photocatalysis. *Journal of Alloys and Compounds* **2017,** *690*, 123-130.
168. Borba, A.; Gómez-Zavaglia, A.; Simões, P. N. N. L.; Fausto, R., Matrix Isolation FTIR Spectroscopic and Theoretical Study of Dimethyl Sulfite. *The Journal of Physical Chemistry A* **2005,** *109* (16), 3578-3586.
169. Luan, Y.; Qi, Y.; Jin, Z.; Peng, X.; Gao, H.; Wang, G., Synthesis of a flower-like Zr-based metal–organic framework and study of its catalytic performance in the Mannich reaction. *RSC Advances* **2015,** *5* (25), 19273-19278.
170. Bai, Y.; Dou, Y.; Xie, L.-H.; Rutledge, W.; Li, J.-R.; Zhou, H.-C., Zr-based metal–organic frameworks: design, synthesis, structure, and applications. *Chemical Society Reviews* **2016,** *45* (8), 2327-2367.
171. Ameloot, R.; Aubrey, M.; Wiers, B. M.; Gómora-Figueroa, A. P.; Patel, S. N.; Balsara, N. P.; Long, J. R., Ionic Conductivity in the Metal–Organic Framework UiO-66 by Dehydration and Insertion of Lithium tert-Butoxide. *Chemistry – A European Journal* **2013,** *19* (18), 5533-5536.
172. Wu, Y.; Xiao, Y.; Yuan, H.; Zhang, Z.; Shi, S.; Wei, R.; Gao, L.; Xiao, G., Imidazolium ionic liquid functionalized UiO-66-NH_2 as highly efficient catalysts for chemical fixation of CO_2 into cyclic carbonates. *Microporous and Mesoporous Materials* **2021,** *310*, 110578.
173. Zhou, Y.; Qu, J., Ionic Liquids as Lubricant Additives: A Review. *ACS Applied Materials & Interfaces* **2017,** *9* (4), 3209-3222.

174. Akçay, A.; Babucci, M.; Balci, V.; Uzun, A., A model to predict maximum tolerable temperatures of metal-oxide-supported 1-n-butyl-3-methylimidazolium based ionic liquids. *Chemical Engineering Science* **2015,** *123*, 588-595.
175. Díaz, M.; Ortiz, A.; Ortiz, I., Progress in the use of ionic liquids as electrolyte membranes in fuel cells. *Journal of Membrane Science* **2014,** *469*, 379-396.
176. Vidal, L.; Riekkola, M.-L.; Canals, A., Ionic liquid-modified materials for solid-phase extraction and separation: A review. *Analytica Chimica Acta* **2012,** *715*, 19-41.
177. Bates, E. D.; Mayton, R. D.; Ntai, I.; Davis, J. H., CO_2 Capture by a Task-Specific Ionic Liquid. *Journal of the American Chemical Society* **2002,** *124* (6), 926-927.
178. Zhou, J.; Sui, H.; Jia, Z.; Yang, Z.; He, L.; Li, X., Recovery and purification of ionic liquids from solutions: a review. *RSC Advances* **2018,** *8* (57), 32832-32864.
179. Kunz, W.; Häckl, K., The hype with ionic liquids as solvents. *Chemical Physics Letters* **2016,** *661*, 6-12.
180. Janani, M.; Prakash, M., Screening of Suitable Size/Pore Dependent IL/UiO-66 Composite for Selective Gas Separation Application. *ECS Transactions* **2022,** *107* (1), 13625-13635.
181. Liu, B.; Li, D.; Yao, J.; Sun, H., Improved CO_2 separation performance and interfacial affinity of mixed matrix membrane by incorporating UiO-66-PEI@[bmim][Tf2N] particles. *Separation and Purification Technology* **2020,** *239*, 116519.
182. Jiang, Y.; Liu, C.; Caro, J.; Huang, A., A new UiO-66-NH_2 based mixed-matrix membranes with high CO_2/CH_4 separation performance. *Microporous and Mesoporous Materials* **2019,** *274*, 203-211.
183. Labropoulos, A. I.; Romanos, G. E.; Kouvelos, E.; Falaras, P.; Likodimos, V.; Francisco, M.; Kroon, M. C.; Iliev, B.; Adamova, G.; Schubert, T. J. S., Alkyl-methylimidazolium Tricyanomethanide Ionic Liquids under Extreme Confinement onto Nanoporous Ceramic Membranes. *The Journal of Physical Chemistry C* **2013,** *117* (19), 10114-10127.
184. Rausch, M. H.; Heller, A.; Herbst, J.; Koller, T. M.; Bahlmann, M.; Schulz, P. S.; Wasserscheid, P.; Fröba, A. P., Mutual and Thermal Diffusivity of Binary Mixtures of the Ionic Liquids [BMIM][C(CN)3] and [BMIM][B(CN)4] with Dissolved CO_2 by Dynamic Light Scattering. *The Journal of Physical Chemistry B* **2014,** *118* (17), 4636-4646.
185. Wißmann, G.; Schaate, A.; Lilienthal, S.; Bremer, I.; Schneider, A. M.; Behrens, P., Modulated synthesis of Zr-fumarate MOF. *Microporous and Mesoporous Materials* **2012,** *152*, 64-70.
186. Zheng, H.-Q.; Zeng, Y.-N.; Chen, J.; Lin, R.-G.; Zhuang, W.-E.; Cao, R.; Lin, Z.-J., Zr-Based Metal–Organic Frameworks with Intrinsic Peroxidase-Like Activity for Ultradeep Oxidative Desulfurization: Mechanism of H_2O_2 Decomposition. *Inorganic Chemistry* **2019,** *58* (10), 6983-6992.
187. Chakarova, K.; Strauss, I.; Mihaylov, M.; Drenchev, N.; Hadjiivanov, K., Evolution of acid and basic sites in UiO-66 and UiO-66-NH_2 metal-organic frameworks: FTIR study by probe molecules. *Microporous and Mesoporous Materials* **2019,** *281*, 110-122.
188. Ganesh, M.; Hemalatha, P.; Peng, M. M.; Cha, W. S.; Jang, H. T., Zr-Fumarate MOF a Novel CO_2-Adsorbing Material: Synthesis and Characterization. *Aerosol and Air Quality Research* **2014,** *14* (6), 1605-1612.
189. Özçelik, G.; Çavuşoğlu, F. C.; Özkara-Aydınoğlu, Ş.; Bayazit, Ş. S., Enhanced & effective phosphate recovery from water by indium fumarate & zirconium fumarate metal-organic frameworks: Synthesis, characterization, adsorption, kinetic and isotherm studies. *Surfaces and Interfaces* **2022,** *29*, 101719.
190. Katz, M. J.; Brown, Z. J.; Colón, Y. J.; Siu, P. W.; Scheidt, K. A.; Snurr, R. Q.; Hupp, J. T.; Farha, O. K., A facile synthesis of UiO-66, UiO-67 and their derivatives. *Chemical Communications* **2013,** *49* (82), 9449-9451.
191. Zeeshan, M.; Keskin, S.; Uzun, A., Enhancing CO_2/CH_4 and CO_2/N_2 separation performances of ZIF-8 by post-synthesis modification with [BMIM][SCN]. *Polyhedron* **2018,** *155*, 485-492.
192. Øien, S.; Wragg, D.; Reinsch, H.; Svelle, S.; Bordiga, S.; Lamberti, C.; Lillerud, K. P., Detailed Structure Analysis of Atomic Positions and Defects in Zirconium Metal–Organic Frameworks. *Crystal Growth & Design* **2014,** *14* (11), 5370-5372.

193. Fang, X.; Wu, S.; Wu, Y.; Yang, W.; Li, Y.; He, J.; Hong, P.; Nie, M.; Xie, C.; Wu, Z.; Zhang, K.; Kong, L.; Liu, J., High-efficiency adsorption of norfloxacin using octahedral UIO-66-NH_2 nanomaterials: Dynamics, thermodynamics, and mechanisms. *Applied Surface Science* **2020,** *518*, 146226.
194. Wu, R.; Qian, X.; Zhou, K.; Liu, H.; Yadian, B.; Wei, J.; Zhu, H.; Huang, Y., Highly dispersed Au nanoparticles immobilized on Zr-based metal–organic frameworks as heterostructured catalyst for CO oxidation. *Journal of Materials Chemistry A* **2013,** *1* (45), 14294-14299.
195. Shaik, M. R.; Adil, S. F.; Alothman, Z. A.; Alduhaish, O. M., Fumarate Based Metal–Organic Framework: An Effective Catalyst for the Transesterification of Used Vegetable Oil. *Crystals* **2022,** *12* (2).
196. Gu, Y.; Anjali, B. A.; Yoon, S.; Choe, Y.; Chung, Y. G.; Park, D.-W., Defect-engineered MOF-801 for cycloaddition of CO_2 with epoxides. *Journal of Materials Chemistry A* **2022,** *10* (18), 10051-10061.
197. Wu, X.; Surendran, A.; Ko, J.; Filonik, O.; Herzig, E. M.; Müller-Buschbaum, P.; Leong, W. L., Ionic-Liquid Doping Enables High Transconductance, Fast Response Time, and High Ion Sensitivity in Organic Electrochemical Transistors. *Advanced Materials* **2019,** *31* (2), 1805544.
198. Deng, J.; Dai, Z.; Deng, L., Synthesis of crosslinked PEG/IL blend membrane via one-pot thiol–ene/epoxy chemistry. *Journal of Polymer Science* **2020,** *58* (18), 2575-2585.
199. Peñalber, C. Y.; Grenoble, Z.; Baker, G. A.; Baldelli, S., Surface characterization of imidazolium-based ionic liquids with cyano-functionalized anions at the gas–liquid interface using sum frequency generation spectroscopy. *Physical Chemistry Chemical Physics* **2012,** *14* (15), 5122-5131.
200. Binaeian, E.; Li, Y.; Tayebi, H.-A.; Yuan, D., Enhancing toxic gas uptake performance of Zr-based MOF through uncoordinated carboxylate and copper insertion; ammonia adsorption. *Journal of Hazardous Materials* **2021,** *416*, 125933.
201. Dai, G.; Li, Z.; Luo, F.; Ai, S.; Chen, B.; Wang, Q., Electrochemical determination of Salmonella typhimurium by using aptamer-loaded gold nanoparticles and a composite prepared from a metal-organic framework (type UiO-67) and graphene. *Microchimica Acta* **2019,** *186* (9), 620.
202. Chen, L.; Chen, H.; Luque, R.; Li, Y., Metal−organic framework encapsulated Pd nanoparticles: towards advanced heterogeneous catalysts. *Chemical Science* **2014,** *5* (10), 3708-3714.
203. Zhang, D.; Zhao, J.; Liu, Q.; Xia, Z., Synthesis and Luminescence Properties of CsPbX3@Uio-67 Composites toward Stable Photoluminescence Convertors. *Inorganic Chemistry* **2019,** *58* (2), 1690-1696.
204. Butova, V. V.; Pankin, I. A.; Burachevskaya, O. A.; Vetlitsyna-Novikova, K. S.; Soldatov, A. V., New fast synthesis of MOF-801 for water and hydrogen storage: Modulator effect and recycling options. *Inorganica Chimica Acta* **2021,** *514*, 120025.
205. Pilcher, J.; Beasley, R., Acute use of oxygen therapy. *Aust Prescr* **2015,** *38* (3), 98-100.
206. Walter, K., Mechanical Ventilation. *JAMA* **2021,** *326* (14), 1452-1452.
207. Boot-Handford, M. E.; Abanades, J. C.; Anthony, E. J.; Blunt, M. J.; Brandani, S.; Mac Dowell, N.; Fernández, J. R.; Ferrari, M.-C.; Gross, R.; Hallett, J. P.; Haszeldine, R. S.; Heptonstall, P.; Lyngfelt, A.; Makuch, Z.; Mangano, E.; Porter, R. T. J.; Pourkashanian, M.; Rochelle, G. T.; Shah, N.; Yao, J. G.; Fennell, P. S., Carbon capture and storage update. *Energy & Environmental Science* **2014,** *7* (1), 130-189.
208. Descamps, C.; Bouallou, C.; Kanniche, M., Efficiency of an Integrated Gasification Combined Cycle (IGCC) power plant including CO_2 removal. *Energy* **2008,** *33* (6), 874-881.
209. Aasberg-Petersen, K.; Bak Hansen, J. H.; Christensen, T. S.; Dybkjaer, I.; Christensen, P. S.; Stub Nielsen, C.; Winter Madsen, S. E. L.; Rostrup-Nielsen, J. R., Technologies for large-scale gas conversion. *Applied Catalysis A: General* **2001,** *221* (1), 379-387.
210. World Health, O. *Oxygen sources and distribution for COVID-19 treatment centres: interim guidance, 4 April 2020*; World Health Organization: Geneva, 2020, 2020.
211. Yang, X.; Yu, Y.; Xu, J.; Shu, H.; Xia, J.; Liu, H.; Wu, Y.; Zhang, L.; Yu, Z.; Fang, M.; Yu, T.; Wang, Y.; Pan, S.; Zou, X.; Yuan, S.; Shang, Y., Clinical course and outcomes of critically ill patients with SARS-CoV-2 pneumonia in Wuhan, China: a single-centered, retrospective, observational study. *Lancet Respir Med* **2020,** *8* (5), 475-481.

212. Arora, A.; Hasan, M. M. F., Flexible oxygen concentrators for medical applications. *Scientific Reports* **2021,** *11* (1), 14317.
213. Moran, A.; Talu, O., Limitations of Portable Pressure Swing Adsorption Processes for Air Separation. *Industrial & Engineering Chemistry Research* **2018,** *57* (35), 11981-11987.
214. Chai, S. W.; Kothare, M. V.; Sircar, S., Rapid Pressure Swing Adsorption for Reduction of Bed Size Factor of a Medical Oxygen Concentrator. *Industrial & Engineering Chemistry Research* **2011,** *50* (14), 8703-8710.
215. Adil, K.; Belmabkhout, Y.; Pillai, R. S.; Cadiau, A.; Bhatt, P. M.; Assen, A. H.; Maurin, G.; Eddaoudi, M., Gas/vapour separation using ultra-microporous metal–organic frameworks: insights into the structure/separation relationship. *Chemical Society Reviews* **2017,** *46* (11), 3402-3430.
216. Li, J.-R.; Kuppler, R. J.; Zhou, H.-C., Selective gas adsorption and separation in metal–organic frameworks. *Chemical Society Reviews* **2009,** *38* (5), 1477-1504.
217. Jaffe, A.; Ziebel, M. E.; Halat, D. M.; Biggins, N.; Murphy, R. A.; Chakarawet, K.; Reimer, J. A.; Long, J. R., Selective, High-Temperature O_2 Adsorption in Chemically Reduced, Redox-Active Iron-Pyrazolate Metal–Organic Frameworks. *Journal of the American Chemical Society* **2020,** *142* (34), 14627-14637.
218. Rosen, A. S.; Mian, M. R.; Islamoglu, T.; Chen, H.; Farha, O. K.; Notestein, J. M.; Snurr, R. Q., Tuning the Redox Activity of Metal–Organic Frameworks for Enhanced, Selective O_2 Binding: Design Rules and Ambient Temperature O_2 Chemisorption in a Cobalt–Triazolate Framework. *Journal of the American Chemical Society* **2020,** *142* (9), 4317-4328.
219. Murray, L. J.; Dinca, M.; Yano, J.; Chavan, S.; Bordiga, S.; Brown, C. M.; Long, J. R., Highly-Selective and Reversible O_2 Binding in Cr_3(1,3,5-benzenetricarboxylate)$_2$. *Journal of the American Chemical Society* **2010,** *132* (23), 7856-7857.
220. Bloch, E. D.; Queen, W. L.; Hudson, M. R.; Mason, J. A.; Xiao, D. J.; Murray, L. J.; Flacau, R.; Brown, C. M.; Long, J. R., Hydrogen Storage and Selective, Reversible O_2 Adsorption in a Metal–Organic Framework with Open Chromium(II) Sites. *Angewandte Chemie International Edition* **2016,** *55* (30), 8605-8609.
221. Bloch, E. D.; Murray, L. J.; Queen, W. L.; Chavan, S.; Maximoff, S. N.; Bigi, J. P.; Krishna, R.; Peterson, V. K.; Grandjean, F.; Long, G. J.; Smit, B.; Bordiga, S.; Brown, C. M.; Long, J. R., Selective Binding of O_2 over N_2 in a Redox–Active Metal–Organic Framework with Open Iron(II) Coordination Sites. *Journal of the American Chemical Society* **2011,** *133* (37), 14814-14822.
222. Xiao, D. J.; Gonzalez, M. I.; Darago, L. E.; Vogiatzis, K. D.; Haldoupis, E.; Gagliardi, L.; Long, J. R., Selective, Tunable O_2 Binding in Cobalt(II)–Triazolate/Pyrazolate Metal–Organic Frameworks. *Journal of the American Chemical Society* **2016,** *138* (22), 7161-7170.
223. Reed, D. A.; Xiao, D. J.; Jiang, H. Z. H.; Chakarawet, K.; Oktawiec, J.; Long, J. R., Biomimetic O_2 adsorption in an iron metal–organic framework for air separation. *Chemical Science* **2020,** *11* (6), 1698-1702.
224. Tang, Y.; Wang, X.; Wen, Y.; Zhou, X.; Li, Z., Oxygen-Selective Adsorption Property of Ultramicroporous MOF Cu(Qc)$_2$ for Air Separation. *Industrial & Engineering Chemistry Research* **2020,** *59* (13), 6219-6225.
225. Southon, P. D.; Price, D. J.; Nielsen, P. K.; McKenzie, C. J.; Kepert, C. J., Reversible and Selective O_2 Chemisorption in a Porous Metal–Organic Host Material. *Journal of the American Chemical Society* **2011,** *133* (28), 10885-10891.
226. Li, Y.; Yang, R. T., Gas Adsorption and Storage in Metal−Organic Framework MOF-177. *Langmuir* **2007,** *23* (26), 12937-12944.
227. Kinik, F. P.; Uzun, A.; Keskin, S., Ionic Liquid/Metal–Organic Framework Composites: From Synthesis to Applications. *ChemSusChem* **2017,** *10* (14), 2842-2863.
228. Durak, O.; Zeeshan, M.; Habib, N.; Gulbalkan, H. C.; Alsuhile, A. A. A. M.; Caglayan, H. P.; Kurtoğlu-Öztulum, S. F.; Zhao, Y.; Haslak, Z. P.; Uzun, A.; Keskin, S., Composites of porous materials with ionic liquids: Synthesis, characterization, applications, and beyond. *Microporous and Mesoporous Materials* **2022,** *332*, 111703.
229. Durak, O.; Zeeshan, M.; Keskin, S.; Uzun, A., [BMIM][OAc] coating layer makes activated carbon almost completely selective for CO_2. *Chemical Engineering Journal* **2022,** *437*, 135436.

230. Drake, H. F.; Day, G. S.; Vali, S. W.; Xiao, Z.; Banerjee, S.; Li, J.; Joseph, E. A.; Kuszynski, J. E.; Perry, Z. T.; Kirchon, A.; Ozdemir, O. K.; Lindahl, P. A.; Zhou, H.-C., The thermally induced decarboxylation mechanism of a mixed-oxidation state carboxylate-based iron metal–organic framework. *Chemical Communications* **2019,** *55* (85), 12769-12772.
231. Salleh, Z.; Wazeer, I.; Mulyono, S.; El-blidi, L.; Hashim, M. A.; Hadj-Kali, M. K., Efficient removal of benzene from cyclohexane-benzene mixtures using deep eutectic solvents – COSMO-RS screening and experimental validation. *The Journal of Chemical Thermodynamics* **2017,** *104*, 33-44.
232. Chin Ting, H.; Warsi Khan, H.; Vijaya Bhaskar Reddy, A.; Goto, M.; Moniruzzaman, M., Extraction of salicylic acid from wastewater using ionic liquid-based green emulsion liquid membrane: COSMO-RS prediction and experimental verification. *Journal of Molecular Liquids* **2022,** *347*, 118280.
233. Daglar, H.; Erucar, I.; Keskin, S., Exploring the performance limits of MOF/polymer MMMs for O_2/N_2 separation using computational screening. *Journal of Membrane Science* **2021,** *618*, 118555.
234. Yan, Y.; Shi, Z.; Li, H.; Li, L.; Yang, X.; Li, S.; Liang, H.; Qiao, Z., Machine learning and in-silico screening of metal–organic frameworks for O_2/N_2 dynamic adsorption and separation. *Chemical Engineering Journal* **2022,** *427*, 131604.
235. Orhan, I. B.; Daglar, H.; Keskin, S.; Le, T. C.; Babarao, R., Prediction of O_2/N_2 Selectivity in Metal–Organic Frameworks via High-Throughput Computational Screening and Machine Learning. *ACS Applied Materials & Interfaces* **2022,** *14* (1), 736-749.
236. Kerlé, D.; Ludwig, R.; Geiger, A.; Paschek, D., Temperature Dependence of the Solubility of Carbon Dioxide in Imidazolium-Based Ionic Liquids. *The Journal of Physical Chemistry B* **2009,** *113* (38), 12727-12735.
237. Indra, S.; Daschakraborty, S., Nonpolar solvation dynamics for a nonpolar solute in room temperature ionic liquid: a nonequilibrium molecular dynamics simulation study. *Journal of Chemical Sciences* **2018,** *130* (1), 3.
238. Feng, D.; Wang, K.; Wei, Z.; Chen, Y.-P.; Simon, C. M.; Arvapally, R. K.; Martin, R. L.; Bosch, M.; Liu, T.-F.; Fordham, S.; Yuan, D.; Omary, M. A.; Haranczyk, M.; Smit, B.; Zhou, H.-C., Kinetically tuned dimensional augmentation as a versatile synthetic route towards robust metal–organic frameworks. *Nature Communications* **2014,** *5* (1), 5723.
239. Khan, M. W.; Sadiq, M. M.; Gopalsamy, K.; Xu, K.; Jannat, A.; Zhang, B. Y.; Mohiuddin, M.; Haris, M.; Ou, R.; Afrin, S.; Alkathiri, T.; Loomba, S.; Mulet, X.; Mahmood, N.; Babarao, R.; Ou, J. Z., Hetero-metallic metal-organic frameworks for room-temperature NO_2 sensing. *Journal of Colloid and Interface Science* **2022,** *610*, 304-312.
240. An, J.-R.; Wang, Y.; Dong, W.-W.; Gao, X.-J.; Yang, O.-Y.; Liu, Y.-L.; Zhao, J.; Li, D.-S., Efficient Visible-Light Photoreduction of CO_2 to CH_4 over an Fe-Based Metal–Organic Framework (PCN-250-Fe3) in a Solid–Gas Mode. *ACS Applied Energy Materials* **2022,** *5* (2), 2384-2390.
241. Mohamed, M. G.; Hsiao, C.-H.; Hsu, K.-C.; Lu, F.-H.; Shih, H.-K.; Kuo, S.-W., Supramolecular functionalized polybenzoxazines from azobenzene carboxylic acid/azobenzene pyridine complexes: synthesis, surface properties, and specific interactions. *RSC Advances* **2015,** *5* (17), 12763-12772.
242. Dias, A. M. A.; Marceneiro, S.; Braga, M. E. M.; Coelho, J. F. J.; Ferreira, A. G. M.; Simões, P. N.; Veiga, H. I. M.; Tomé, L. C.; Marrucho, I. M.; Esperança, J. M. S. S.; Matias, A. A.; Duarte, C. M. M.; Rebelo, L. P. N.; de Sousa, H. C., Phosphonium-based ionic liquids as modifiers for biomedical grade poly(vinyl chloride). *Acta Biomaterialia* **2012,** *8* (3), 1366-1379.
243. Doney, S. C.; Fabry, V. J.; Feely, R. A.; Kleypas, J. A., Ocean acidification: The other CO_2 problem. *Ann. Rev. Mar. Sci.* **2009,** *1*, 169-192.
244. Panwar, N. L.; Kaushik, S. C.; Kothari, S., Role of renewable energy sources in environmental protection: A review. *Renew. Sustain. Energy Rev.* **2011,** *15* (3), 1513-1524.
245. Li, L.; Wong-Ng, W.; Huang, K.; Cook, L., *Materials and Processes for* CO_2 *Capture, Conversion, and Sequestration*. John Wiley & Sons, Inc.: 2018.
246. D'Alessandro, D. M.; Smit, B.; Long, J. R., Carbon dioxide capture: Prospects for new materials. *Angew. Chem. Int. Ed.* **2010,** *49* (35), 6058-6082.

247. Rada, Z. H.; Abid, H. R.; Shang, J.; Sun, H.; He, Y.; Webley, P.; Liu, S.; Wang, S., Functionalized UiO-66 by Single and Binary (OH)2 and NO_2 Groups for Uptake of CO_2 and CH_4. *Ind. Eng. Chem. Res.* **2016,** *55* (29), 7924-7932.
248. Harlick, P. J. E.; Tezel, F. H., Adsorption of carbon dioxide, methane and nitrogen: pure and binary mixture adsorption for ZSM-5 with SiO_2/Al_2O_3 ratio of 280. *Sep. Purif. Technol.* **2003,** *33* (2), 199-210.
249. McEwen, J.; Hayman, J.-D.; Yazaydin, A. O., A comparative study of CO_2, CH_4 and N_2 adsorption in ZIF-8, Zeolite-13X and BPL activated carbon. *Chem. Phys.* **2013,** *412*, 72-76.
250. Ganesan, A.; Shaijumon, M. M., Activated graphene-derived porous carbon with exceptional gas adsorption properties. *Microporous Mesoporous Mater.* **2016,** *220*, 21-27.
251. Li, Y.; Xu, R.; Wang, B.; Wei, J.; Wang, L.; Shen, M.; Yang, J., Enhanced N-doped Porous Carbon Derived from KOH-Activated Waste Wool: A Promising Material for Selective Adsorption of CO_2/CH_4 and CH_4/N_2. *Nanomaterials* **2019,** *9* (2), 266.
252. Sui, Z.-Y.; Meng, Y.-N.; Xiao, P.-W.; Zhao, Z.-Q.; Wei, Z.-X.; Han, B.-H., Nitrogen-Doped Graphene Aerogels as Efficient Supercapacitor Electrodes and Gas Adsorbents. *ACS Appl. Mater. Interfaces* **2015,** *7* (3), 1431-1438.
253. Sawant, S. Y.; Somani Rs Fau - Bajaj, H. C.; Bajaj Hc Fau - Sharma, S. S.; Sharma, S. S., A dechlorination pathway for synthesis of horn shaped carbon nanotubes and its adsorption properties for CO_2, CH_4, CO and N_2. *J. Hazard. Mater.* **2012,** *227-228* (1873-3336 (Electronic)).
254. Li, D.; Wang, Y.; Zhang, X.; Zhou, J.; Yang, Y.; Zhang, Z.; Wei, L.; Tian, Y.; Zhao, X., Effects of compacting activated carbons on their volumetric CO_2 adsorption performance. *Fuel* **2020,** *262*, 116540.
255. Zhang, X.-X.; Xiao, P.; Chen, G.-J.; Sun, C.-Y.; Yang, L.-Y., Separation of Methane and Carbon Dioxide Gas Mixtures Using Activated Carbon Modified with 2-Methylimidazole. *Chem. Eng. Technol.* **2018,** *41* (9), 1818-1825.
256. Himeno, S.; Komatsu, T.; Fujita, S., High-Pressure Adsorption Equilibria of Methane and Carbon Dioxide on Several Activated Carbons. *J. Chem. Eng. Data* **2005,** *50* (2), 369-376.
257. Pires, J.; Saini, V. K.; Pinto, M. L., Studies on Selective Adsorption of Biogas Components on Pillared Clays: Approach for Biogas Improvement. *Environ. Sci. Technol.* **2008,** *42* (23), 8727-8732.
258. Bae, Y.-S.; Snurr, R. Q., Development and Evaluation of Porous Materials for Carbon Dioxide Separation and Capture. *Angew. Chem. Int. Ed.* **2011,** *50* (49), 11586-11596.
259. Choi, S.; Drese, J. H.; Jones, C. W., Adsorbent materials for carbon dioxide capture from large anthropogenic point sources. *ChemSusChem* **2009,** *2* (9), 796-854.
260. Rios, R. B.; Stragliotto, F. M.; Peixoto, H. R.; Torres, A. E. B.; Bastos-Neto, M.; Azevedo, D. C. S.; Cavalcante Jr, C. L., Studies on the adsorption behavior of CO_2-CH_4 mixtures using activated carbon. *Braz. J. Chem. Eng.* **2013,** *30*, 939-951.
261. Oschatz, M.; Antonietti, M., A search for selectivity to enable CO_2 capture with porous adsorbents. *Energy Environ. Sci.* **2018,** *11* (1), 57-70.
262. Xu, C.; Hedin, N., Microporous adsorbents for CO_2 capture – a case for microporous polymers? *Mater. Today* **2014,** *17* (8), 397-403.
263. Patel, H. A.; Byun, J.; Yavuz, C. T., Carbon Dioxide Capture Adsorbents: Chemistry and Methods. *ChemSusChem* **2017,** *10* (7), 1303-1317.
264. Fujie, K.; Kitagawa, H., Ionic liquid transported into metal–organic frameworks. *Coord. Chem. Rev.* **2016,** *307*, 382-390.
265. Cota, I.; Fernandez Martinez, F., Recent advances in the synthesis and applications of metal organic frameworks doped with ionic liquids for CO_2 adsorption. *Coord. Chem. Rev.* **2017,** *351*, 189-204.
266. Zhang, Y.; Wu, M.-X.; Zhou, G.; Wang, X.-H.; Liu, X., A Rising Star from Two Worlds: Collaboration of COFs and ILs. *Adv. Funct. Mater.* **2021,** *n/a* (n/a), 2104996.
267. Ferreira, T. J.; Ribeiro, R. P. P. L.; Mota, J. P. B.; Rebelo, L. P. N.; Esperança, J. M. S. S.; Esteves, I. A. A. C., Ionic Liquid-Impregnated Metal–Organic Frameworks for CO_2/CH_4 Separation. *ACS Applied Nano Materials* **2019,** *2* (12), 7933-7950.

268. Ramos, V. C.; Han, W.; Zhang, X.; Zhang, S.; Yeung, K. L., Supported ionic liquids for air purification. *Current Opinion in Green and Sustainable Chemistry* **2020,** *25*, 100391.
269. Chen, C.; Feng, N.; Guo, Q.; Li, Z.; Li, X.; Ding, J.; Wang, L.; Wan, H.; Guan, G., Surface engineering of a chromium metal-organic framework with bifunctional ionic liquids for selective CO_2 adsorption: Synergistic effect between multiple active sites. *J. Colloid Interface Sci.* **2018,** *521*, 91-101.
270. Maginn, E. *Design and Evaluation of Ionic Liquids as Novel* CO_2 *Absorbents. Quarterly Technical Report to DOE.*; 01/01, 2007.
271. Zeng, S.; Zhang, X.; Bai, L.; Zhang, X.; Wang, H.; Wang, J.; Bao, D.; Li, M.; Liu, X.; Zhang, S., Ionic-Liquid-Based CO_2 Capture Systems: Structure, Interaction and Process. *Chem. Rev.* **2017,** *117* (14), 9625-9673.
272. Gurkan, B. E.; de la Fuente, J. C.; Mindrup, E. M.; Ficke, L. E.; Goodrich, B. F.; Price, E. A.; Schneider, W. F.; Brennecke, J. F., Equimolar CO_2 Absorption by Anion-Functionalized Ionic Liquids. *J. Am. Chem. Soc.* **2010,** *132* (7), 2116-2117.
273. Shi, W.; Myers, C. R.; Luebke, D. R.; Steckel, J. A.; Sorescu, D. C., Theoretical and Experimental Studies of CO_2 and H_2 Separation Using the 1-Ethyl-3-methylimidazolium Acetate ([emim][CH3COO]) Ionic Liquid. *J. Phys. Chem. B.* **2012,** *116* (1), 283-295.
274. MacFarlane, D. R.; Forsyth, M.; Howlett, P. C.; Kar, M.; Passerini, S.; Pringle, J. M.; Ohno, H.; Watanabe, M.; Yan, F.; Zheng, W.; Zhang, S.; Zhang, J., Ionic liquids and their solid-state analogues as materials for energy generation and storage. *Nature Reviews Materials* **2016,** *1* (2), 15005.
275. Greer, A. J.; Jacquemin, J.; Hardacre, C., Industrial Applications of Ionic Liquids. *Molecules* **2020,** *25* (21).
276. Ban, Y.; Li, Z.; Li, Y.; Peng, Y.; Jin, H.; Jiao, W.; Guo, A.; Wang, P.; Yang, Q.; Zhong, C.; Yang, W., Confinement of Ionic Liquids in Nanocages: Tailoring the Molecular Sieving Properties of ZIF-8 for Membrane-Based CO_2 Capture. *Angew. Chem. Int. Ed.* **2015,** *54* (51), 15483-15487.
277. Besnard, M.; Cabaço Mi Fau - Chávez, F. V.; Chávez Fv Fau - Pinaud, N.; Pinaud N Fau - Sebastião, P. J.; Sebastião Pj Fau - Coutinho, J. A. P.; Coutinho Ja Fau - Danten, Y.; Danten, Y., On the spontaneous carboxylation of 1-butyl-3-methylimidazolium acetate by carbon dioxide. *Chem. Commun.* **2012,** (1364-548X (Electronic)).
278. Besnard, M.; Cabaço, M. I.; Vaca Chávez, F.; Pinaud, N.; Sebastião, P. J.; Coutinho, J. A. P.; Mascetti, J.; Danten, Y., CO_2 in 1-Butyl-3-methylimidazolium Acetate. 2. NMR Investigation of Chemical Reactions. *J. Phys. Chem. A* **2012,** *116* (20), 4890-4901.
279. Mao, J. X.; Steckel, J. A.; Yan, F.; Dhumal, N.; Kim, H.; Damodaran, K., Understanding the mechanism of CO_2 capture by 1,3 di-substituted imidazolium acetate based ionic liquids. *Phys. Chem. Chem. Phys.* **2016,** *18* (3), 1911-1917.
280. Shiflett, M. B.; Kasprzak, D. J.; Junk, C. P.; Yokozeki, A., Phase behavior of {carbon dioxide+[bmim][Ac]} mixtures. *J. Chem. Thermodyn.* **2008,** *40* (1), 25-31.
281. Gurau, G.; Rodríguez, H.; Kelley, S. P.; Janiczek, P.; Kalb, R. S.; Rogers, R. D., Demonstration of Chemisorption of Carbon Dioxide in 1,3-Dialkylimidazolium Acetate Ionic Liquids. *Angew. Chem. Int. Ed.* **2011,** *50* (50), 12024-12026.
282. Hara, M.; Yoshida, T.; Takagaki, A.; Takata, T.; Kondo, J. N.; Hayashi, S.; Domen, K., A Carbon Material as a Strong Protonic Acid. *Angew. Chem. Int. Ed.* **2004,** *43* (22), 2955-2958.
283. Wang, Y.; Gao S Fau - Zang, X.; Zang X Fau - Li, J.; Li J Fau - Ma, J.; Ma, J., Graphene-based solid-phase extraction combined with flame atomic absorption spectrometry for a sensitive determination of trace amounts of lead in environmental water and vegetable samples. *Anal. Chim. Acta.* **2012,** (1873-4324 (Electronic)).
284. Sivachidambaram, M.; Vijaya, J. J.; Kennedy, L. J.; Jothiramalingam, R.; Al-Lohedan, H. A.; Munusamy, M. A.; Elanthamilan, E.; Merlin, J. P., Preparation and characterization of activated carbon derived from the Borassus flabellifer flower as an electrode material for supercapacitor applications. *New J. Chem.* **2017,** *41* (10), 3939-3949.
285. Sadezky, A.; Muckenhuber, H.; Grothe, H.; Niessner, R.; Pöschl, U., Raman microspectroscopy of soot and related carbonaceous materials: Spectral analysis and structural information. *Carbon* **2005,** *43* (8), 1731-1742.

286. Tunçkol, M.; Serp, P.; Durand, J., Carbon nanomaterial–ionic liquid hybrids. *Carbon* **2012,** *50*, 4303.
287. Fukushima, T.; Kosaka, A.; Ishimura, Y.; Yamamoto, T.; Takigawa, T.; Ishii, N.; Aida, T., Molecular Ordering of Organic Molten Salts Triggered by Single-Walled Carbon Nanotubes. *Science* **2003,** *300* (5628), 2072.
288. Sebastián, D.; Suelves, I.; Moliner, R.; Lázaro, M. J., The effect of the functionalization of carbon nanofibers on their electronic conductivity. *Carbon* **2010,** *48* (15), 4421-4431.
289. Tsuzuki, S.; Honda, K.; Uchimaru, T.; Mikami, M.; Tanabe, K., The Magnitude of the CH/π Interaction between Benzene and Some Model Hydrocarbons. *J. Am. Chem. Soc.* **2000,** *122* (15), 3746-3753.
290. Ding, Y.; Su, D. S., Host-guest nanocomposites of multiwalled carbon nanotubes and ionic liquids with controllable composition. *ChemSusChem* **2014,** *7* (6), 1542-1546.
291. Liu, Y.; Zhang, Y.; Wu, G.; Hu, J., Coexistence of Liquid and Solid Phases of Bmim-PF6 Ionic Liquid on Mica Surfaces at Room Temperature. *J. Am. Chem. Soc.* **2006,** *128* (23), 7456-7457.
292. Chowdhury, F. A.; Hossain, M. A.; Uchida, K.; Tamura, T.; Sugawa, K.; Mochida, T.; Otsuki, J.; Mohiuddin, T.; Boby, M. A.; Alam, M. S., Graphene oxide/carbon nanoparticle thin film based IR detector: Surface properties and device characterization. *AIP Advances* **2015,** *5* (10), 107228.
293. Aydogan Gokturk, P.; Salzner, U.; Nyulászi, L.; Ulgut, B.; Kocabas, C.; Suzer, S., XPS-evidence for in-situ electrochemically-generated carbene formation. *Electrochim. Acta* **2017,** *234*, 37-42.
294. Sobota, M.; Happel, M.; Amende, M.; Paape, N.; Wasserscheid, P.; Laurin, M.; Libuda, J., Ligand Effects in SCILL Model Systems: Site-Specific Interactions with Pt and Pd Nanoparticles. *Adv. Mater.* **2011,** *23* (22-23), 2617-2621.
295. Meusel, M.; Lexow, M.; Gezmis, A.; Bayer, A.; Maier, F.; Steinrück, H.-P., Growth of Multilayers of Ionic Liquids on Au(111) Investigated by Atomic Force Microscopy in Ultrahigh Vacuum. *Langmuir* **2020,** *36* (45), 13670-13681.
296. Geng, A.; Loh, K.-C., Heterogeneity of Surface Energies in Reversed-Phase Perfusive Packings. *J. Colloid Interface Sci.* **2001,** *239* (2), 447-457.
297. Thomas, J. M., The existence of endothermic adsorption. *J. Chem. Educ.* **1961,** *38* (3), 138.
298. Bastos-Neto, M.; Canabrava, D.; Torres, A.; Rodriguez-Castellon, E.; Jiménez-López, A.; Azevedo, D.; Cavalcante Jr, C., Effects of textural and surface characteristics of microporous activated carbons on the methane adsorption capacity at high pressures. *Appl. Surf. Sci.* **2007,** *253*, 5721-5725.
299. Liu, Y.; Wilcox, J., Effects of Surface Heterogeneity on the Adsorption of CO_2 in Microporous Carbons. *Environ. Sci. Technol.* **2012,** *46* (3), 1940-1947.
300. Acevedo, S.; Giraldo, L.; Moreno-Piraján, J. C., Adsorption of CO_2 on Activated Carbons Prepared by Chemical Activation with Cupric Nitrate. *ACS Omega* **2020,** *5* (18), 10423-10432.
301. Lee, S.-Y.; Park, S.-J., Determination of the optimal pore size for improved CO_2 adsorption in activated carbon fibers. *J. Colloid Interface Sci.* **2013,** *389* (1), 230-235.
302. Yan-Fe, C.; Yan-Hong, C.; Dong-Shun, D.; Ning, A.; Long, Y., Density Functional Theory Study on the Mechanism of Absorption of CO_2 by the Ionic Liquid 1-Butyl-3-Methylimidazolium Acetate. *Prog. React. Kinet. Mec.* **2014,** *39* (2), 197-208.
303. Shi, W.; Thompson, R. L.; Albenze, E.; Steckel, J. A.; Nulwala, H. B.; Luebke, D. R., Contribution of the Acetate Anion to CO_2 Solubility in Ionic Liquids: Theoretical Method Development and Experimental Study. *J. Phys. Chem. B.* **2014,** *118* (26), 7383-7394.
304. Tian, Q.; Li, R.; Sun, H.; Xue, Z.; Mu, T., Theoretical and experimental study on the interaction between 1-butyl-3-methylimidazolium acetate and CO_2. *J. Mol. Liq.* **2015,** *208*, 259-268.
305. Lee, M.-S.; Park, M.; Kim, H. Y.; Park, S.-J., Effects of Microporosity and Surface Chemistry on Separation Performances of N-Containing Pitch-Based Activated Carbons for CO_2/N_2 Binary Mixture. *Sci. Rep.* **2016,** *6* (1), 23224.
306. Lv, G.; Li, Z.; Jiang, W.-T.; Xu, S.; Larson, T. E., Ionic liquid modification of zeolite and its removal of chromate from water. *Green Chemistry Letters and Reviews* **2014,** *7* (2), 191-198.

307. Subraveti, S. G.; Roussanaly, S.; Anantharaman, R.; Riboldi, L.; Rajendran, A., How much can novel solid sorbents reduce the cost of post-combustion CO_2 capture? A techno-economic investigation on the cost limits of pressure–vacuum swing adsorption. *Appl. Energy* **2022,** *306*, 117955.
308. Nordio, M.; Wassie, S. A.; Van Sint Annaland, M.; Pacheco Tanaka, D. A.; Viviente Sole, J. L.; Gallucci, F., Techno-economic evaluation on a hybrid technology for low hydrogen concentration separation and purification from natural gas grid. *Int. J. Hydrogen Energy* **2021,** *46* (45), 23417-23435.
309. Ho, M. T.; Allinson, G. W.; Wiley, D. E., Reducing the Cost of CO_2 Capture from Flue Gases Using Pressure Swing Adsorption. *Ind. Eng. Chem. Res.* **2008,** *47* (14), 4883-4890.
310. Sava Gallis, D. F.; Parkes, M. V.; Greathouse, J. A.; Zhang, X.; Nenoff, T. M., Enhanced O_2 Selectivity versus N_2 by Partial Metal Substitution in Cu-BTC. *Chemistry of Materials* **2015,** *27* (6), 2018-2025.
311. Rallapalli, P.; Prasanth, K. P.; Patil, D.; Somani, R. S.; Jasra, R. V.; Bajaj, H. C., Sorption studies of CO_2, CH_4, N_2, CO, O_2 and Ar on nanoporous aluminum terephthalate [MIL-53(Al)]. *Journal of Porous Materials* **2011,** *18* (2), 205-210.
312. Bae, Y.-S.; Spokoyny, A. M.; Farha, O. K.; Snurr, R. Q.; Hupp, J. T.; Mirkin, C. A., Separation of gas mixtures using Co(ii) carborane-based porous coordination polymers. *Chemical Communications* **2010,** *46* (20), 3478-3480.
313. Mahurin, S. M.; Górka, J.; Nelson, K. M.; Mayes, R. T.; Dai, S., Enhanced CO_2/N_2 selectivity in amidoxime-modified porous carbon. *Carbon* **2014,** *67*, 457-464.
314. Zhu, X.; Fu, Y.; Hu, G.; Shen, Y.; Dai, W.; Hu, X., CO_2 Capture with Activated Carbons Prepared by Petroleum Coke and KOH at Low Pressure. *Water Air Soil Pollu.* **2012,** *224* (1), 1387.
315. Khalili, S.; Khoshandam, B.; Jahanshahi, M., A comparative study of CO_2 and CH_4 adsorption using activated carbon prepared from pine cone by phosphoric acid activation. *Korean J. Chem. Eng.* **2016,** *33* (10), 2943-2952.
316. Yang, F.; Wang, J.; Liu, L.; Zhang, P.; Yu, W.; Deng, Q.; Zeng, Z.; Deng, S., Synthesis of Porous Carbons with High N-Content from Shrimp Shells for Efficient CO_2-Capture and Gas Separation. *ACS Sustain. Chem. Eng.* **2018,** *6* (11), 15550-15559.
317. Yuan, B.; Wu, X.; Chen, Y.; Huang, J.; Luo, H.; Deng, S., Adsorption of CO_2, CH_4, and N_2 on Ordered Mesoporous Carbon: Approach for Greenhouse Gases Capture and Biogas Upgrading. *Environ. Sci. Technol.* **2013,** *47* (10), 5474-5480.
318. Christian Kemp, K.; Chandra, V.; Saleh, M.; Kim, K. S., Reversible CO_2adsorption by an activated nitrogen doped graphene/polyaniline material. *Nanotechnology* **2013,** *24* (23), 235703.
319. Ma, X.; Cao, M.; Hu, C., Bifunctional HNO_3 catalytic synthesis of N-doped porous carbons for CO_2 capture. *J. Mater. Chem. A* **2013,** *1* (3), 913-918.
320. Saini, V. K.; Andrade, M.; Pinto, M. L.; Carvalho, A. P.; Pires, J., How the adsorption properties get changed when going from SBA-15 to its CMK-3 carbon replica. *Sep. Purif. Technol.* **2010,** *75* (3), 366-376.
321. Himeno, S.; Komatsu, T.; Fujita, S., Development of a New Effective Biogas Adsorption Storage Technology. *Adsorption* **2005,** *11* (1), 899-904.
322. Huang, W.; Zhou, X.; Xia, Q.; Peng, J.; Wang, H.; Li, Z., Preparation and Adsorption Performance of GrO@Cu-BTC for Separation of CO_2/CH_4. *Ind. Eng. Chem. Res.* **2014,** *53* (27), 11176-11184.
323. Xue, C.; Hao, W.; Cheng, W.; Ma, J.; Li, R., CO Adsorption Performance of CuCl/Activated Carbon by Simultaneous Reduction–Dispersion of Mixed Cu(II) Salts. *Materials* **2019,** *12* (10).
324. Mane, S.; Kanase, D. G., Catalyst-free development of high yielded N-doped microporous carbons for efficient selective CO_2 separation. *New J. Chem.* **2021**.
325. Wang J Fau - Krishna, R.; Krishna, R.; Yang, J.; Deng, S., Hydroquinone and Quinone-Grafted Porous Carbons for Highly Selective CO_2 Capture from Flue Gases and Natural Gas Upgrading. *Environ. Sci. Tech.* **2015,** *49* (15), 9364-9373.
326. Banaei, M.; Anbia, M.; Kazemipour, M., Enhancement of CO_2/CH_4 Adsorptive Selectivity by Functionalized Nano Zeolite. *J. Ultrafine Grained Nanostruct. Mater.* **2018,** *51* (2), 174-182.
327. Nugent, P.; Belmabkhout Y Fau - Burd, S. D.; Burd Sd Fau - Cairns, A. J.; Cairns Aj Fau - Luebke, R.; Luebke R Fau - Forrest, K.; Forrest K Fau - Pham, T.; Pham T Fau - Ma, S.; Ma S Fau -

Space, B.; Space B Fau - Wojtas, L.; Wojtas L Fau - Eddaoudi, M.; Eddaoudi M Fau - Zaworotko, M. J.; Zaworotko, M. J., Porous materials with optimal adsorption thermodynamics and kinetics for CO_2 separation. *Nature* **2013,** *495* (7439), 80-84.
328. Bae, Y.-S.; Mulfort, K. L.; Frost, H.; Ryan, P.; Punnathanam, S.; Broadbelt, L. J.; Hupp, J. T.; Snurr, R. Q., Separation of CO_2 from CH_4 Using Mixed-Ligand Metal−Organic Frameworks. *Langmuir* **2008,** *24* (16), 8592-8598.
329. Mishra, P.; Mekala, S.; Dreisbach, F.; Mandal, B.; Gumma, S., Adsorption of CO_2, CO, CH_4 and N_2 on a zinc based metal organic framework. *Sep. Purif. Technol.* **2012,** *94*, 124-130.
330. Mu, B.; Li, F.; Walton, K. S., A novel metal–organic coordination polymer for selective adsorption of CO_2 over CH_4. *Chem. Commun.* **2009,** (18), 2493-2495.
331. Liu, X.; Li, J.; Zhou, L.; Huang, D.; Zhou, Y., Adsorption of CO_2, CH_4 and N_2 on ordered mesoporous silica molecular sieve. *Chem. Phys. Lett.* **2005,** *415* (4), 198-201.
332. Belmabkhout, Y.; Sayari, A., Adsorption of CO_2 from dry gases on MCM-41 silica at ambient temperature and high pressure. 2: Adsorption of CO_2/N_2, CO_2/CH_4 and CO_2/H_2 binary mixtures. *Chem. Eng. Sci.* **2009,** *64* (17), 3729-3735.
333. Wang, Z.; Zheng, B.; Liu, H.; Lin, X.; Yu, X.; Yi, P.; Yun, R., High-Capacity Gas Storage by a Microporous Oxalamide-Functionalized NbO-Type Metal–Organic Framework. *Cryst. Growth Des.* **2013,** *13* (11), 5001-5006.
334. Zheng, B.; Lin, X.; Wang, Z.; Yun, R.; Fan, Y.; Ding, M.; Hu, X.; Yi, P., Enhanced water stability of a microporous acylamide-functionalized metal–organic framework via interpenetration and methyl decoration. *CrystEngComm* **2014,** *16* (41), 9586-9589.
335. Zheng, B.; Wang, H.; Wang, Z.; Ozaki, N.; Hang, C.; Luo, X.; Huang, L.; Zeng, W.; Yang, M.; Duan, J., A highly porous rht-type acylamide-functionalized metal–organic framework exhibiting large CO_2 uptake capabilities. *Chem. Commun.* **2016,** *52* (88), 12988-12991.
336. Wang, Z.; Luo, X.; Zheng, B.; Huang, L.; Hang, C.; Jiao, Y.; Cao, X.; Zeng, W.; Yun, R., Highly Selective Carbon Dioxide Capture and Cooperative Catalysis of a Water-Stable Acylamide-Functionalized Metal–Organic Framework. *Eur. J. Inorg. Chem.* **2018,** *2018* (11), 1309-1314.
337. Zhang, W.; Huang H Fau - Zhong, C.; Zhong C Fau - Liu, D.; Liu, D., Cooperative effect of temperature and linker functionality on CO_2 capture from industrial gas mixtures in metal-organic frameworks: a combined experimental and molecular simulation study. *Phys. Chem. Chem. Phys.* **2012,** *14* (1463-9084 (Electronic)).
338. Kavak, S.; Polat, H.; Kulak, H.; Keskin, S.; Uzun, A., MIL-53(Al) as a Versatile Platform for Ionic-Liquid/MOF Composites to Enhance CO_2 Selectivity over CH_4 and N_2. (1861-471X (Electronic)).
339. He, T.; Zhang, Y. Z.; Wu, H.; Kong, X. J.; Liu, X. M.; Xie, L. H.; Dou, Y.; Li, J. R., Functionalized Base-Stable Metal-Organic Frameworks for Selective CO_2 Adsorption and Proton Conduction. *ChemPhysChem* **2017,** *18* (1439-7641 (Electronic)).
340. Stavitski, E.; Pidko, E. A.; Couck, S.; Remy, T.; Hensen, E. J. M.; Weckhuysen, B. M.; Denayer, J.; Gascon, J.; Kapteijn, F., Complexity behind CO_2 Capture on NH_2-MIL-53(Al). *Langmuir* **2011,** *27* (7), 3970-3976.
341. Ning, H.; Yang, Z.; Yin, Z.; Wang, D.; Meng, Z.; Wang, C.; Zhang, Y.; Chen, Z., A Novel Strategy to Enhance the Performance of CO_2 Adsorption Separation: Grafting Hyper-cross-linked Polyimide onto Composites of UiO-66-NH_2 and GO. *ACS Appl. Mater. Interfaces* **2021**.
342. Song, Y.; Zhou, X.; Wang, J. A., Adsorption performance of activated carbon for methane with low concentration at atmospheric pressure. *Energ. Source Part A* **2021,** *43* (11), 1337-1347.
343. Ren, H.; Cunha, E.; Sun, Q.; Li, Z.; Kinloch, I. A.; Young, R. J.; Fan, Z., Surface functionality analysis by Boehm titration of graphene nanoplatelets functionalized via a solvent-free cycloaddition reaction. *Nanoscale Adv.* **2019,** *1* (4), 1432-1441.
344. Meyer, K.; Klobes, P., Comparison between different presentations of pore size distribution in porous materials. *Fresenius J Anal Chem* **1999,** *363* (2), 174-178.
345. Sonal, S.; Prakash, P.; Mishra, B. K.; Nayak, G. C., Synthesis, characterization and sorption studies of a zirconium(iv) impregnated highly functionalized mesoporous activated carbons. *RSC Advances* **2020,** *10* (23), 13783-13798.

346. Okamura, M.; Takagaki, A.; Toda, M.; Kondo, J. N.; Domen, K.; Tatsumi, T.; Hara, M.; Hayashi, S., Acid-Catalyzed Reactions on Flexible Polycyclic Aromatic Carbon in Amorphous Carbon. *Chem. Mater.* **2006,** *18* (13), 3039-3045.
347. do Amaral Junior, M.; Matsushima, J.; Rezende, M. C.; Gonçalves, E.; Marcuzzo, J.; Baldan, M., Production and Characterization of Activated Carbon Fiber from Textile PAN Fiber. *J. Aerosp. Technol. Manag.* **2017,** *9*, 423-430.
348. Saenko, N. S., The X-ray diffraction study of three-dimensional disordered network of nanographites: Experiment and theory. *Phys. Procedia* **2012,** *23*, 102-105.
349. Claramunt, S.; Varea, A.; López-Díaz, D.; Velázquez, M. M.; Cornet, A.; Cirera, A., The Importance of Interbands on the Interpretation of the Raman Spectrum of Graphene Oxide. *J. Phys. Chem. C.* **2015,** *119* (18), 10123-10129.
350. Wang, Y.; Alsmeyer, D. C.; McCreery, R. L., Raman spectroscopy of carbon materials: structural basis of observed spectra. *Chem. Mater.* **1990,** *2* (5), 557-563.
351. Jawhari, T.; Roid, A.; Casado, J., Raman spectroscopic characterization of some commercially available carbon black materials. *Carbon* **1995,** *33* (11), 1561-1565.
352. Chen, W.; Zhou, X.; Shi, S.; Thiphuong, N.; Chen, M., Synergistical enhancement of the electrochemical properties of lignin-based activated carbon using $NH_3 \cdot H_2O$ dielectric barrier discharge plasma. *RSC Advances* **2017,** *7* (12), 7392-7400.
353. Liu, Y.; Liu, X.; Dong, W.; Zhang, L.; Kong, Q.; Wang, W., Efficient Adsorption of Sulfamethazine onto Modified Activated Carbon: A Plausible Adsorption Mechanism. *Sci. Rep.* **2017,** *7*.
354. Romanos, J.; Beckner, M.; Stalla, D.; Tekeei, A.; Suppes, G.; Jalisatgi, S.; Lee, M.; Hawthorne, F.; Robertson, J. D.; Firlej, L.; Kuchta, B.; Wexler, C.; Yu, P.; Pfeifer, P., Infrared study of boron–carbon chemical bonds in boron-doped activated carbon. *Carbon* **2013,** *54*, 208-214.
355. Anisuzzaman, S. M.; Joseph, C. G.; Taufiq-Yap, Y. H.; Krishnaiah, D.; Tay, V. V., Modification of commercial activated carbon for the removal of 2,4-dichlorophenol from simulated wastewater. *J. King Saud Univ. Sci.* **2015,** *27* (4), 318-330.
356. Tran, H. N.; Huang, F.-C.; Lee, C.-K.; Chao, H.-P., Activated carbon derived from spherical hydrochar functionalized with triethylenetetramine: synthesis, characterizations, and adsorption application. *Green Process. Synth.* **2017,** *6* (6), 565-576.
357. Wang, Y.-L.; Laaksonen, A.; Fayer, M. D., Hydrogen Bonding versus π–π Stacking Interactions in Imidazolium–Oxalatoborate Ionic Liquid. *J. Phys. Chem. B.* **2017,** *121* (29), 7173-7179.
358. Ebrahimi, A.; Karimi, P.; Badichi Akher, F.; Behazin, R.; Mostafavi, N., Investigation of the π-π Stacking interactions without direct electrostatic effects of substituents: The aromatic aromatic and aromatic anti-aromatic complexes. *Mol. Phys.* **2014,** *112*.
359. Hashisho, Z.; Rood, M. J.; Barot, S.; Bernhard, J., Role of functional groups on the microwave attenuation and electric resistivity of activated carbon fiber cloth. *Carbon* **2009,** *47* (7), 1814-1823.
360. Lee, J. J.; Yamaguchi, A.; Alam, M. A.; Yamamoto, Y.; Fukushima, T.; Kato, K.; Takata, M.; Fujita, N.; Aida, T., Discotic Ionic Liquid Crystals of Triphenylene as Dispersants for Orienting Single-Walled Carbon Nanotubes. *Angew. Chem. Int. Ed.* **2012,** *51* (34), 8490-8494.
361. Zhang, Z.; Huang, H.; Yang, X.; Zang, L., Tailoring Electronic Properties of Graphene by π–π Stacking with Aromatic Molecules. *J. Phys. Chem. Lett.* **2011,** *2* (22), 2897-2905.
362. Yesudass, S.; Olasunkanmi, Lukman O.; Bahadur, I.; Kabanda, M. M.; Obot, I. B.; Ebenso, Eno E., Experimental and theoretical studies on some selected ionic liquids with different cations/anions as corrosion inhibitors for mild steel in acidic medium. *J. Taiwan Inst. Chem. Eng.* **2016,** *64*, 252-268.
363. Wang, J.; Chu, H.; Li, Y., Why Single-Walled Carbon Nanotubes Can Be Dispersed in Imidazolium-Based Ionic Liquids. *ACS Nano* **2008,** *2* (12), 2540-2546.
364. Ramesh, S.; Ericson, L. M.; Davis, V. A.; Saini, R. K.; Kittrell, C.; Pasquali, M.; Billups, W. E.; Adams, W. W.; Hauge, R. H.; Smalley, R. E., Dissolution of Pristine Single Walled Carbon Nanotubes in Superacids by Direct Protonation. *J. Phys. Chem. B.* **2004,** *108* (26), 8794-8798.

365. Ciunik, Z.; Berski, S.; Latajka, Z.; Leszczyński, J., New aspects of weak C・H···π bonds: intermolecular interactions between alicyclic and aromatic rings in crystals of small compounds, peptides and proteins. *J. Mol. Struct.* **1998,** *442* (1), 125-134.
366. Grabowski, S. J., What Is the Covalency of Hydrogen Bonding? *Chem. Rev.* **2011,** *111* (4), 2597-2625.
367. Di, S.; Xu, Y.; Zhang, Q.; Xu, X.; Zhai, Y.; Wang, B.; He, H.; Wang, Q.; Xu, H.; Jiang, Y.; Zhao, J.; Li, X., Insight into the dispersion behavior of 1-butyl-3-methylimiazolium chloride confined in nanoscale pores of carbon materials. *RSC Advances* **2018,** *8* (43), 24094-24100.
368. Zhang, L.; Tu, L.-y.; Liang, Y.; Chen, Q.; Li, Z.-s.; Li, C.-h.; Wang, Z.-h.; Li, W., Coconut-based activated carbon fibers for efficient adsorption of various organic dyes. *RSC Advances* **2018,** *8* (74), 42280-42291.
369. Hubetska, T.; Kobylinska, N.; García, J. R., Efficient adsorption of pharmaceutical drugs from aqueous solution using a mesoporous activated carbon. *Adsorption* **2020,** *26* (2), 251-266.
370. Nie, Z.; Huang, Y.; Ma, B.; Qiu, X.; Zhang, N.; Xie, X.; Wu, Z., Nitrogen-doped Carbon with Modulated Surface Chemistry and Porous Structure by a Stepwise Biomass Activation Process towards Enhanced Electrochemical Lithium-Ion Storage. *Sci. Rep.* **2019,** *9* (1), 15032.
371. Li, Z.; Zhang, L.; Li, B.; Liu, Z.; Liu, Z.; Wang, H.; Li, Q., Convenient and large-scale synthesis of hollow graphene-like nanocages for electrochemical supercapacitor application. *Chem. Eng. J.* **2017,** *313*, 1242-1250.
372. Ryu, Z.; Rong, H.; Zheng, J.; Wang, M.; Zhang, B., Microstructure and chemical analysis of PAN-based activated carbon fibers prepared by different activation methods. *Carbon* **2002,** *40* (7), 1144-1147.
373. Smith, E. F.; Rutten, F. J. M.; Villar-Garcia, I. J.; Briggs, D.; Licence, P., Ionic Liquids in Vacuo: Analysis of Liquid Surfaces Using Ultra-High-Vacuum Techniques. *Langmuir* **2006,** *22* (22), 9386-9392.
374. Villar-Garcia, I. J.; Lovelock, K. R. J.; Men, S.; Licence, P., Tuning the electronic environment of cations and anions using ionic liquid mixtures. *Chem. Sci.* **2014,** *5* (6), 2573-2579.
375. Men, S.; Mitchell, D. S.; Lovelock, K. R. J.; Licence, P., X-ray Photoelectron Spectroscopy of Pyridinium-Based Ionic Liquids: Comparison to Imidazolium- and Pyrrolidinium-Based Analogues. *ChemPhysChem* **2015,** *16* (10), 2211-2218.
376. Song, X.; Wang, L. a.; Gong, J.; Zhan, X.; Zeng, Y., Exploring a New Method to Study the Effects of Surface Functional Groups on Adsorption of CO_2 and CH_4 on Activated Carbons. *Langmuir* **2020,** *36* (14), 3862-3870.
377. Song, X.; Wang, L. a.; Ma, X.; Zeng, Y., Adsorption equilibrium and thermodynamics of CO_2 and CH_4 on carbon molecular sieves. *Appl. Surf. Sci.* **2017,** *396*, 870-878.
378. Scarano, D.; Bertarione, S.; Spoto, G.; Zecchina, A.; Otero Areán, C., FTIR spectroscopy of hydrogen, carbon monoxide, and methane adsorbed and co-adsorbed on zinc oxide. *Thin Solid Films* **2001,** *400* (1), 50-55.
379. Hao, S.; Yu, Z.; Liu, X., Surface Modification of Activated Carbon and its Effects on Methane Adsorption. *Appl. Mech. Mater.* **2013,** *395-396*, 605-609.
380. Wang, Z.; Zhang, S.; Zhang, X.; Li, P.; Li, J., Effect of microstructure and chemical composition of coal on methane adsorption. *J. Nat. Gas. Sc.i Eng.* **2020,** *82*, 103507.
381. Rehman, A.; Park, M.; Park, S.-J., Current Progress on the Surface Chemical Modification of Carbonaceous Materials. *Coatings* **2019,** *9* (2).
382. Zheng, Y.; Li, Q.; Yuan, D.; Zhang, G.; Liu, J.; Yuan, C.; Tao, Q., Chemical structure of coal surface and its effects on methane adsorption under different temperature conditions. *Adsorption* **2018,** *24* (7), 613-628.
383. Yoshida, H.; Yamazaki, T.; Ozawa, S., IR Spectra of CH_4 Physisorbed on an Active Carbon at Low Temperature. *J. Colloid Interface Sci.* **2000,** *224* (2), 261-264.
384. Li, C.; Li, G.; Xin, Q., FT-IR Spectroscopic Studies of Methane Adsorption on Magnesium Oxide. *J. Phys. Chem.* **1994,** *98* (7), 1933-1938.

385. Errahali, M.; Gatti, G.; Tei, L.; Canti, L.; Fraccarollo, A.; Cossi, M.; Marchese, L., Understanding Methane Adsorption in Porous Aromatic Frameworks: An FTIR, Raman, and Theoretical Combined Study. *J. Phys. Chem. C.* **2014,** *118* (19), 10053-10060.
386. Hesse-Ertelt, S.; Heinze, T.; Kosan, B.; Schwikal, K.; Meister, F., Solvent Effects on the NMR Chemical Shifts of Imidazolium-Based Ionic Liquids and Cellulose Therein. *Macromol. Symp.* **2010,** *294* (2), 75-89.
387. Tommasi, I.; Sorrentino, F., Synthesis of 1,3-dialkylimidazolium-2-carboxylates by direct carboxylation of 1,3-dialkylimidazolium chlorides with CO_2. *Tetrahedron Lett.* **2006,** *47* (36), 6453-6456.
388. Zhuang, J.; Li, M.; Pu, Y.; Ragauskas, A. J.; Yoo, C. G., Observation of Potential Contaminants in Processed Biomass Using Fourier Transform Infrared Spectroscopy. *Appl. Sci.* **2020,** *10* (12).
389. Leary, M. H.; Jaworski, R. J.; Hartman, F. C., C nuclear magnetic resonance study of the CO_2 activation of ribulosebisphosphate carboxylase fro. *Proceedings of the National Academy of Sciences* **1979,** *76* (2), 673.
390. Dillinger, S.; Mohrbach, J.; Hewer, J.; Gaffga, M.; Niedner-Schatteburg, G., Infrared spectroscopy of N_2 adsorption on size selected cobalt cluster cations in isolation. *Phys. Chem. Chem. Phys.* **2015,** *17* (16), 10358-10362.
391. D'Alessandro, D. M.; Smit, B.; Long, J. R., Carbon Dioxide Capture: Prospects for New Materials. *Angew. Chem. Int. Ed.* **2010,** *49* (35), 6058-6082.